The Cosmic Twilight Polarimeter: A Model-Independent Approach to Constrain the Synchrotron Foreground Spectrum for Global 21-cm Cosmology

by

Bang D. Nhan

B.S., University of California, Santa Barbara, 2010

M.S., University of Colorado, Boulder, 2013

A thesis submitted to the

Faculty of the Graduate School of the

University of Colorado in partial fulfillment

of the requirements for the degree of

Doctor of Philosophy

Department of Astrophysical and Planetary Sciences

2018

This thesis entitled:
The Cosmic Twilight Polarimeter:
A Model-Independent Approach to Constrain the Synchrotron Foreground Spectrum for Global 21-cm Cosmology
written by Bang D. Nhan
has been approved for the Department of Astrophysical and Planetary Sciences

Prof. Jack O. Burns

Prof. Richard F. Bradley

Prof. Jason Glenn

Prof. Nils W. Halverson

Prof. Mihály Horányi

Date

The final copy of this thesis has been examined by the signatories, and we find that both the content and the form meet acceptable presentation standards of scholarly work in the above mentioned discipline.

Nhan, Bang D. (Ph.D., Astrophysics)

The Cosmic Twilight Polarimeter:

A Model-Independent Approach to Constrain the Synchrotron Foreground Spectrum for Global 21-cm Cosmology

Thesis directed by Prof. Jack O. Burnsand Prof. Richard F. Bradley

Detecting the cosmological sky-averaged (global) 21-cm spectrum as a function of observed frequency will provide a powerful tool to study the ionization and thermal history of intergalactic medium (IGM) in the high-redshift Universe ($\sim$ 400 million years after the Big Bang). The biggest challenge in conventional ground-based total-power global 21-cm experiments is the removal of the Galactic and extragalactic synchrotron foreground ($\sim 10^4 - 10^5$ K) to uncover the weak cosmological signal ($\sim 10-100$ mK) due to corruption on the spectral smoothness of foreground spectrum by instrumental effects. Although an absorption profile has been reported recently at 78 MHz in the sky-averaged spectrum by the Experiment to Detect the Global Epoch of Reionization Signature (EDGES) experiment, it is necessary to confirm that the proposed observation is indeed the global 21-cm signal with an independent approach.

In this thesis, we propose a new polarimetry-based observational approach that relies on the dynamic characteristics of the foreground emission at the circumpolar region to track and remove the foreground spectrum directly, without relying on any parametric foreground models as in conventional approaches. Due to asymmetry and the Earth's rotation, the projection of the anisotropic foreground sources onto a wide-view antenna pointing at the North Celestial Pole (NCP) can induce a net polarization which varies with time with a unique twice-diurnal periodicity. Different from the zenith-pointing global 21-cm experiments, by using this twice-diurnal signature, the Cosmic Twilight Polarimeter (CTP) is designed to measure and separate the varying foreground from the isotropic cosmological background

simultaneously in the same observation. By combining preliminary results of the proof-of-concept instrument with numerical simulations, we present a detailed evaluation for this technique and its feasibility in conducting an independent global 21-cm measurement in the near future.

Dedication

To the memory of my dear friend and climbing partner, Edward Tom (1971-2013).

Acknowledgements

There are always better positions and lifestyle for one to be in, yet without the ability to foresee the future and change the past, I can only be grateful for the opportunities I have been given to. I am indebted to both of my advisors, Prof. Jack O. Burns at CU Boulder and Prof. Richard F. Bradley at NRAO. They have given me freedom and resources to investigate cutting-edge problems and inquire new technical skills. I consider myself extremely fortunate to be able to participate in forefront research in the field of 21-cm cosmology.

Besides the support from APS and CASA, I am deeply thankful to the hospitality of the staffs at NRAO's CDL during my residency for the past 5 years at the lab. In particular, technicians in Rich's group, Pat Klima and Dan Boyd, have saved me in many occasions by repairing damaged electronics for me to continue my experiments. Along with Rich, they have made me feel as part of the team at the lab instead of just a visitor. I also want to thanks Rich and Becky for opening their farm to host my instruments during my thesis.

I want to thank my parents and my aunts in Vietnam, and my brother in the US, for being patient and supportive of my academic endeavor far from home. On my journey, I feel lucky to have made many close friends from rock climbing during grad school, especially Joe Migler, Charles Romero, Matthew Wikswo, and my late friend, Edward Tom. I have missed all the great adventures we shared on the same rope when hanging on a cliff. I also appreciate all the insightful discussion about science and philosophy with my friend, Tom (Hok Chuen) Cheng. Last but not least, I am grateful for the emotional support and the love from my girlfriend, Nora E. Bungard, in the past year, especially all the delicious pies she bakes.

Contents

Chapter

Tables

Table

Figures

Figure

Chapter 1

Introduction

> "Nothing in life is to be feared, it is only to be understood. Now is the time to understand more, so that we may fear less. "
>
> — Marie Curie (1867-1934), physicist and chemist

"What were the first objects to light up the Universe, and when did they do it?" are two of the frontier questions posed at the Astrophysical Decadal Survey (National Research Council, 2010). They reflect the constant quest for knowledge and understanding of the Universe we live in as well as its origin. This introductory chapter provides the context for this thesis fits into landscape of experimental 21-cm cosmology. Section 1.1 gives an overview of the earlier epochs of the high redshift[1] Universe. Meanwhile, Section 1.2 explains how and why the neutral hydrogen hyperfine 21-cm transition has increasingly played a prominent role in the subfield of high-z cosmology. A general description for the global (sky-averaged) 21-cm observation is provided in Section 1.3, along with their existing challenges. These will serve as the basis for the two main objectives of this thesis as outlined in Section 1.4.

1.1 High-z Universe

Progress in observational cosmology has provided profound understanding of the content, structure, and evolutionary history of the Universe beyond our nearby surroundings. Nonetheless, all of our knowledge about the early Universe has been constrained so far by

[1] In this thesis, adopted from conventional terminology in the 21-cm cosmology literature, high redshift refers to $z > 3$

two observable transition phases, namely the Cosmic Microwave Background (CMB), about four hundred thousand years after the Big Bang, and the Gunn-Peterson troughs imprinted on the spectra of quasars situated at high redshift[2] when the intergalactic medium (IGM) completely absorbed the quasars' redshifted Lyman-α (Ly-α) photons of rest energy at about 13.6 eV. The intervening period between these two events (about one billion years, $\sim$Gyr), during which the first luminous objects formed, is still very poorly understood. This section aims to provide a general understanding, based on theoretical models and simulations, of some of the major epochs that may have helped to shape the cosmic landscape into its present state. A sketch of these periods is depicted in Figure 1.1 as a guide.

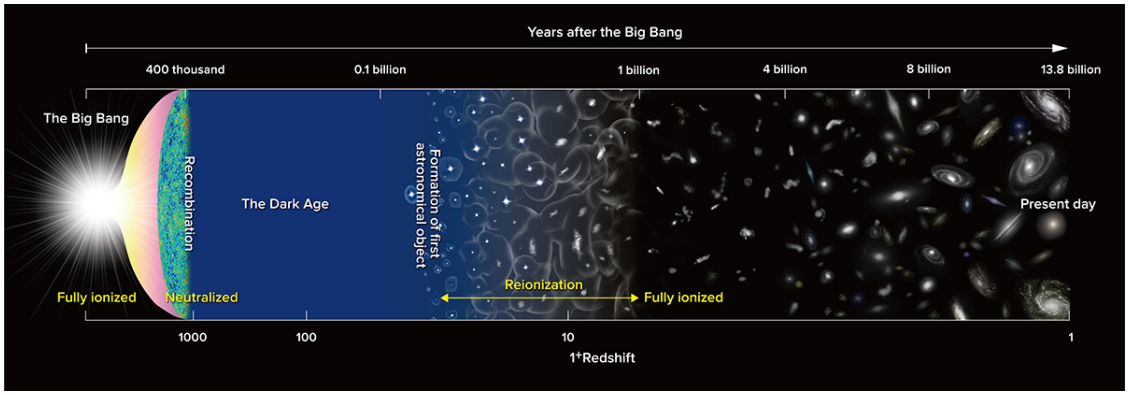

Figure 1.1: The illustration presents the evolution of the Universe through out different major phases (starting from the left to right). After Recombination at $z \sim 1100$ or 400,000 years after the Big Bang, the Universe cools adiabatically to form neutral hydrogen. The Universe stays neutral for the next billion years during the **Dark Age** ($1100 \gtrsim z \gtrsim 30$) before the first stars and galaxies are born during the **Cosmic Dawn** ($30 \gtrsim z \gtrsim 15$). Once these astronomical objects begin ionizing the neutral reservoir, this signifies the beginning of the **Epoch of Reionization (EoR)** until all the neutral contents arre depleted ends at $z \sim 6$. The landscape of the Universe continues to shape into what we can observe in the present day. Source: National Astronomical Observatory of Japan (NAOJ)

[2] Simply put, the redshift z of an emitting source determines the fraction of wavelength $\lambda_{\rm em}$ of the emitted photon being "stretched" when it travels from the source to an observer when measured at $\lambda_{\rm obs}$. The redshift is defined as $z = (\lambda_{\rm obs} - \lambda_{\rm em})/\lambda_{\rm em} = (\nu_{\rm em} - \nu_{\rm obs})/\nu_{\rm obs}$, where ν is the corresponding frequency. A redshifted photon's emission appears to be shifted toward the redward (longer wavelength)) end of its spectrum. The main causes of redshift include when an object moves away from its observer (Doppler redshift) or when the Universe is expanding if it is far enough from the observer (cosmological redshift). In essence, the redshift represents the age and distance of cosmological objects (for more details, see Hogg, 1999).

1.1.1 CMB and Dark Age

According to the standard ΛCDM model of Big Bang cosmology, in the first few minutes after the Big Bang, the Universe was filled with hot and ionized plasma consisting of photons from black body radiation coupled to atomic nuclei and free electrons. This plasma was opaque to thermal electromagnetic radiation since the photons within it could only travel so far before being scattered by free electrons due to Thomson scattering. Not until around 400,000 years later, due to cosmic expansion, did the plasma cool adiabatically to a temperature of about 3,000 K, low enough for the free electrons to combine with the protons to form neutral hydrogen (HI) atoms. This period is known as the epoch of **Recombination**.

Since these newly formed neutral atoms could no longer absorb the thermal radiation after the free electrons were depleted, the photons scattered the remaining free electrons for the last time before decoupling from the baryonic matter to stream freely through the Universe. This surface of last scattering has been confirmed by the detection of the CMB at $z \sim 1100$ independently by experiments, such as the Cosmic Background Explorer (CoBE Smoot et al., 1990), Wilkinson Microwave Anisotropy Probe (WMAP Bennett et al., 2003), and Planck instrument(Planck Collaboration et al., 2014). The most recent CMB data map released by the Planck satellite is shown in Figure 1.2. The CMB suggests that the early Universe is smooth and homogeneous with density anisotropies, as observed in terms of temperature fluctuations, on the order of 10^{-5}. Theory suggests that the neutral content stayed neutral and transparent for about another billion years over a period known as the **Dark Ages** ($1100 \gtrsim z \gtrsim 30$). The end of the Dark Age was marked by the birth of the very first luminous object in the Universe.

1.1.2 Cosmic Dawn

Eventually, under the influence of gravity, tiny density perturbations started to grow into gas clouds in dark matter (DM) halos. According to the Jean's instability, when the

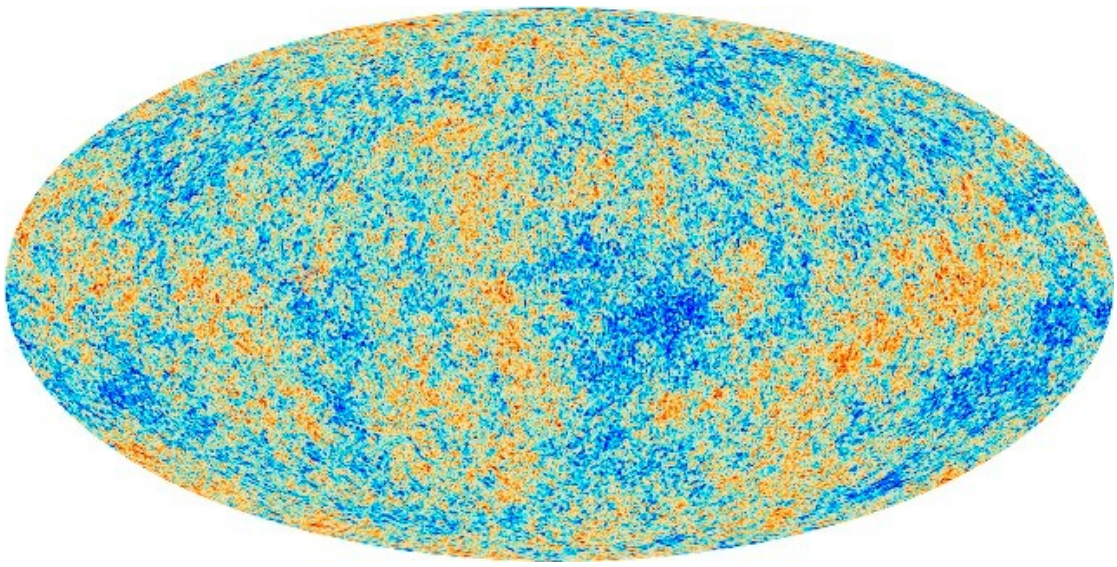

Figure 1.2: The latest released map of the CMB by the Planck satellite, noting that the temperature fluctuations are on the order of 10^{-5}. Source: The Planck Collaboration.

inward gravitational pull of these primordial gas clouds overcame their internal thermal pressure, the clouds would collapse to form the first light-emitting objects, which are also known as the Population III[3] (Pop III) stars. This period is commonly referred to as the **Cosmic Dawn** ($30 \gtrsim z \gtrsim 15$).

For the neutral gas clouds to collapse and form stars, they would have had to release their internal energy through radiative or collisional cooling. Since the Pop III stars were born out of the primordial neutral gas reservoir in the early halos, they did not have other previous generations to cycle the materials into metals. Without metals as coolants, it would have been difficult for Pop III stars to cool. In fact, it has been shown that atomic cooling alone is not efficient enough for stars to have formed in such an early time. This is because collisions among the H and He atoms alone do not transfer enough energy to have excited them and radiated the energy away as they decayed back down from the higher energy states.

[3] This terminology is designated to distinguish the Pop III stars from the later Pop II stars which contain a higher amount of elements heavier than helium, commonly referred to as metals by astronomers. Meanwhile, Pop I stars refer to the youngest stars which have the highest abundance of metal and currently exist in the Milky Way, e.g., the Sun. In the context of low-z astronomy, Pop II stars are sometimes referred to as metal poor, and Pop I as metal rich.

Simulations suggest that the primordial gas would have had to reach a temperature about 10^4 K for atomic cooling to be efficient (Barkana and Loeb, 2001).

Faster cooling is not possible unless molecular hydrogen H_2 is considered in the process (Lepp and Shull, 1984). The gas clouds could cool more efficiently because the H_2 molecule has a series rotational-vibrational transitions that allow excitation to occur at a lower energy (at temperature on the order of ~ 100 K). The effectiveness of the H_2 in cooling is illustrated in Figure 1.3 for the volume cooling rate $\Lambda(T)$ as a function of gas temperature.

As a result, the efficient cooling might have allowed the gas clouds to grow into massive halos ($M_h > 10^5$ solar mass $M_\odot$) to form stars at around $z \sim 30$ (e.g., Haiman et al., 1996; Tegmark et al., 1997). Simulations from early studies have suggested that the Pop III stars formed from these halos could be as heavy as few hundreds $M_\odot$ (Bromm et al., 1999; Abel et al., 2002), which is quite massive compared to the current star population in the present Universe.

Initially, because the UV photons emitted by the Pop III stars could easily be absorbed by the neutral IGM, the UV ionization front would not have traveled far, thus leaving the star-forming regions isolated from their surroundings. As soon as the first stars formed, they emitted soft UV photons, mostly from the Lyman-Werner (LW) band between 11.2-13.6 eV. These LW photons are energetic enough to photo-dissociate the H_2 molecules through a two-step process known as the Solomon Process (Stecher and Williams, 1967). This LW background would have suppressed[4] the cooling, and thus shortened the Pop III star formation period, unless there were other feedback processes to sustain the star formation and cycle the chemical composition for subsequent generations of stars. Some of these feedback processes include positive radiative feedback from the X-ray, mechanical heating and chemical enrichment from shocks and winds.

[4] Although the outer layers of a DM halo can be dense enough to shield the H_2 within inner layers of the gas clouds from being dissociated by the LW photons, this shelf-shielding is expected to be less effective in gas clouds that have large velocity gradients like ones with active star formation (Loeb and Furlanetto, 2013).

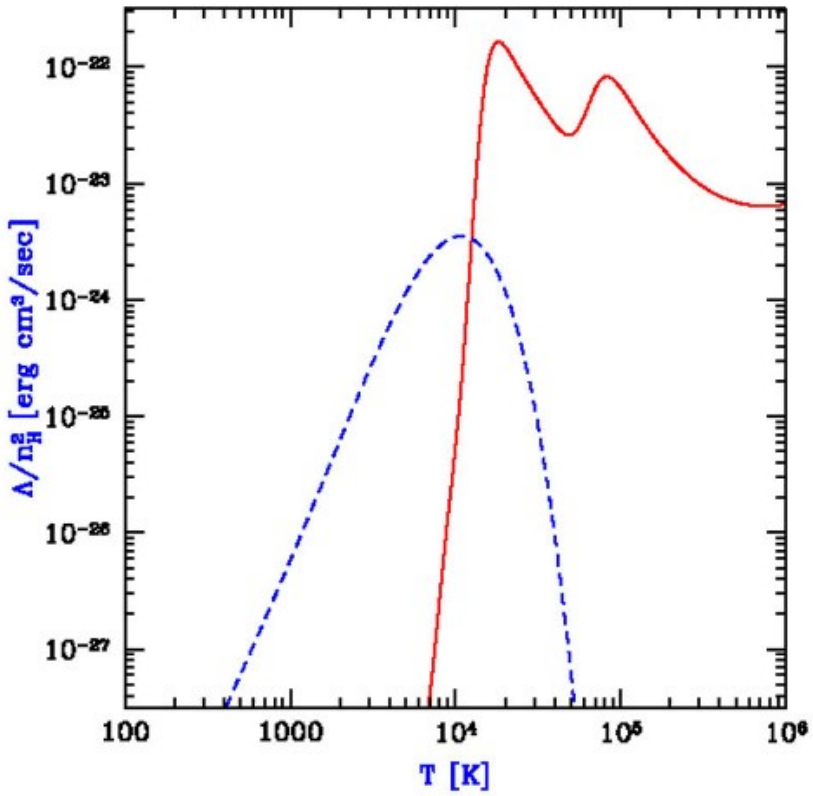

Figure 1.3: Simulation illustrates the volume cooling rate Λ is function of temperature for atomic cooling (solid curve), and H_2 molecular cooling (dashed curve). Note that the atomic cooling is not efficient until the temperature reaches about 10^4 K. Hence, H_2 is a more crucial coolant for the primordial gas clouds to collapse and forming stars. Source: Figure adopted from Barkana and Loeb (2001)

In particular, radiative feedback from the X-ray background could reverse the H_2 photo-dissociation since the X-ray photons can travel much farther than the UV photons into the surrounding IGM. This is evident from the comoving mean free path $l_{\nu,X}$ of an X-ray photon with energy $h\nu$ traveling in a uniform neutral medium consisting of hydrogen and helium. The mean free path is composed of contributions from different absorption species and is typically defined as,

$$l_{\nu,X} = \left(\sum_j n_j \sigma_{\nu,j} \right)^{-1} \tag{1.1}$$

where n_j is the number density of absorbing species j, and $\sigma_{j,\nu}$ is its associated bound-

free absorption cross-section area. For X-rays, the absorption cross section of hydrogen and helium can approximated as a power law as,

$$\sigma_{\nu,j} \approx \sigma_{0,j} \left(\frac{h\nu}{h\nu_{0,j}} \right)^{-3} \tag{1.2}$$

where $h\nu_{0,j}$ is the ionization energy and $\sigma_{0,j}$ is the cross section at that energy of the species j. By substituting Eq. (1.2) into Eq. (1.1), replacing n_j with the neutral fraction of the hydrogen $x_{\rm HI}(z)$ and helium $x_{\rm He}(z)$, and assuming 25% He and 75% HI, one arrives (Loeb and Furlanetto, 2013),

$$l_{\nu,X} \approx 11 \bar{x}_{\rm HI}^{-1} \left(\frac{1+z}{10} \right)^{-2} \left(\frac{h\nu}{300{\rm eV}} \right)^{3} \ {\rm cMpc}, \tag{1.3}$$

where $\bar{x}_{\rm HI}(z) = n_{\rm HI}/(n_{\rm HI} + n_{\rm He})$, and the unit is in comoving Mega-parsec, cMpc.

Additionally, the cross sections are proportional to $(h\nu)^{-3}$. This suggests that soft X-rays ($1 \leq h\nu \leq 10$ keV) dominates the heating mechanism (Furlanetto et al., 2006; Pritchard and Loeb, 2012). In other words, the X-ray photons could escape to preionize and preheat the neutral gas far outside the ionized bubble before the UV-ionizing front arrived. Based on X-ray luminosity, L_X, from near-by star-forming galaxies, measured over energy range of 0.5-8 keV, a relation between L_X and star-formation rate (SFR) (also known as the L_X-SFR relation Grimm et al., 2003; Gilfanov et al., 2004; Mineo et al., 2012) is empirically fitted as,

$$L_X = 2.6 \times 10^{39} f_X \left(\frac{\rm SFR}{M_\odot {\rm yr}^{-1}} \right) \ {\rm ergs}^{-1}, \tag{1.4}$$

where the factor f_X is a normalization factor to correct for extrapolation to high z. Typically, f_X is on the order of unity but its precise values is still unconstrained.

When these massive Pop III stars eventually died, they collapse and explode as supernova remnants (SNRs), such as black holes (BHs) which through their accretion disks generating X-ray remission. In the presence of the radiative feedback from the Ly-α and X-ray backgrounds, the mechanical and chemical enrichment of the nearby gas clouds from the SNRs' shocks and winds, a new generation of stars may start forming protogalaxies and

protoclusters. Specific details of each process are still an active area of research, mostly relying on insights from theoretical frameworks and numerical simulations. Nonetheless, the first stars and galaxies, through their Ly-α and X-ray backgrounds, have undeniably played a crucial role in determining the ionization and thermal history of the Universe.

1.1.3 Epoch of Reionization

As subsequent generations of stars were born and died, the neutral content in the early Universe was slowly being depleted through ionization and heating. The materials were being cycled until heavier metals were produced. This signified the beginning of the **Epoch of Reionization** (EoR). Using the free electron optical depth τ_e measured from the WMAP and Planck recently, as well as high-z galaxy candidates, EoR is predicted to have started as early as $z_{\rm re} \sim 17$ or a billion years after the Big Bang, with the latest value of $z_{\rm re} \sim 8.8$ from Planck (see Table 1.1). Furthermore, the observation of the Gunn-Peterson absorption

Table 1.1: Comparison of different electron optical depth τ_e measured by different space-based experiments. The average value of the constrained τ_e suggests that the EoR might have started as early as $z_{\rm re} \sim 17$ and as late as $z_{\rm re} \sim 8.8$ based on analysis from the latest Planck's data

τ_e	$z_{\rm re}$	Experiment	Reference
0.170 ± 0.060	17.0 ± 4.0	WMAP-1	Spergel et al. (2003)
0.088 ± 0.030	11.3 ± 2.0	WMAP-3	Spergel et al. (2007)
0.084 ± 0.016	10.9 ± 1.4	WMAP-5	Komatsu et al. (2009)
0.088 ± 0.015	10.6 ± 1.2	WMAP-7	Komatsu et al. (2011)
0.089 ± 0.014	10.6 ± 1.1	WMAP-9	Hinshaw et al. (2013)
0.066 ± 0.016	$8.8^{+1.7}_{-1.4}$	Planck	Planck Collaboration et al. (2016)

troughs, which appear as the lack of emission at the blueward side (shorter wavelength) of the Ly-α emission in the redshifted quasars spectra, strongly indicates that the Universe is more neutral at $z \gtrsim 6$. In other words, this implies that the EoR has ended by $z \sim 6$ (Fan et al., 2006). From that point onward to the present time, the high-z neutral content has been depleted, which in return allows the Ly-α photons to stream through the Universe to

the present day.

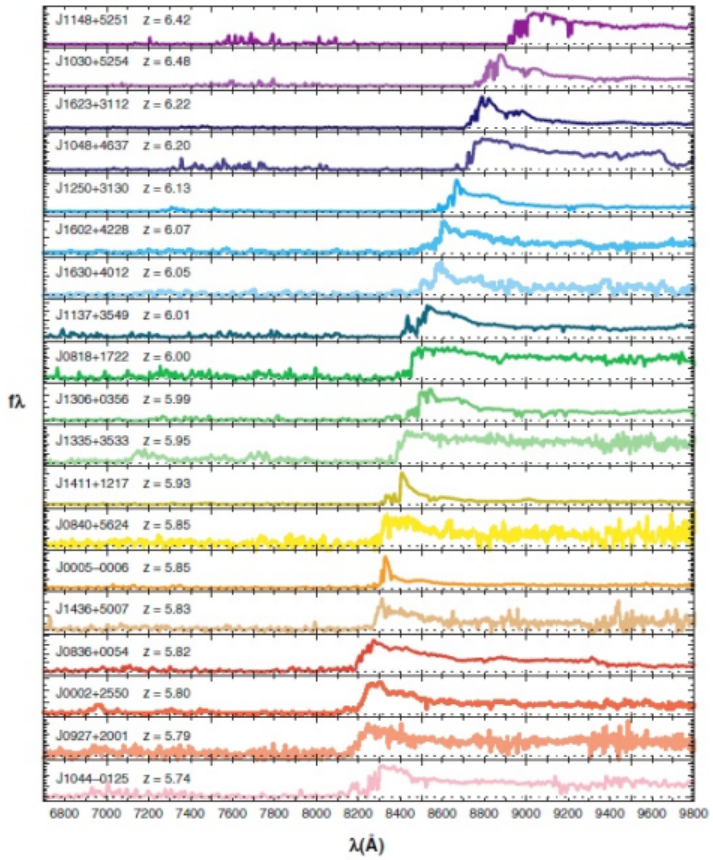

Figure 1.4: Spectra for high redshift SDSS (Sloan Digital Sky Survey) quasars. The Gunn-Peterson trough is evident as the lack emission on the blueward side of the Ly-α emission for quasars at $z \gtrsim 6$. This strongly indicates that the Universe is more neutral at these redshift, hence implies that the EoR has ended at $z \sim 6$. Source: Figure is adopted from Fan et al. (2006).

While the theoretical models describing these transition phases are compelling for decades, no direct observation has been made to constrain the intervening period between the Dark Ages and EoR due to the limited emitting sources in such an early time. Although the Hubble Space Telescope (HST) has identified multiple high-redshift galaxy candidates at redshift as high as 12 (e.g., Bouwens et al., 2011; Oesch et al., 2012; Ellis et al., 2013; Oesch et al., 2016), individual ultra-luminous sources at high redshift do not provide a complete picture of how the IGM's neutral content allowed the very first stars and galaxies

to form and then be reheated by X-rays (Pritchard and Furlanetto, 2007). A direct means to study the IGM evolution is desirable. This is where the neutral hydrogen hyperfine 21-cm transition comes in. Theoretical studies have suggested that measuring the evolution of the 21-cm brightness temperature as a function of redshift can provide insight into the intensity of the Ly-α and X-ray backgrounds, which in return can determine the ionization and thermal history of the IGM as and after the first stars appeared (e.g., Furlanetto et al., 2006; Pritchard and Loeb, 2012). The details of how to measure and apply the 21-cm line for high-z Universe are presented in the next section.

1.2 21-cm Cosmology

Not until the early twentieth century did Dutch astronomer Jan Oort and his former student H.C. Van de Hulst predict that the hyperfine splitting in the ground state of the HI could produce a photon with wavelength about 21 cm (or at rest frequency $\nu_0 \sim 1420.406$ MHz, Van de Hulst, 1945). It took about half a decade before the 21-cm transition line was verified observationally (Ewen and Purcell, 1951; Muller and Oort, 1951). Since then, the 21-cm line has been an instrumental tool in astronomy for studying the interstellar medium (ISM) at low redshifts ($z \lesssim 3$). Meanwhile, some researchers in the high-z astrophysics community have considered using the HI 21-cm line to probe galaxies and IGM in the early Universe (Sunyaev and Zeldovich, 1972, 1975; Hogan and Rees, 1979; Oort, 1984; Baldwin, 1986; Swarup and Subrahmanyan, 1987; Scott and Rees, 1990). In this thesis, I will primarily focus on the applications of the 21-cm line for high-z Universe.

1.2.1 Basic Physics

The HI hyperfine transition happens at the $1s\ ^2\mathrm{S}_{1/2}$ ground state of the hydrogen atom in a gas cloud when the magnetic dipole moments of the proton and electron flip from parallel (triplet state, $\uparrow\uparrow$) to antiparallel (singlet state, $\uparrow\downarrow$) at lower energy (Purcell and Field, 1956). The energy difference between these two levels is $\Delta E \sim 6.7 \times 10^{-6}$ eV corresponds to a rest

wavelength of $\lambda_{0,21\mathrm{cm}} \sim 21.105$ cm. The scale of this transition is illustrated in Figure 1.5 in contrast to the larger fine-structures splitting.

The probability for the spin flip to occur depends strongly on the relative number density of the hydrogen atoms in each spin state, which is determined by the temperature and ionization state of the HI gas cloud. This is represented by the ratio of particles numbers in the triplet state N_1 to the singlet state N_0, which follows the Boltzmann distribution as,

$$\frac{N_1}{N_0} = \frac{g_1}{g_0} \exp\left(-\frac{h\nu}{k_B T_S}\right) \tag{1.5}$$

where g_1 and g_0 are respective statistical weights of the two states for a given spin temperature T_S. In fact, as derived from detailed balance for a system in thermal equilibrium, the characteristic time scale for this spin-flip transition to occur spontaneously is,

$$t_{1/2} \approx A_{10}^{-1} = 3.49 \times 10^{14}\ \mathrm{s} \approx 1.1 \times 10^{7}\ \mathrm{yr} \tag{1.6}$$

where $A_{10} = 2.86888(7) \times 10^{-15}\ \mathrm{s}^{-1}$ is the Einstein coefficient for spontaneous emission between from triplet and singlet states. In other words, it would have taken a long time for the spin-flip transition to occur, unless the neutral content had been abundant or there had been other radiation sources contributing to the excitation. In fact, according to Eq. (1.5), the spin temperature T_S dictates the number density.

By considering the optical depth τ_ν for an HI region at a given redshift with spin temperature T_S, a differential brightness temperature $\delta T_{\mathrm{b,21cm}}(z)$ for the 21-cm transition relative to the CMB can be parametrized as (Madau et al., 1997; Furlanetto, 2006),

$$\begin{aligned}\delta T_{\mathrm{b,21cm}}(z) = 27 x_{\mathrm{HI}}(1+\delta)\left(\frac{\Omega_{b,0}h^2}{0.023}\right)\left(\frac{0.15}{\Omega_{m,0}h^2}\frac{1+z}{10}\right)^{1/2} \times \\ \left(1-\frac{T_\gamma}{T_S}\right)\left[\frac{H(z)}{(1+z)\mathrm{d}v_\parallel/\mathrm{d}r_\parallel}\right]\ \mathrm{mK},\end{aligned} \tag{1.7}$$

where x_{HI} is the hydrogen neutral fraction, δ is the fractional overdensity, h is the Hubble parameter today in unit of 100 km s^{-1} Mpc^{-1}, $\Omega_{b,0}$ and $\Omega_{m,0}$ are the fractional contributions of baryons and all matter to the critical energy density for a given Hubble parameter $H(z)$,

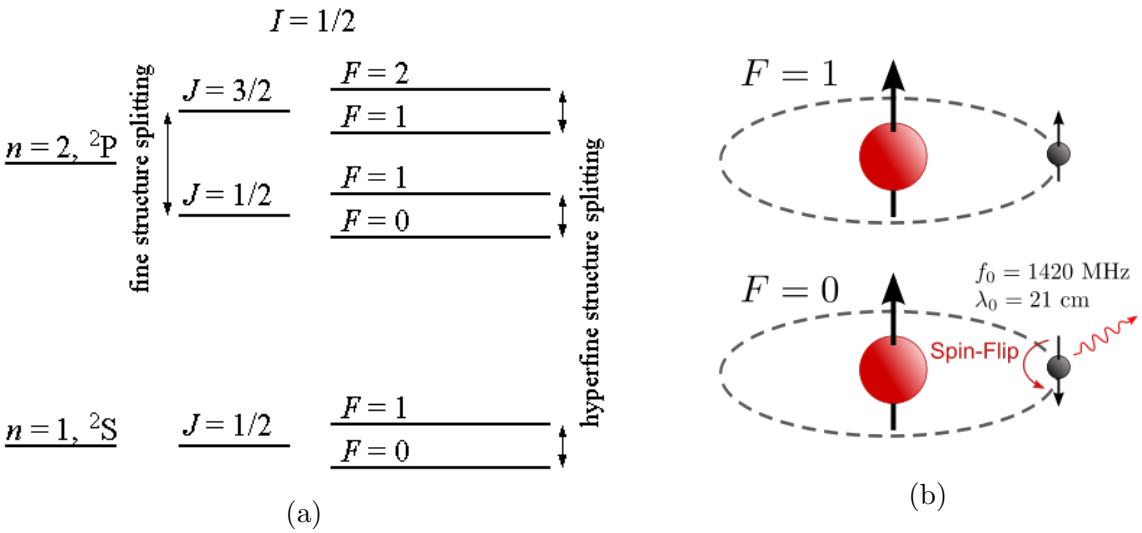

,

Figure 1.5: (a) Energy diagram of the hyperfine transition in contrast to the fine structure splitting. (b) Illustration on how the spins between the the electron and proton flip in the $1s\ ^2S_{1/2}$ state of the HI atom. The energy difference between $F = 1$ and $F = 0$ is what produces the 21-cm photon at with emitting frequency $\nu_{\rm em} \sim 1420$ MHz, where $F = |I + S|$ is the total spin number of the atom, whereas I is the nuclear spin along with the electronic spin S. I and S can be $\pm 1/2$.

and $T_\gamma = T_{\gamma,0}(1+z)$ is the CMB temperature at z with present day value $T_{\gamma,0} = 2.725$ K. The last term consisting of the velocity gradient along line-of-sight describes the subtle shift in the 21-cm line due to the gas cloud's peculiar velocity in addition to redshift caused by the cosmic expansion. This term is sometimes referred to as the redshift-space distortion or Kaiser effect (Kaiser, 1987).

The spin temperature T_S is determined by three competing processes affecting the population of the hyperfine levels in the ground state of HI: CMB radiation, collisional coupling between H-H (Zygelman, 2005) and H-e$^-$ (Smith, 1966) interactions, and Ly-α radiation (Loeb and Furlanetto, 2013). The overall statistical balance between these processes provides the following relation (Loeb and Furlanetto, 2013),

$$T_S^{-1} \approx \frac{T_\gamma^{-1} + x_c T_K^{-1} + x_\alpha T_\alpha^{-1}}{1 + x_c + x_\alpha} \tag{1.8}$$

where $T_\gamma = T_{\gamma,0}(1+z)$ is the mean CMB temperature at z with present day value $T_{\gamma,0} = 2.725$ K, T_K is the gas kinetic temperature, and T_α is the color temperature of the Ly-α radiation field which is closely coupled to T_K by recoil during repeated scattering. Meanwhile, x_c and x_α are the collisional and Ly-α scattering coupling coefficients. The last term in the numerator of Eq. (1.8) represents the coupling of the HI spin temperature to the Ly-α radiation from the first stars by photo-exciting the HI atoms to their Lyman resonant transitions. This is commonly known as the Wouthuysen-Field (WF) coupling (Wouthuysen, 1952; Field, 1958), and is illustrated in Figure 1.6. It is apparent from Eq. (1.8), T_S becomes strongly coupled to T_K when $x_c + x_\alpha \gtrsim 1$, and approaches T_γ when $x_c + x_\alpha \ll 1$.

1.2.2 Interferometric EoR Experiments

Traditionally, most ground-based observational efforts have focused on measuring the spatial fluctuations between the HI regions and the ionized HII regions during the EoR using large interferometric antenna arrays. In principle, the spatial fluctuations of the 21-cm temperature, $\delta T_{\mathrm{b,21cm}}(\nu, \theta, \phi)$, can be measured as the power spectrum $\Delta^2_{21}(k)$ in their

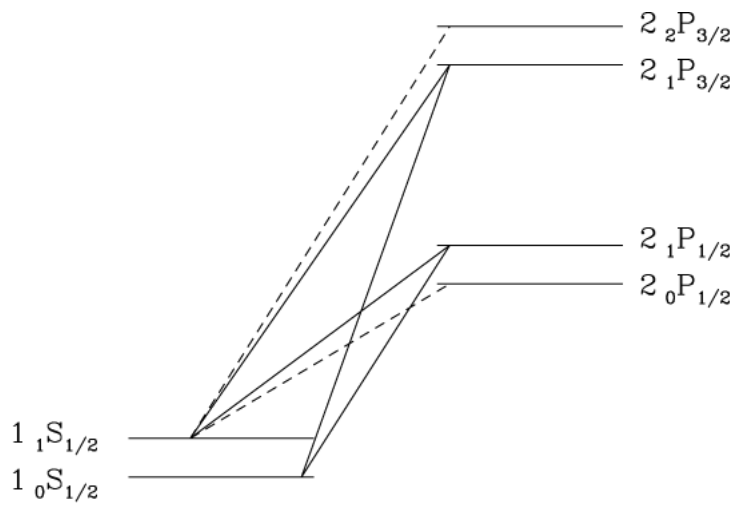

Figure 1.6: Energy-level diagram showing the Wouthuysen-Field effect. This shows the permitted transitions that allow Ly-α couples to the HI atom to produce a spin-flip emission (solid lines), and the complementary transitions that couple the Ly-α to the HI but do not contribute to the spin flips (dashed lines). Source: Figure adopted from Pritchard and Loeb (2012).

Fourier space (or k-space), an example from the 21cmFAST simulation (Mesinger et al., 2011) is shown in Figure 1.7. By measuring the fraction of HI regions being ionized into HII region over time or redshift, the ionization and thermal history can be constrained based on the slope and evolution of the $\Delta^2_{21}(k)$. The array experiments include the Murchison Widefield Array (MWA, Tingay et al., 2013; Bowman et al., 2013), the Donald C. Backer Precision Array for Probing the Epoch of Reionization (PAPER, Parsons et al., 2010), the Low Frequency Array (LOFAR, van Haarlem et al., 2013), and the Giant Metrewave Radio Telescope (GMRT, Paciga et al., 2011). Ultimately, imaging the 21-cm field, or namely tomography, is what future telescopes are designed for.

So far, removal of the Galactic and extragalactic synchrotron emission in the foreground along with instrumental distortion have been the biggest complications preventing these experiment from achieving the requisite sensitivity for detecting the 21-cm signal. These observations are further corrupted by other systematic errors such as ionospheric effects,

radio frequency interference (RFI). Significant efforts have been made to reduce these effects by placing these telescope at remote sites such as the Karoo region in South Africa and the Western Australia outback. In fact, larger arrays, such as the Square Kilometer Array (SKA, Mellema et al., 2013) and the Hydrogen Epoch of Reionization Array (HERA, Pober et al., 2014), are currently underway with the aim to boost the detection sensitivity significantly by increasing the collection area. Nonetheless, developing these instruments are costly and will not be available for another decade or more.

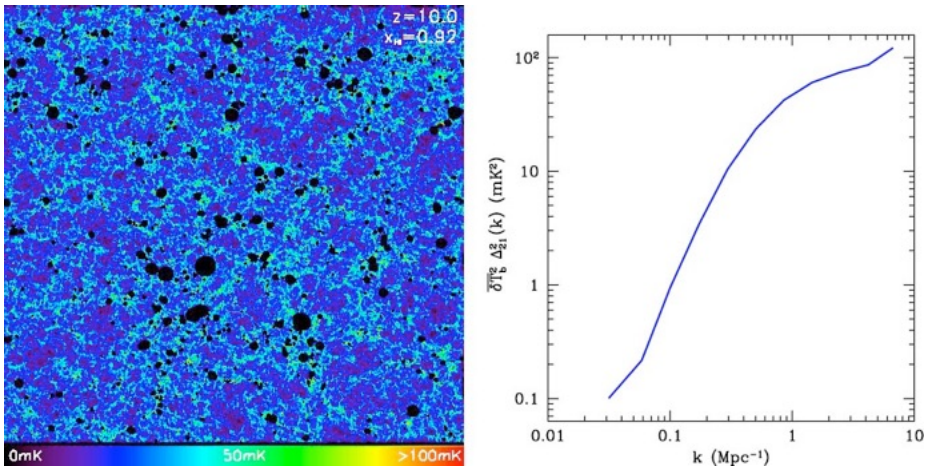

Figure 1.7: Simulation results from the 21cmFAST illustrates: (Left) The spatial fluctuation of the 21-cm emission at $z = 10$ with neutral fraction of HI at $x_{\rm HI} = 0.92$. (Right) The power spectrum $\Delta^2_{21}(k)$ in k-space for the spatial fluctuations of the 21-cm emission among between the HII bubbles that can be potentially detected with interferometers. The shape of the power spectrum curve is expected to change as the ratio of the HI and HII regions varies as a function of redshift. Source: Figure is adopted from Mesinger et al. (2011).

1.2.3 Global 21-cm Signal

Not until two decades ago was the 21-cm temperature as a spatially averaged value first considered to be a meaningful quantity to study the high-z Universe (Shaver et al., 1999). That study has shown that the spin temperature T_S can decouple from the CMB radiation T_γ in diffuse IGM at certain redshifts to give rise spectral features on much larger spatial scales. In contrast to the need of resolving fine spatial structures of the HI emission in

interferometric approach, the global (sky-average) 21-cm signal can potentially be detected by radio telescopes with low spatial resolution. By considering only the averaged value for HI differential brightness temperature, one can assume the gas density to be the cosmic mean value (hence $\delta \sim 0$), and the Kaiser redshift-space distortion to be unity, and thus Eq. (1.7) is reduced to,

$$\delta T_{\rm b,21cm}(z) \approx \ 27\bar{x}_{\rm HI} \left(\frac{\Omega_{b,0}h^2}{0.023}\right) \left(\frac{0.15}{\Omega_{m,0}h^2}\frac{1+z}{10}\right)^{1/2} \left(1-\frac{T_\gamma}{T_S}\right) \ {\rm mK}, \tag{1.9}$$

where $\bar{x}_{\rm HI}$ is the spatially averaged neutral fraction. In the literature, this spatially-averaged $\delta T_{\rm b,21cm}$ is also referred to as the spatial monopole, a term used for spherical harmonic analysis.

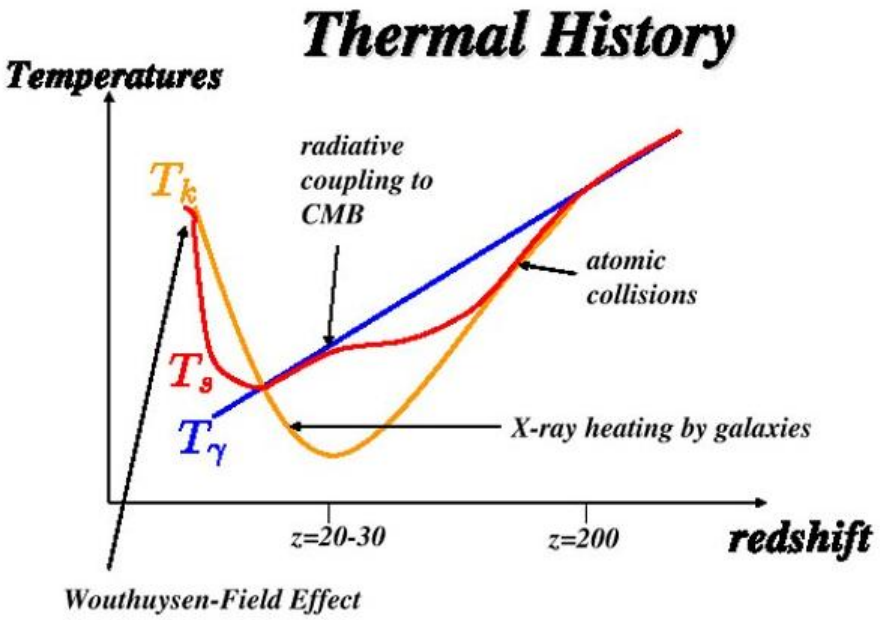

Figure 1.8: Qualitative illustration of interactions of different temperatures that determine the shape of the spin temperature as a function of redshift. However, the exact redshifts of different phases in this figure are not necessarily exact. Source: Figure is adopted from Loeb (2006).

Each of the three competing processes in Eq. (1.8) plays a role in shaping T_S as the Universe evolves. Figures 1.8 and 1.9 present a qualitative illustration on the interactions

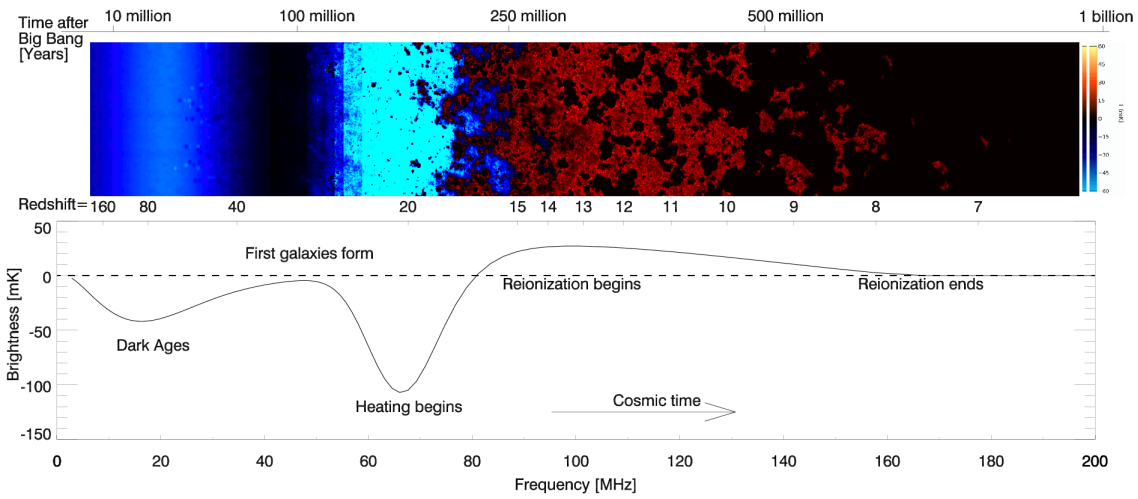

Figure 1.9: (Top) Simulated illustration of the ionization evolution of the early Universe at different phases. The color bar indicating the 21-cm temperature with red is positive and blue is negative values in mK. (Bottom) Evolution of the 21-cm spin temperature in contrast to the CMB and the gas temperature. The redshift axis is inverted comparing to 1.8. Source: Figure is adopted from Pritchard and Loeb (2012)

between these three processes during each phase of the thermal history. Although there are variations in magnitude, simulations from different studies have predicted a $\delta T_{\rm b,21cm}(\nu)$ spectrum that shares a general shape with features that describe the following phases (Loeb, 2006; Pritchard and Loeb, 2012; Loeb and Furlanetto, 2013):

- In the early stage after the Recombination at $1100 \gtrsim z \gtrsim 200$, due to Compton scattering of CMB photons to residual free electrons, thermal coupling allows the gas's T_K, hence T_S, to couple to the CMB's T_γ so $T_S \sim T_\gamma$ and no 21-cm signal is observable.

- Between $200 \gtrsim z \gtrsim 30$ during the Dark Age, when the gas cools adiabatically, its kinetic temperature is decoupled from the CMB so $T_K < T_\gamma$. Meanwhile, collisional coupling becomes dominant which sets $T_S < T_\gamma$ and results in an early absorption in $\delta T_{\rm b,21cm}$.

- As the cosmic expansion continues, collisional coupling becomes ineffective at $z \leq 30$

when the gas density decreases, hence T_S is dominated by T_γ as $T_K \to 0$ causing zero $\delta T_{\rm b,21cm}$ until Pop III stars and BHs appears.

- As soon as the first source is turned on, its Ly-α background is coupled to the cold gas, so $T_S \sim T_K$ with $T_K < T_\gamma$, this gives rise of the second absorption feature.

- Subsequently, as the Ly-α background saturates, X-ray heating becomes more significant than Ly-α coupling and raises the overall temperature causing an inflection point around $z \sim 20$.

- The heating continues to start the EoR at $z_{\rm re}$, which imposes an emission feature for $\delta T_{\rm b,21cm}$, until it saturates after all the neutral content has been depleted, then $\delta T_{\rm b,21cm} \to 0$.

According to Eq. (1.7), we can, in principle, recover the underlying $x_{\rm HI}(z)$ to constrain the ionization history of the IGM in the early Universe by measuring the differential brightness temperature $\delta T_{\rm b,21cm}(\nu)$. This is complementary to the integral constraints on reionization derived by the CMB experiments through the scattering electron optical depth τ_e as shown in Table 1.1. Similarly, the ionization history probed by the 21-cm line will also complement high-z galaxy surveys since current approaches primarily model the ionization history based only upon the galaxy population that is sensitive to existing telescopes, which may not be complete. More importantly, the 21-cm measurement can recover $T_S(z)$ to characterize the thermal history of the IGM. As suggested by Eq. (1.8), the spin temperature can then constrain the emergence of the Ly-α as well as the X-ray background which in turns provide great insights into the first stars, galaxies and BHs. Both are currently inaccessible to high-z galaxy surveys or CMB experiments. However, the exact details of the signal are highly uncertain and highly dependent on the astrophysical properties of the first stars and galaxies. For example, the shape and features in the global 21-cm spectrum can shift drastically for different scaling factors for the luminosity of the Ly-α (f_α) and X-ray (f_X)

backgrounds as shown in Figure 1.10.

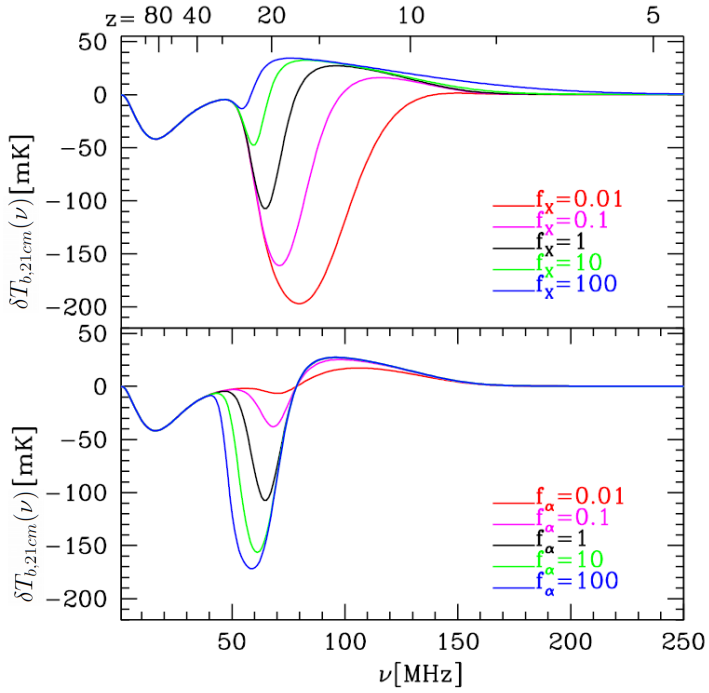

Figure 1.10: Different global 21-cm models with different scaling factors for the Ly-α(f_α) and X-ray (f_X) backgrounds. The depth of the main absorption trough during X-ray heating gets larger and later when the X-ray heating rate decreases (smaller f_X). On the other hand, at a fixed f_X, the more efficient the Ly-αheating is (larger f_α), the deeper absorption trough can be, because of the larger decoupling of the spin temperature from the CMB. Hence by constraining the shape of the global 21-cm signal, one can infer the underlying astrophysical parameters. Source: Figure is adopted from Pritchard and Loeb (2012)

1.3 Global 21-cm Observation

1.3.1 General Approaches

By the nature of the global 21-cm signal, its low spatial resolution allows radio telescopes to have large antenna beam patterns. This alleviates the need for narrow beam such as from an interferometer, which in principle mitigates systematics that are susceptible to the interferometric approach like cross-coupling between elements. In the last decade or so,

many ground-based global 21-cm experiments have emerged. They utilize either a single antenna or a compact array consisting of a small number of antenna elements to target the global 21-cm spectrum over large range of frequencies ($\sim 40 \leq \nu \leq 200$ MHz). The measured sky signal consists of both the synchrotron foreground spectrum and 21-cm background. Similar to the interferometric approach, the foreground and instrument systematics need to be corrected.

Some of the current global 21-cm experiments using a single antenna element include EDGES[5] I & II (Experiment to Detect the Global Epoch of Reionization Signature, Bowman et al., 2008; Bowman and Rogers, 2010; Monsalve et al., 2017a), SARAS 1 & 2 (the Shaped Antenna Measurement of the Background Radio Spectrum, Patra et al., 2013; Singh et al., 2017), SCI-HI (Sonda Cosmologica de las Islas para la Deteccion de Hidrogeno Neutro, Voytek et al., 2014), and BIGHORNS (Broadband Instrument for Global Hydrogen Reionization Signal, Sokolowski et al., 2015a). Meanwhile, LEDA (Large aperture Experiment to detect the Dark Ages, Greenhill and LEDA Collaboration, 2015) and LOCOS (LOfar COsmic-dawn Search, Vedantham et al., 2015) rely on using compact antenna arrays for the measurement. Brief details of the these experiments are summarized in Table 1.2, along with pictures depicting these instruments in Figure 1.11.

1.3.2 Observational Challenges

Regardless of the differences in techniques, both the large array and the global approaches are susceptible to a wide range of observational and systematic challenges. Some of the common problems include, but are not limited to, separating contaminants such as the strong foreground synchrotron emission, ionospheric distortions, and terrestrial RFI from the weak 21-cm background. In addition, measurement and systematic errors, like the frequency-dependent antenna-beam effects, accuracy in absolute instrument calibration, and

[5] EDGES II consists of three separate instruments: one high band for 90-200 MHz, and two low bands (low 1 & 2) for 50-100 MHz.

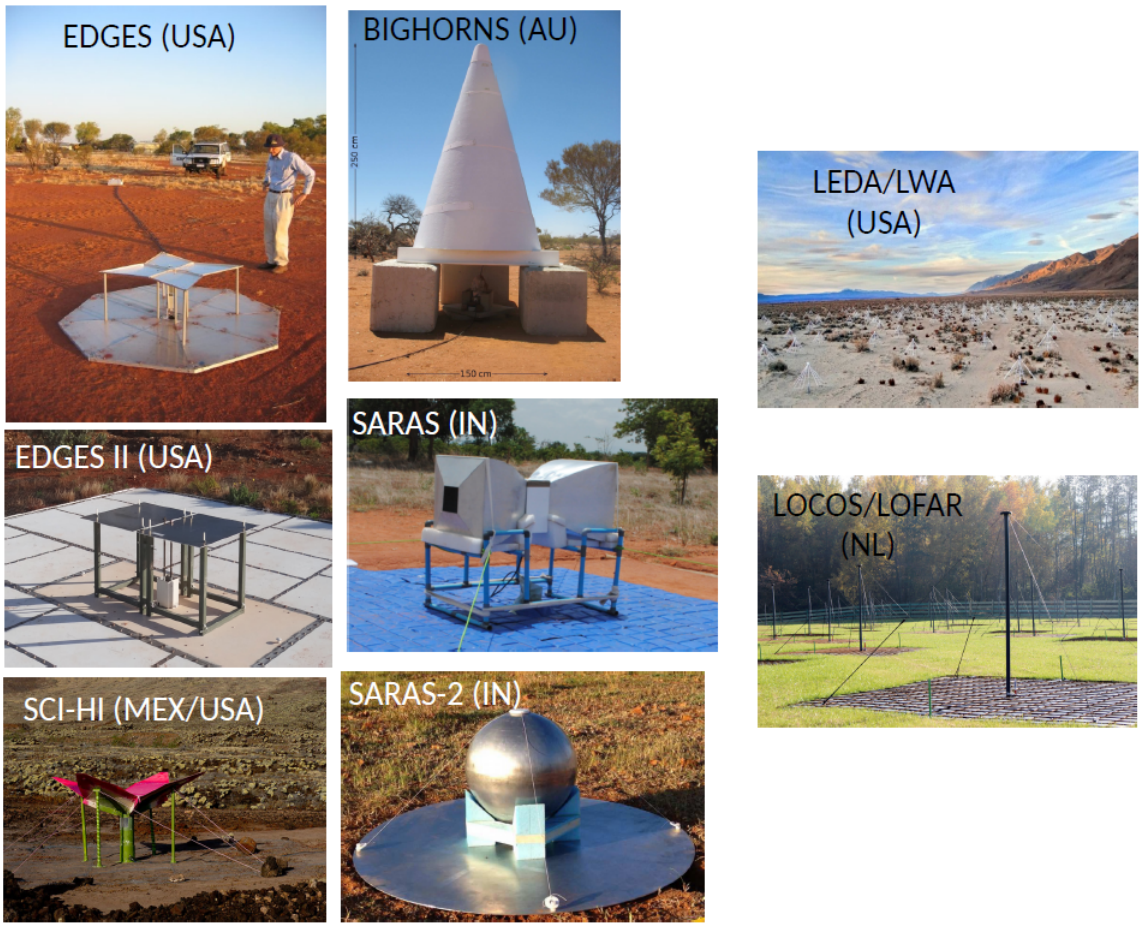

Figure 1.11: Compilation of the existing global 21-cm experiments, including both the single antenna approach as well as close compact arrays, namely LEDA and LOCOS. There is a wide range of antenna designs, especially for the single antennas which are designed to balance between the broad bandwidth and the smoothness of the frequency response. Credit: to the respective teams.

polarization leakage, also need to be corrected. Among these, the foreground emission is the most dominant since it has an averaged brightness temperature of at least four orders of magnitude stronger than the predicted 21-cm signal (Shaver et al., 1999). The magnitudes for some of these contaminants are contrasted with the cosmological 21-cm signal in Figure 1.12.

Foreground Removal:

By design, the measured sky signal in global experiments is a beam-weighted average value,

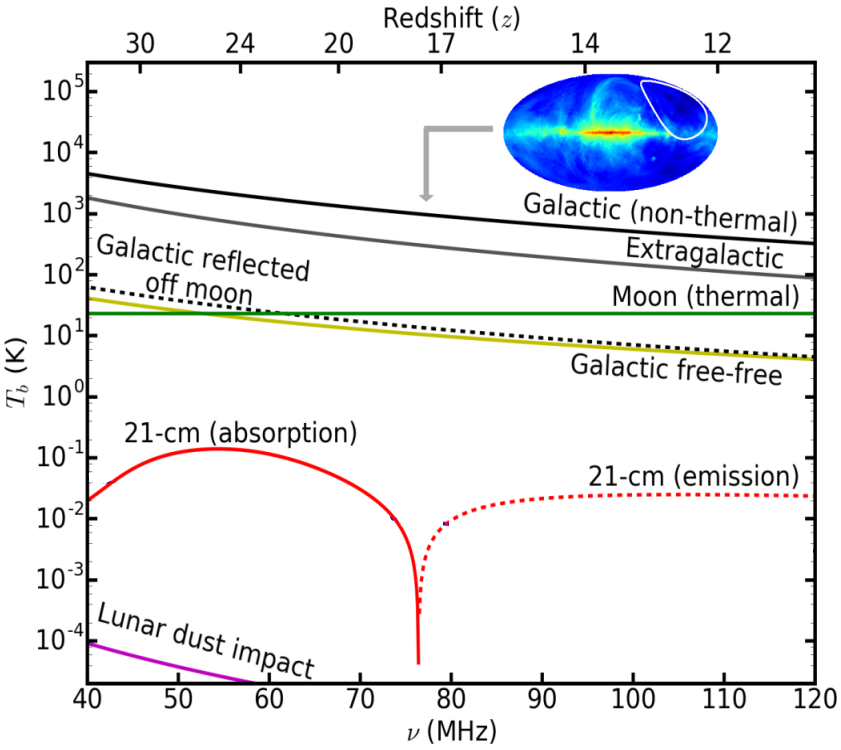

Figure 1.12: Show order of magnitude comparison between foreground ans 21-cm. Note the much stronger foreground spectrum relative to the weak 21-cm background (at least 5 orders of magnitude in dynamic range), along with other contaminants. Source: Figure is adopted from Burns et al. (2017)

which is defined by the equivalent antenna temperature $T_{\rm ant}(\nu)$ as,

$$T_{\rm ant}(\nu) = \frac{\int_{\Omega_B} T_{\rm sky}(\nu,\theta,\phi) F(\nu,\theta,\phi)\,{\rm d}\Omega}{\int_{\Omega_B} F(\nu,\theta,\phi)\,{\rm d}\Omega} \tag{1.10}$$

where ${\rm d}\Omega = \sin\theta\,{\rm d}\theta\,{\rm d}\phi$ is the differential solid angle, and $F(\nu,\theta,\phi)$ is the antenna power beam pattern as a function of frequency and position, with the beam solid angle Ω_B. Since the sky temperature $T_{\rm sky}(\nu,\theta,\phi)$ can be written as a linear combination of the 21-cm background $T_{\rm b,21cm}(\nu,\theta,\phi)$ and the Galactic and extragalactic foreground synchrotron emission $T_{\rm fg}(\nu,\theta,\phi)$, the beam-weighted antenna temperature can be written as,

$$\begin{aligned} T_{\rm ant}(\nu) &= \frac{\int_{\Omega_B} \left[T_{\rm fg}(\nu,\theta,\phi) + \delta T_{\rm b,21cm}(\nu,\theta,\phi)\right] F(\nu,\theta,\phi)\,{\rm d}\Omega}{\int_{\Omega_B} F(\nu,\theta,\phi)\,{\rm d}\Omega} \\ &= T_{\rm fg}(\nu) + \delta T_{\rm b,21cm}(\nu) \end{aligned} \tag{1.11}$$

where the spatial dependence of the sky signal components have been removed to represent their corresponding beam-weighted values. In fact, this is one of the main reasons why the global 21-cm approach is appealing. In principle, at a small fraction of the cost of a large array, one can measure the evolution of the mean 21-cm signal with just a single antenna element without the need for high spatial resolution.

From Eq. (1.11), it is trivial that one can recover the $\delta T_{\rm b,21cm}(\nu)$ by subtracting the $T_{\rm fg}(\nu)$ from $T_{\rm ant}(\nu)$. However, one of the primary challenges is how to characterize and remove $T_{\rm fg}(\nu)$ accurately from the measured spectrum. At low frequencies[6] , the foreground emission is dominated by non-thermal synchrotron radiation originating from high-energy cosmic-ray (CR) electrons interacting with magnetic field in the Galaxy and other extragalactic sources (Kogut, 2012). Motivated by the theory of diffusive shock acceleration (or Fermi acceleration), which predicts a power-law energy distribution for the charged particles moving in magnetized gas clouds, the observed foreground spectrum is generally parametrized as a spectrally smooth power law with a running spectral index (Shaver et al., 1999; Tegmark et al., 2000; Kogut, 2012). One of a more commonly adopted parametrization is a polynomial in log-log space (Pritchard and Loeb, 2010; Bowman and Rogers, 2010; Harker et al., 2012; Bernardi et al., 2015) as,

$$\log \widehat{T}_{\rm fg}(\nu) = \sum_{m=0}^{M>0} c_m \left(\log \nu\right)^m \tag{1.12}$$

where $\widehat{T}_{\rm fg}(\nu)$ is the estimated foreground spectrum with polynomial coefficient c_m of order m up to some order $M > 0$. This is also known as the "trend removal" approach. In principle, the estimated foreground such as one in Eq. (6.1) can be subtracted from the measured spectrum to reveal the global 21-cm spectrum in Eq. (1.11).

Beam Chromaticity:

The trend removal is statistically justified to extract the weak 21-cm spectrum which has distinct small-scaled frequency structures in contrast to the smoothly varying foreground

[6] See Appendix B for detailed definition of different frequency ranges. In short, here low frequency is equivalent to $\nu \leq 200$ MHz.

(Petrovic and Oh, 2011). However, this approach is limited by having to separate and infer the weak cosmological signal from the foreground emission from a single total-power spectrum $T_{\rm ant}(\nu)$ averaged overtime. Unless the foreground spectrum is measured to a precision of a few millikelvins, subtracting such a bright foreground directly from across the frequency band will unavoidably introduce error structures whose magnitudes can be equivalent to, if not greater than, the $\delta T_{\rm b,21cm}(\nu)$ (Petrovic and Oh, 2011; Harker, 2015). Additionally, free-free emission, recombination lines, and instrumental biases can also distort the spectral smoothness of the foreground spectrum.

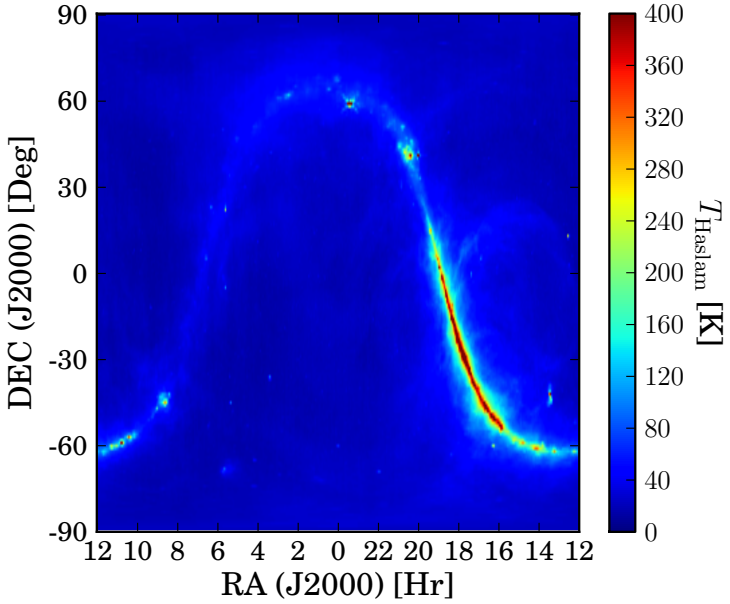

Figure 1.13: The Haslam full-sky survey map at 408 MHz. Source: Data are acquired from NASA's archival database, based on Haslam et al. (1982).

In fact, recent studies (Bernardi et al., 2015; Mozdzen et al., 2016) find that nonlinear frequency dependence of the antenna beam pattern $F(\nu, \theta, \phi)$ can distort the smoothness of the foreground spectrum and further complicate the removal process. Such a type of distortion is sometimes referred to as the **beam chromatic effect**. We illustrate this by computing the beam-weighted antenna foreground sky temperature $T_{\rm ant}(\nu)$ between a frequency-independent beam and a chromatic beam models. Mock sky maps are created by

extrapolating Haslam full-sky survey map[7] (Figure 1.13) from its observed frequency at 408 MHz to 60-82 MHz using a power-law parametrization with a mean spectral index $\beta = 2.47$ as suggested by previous observations (Bowman et al., 2008),

$$T_{\rm fg}(\theta, \phi, \nu) = T_{\rm Haslam}(\theta, \phi) \left(\frac{\nu}{408 \text{ MHz}}\right)^{-\beta} \tag{1.13}$$

In Figure 1.14, we compare the residual antenna temperature, $T_{\rm res}(\nu) = \widehat{T}_{\rm fg}(\nu) - T_{\rm fg}(\nu)$, for the log-log polynomial fit (with m = 5-9) for the foreground spectrum between the frequency-independent beam and the chromatic beam. The effect of beam chromaticity is evidenced by the much larger residual for the polynomial fit subtraction when the smoothness of foreground spectrum is corrupted by the beam spectral structures. Hence, it is inadequate to remove the foreground spectrum with a parametric fit unless the antenna beam structures are well-understood or characterized.

Experiments, like EDGES and SARAS-1, have attempted to correct the beam structure in post processing by least-square fitting the beam using simulated beams from computational electromagnetics (CEM) software, such as CST[8] (Computer Simulation Technology), HFSS[9] (Frequency Electromagnetic Field Simulation), and FEKO[10] (FEldberechnung fr Krper mit beliebiger Oberflche). Meanwhile the SARAS-2 experiment has attempted to achieve a smooth antenna frequency response by designing antennas with unique shape and characteristics to compensate for the beam chromatic variations. These are impressive efforts to mitigate the beam chromaticity. Nonetheless, most of the existing global 21-cm experiments still suffer from various observational and systematic limitations.

Other Contaminants:

Ground-based observation at low frequencies are also susceptible to distortion and corruptions from RFI, ionosphere, and solar activities, to name just a few. For RFI, as mentioned

[7] Data acquired from NASA's archival database (Haslam et al., 1982):
`https://lambda.gsfc.nasa.gov/product/foreground/fg_2014_haslam_408_info.cfm`

[8] By Dassault Systemes, `https://www.cst.com/`

[9] By Ansys, Inc., `https://www.ansys.com/Products/Electronics/ANSYS-HFSS`

[10] By Altair Engineering, `https://www.feko.info/`

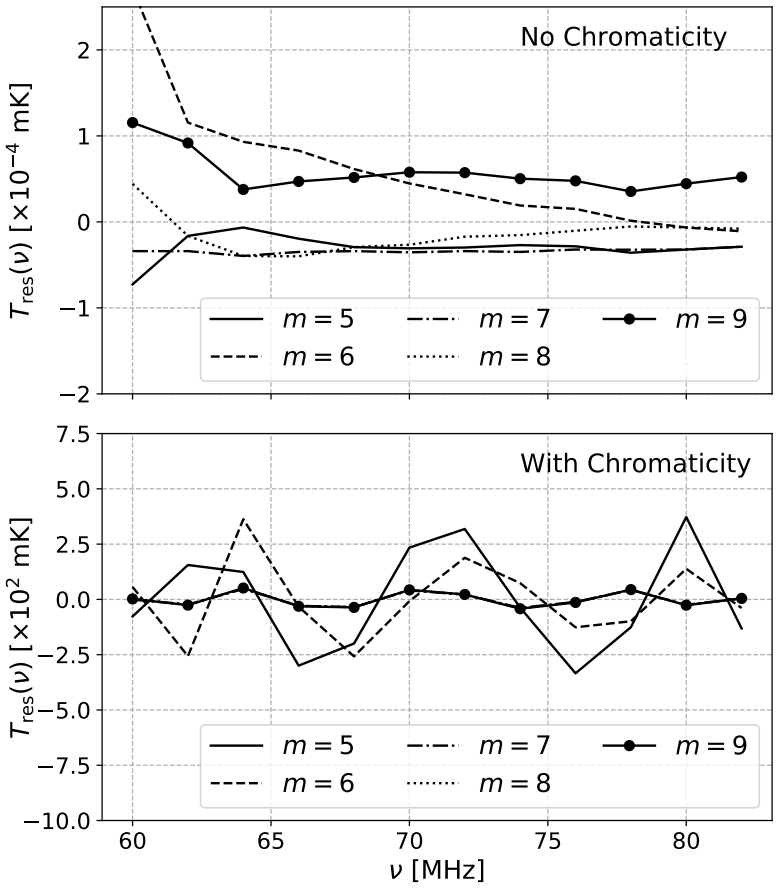

Figure 1.14: Comparison of the residual antenna temperature, $T_{\rm res}(\nu)$ for removing the foreground spectrum $T_{\rm fg}(\nu)$ with a log-log polynomial fit. The residual (top) is much smaller without the beam chromaticity, whereas the beam chromaticity has resulted in much larger (several orders of magnitude) residual (bottom). Hence, the fitting a foreground spectrum with a parametrized function is inadequate unless the frequency response of the antenna beam is characterized. Noting that curves for $m = 7,\ 8,\ 9$ are overlapped in the bottom plot.

earlier, the instruments are located in radio-quiet sites remote from populated cities such as the Karoo region in South Africa (e.g., SCI-HI), the outback of Western Australia (e.g., EDGES, BIG HORNS), and remote islands on the western coast of Mexico (e.g., SCI-HI). For the global experiments that are carrying out in marginally acceptable RFI environments, RFI excision algorithms such as kurtosis-based ones are deployed to flag and remove contaminated frequency data channels.

There are also several ionospheric effects that can affect low-frequency observation from the ground, such as the refraction due to signal propagating through dynamic ionospheric layers (Vedantham et al., 2014), ionospheric attenuation during periods with strong solar activities (Sauer and Wilkinson, 2008), or transient ionospheric scintillation imposing spurious signal to the measurement. Since the ionospheric distortion is inversely proportional to the observed frequency (ν^{-2}), its effects have been shown to be minute for global experiments operating above 100 MHz. As the demand shifts to lower frequencies to explore higher redshifts, different methods have been developed to correct these ionospheric effect, such as using GPS surveys or other remote sensing missions for monitoring the ionospheric environment (Datta et al., 2016). So far, the ionospheric effects have not been fully addressed by most global experiments. The mixed results could potentially due to the locations of the local observers (Sokolowski et al., 2015b; Datta et al., 2016).

1.3.3 Latest Results

As of late 2017, the EDGES-II high-band experiment has ruled out tanh-based reionization models, $\delta T_{\rm b,21cm} = T_{21} \tanh[(z - z_{\rm re})/\Delta z]$, with duration of at least $\Delta z \lesssim 1.0$ for $14.8 \geq z_{\rm re} \geq 6.5$ between 90-190 MHz (Monsalve et al., 2017b). Meanwhile, using the smooth antenna-response design, SARAS-2 has attempted to rule out the class of models that feature weak X-ray heating with $f_X \lesssim 0.1$ and rapid reionization between 110-200 MHz (Singh et al., 2017). Meanwhile, in March of 2018, an absorption profile in the sky-averaged spectrum has been observed by the EDGES-II low band instruments (Bowman et al., 2018). The absorption feature is center at 78 ± 1 MHz with amplitude of $0.5^{+0.5}_{-0.2}$ K and full-width at half-maximum (FWHM) of 19^{+4}_{-2} MHz. However, unlike all the predicted global 21-cm models so far, this detected absorption feature has a flattened bottom as shown in Figure 1.15.

The validity and interpretation of this result are currently being debated within the low-frequency radio astronomy and IGM community (e.g., Mirocha and Furlanetto, 2018). One study suggests that potentially unknown interaction between baryons and dark-matter

particles could provide an explanation for the flatness in the absorption (Barkana, 2018). Nonetheless, as pointed out by the EDGES team, although their results have passed many of their confidence tests, an independent confirmation for such a absorption structure from other global experiments is necessary (Bowman et al., 2018).

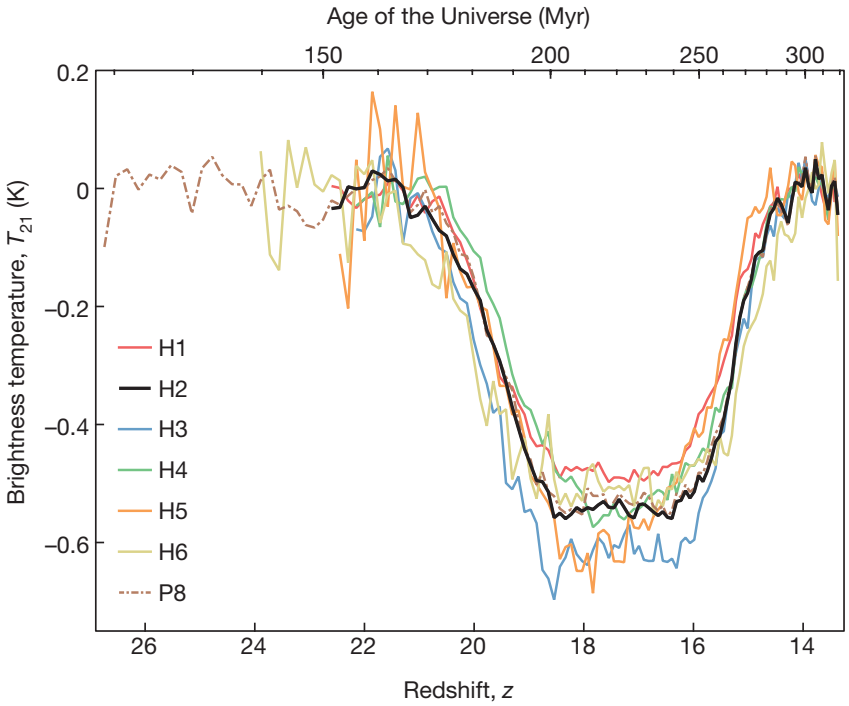

Figure 1.15: Detection of absorption feature centered at 78 MHz from the EDGES II low band experiment. Different curves represent different observation sessions with various instrument configurations. The best fit of the absorption profile suggests the center frequency to be 78 ± 1 MHz with amplitude of $0.5^{+0.5}_{-0.2}$ K and full-width at half-maximum (FWHM) of 19^{+4}_{-2} MHz. Source: Figure adopted from Bowman et al. (2018).

1.4 Motivations and Thesis Outline

Facing the limitations from the conventional approaches, it is desirable to have a direct means to constrain and separate the $T_{\rm fg}(\nu)$ from $\delta T_{\rm b,21cm}(\nu)$ in the same observation without relying on any fitting to a parametrized foreground model. Efforts to isolate the foreground from the background signal observationally have been explored in previous stud-

ies. For example, the PAPER and HERA experiments adopt the delay-filtering technique in an attempt to separate the foreground in delay space instead of frequency space (Parsons et al., 2012). For the global signal, a singular value decomposition (SVD) analysis is used to construct suitable spectral basis to capture the time-variable component of the measured dynamic spectra to constrain the foreground spectrum (Vedantham et al., 2014; Tauscher et al., 2018). Meanwhile, a principle component analysis (PCA) is adopted to determine contaminated spectral modes in the smooth foreground spectrum based on its spatial fluctuations (Switzer and Liu, 2014).

One of the two main goals of this thesis is to revisit some of the common measurement challenges in conventional global 21-cm experiments, such as gain calibration and beam chromaticity correction, with a case-study instrument. As described in Chapter 2, inspired by conventional global experiments, I developed a precursor single-antenna experiment to evaluate the total-power spectrum measurement approach and the conventional on-off load flux calibration scheme. The lessons learned from this instrument were incorporated into the development of its successor, the Cosmic Twilight Polarimeter (CTP).

This bring us to the second goal of this thesis: I will present a new observational technique which I has devised to exploit the dynamic nature and spatial anisotropy of the foreground in order to separate its spectrum from the 21-cm background through polarimetry. The general theory and simulated results demonstrating how the projection-induced polarization effect (PIPE) helps to separate and constrain the foreground are detailed in Chapter 3. In Chapter 4, I will present the description and details of the CTP as an proof-of-concept instrument for the PIPE. Chapter 5 will focus on the preliminary results and the evaluation for the feasibility in applying this technique to the global 21-cm experiment. Finally, in Chapter 6, I will conclude this thesis with suggestions and potential improvements to refine the CTP further in the near future.

Throughout this dissertation work, lab technicians, Pat Klima and Dan Boyd, along with Prof. Bradley have designed and populated the printed circuit board (PCB) for the

front-end electronics for both the bicone and CTP systems. In addition, Prof. Bradley has helped me to run the computer simulations on the antenna beams and circuit design models. Prof. Bradley has personally helped me to prepare deployment sites as well as relocating both instruments to the field. Staff engineer at CDL has helped us to design and provide the CSD drawings for the bicone system. Meanwhile, I am the sole author for the CAD drawings for all the components of the CTP system later on.

I have also conducted majority of the laboratory testing and measurement for the front-end and back-end units for both instruments. In the beginning of the project, I have received assistance from Prof. Abhirup Datta on repurposing his signal reduction pipeline for the bicone system. Later, for the CTP system, I am the sole author of the data acquisition and reduction pipeline. I have also written the original simulations for the PIPE described in Chapter 3. Since 2017, David Bordenave, a PhD candidate in the Department of Astronomy at the University of Virginia, has adapted and improve the PIPE simulation code significantly. I have used this new code for all the analysis done beyond Chapter 3.

Table 1.2: A summary of the current global 21-cm experiments and their status

Experiment	Site	Band [MHz]	Antenna Design	Features	Status
EDGES	Australia	100-200	Four-point dipole	Multi-load calibration	First science results
EDGES II	Australia	90-190 (high band)	Dipole-like flat blade	Smooth antenna beam pattern & multi-load calibration	Rule out models with $\Delta z \lesssim 1.0$ for $14.8 \geq z_{\rm re} \geq 6.5$
		50-100 (low 1 & 2)			**First detection** of absorption feature at 78 ± 1 MHz with amplitude of $0.5^{+0.5}_{-0.2}$ K and FWHM of 19^{+4}_{-2} MHz
BIGHORNS	Australia	70-150	Conical log-spiral	Optimized antenna match	Initial results
SARAS 1	India	87-175	Shaped fat dipole	Noise source cross-correlation	Preliminary results
SARAS 2	India	110-200	Sphere-disk monopole	Smooth antenna response	Disflavor models with weak X-ray heating & rapid reionization
SCI-HI	Mexico & South Africa	40-80 (low) 75-130 (high)	Hibiscus-inspired dipole	Multi-load calibration	Initial results
LEDA	NM, USA	30-70	Inverted-V dipoles	Correlation receiver for compact interferometric array	Testing
LOCOS	Netherlands	35-85	LOFAR Low-band	Interferometric and total power mode with lunar occultation for foreground measurement	Initial result

Chapter 2

Precursor: A Total-power Global 21-cm Experiment with a Finite-biconical Antenna

> "Science, my lad, is made up of mistakes, but they are mistakes which it is useful to make, because they lead little by little to the truth."
>
> — Jules Verne (1828-1905), novelist

Between the summer of 2013 and fall of 2015, a precursory total-power global 21-cm experiment prototype was constructed and evaluated at the NRAO's Central Development Laboratory (CDL) in Charlottesville, VA. Major system testing and evaluation were carried out at the CDL before we deployed this system in the Green Bank Observatory (GBO), West Virginia, within the National Radio Quiet Zone (NRQZ) in early 2014 (which is about 120 miles away from the CDL, Figure 2.1). In late 2015, we relocated the system to the Equinox Farm, LLC in Troy, Virginia (about 20 miles away) for closer evaluation and testing. Because of the biconical antenna design used on this instrument, we will refer it as the **bicone system** hereafter. The instrument design will be described in Section 2.2. Section 2.4 will discuss the major technical shortcomings and provide the potential remedies to these challenges.

2.1 System Overview and Rationales

The bicone system was developed to evaluate the efficacy of using a single antenna element in constraining the foreground spectrum $T_{\rm fg}(\nu)$ for the global 21-cm background $\delta T_{\rm b,21cm}(\nu)$. Although significant efforts have been devoted in similar systems by other

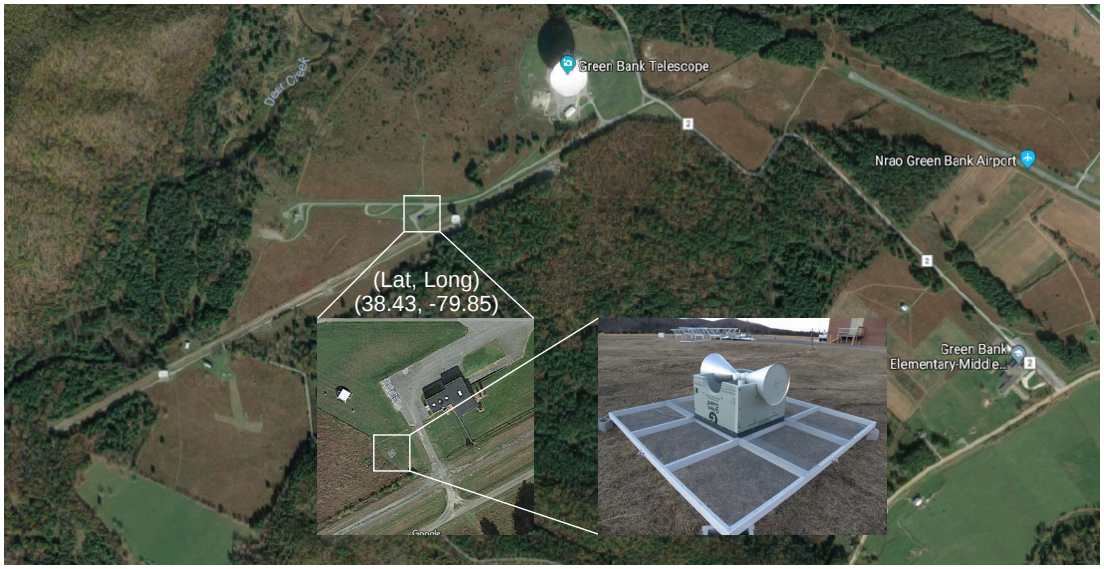

Figure 2.1: The original deployment site for the bicone system at GBO inside the NRQZ between 2014-2015. Credit: Google Map

groups as mentioned in the last chapter, developing our own prototype provides us direct access to an instrument for testing.

The global 21-cm spectrum consists of structures spanning over a large frequency range ($\sim$ 20-200 MHz, as suggest in Figure 1.9). It is ideal to observe all the spectral features (minima and maxima) of the $\delta T_{\rm b,21cm}(\nu)$ simultaneously to provide the optimal constraints on all phases for the astrophysical parameters, such as the averaged neutral fraction of HI $\bar{x}_{\rm HI}$, the luminosity scaling factor for the Ly-α (f_α) and X-ray (f_X) backgrounds. In practice, a receiving antenna only covers certain range of frequency because of the antenna's matching circuit is only sensitive to signal of the given frequency range. For example, the broad-band antenna used by other global 21-cm experiments at best can only provide a 2-to-1 bandwidth, which is twice of the lowest frequency of the band (e.g., see Column 3 of Table 1.2).

This creates a challenge in choosing an antenna design for proper frequency coverage to include the important features of the global 21-cm spectrum, especially when the actual details and structures of the $\delta T_{\rm b,21cm}(\nu)$ are highly uncertain. So far, most instruments in Table 1.2 primarily focus on detecting the Epoch of Reionization (EoR) which is expected to

be at the higher frequency range, $\sim$ 100-200 MHz. The finite-biconical antenna was designed to extend the frequency range to 60-120 MHz to include potential absorption feature during the Cosmic Dawn.

Being a prototype, many electronic hardware components of the bicone instrument were converted from existing components of the PAPER project, which was developed by Dr. Richard F. Bradley's group at the CDL. Except the antenna design, the bicone system's general design emulated conventional global experiment approach. The system consisted of an internal broadband reference calibrator (50 Ω resistive load) for the system gain and noise temperature, a balun, low-noise amplifiers (LNAs) and band-pass filters (BPFs) in the front-end (FE) unit. The signal is transmitted through a long coaxial cable to an indoor data acquisition (DAQ) system consisting of a receiver unit and a back end (BE) made of a commercial off-the-shelf (COTS) high-speed analog-to-digital (ADC) digitizer mounted on a PC. Additionally, temperature sensors are used to monitor the FE unit and the indoor receiver. The recorded temperatures are used for the FE calibration in post-processing. Such an antenna-receiver system is commonly referred to as a total-power radiometer, or simply radiometer. The four major components of this system is illustrated in Figure 2.2.

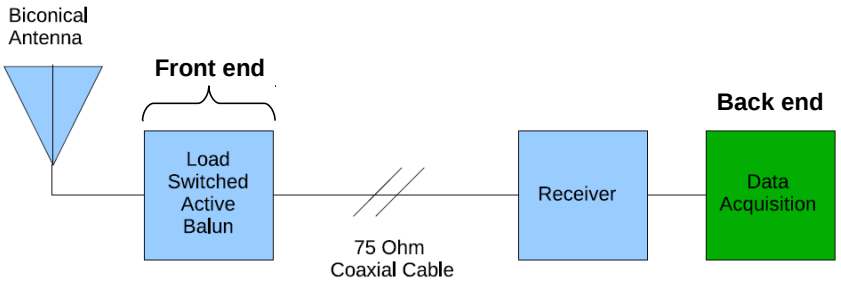

Figure 2.2: Block Diagram for the Bicone system which consists of four main components: the antenna, the front-end electronics (contains the active balun with built in LNAs and the calibrating 50 Ωload), the receiver box, and the back-end DAQ system mounted on a local PC.

2.2 Bicone Instrumentation

In this section, technical details of the DAQ pipeline used to record the data using the bicone radiometer will be provided.

2.2.1 Finite-biconical Antenna

By definition, a biconical antenna is a traveling-wave antenna if its biconical elements are extended out to infinity. However, we use a truncated bicone as a thick, or fat, dipole as the receiving element of the system. The biconical antenna is a balanced two-wire, uniformly tapered, transmission line. Each side of the antenna has a conical geometry that open away from its terminals as shown in Figure 2.3.

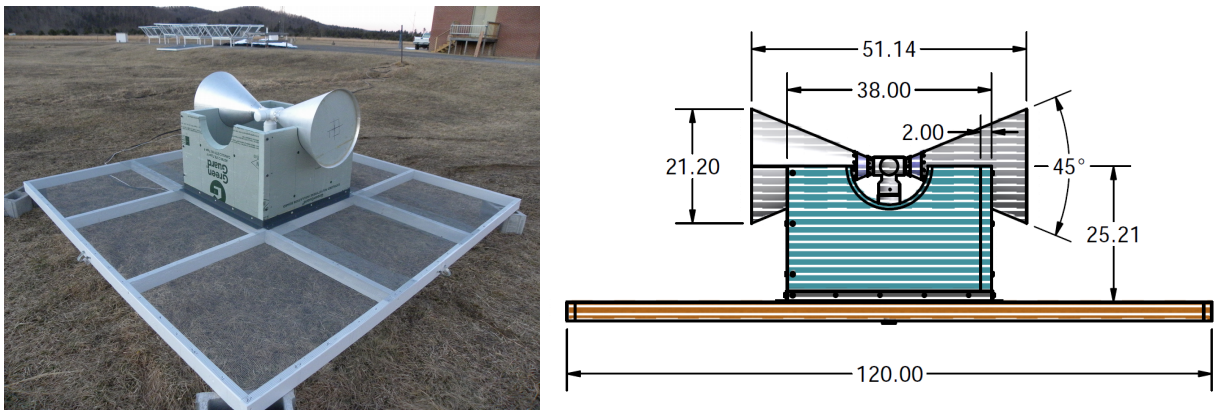

Figure 2.3: (Left) The bicone antenna with the square ground plane were deployed at GBO between 2014-2015. The bicone system consists of a single polarization. (Right) Physical dimension of the bicone antenna. Notes the green-colored box supporting structure is made of lossless closed-cell extruded polystyrene (XPS) foam to minimize its effects on the antenna's EM characteristics.

An antenna's performance can generally be quantified with the antenna impedance $Z_{\text{ant}} = R + jX$, which a complex linear combination of the real resistance R and reactance X. Fore example, the antenna impedance Z_{ant} of an infinite bicone is a function of the

bicone's flaring angle α_{bicone} as,

$$Z_{\text{ant}} = 120 \ln \left[\tan^{-1} \left(\frac{\alpha_{\text{bicone}}}{2} \right) \right], \tag{2.1}$$

where the flaring angle is illustrated in Figure 2.4.

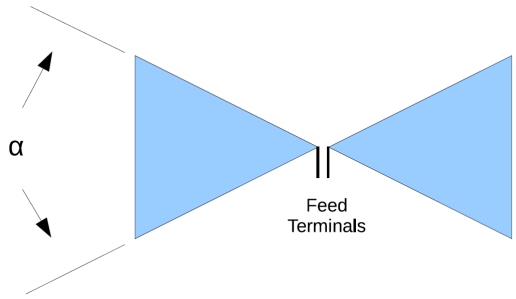

Figure 2.4: For an finite-biconical antenna, the impedance is a function of the flaring angle α_{bicone}.

In practice, for a bicone with a finite size, its impedance is more complicated than the analytical form. It was measured indirectly through the antenna reflection coefficient $\Gamma_{\text{ant}}(\nu)$. The antenna reflection coefficient was measured with a Vector Network Analyzer (VNA) in the field after the bicone system was deployed to GBO in early 2014. By definition, Z_{ant} can be derived from the antenna reflection coefficient using,

$$\Gamma_{\text{ant}} = \frac{V_{\text{reflected}}}{V_{\text{incident}}} = \frac{Z_{\text{ant}} - Z_0}{Z_{\text{ant}} + Z_0}, \tag{2.2}$$

where V_{reflect} is the reflected voltage, V_{incident} is the incident voltage, and Z_0 is reference impedance typically chosen as 50 Ω.

Another property of the antenna that needs to be characterized is its farfield radiation beam pattern, as $F(\nu, \theta, \phi)$ in Eq. (1.10). At high frequency, it is common to measure the antenna either in an indoor anechoic chamber or an outdoor antenna range. For the low frequency application, some researchers measure a scaled version of the antenna at higher frequencies in order to extrapolate the results down to the lower one. Due to the lack of access to measuring facilities, complications in logistics, and inaccuracy of extrapolation

methods, the CST[1] 3D computational electromagnetics (CEM) simulation software was utilized instead to obtain a set of beam pattern results between 30 to 130 MHz. The beam at 90 MHz is shown in Figure 2.5 as an example. The beam chromaticity is apparent in Figure 2.6 as the beam shape varies as a function of frequency.

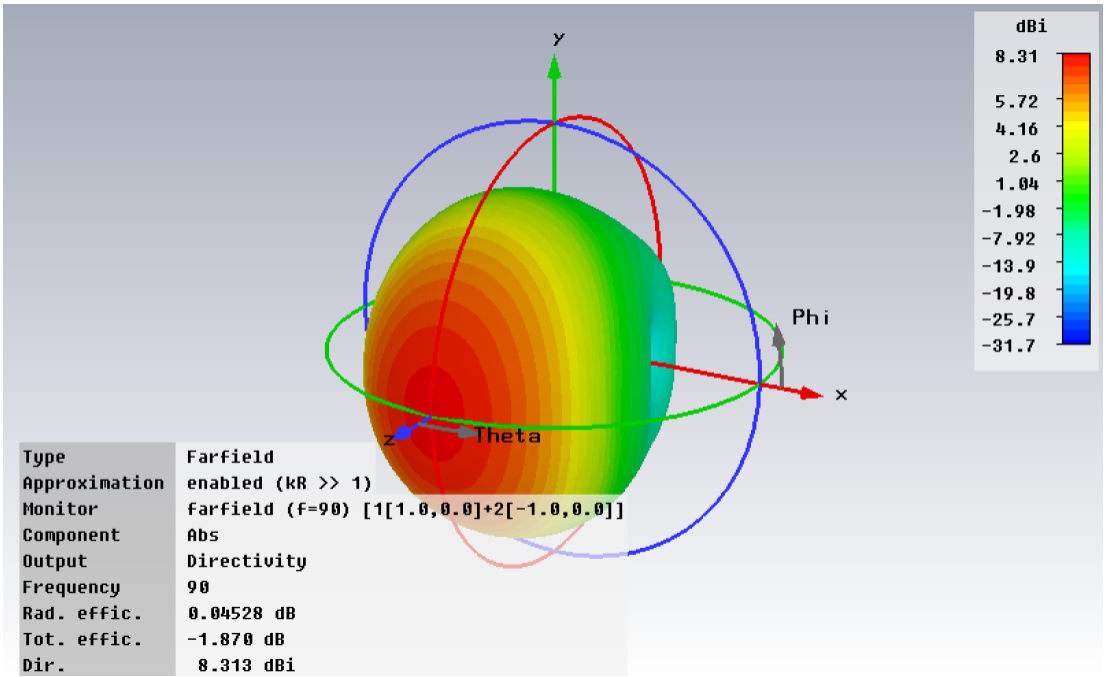

Figure 2.5: CST simulation farfield beam for the finite-bicone antenna at 90 MHz

Because of the lack of complete details of the antenna's surrounding environment like ground soils beneath the antenna, the numerical simulations we have run can only provide a qualitative beam pattern. One of the few ways to ensure consistency between a simulation and the antenna under test (AUT) is by comparing the measured $\Gamma_{\text{ant}}(\nu)$ to the simulation results. With this constraint, one can iteratively refine the details of the CST model to improve the accuracy of the beam pattern indirectly. As shown in Figure 2.7, the bicone system's VNA value is consistent to the CST model except the minor ripples in the CST model. This is acceptable since we don't expect the CST model to be a perfect match

[1] By Dassault Systemes, `https://www.cst.com/`.

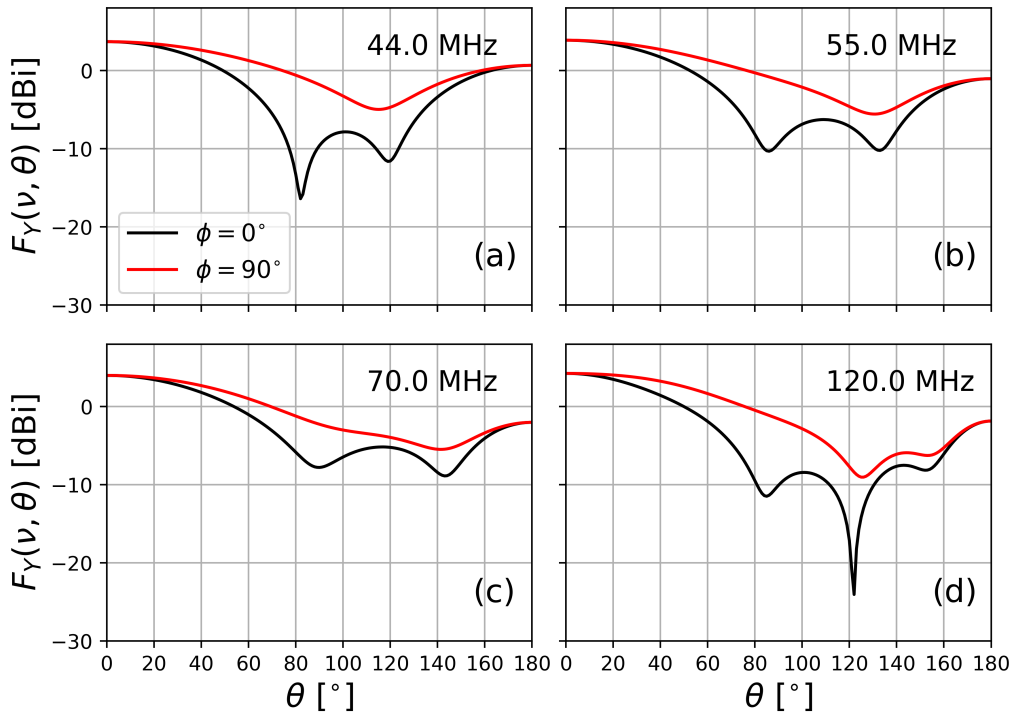

Figure 2.6: The bicone antenna's beam exhibits the beam chromaticity at different frequencies. Furthermore, the beam elongation is apparent by the difference between the beams at $\phi =$ 0° and 90°.

with the measurement due to the complexity in capturing all real-life characteristics of the antenna's surrounding, such as ground soil. After all, we only use the VNA measurement in the calibration, and the CST for diagnostic purposes.

2.2.2 Active Balun Front-end System

As the incoming electromagnetic radiation excites the antenna, a voltage is produced at the antenna terminal ports corresponding to the given Z_{ant}. This output signal from the antenna is called balanced signal because the currents on both antenna elements flow back and forth relative to each other instead of a grounded return path. To be measured through a transmission line like a coaxial cable, this balanced signal is converted to one that has a grounded return path with impedance matched for the input device. This is achieved by passing the signal through a type of transformer called a balun (which is short

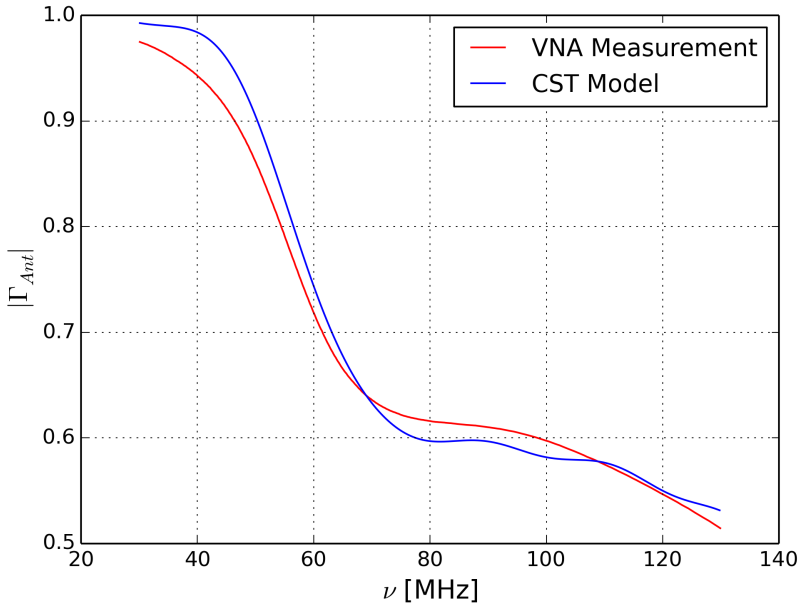

Figure 2.7: Comparison of the antenna reflection coefficient between the VNA measurement and the CST simulation. The measurement is consistent to the CST model except the minor rippling artifacts in the simulation, which is acceptable since we only use the VNA measurement in the calibration, and the CST for diagnostic purposes

for "balanced to unbalanced"). For the bicone instrument, we adopted the active balun from the PAPER project, which used a LNA to transform the incoming balanced signal and amplifies it simultaneously.

The active balun used two bipolar-junction transistor (BJT) LNA in series to amplify the incoming signal. To achieve a high dynamic range over a broadband, the active balun was based on a lossless-feedback common-base Norton-type amplifier design (Norton and Podell, 1975; Parashare and Bradley, 2005). Depending on which input mode the acquisition was set for a given moment, an RF electronic switch alternatively connected the FE to the antenna port and the internal 50 Ω calibrator (see Figure 2.8). The input signal was then amplified by a monolithic microwave integrated circuit(MMIC) field-effective transistor (FET) LNA (Hittitie HMC476MP86). Subsequently, a 180-degree hybrid coupler combined the signal from each side of the bicone antenna together into a composite unbalanced signal optimized

for a 75 Ω output terminal. The stages for this signal chain are illustrated Figure 2.8. The active balun also contained two LM235 Zener diode temperature sensors to record the physical temperature for both 50 Ω load for the on-off load calibration process described below.

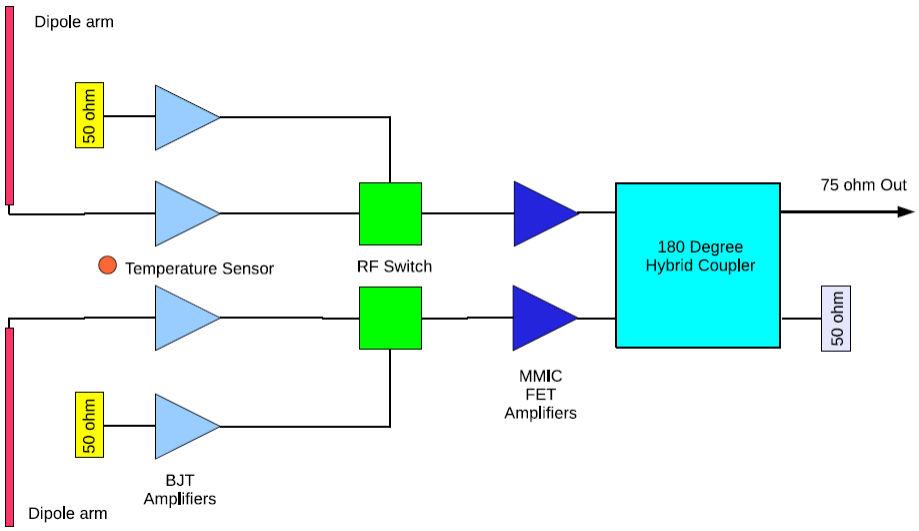

Figure 2.8: Antenna and FE system block diagram

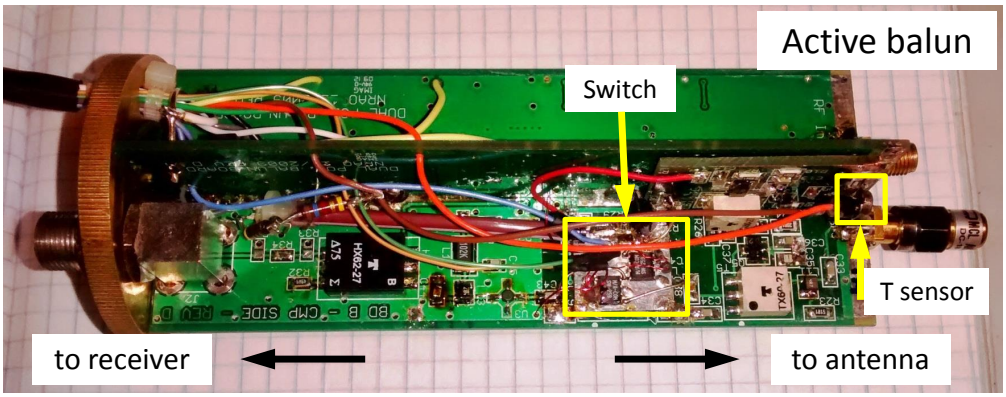

Figure 2.9: Active balun being display in the laboratory

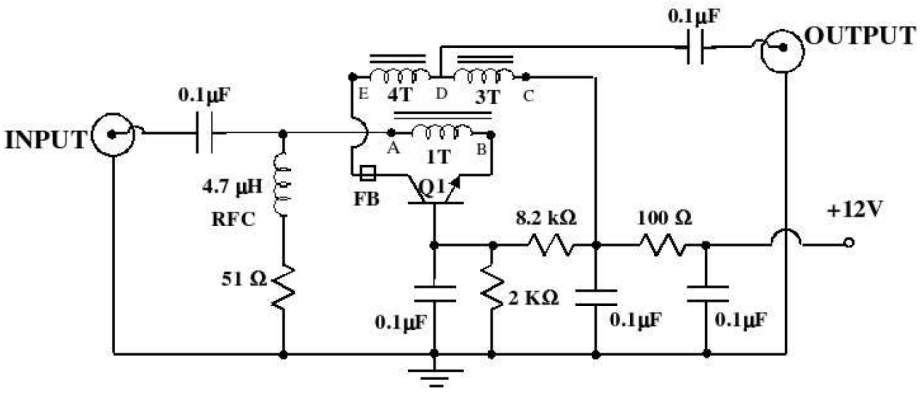

Figure 2.10: Simplified schematic diagram of the Norton-type BJT LNA, which used a common base transformer feedback design to achieve high dynamic range and wide band width. Source: Figure adopted from Parashare and Bradley (2005)

2.2.3 Receiver and DAQ System

The unbalanced RF signal from the FE unit was transmitted from the field through 200 feet of 75 Ω coaxial cable and enter a receiver stored indoors. The output signal from the receiver[2] (Figure 2.12) is then digitized by an indoor DAQ. The DAQ unit is a high-speed FPGA[3] -based digitizer (Signatec Model 14400A)[4] mounted on a PC through a peripheral component interconnect (PCI) port (Figure 2.11). Both the receiver and the DAQ system were contained inside a low-cost Faraday enclosure, as shown in Figure 2.13, to prevent self-generating RFI corrupting the measurement. The metadata from the temperature sensors in the FE were digitized separately from the RF signal using a USB-readable DAQ unit (LabJack U3, in Figure 2.14).

The receiver unit consisted of a series of LNAs to ensure the signal was amplified gradually. To prevent the output signal from a previous amplification stage from saturating the next LNA, small built-in attenuators (varies between 3-10 dB) were used to buffer between

[2] For clarity, technically, the receiver includes the 200-foot cable and the receiver unit.

[3] FPGA = Field Programmable Gate Array

[4] I would like to thank Prof. Judd Bowman at the Arizona State University for providing us the Signatec and LabJack digitizers when I started the project in summer 2013.

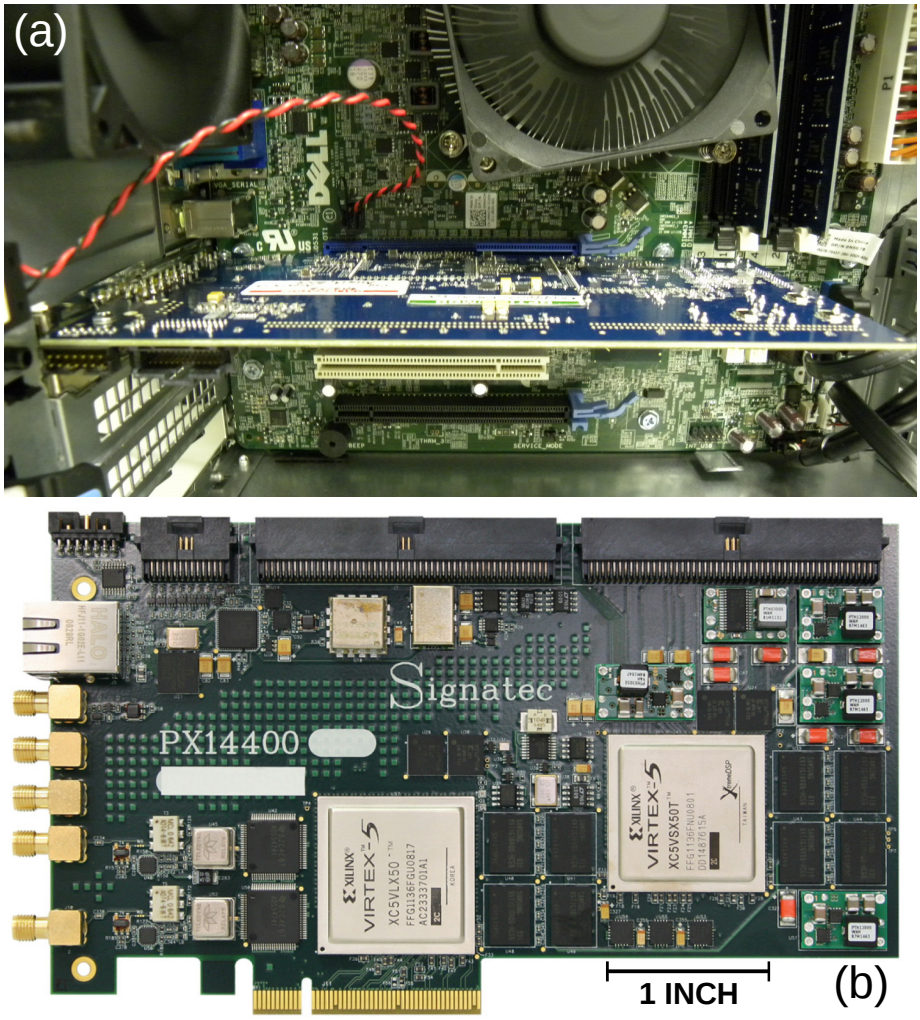

Figure 2.11: Signatec PX14400A high-speed digitizer, PCI-mounted to a PC.

them. As highlighted by the red boxes in Figure 2.12, the entering RF signal was first amplified by a BJT LNA similar to ones in the active balun. This was followed by four more MMIC LNAs (same Hittitie HMC476MP86 as in the FE), and a BPF for 20-140 MHz sandwiched between. The BPF is chosen to be wider than 60-120 MHz to provide extra buffer on each side of the band in the data. The receiver also transformed the signal impedance from 75 Ω to 50 Ω to match the digitizer's input impedance. The overall power gain of the receiver unit was measured to be about 40.5 dB with the VNA with measured efficient noise temperature T_n about 500 K with the Noise Figure Analyzer (NFA).

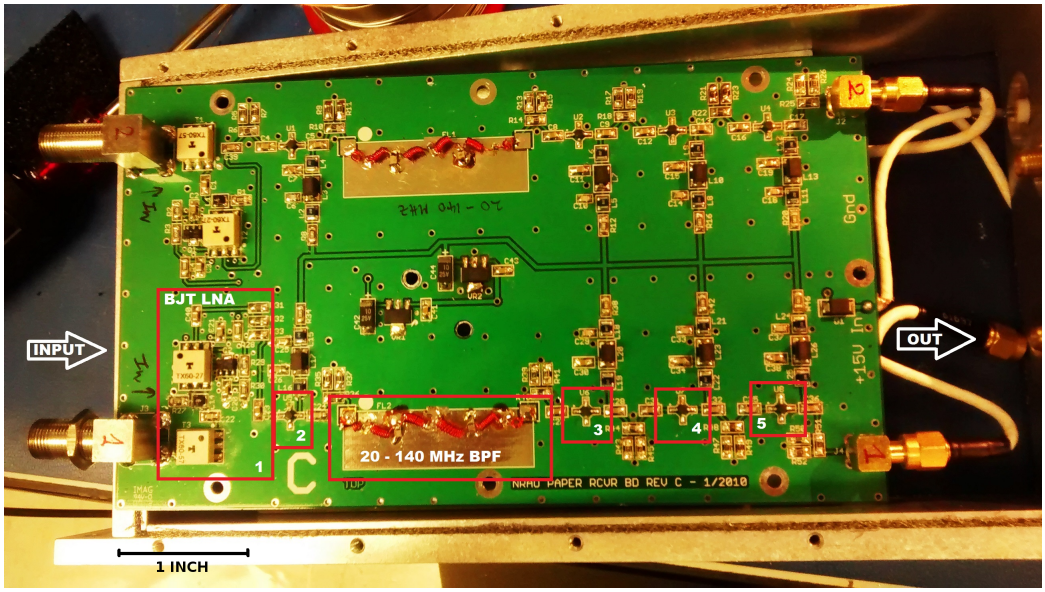

Figure 2.12: The receiver unit consists of on stage of BJT LNA, one BPF for 20-140 MHz, and three MMIC LNA in series. Attenuators of values between 3 to 10 dB are distributed among the stages to prevent saturating the later LNA by the amplified signal from an previous stage. Only one of the two channels shown here was used for the bicone experiment.

2.2.4 Data Product: RF Power Spectrum

The acquired signal from the antenna needs to be digitized and stored on the computer of further analysis. The fidelity of data being sampled digitally depends on the sampling rate of the ADC and how the raw data are formatted during the acquisition. The signal output by the receiver was oversampled[5] into digital voltage by a ADC with a sample rate of $f_s = 375.0$ Mega-sample per second (Ms/s). The digitized voltage was converted to total-power spectrum in RF frequency space using the FFTW3[6] fast Fourier transform software. The resulting spectrum was contained within the band of $[\nu_{min}, \nu_{max}] = [0, f_s/2] = [0, 187.5 \text{ MHz}]$.

The DAQ PC digitized and recorded the data by acquiring a burst of RF data with

[5] In signal processing, oversampling refers to the process of sampling a signal at f_s much higher than the minimal required Nyquist rate, a lower bound which ensures the data are alias-free. The opposite of oversampling is undersampling.

[6] FFTW3 stands for the Fastest Fourier Transform in the West version 3 (Frigo and Johnson, 2005).

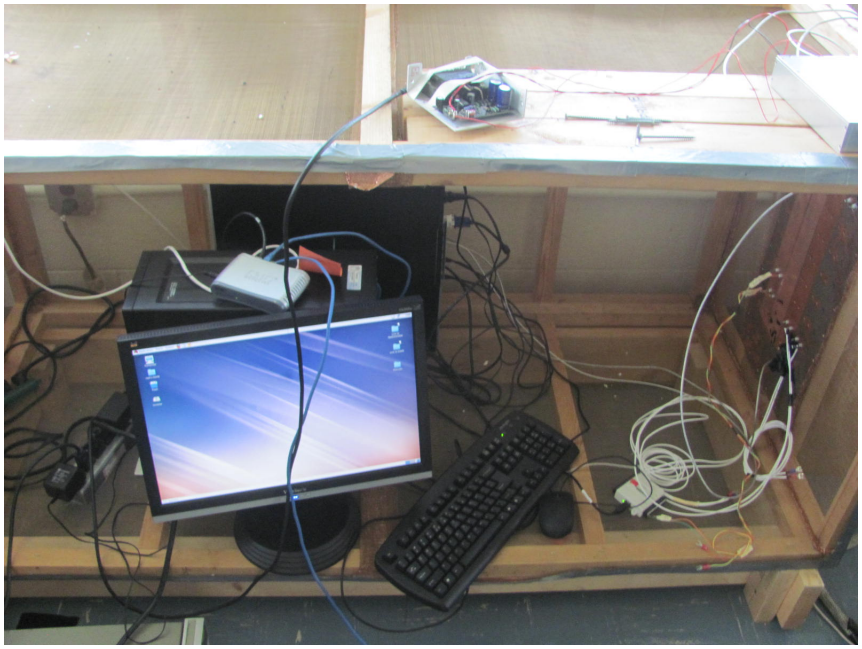

Figure 2.13: The indoor receiver and DAQ system are contained inside low-cost Faraday enclosure to comply to the requirements of the GBO and prevent self-generating RFI corrupting the observation. Shown here, the front cover was removed during a diagnostic session.

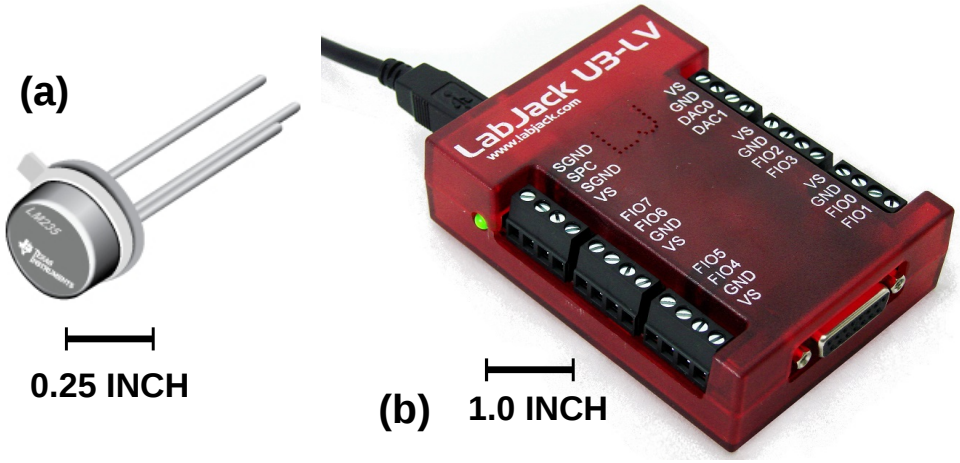

Figure 2.14: Stock images of (a) the LM235 Zener diode temperature sensor, and (b) the LabJack U3 DAQ unit used to record the metadata and controlling the RF switch in the FE. Source: Texas Instruments and LabJack Corporation.

buffer size N_{buff}, which FFTW3 required to be a base-2 integer. The temporal voltage data in the buffer was then divided into N_{FFT} number of FFT segments, each segment had a sample

length of $N_{\rm 1seg} = N_t = 2N_{\rm chan}$ where $N_{\rm chan}$ is the number of observed (or RF) frequency channels. The DAQ buffer size is summarized as,

$$N_{\rm buff} = N_{\rm FFT} \times N_{\rm 1seg} = N_{\rm FFT} \times (2N_{\rm chan}), \tag{2.3}$$

For this particular instrument, by balancing between optimal observation cadence and channel-bandwidth for the kurtosis-based RFI excision algorithm, the final DAQ setting was configured to: $N_{\rm FFT} = 10$, $N_{\rm chan} = 2^{16} = 65,536$. This produced a resolution bandwidth (RBW) of,

$$\text{RBW} = \Delta\nu = \frac{f_s}{N_t} = \frac{375 \text{ MHz}}{2 \times 65536} \approx 5.72 \text{ kHz}, \tag{2.4}$$

For each data segment of length N_t, the observed voltage $V_{\rm obs}(t)$ was converted from the 14-bit ADC as,

$$V_{\rm obs}(t) = \left[\frac{S(t)}{65532}\right] V_{\rm pp} - \frac{V_{\rm pp}}{2}, \tag{2.5}$$

where $S(t)$ is the sample value between 0 and 65532 (or FFFC in hexadecimal), and $V_{\rm pp}$ is the input peak-to-peak voltage range defined at the digitizer card's input ports. For the bicone system, R was given as 1.1 V by default on our version of the Signatec card. This gives a quantization step size of (Ifeachor and Jervis, 2002),

$$q = \frac{V_{\rm pp}}{2^{N_b} - 1} = \frac{1.1 \text{ V}}{2^{14} - 1} \approx 0.067 \text{ mV}, \tag{2.6}$$

which can be used to estimate the mean squared quantization noise power as

$$\sigma_q^2 \approx \frac{q^2}{12} = 3.75 \times 10^{-4} \text{ mV}^2 \tag{2.7}$$

which is equivalent to a noise power of about -81.25 dBm[7] . This is relatively small for the purpose of this experiment.

Subsequently, the Fourier transform of $V_{\rm obs}(t)$, written as

$$\widetilde{V}_{\rm obs}(\nu) = \sum_{t=1}^{N_t} w_{\rm bh4}(t) V_{\rm obs}(t) e^{-j\nu t/N_t}, \tag{2.8}$$

[7] $P[\text{dBm}] = 10\log_{10}(P[\text{mW}]/1\text{mW})$.

was computed with the efficient FFTW3 algorithm, where $j = \sqrt{-1}$ and $w_{\rm bh4}(t)$ is the four-term Blackman-Harris (BH4) window function to prevent power leakage among spectral channels when transforming a finite sample segment into frequency space. Among all types of window functions, the BH4 window was chosen to achieve an optimal balance between side-lobe suppression and power preservation (as suggested by, Heinzel et al., 2002). The BH4 window is defined as,

$$w_{\rm bh4}(t) = c_0 - c_1 \cos\left(\frac{2\pi t}{N_t - 1}\right) + c_2 \cos\left(\frac{4\pi t}{N_t - 1}\right) - c_3 \cos\left(\frac{6\pi t}{N_t - 1}\right), \tag{2.9}$$

with $c_0 = 0.35875,\ c_1 = 0.48829,\ c_2 = 0.14128,\ c_3 = 0.01168$. The frequency response of the BH4 window is shown in Figure 2.15.

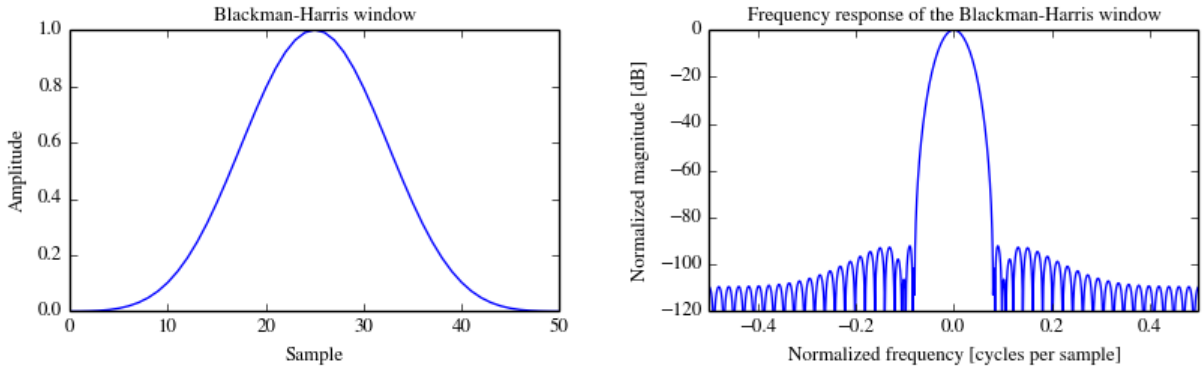

Figure 2.15: Time (left) and frequency (right) response of the BH4 window function which was used for converting the sampled voltage $V_{\rm obs}(t)$ to RF power spectrum $P_{\rm obs}(\nu)$.

The RF power spectrum of the signal for each segment was computed as the squared magnitude of $V_{\rm obs}(t)$ and converted to proper power unit in Watts as,

$$P^i_{\rm obs}(\nu) = \frac{2}{N_t^2}\left[\frac{|\widetilde{V}_{\rm obs}(\nu)|}{\sqrt{2}}\right]^2 = \left[\frac{|\widetilde{V}_{\rm obs}(\nu)|}{N_t}\right]^2 \quad \text{W}, \tag{2.10}$$

where the factor of 2 in the numerator is for converting a two-sided spectrum to single-sided spectrum and the $\sqrt{2}$ is for the RMS value of the voltage. This power spectrum was then integrated over $N_{\rm FFT}$ number of FFT before being stored on the hard disk drive (HDD) on

PC as,

$$P_{\rm obs}(\nu) = \frac{\sum_{i=1}^{N_{\rm FFT}} P_{\rm obs}^{i}(\nu)}{N_{\rm FFT}}, \tag{2.11}$$

At the end of each data acquisition scan, metadata from the two temperature sensors at the FE were saved through the LabJack unit. At the same time, the software controlled the LabJack unit to send out a digital TTL (transistor-transistor logic) signal to toggle the RF switch from the antenna port ($P_{\rm obs} = P_{\rm ant}$) to the 50 Ω load ($P_{\rm obs} = P_{50\Omega}$). The whole process repeated after each scan was stored in the HDD since the system was configured to record data continuously around the clock. The RF power and metadata (for timestamps and temperatures) of individual day were stored in separate files for post processing. An example of the uncalibrated power spectra for both states is displayed in Figure 2.16.

Table 2.1: Summary of the bicone data pipeline parameters.

Effective passband	$B_{\rm eff}$	20-140 MHz
Sampling frequency	f_s	375.5 MHz
Sampling buffer size per scan	$N_{\rm buff}$	10×2^{17}
Number of FFT segments averaged per scan	$N_{\rm FFT}$	10
Number of spectral channel	$N_{\rm chan}$	2^{17}
Resolution bandwidth (RBW)	$\Delta\nu$	5.72 kHz
Integration interval	$\Delta\tau_{\rm int}$	0.87 ms
Quantization error	σ_q^2	-81.25 dBm

2.3 Data Reduction and Calibration

The previous section has described the details on how the bicone experiment acquired and stored the sampled spectra. As in any empirical experiments, the measuring instrument needs to be calibrated to a known standard or reference value. Hence, this section will summarize how the system's power gain and noise temperature were corrected for the RF power spectrum through the "on-off load" calibration scheme. Further discussion on the results and the bicone approach will be followed in the next section of this chapter.

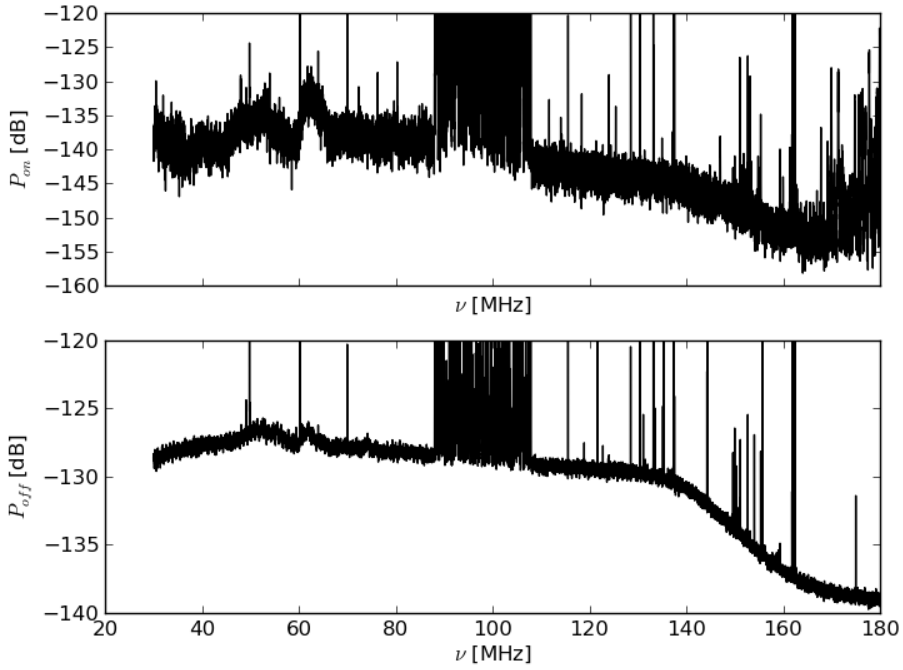

Figure 2.16: Uncalibrated RF power spectrum for when the RF switch set at the antenna input (a) and the 50 Ω load (b). The upper band edge of the BPF is visible around 140 MHz, as the signal attenuates away into the higher frequencies. Note the strong RFI from FM band (88-108 MHz) and other strong transmission even when we observed in the NRQZ. The strong RFI also leaked into the system when the RF switch was connecting the load. These corrupted channels were removed before the analysis.

In brief, since the measurements were made consecutively between the antenna and the load, we assumed that the system behavior had not altered within time period between reading the two inputs. Hence constraining the systematics in the load state would help to recover the systematics in the antenna state. For this calibration pipeline, the averaged RF power spectra were processed by a kurtosis-based RFI excision algorithm[8] to flag potentially corrupted channels (Nita et al., 2007; Nita and Gary, 2010). The effectiveness of the spectral kurtosis in removing strong RFI is evidenced by comparing the waterfall plot of the raw

[8] In short, the kurtosis-based algorithm compare the statistics of the measured data to ones of a Gaussian distribution. If the data in certain channel deviate from a Gaussian over certain threshold, that channel is flagged as RFI. Details of this algorithm is provided in Appendix C.

(Figure 2.17) and the RF-excised (Figure 2.18) data of the entire day on April 24$^{\text{th}}$, 2014. The strong RFI from the FM band (88-108 MHz) and the digital TV band (62-64 MHz) are flagged and removed. The bright structure on the waterfall plot is the Galaxy when it reached zenith at around at 10 hour UTC on that day.

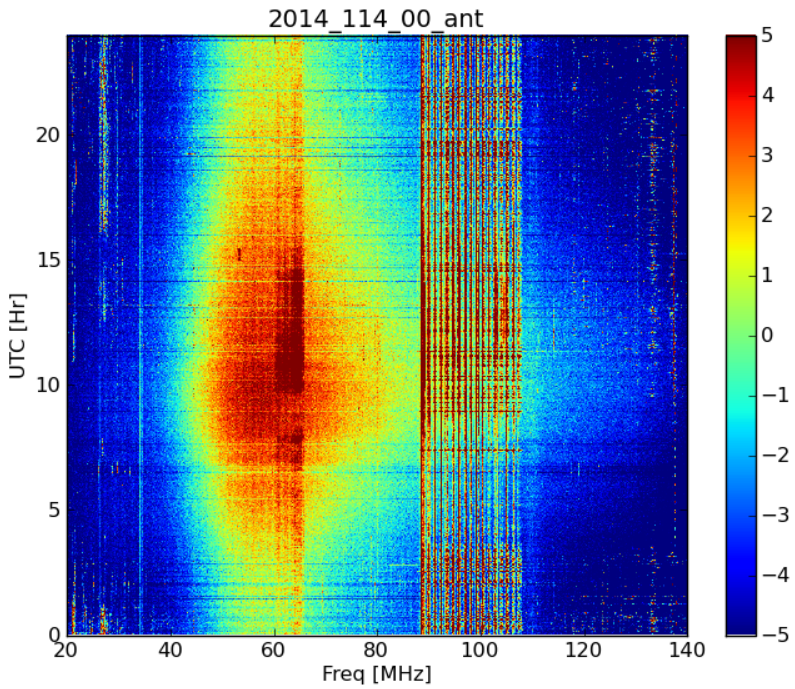

Figure 2.17: Waterfall plot for the raw data acquired on April 24$^{\text{th}}$, 2014 (day of year = 114). The strong RFI from the FM band (88-108 MHz) and digital TV band (62-64 MHz)are visible. The bright region in the center of the plot is when the Galaxy when it reached the zenith at around 10 Hour UTC.

Then the system's transducer gain $G_T(\nu)$ and noise temperature $T_n(\nu)$ were corrected by comparing the sky power $P_{\text{ant}}(\nu)$ measured by the antenna to the noise power $P_{50\Omega}(\nu)$ of an internal 50 Ω load whose physical temperature $T_{50\Omega}$ was recorded by the temperature sensor. Further analysis to recover the foreground spectrum and cosmological signature were done on the final calibrated $T_{\text{ant}}(\nu)$.

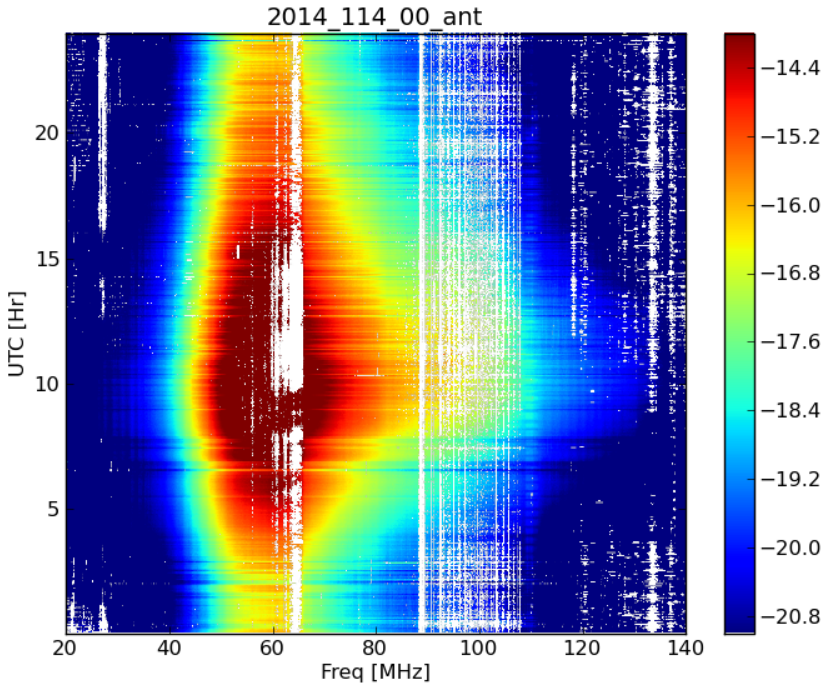

Figure 2.18: Waterfall plot for the RFI-excised data on the same day as in Figure 2.17. The blank regions are where the RFI have been flagged and removed. This illustrates the effectiveness of the spectral kurtosis algorithm for strong and low-level RFI.

2.3.1 On-off Load Calibration Scheme

A single antenna at low frequency has a large beam and no meaningful spatial resolution for astronomical source calibration. After all, this is what global experiments rely on by design, to measure the monopole 21-cm background and smooth out the high spatial features. Additionally, single antennas used in global experiments are typically stationary on the ground—they are neither steerable nor have the ability to artificially form a narrower beam like an arrays to change the pointing in real time. More importantly, the global experiment is sky noise dominated. Hence, it is impractical, if not impossible, to implement the conventional hot-cold load[9] , or on-off source comparison, as other radio telescopes (Kraus,

[9] Hot-cold load is common for horn or aperture antenna since an absorber at a given temperature can be placed in front of the antenna. For large single dipole at low frequency, one would need a large absorber that is at least several wavelength in thickness.

1966).

Given the broadband nature of the global experiment, an internal broadband noise source is commonly used. This can be a noise diode or a resistive load. In fact, the EDGES experiment uses at least three different standards (50 Ω load, an open, and a shorted termination) for their more sophisticated calibration procedure (e.g., Monsalve et al., 2017a). As a proof of concept, we only adopted a 50 Ω resistor as the reference for the bicone radiometer. Recalling that the measurements were made consecutively, thus the system behavior was assumed not being altered within the short time period between reading the two inputs (~ 4 s). Hence, constraining the systematics in the load state would help to recover the systematics in the antenna state. Quantitatively, after the signal passed through the FE with gain $G_{\rm FE}(\nu)$ and noise $T_{n,\rm FE}(\nu)$, and then the receiver with gain $G_{\rm rcv}(\nu)$ and noise $T_{n,\rm rcv}(\nu)$[10] , the measured power spectra for both states were parametrized as,

$$P_{\rm ant} = k_B \Delta\nu \left[G_{\rm FE} G_{\rm rcv} \left(T_{\rm ant} + T_{n,\rm FE} \right) + G_{\rm rcv} T_{n,\rm rcv} \right], \tag{2.12}$$

$$P_{50\Omega} = k_B \Delta\nu \left[G_{\rm FE} G_{\rm rcv} \left(T_{50\Omega} + T_{n,\rm FE} \right) + G_{\rm rcv} T_{n,\rm rcv} \right], \tag{2.13}$$

where k_B is the Boltzmann constant, $\Delta\nu$ is the resolution bandwidth, and the frequency dependence notation is left out for the ease of reading.

Similar to calibration techniques which compare the unknown measurement to a reference signal to correct the systematics, such as the Dicke switching (Dicke, 1982), both gains and noise temperatures were assumed to be identical among both states over the short time interval between switching. Hence, $T_{\rm ant}(\nu)$ in Eq. (2.12) was solved for by substituting the gain and noise temperature from Eq. (2.13) in (2.12) such that,

$$T_{\rm ant}(\nu) = \frac{1}{k_B} \left[\frac{P_{\rm ant}(\nu) - P_{50\Omega}(\nu)}{G_{\rm FE}(\nu) G_{\rm rcv}(\nu)} \right] + T_{50\Omega}(\nu), \tag{2.14}$$

where $T_{n,\rm FE}(\nu)$ and $T_{n,\rm rcv}(\nu)$ canceled out between the two states. By determining the product $G_{\rm FE}(\nu) G_{\rm rcv}(\nu)$ in Eq. (2.14), $T_{\rm ant}(\nu)$ was obtained to recover the spectrum of the

[10] This thesis adopted the convention where the noisy DUT is mathematically equivalent to a noise-free device with a noise temperature $T_n(\nu)$ at the input (Engberg and Larsen, 1995).

spatially-averaged sky signal in Eq. (1.11).

2.3.2 Transducer Gain Derivation

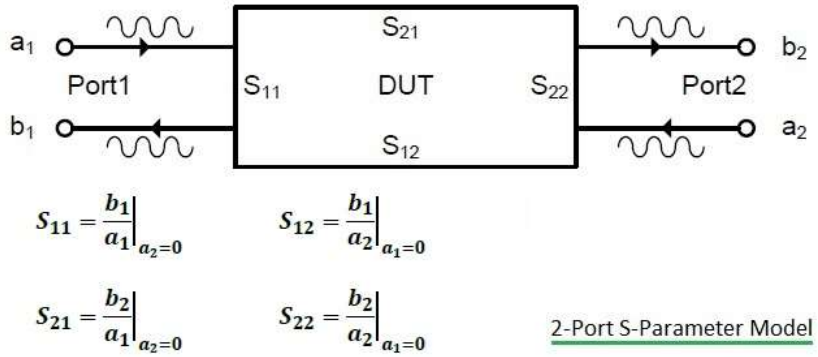

Figure 2.19: Diagram describes the network model for a two-port DUT. By convention, a_1 and a_2 are the incoming signal waves at the input and output ports respectively. b_1 and b_2 are the outgoing waves at the respective ports. The relations between the four waves are described by the four S-parameters shown here, which are intrinsic to each individual device and independent on the impedances on the external ports.

In electrical network theory, for a two-port network similar to the bicone system's FE unit (one input and one output as illustrated in Figure 2.19), the transducer gain of the device under test (DUT) is defined as the ratio of the power delivered to the system over the the total available power. In terms of scattering (or S-) parameters[11] , $G_T(\nu)$ is given as (Collin, 2007),

$$\begin{aligned} G_T(\nu) &\equiv \frac{\text{Power delivered to load}}{\text{Power available from source}} \\ &= \frac{\left(1-|\Gamma_{\rm src}|^2\right)\left(1-|\Gamma_{\rm load}|^2\right)|S_{21}|^2}{\left|\left(1-S_{11}\Gamma_{\rm src}\right)\left(1-S_{22}\Gamma_{\rm load}\right)-S_{12}S_{21}\Gamma_{\rm src}\Gamma_{\rm load}\right|^2}, \end{aligned} \tag{2.15}$$

where $S_{11}(\nu)$, $S_{12}(\nu)$, $S_{21}(\nu)$, and $S_{22}(\nu)$ are the complex components of the scattering matrix which describes the intrinsic properties a DUT. Meanwhile the reflection coefficients of the DUT due to the source $\Gamma_{\rm src}(\nu)$ and load $\Gamma_{\rm load}(\nu)$ depends on the impedance of the external devices being connected to it.

[11] For a two-port network, S-parameters are elements of a 2×2 matrix that describes the relationship between the input and output signal voltages, more detailed can be found in (Collin, 2007) .

Conventionally, when measuring the DUT with a laboratory apparatus, the impedance at the input and output of the device were optimized such that there are minimal loss, hence $G_T \sim |S_{21}|^2$. Due to the complication of the antenna impedance on the bicone system, the FE gain needs to be derived with all the extra terms in Eq. (2.15). However, since only the FE was switching between two different inputs and $G_{\mathrm{rcv}}(\nu)$ was consistently shared by the two states in the later stage where the input and output impedance were well matched, only $G_{\mathrm{FE}}(\nu)$ had to be estimated by using the transducer gain equation. The $G_{\mathrm{rcv}}(\nu)$ was measured with the VNA in the lab.

Furthermore, since S_{12} of the FE can be assumed small if the reverse isolation built in the active balun is large (≥ 20 dB), Eq. (2.16) was simplified to,

$$G_{T,u}(\nu) \approx \frac{(1-|\Gamma_{\mathrm{src}}|^2)\,(1-|\Gamma_{\mathrm{load}}|^2)\,|S_{21}|^2}{|\,(1-S_{11}\Gamma_{\mathrm{src}})\,(1-S_{22}\Gamma_{\mathrm{load}})\,|^2}, \tag{2.16}$$

This is sometimes known as the unilateral gain. Additionally, since the output port of the balun was designed to match the impedance of the 75 Ω cable, this allowed me to assume that reflection coefficient $\Gamma_{\mathrm{load}}(\nu)$ to be small to simplify the transducer gain further as,

$$G_{\mathrm{FE}}(\nu) \approx \frac{(1-|\Gamma_{\mathrm{src}}|^2)\,|S_{21}|^2}{|\,(1-S_{11}\Gamma_{\mathrm{src}})\,|^2}, \tag{2.17}$$

Since the four S-parameters here were intrinsic to the FE, they were measured directly in the laboratory with a VNA. Meanwhile, when the FE was switched to the antenna, Γ_{src} is equivalent to $\Gamma_{\mathrm{ant}}(\nu)$ which was measured in the field with the VNA as shown in Figure 2.7. As a result, a direct way to calculate the FE gain was secured.

2.3.3 Thermal Dependence of the Transducer Gain

Since the characteristics of electronic components depend on operating temperature, the performance of a device also is also susceptible to its environment. As a result, this alters the frequency response of a device, hence the transducer gain. In fact, when the radiometer was exposed to the ambient environment at the site, the spectral structure of

$G_{\mathrm{FE}}(\nu)$ was naturally altered. Namely, the derived gain in the previous section would have been inaccurate unless proper temperature correction to the S-parameters was applied for a given time.

To be able to apply the correct amount of change to the gain, the gain was parametrized both as a function of temperature and frequency. The parametrization procedure was formulated by empirically measuring the FE unit S-parameters in a thermally controlled capsule in the lab with the VNA. After letting the system reach thermal equilibrium at a temperature T_{set}, the VNA recorded the full set of S-parameters for 30-130 MHz. Then, the process repeated for a new temperature setting. The lab apparatus produced measurements from 17-31 °C. In the end, the real and imaginary components of each S-parameters were fitted separately with a fourth degree polynomial as a function of frequency to obtain a set of coefficients a_n as,

$$\begin{aligned} S_{kl}(\nu) &= \left[\sum_{n=0}^{4} a_n(T)\nu^n\right]_{kl} \\ &= \left[a_0(T) + a_1(T)\nu + a_2(T)\nu^2 + a_3(T)\nu^3 + a_4(T)\nu^4\right]_{kl}, \end{aligned} \tag{2.18}$$

where $k, l \in \{1, 2\}$ for each of the four S-parameters. Subsequently, the $a_n(T)$ coefficients in Eq. (2.14) were fitted with another fourth degree polynomial with respect to the temperature with the new b_{nm} coefficients,

$$\begin{aligned} [a_n(T)]_{kl} &= \left[\sum_{m=0}^{4} b_{nm}T^m\right]_{kl} \\ &= \left[b_{n0} + b_{n1}T + b_{n2}T^2 + b_{n3}T^3 + b_{n4}T^4\right]_{kl}, \end{aligned} \tag{2.19}$$

As a result, for each of the four S-parameters,a set of 4 b_{nm} were obtained for each of the 4 a_n for either real of imaginary components, i.e., $4 \times 4 \times 2 = 32$ coefficients.

In principle, by using these a_n and b_{nm} coefficients, within measurement uncertainties of the VNA and the temperature range measured in the lab, the $G_{\mathrm{FE}}(\nu, T)$ for any arbitrary temperature can be extrapolated. In another words, from the metadata recorded by the temperature sensors during the observation, the transducer gain was computed using these

polynomial coefficients acquired in the laboratory to calibrate the $G_{\rm FE}(\nu, T)$. For example, the VNA's S-parameters are compared with the reconstructed values using the aforementioned polynomial fitting for the laboratory measurement are shown in Figure 2.20

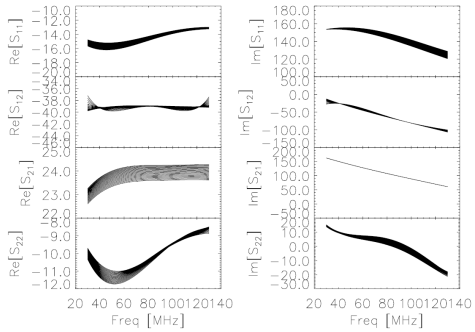

Figure 2.20: The S-parameters are a function of temperature, as can be seen on the real (left) and imaginary (right) parts over a range of orating temperature measured in the thermal control enclosure in the lab (17-31 °C). As they change with temperature, their frequency responses also change. However, the change is smooth spectrally, and hence can be extrapolated for a given temperature T if we fit a set of coefficients to their functional form.

In summary, the transducer gain is calibrated as the following steps,

(1) In the lab, measure the set of S-parameters for the FE unit (active balun module) with the VNA over a range of temperature in the thermal control housing,

(2) Polynomial fit the real and imaginary parts of all S-parameters as described in Eq. (2.18) and (2.19) over that same range of temperature,

(3) During observation, use that set of lab-fitted coefficients in Step 2 to extrapolate the S-parameters based on the temperature recorded by the sensors in the field using Eq. (2.18) and (2.19),

(4) Use these extrapolated S-parameters to calculate the corresponding unilateral transducer gain $G_T(\nu, T)$ for the FE module as Eq. 2.22,

(5) Apply the gain correction as Eq. (2.14) to obtain the antenna temperature $T_{\rm ant}(\nu)$ for the sky spectrum.

2.4 Results and Lessons Learned

From the evaluation of the bicone system, we have identified three major shortcomings in the bicone system, some of which are intrinsic to the conventional approach to the global 21-cm experiment. In this section, we will discuss the nature and potential remedies for these issues. In brief, the first two limitations are related to the accuracy of the flux calibration due to using a broadband noise source as an internal calibrator and exposing FE to the uncontrolled ambient environment. The remaining concern is the antenna beam chromatic effects of the bicone antenna. All these constraints strongly suggest that the spectral smoothness of the foreground spectrum has been compromised. As a result, it becomes extremely challenging, if not implausible, to constrain the foreground spectrum to the required accuracy for extracting the 21-cm signal using the conventional trend removal approach. In the next chapter, a new observational technique to alleviate some of these challenges will be presented.

2.4.1 Accuracy of the On-off Load Calibration

As pointed out earlier in this chapter, although the S-parameters are intrinsic to each given DUT, the transducer gain $G_T(\nu)$ in Eq. (2.15) is also a function of input $\Gamma_{\rm src}(\nu)$ and output $\Gamma_{\rm load}(\nu)$ reflection coefficients. In another words, for an identical system, the gains are different when the system's input are connected to different sources. In fact, for our on-off load switching, it is inaccurate to assume $G_{\rm FE}(\nu)$ to be identical as in Eq. (2.14) between the antenna and the load states since $\Gamma_{\rm src} = \Gamma_{\rm ant}$ is not the same as $\Gamma_{\rm src} = \Gamma_{50\Omega}$.

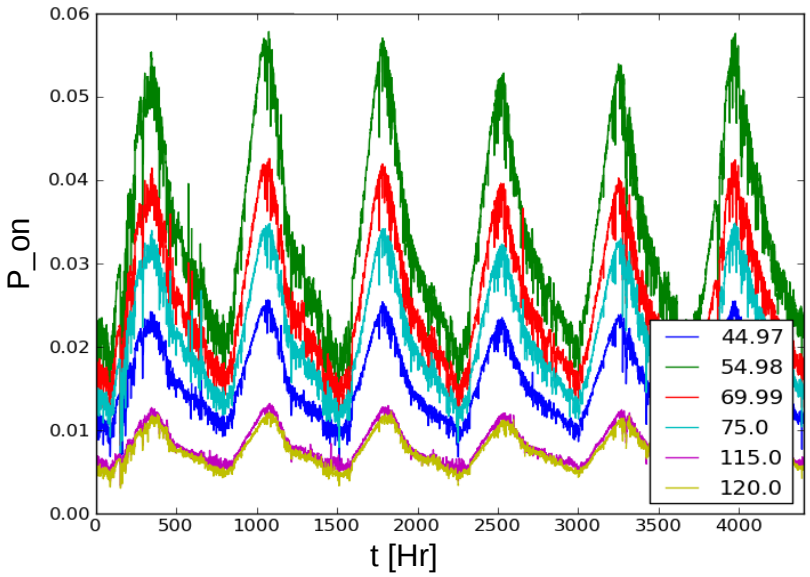

Figure 2.21: Raw power P_{on} from April 19$^{\text{th}}$-24$^{\text{th}}$, 2014 for plotted as function of observation times in hours. The listed frequency channel in MHz are plotted with the corresponding colors. The strong diurnal variation due to the rise and set of the Galaxy over the observer's zenith is visible. The power is inversely proportional to the frequency, but since the 44.97 MHz is outside the passband of the BPF, its power is attenuated.

This minor difference is apparent when Eq. (2.15) is rewritten for both states as,

$$G_{\text{FE,ant}} = \frac{(1-|\Gamma_{\text{ant}}|^2)\,(1-|\Gamma_{\text{rcv}}|^2)\,|S_{21}|^2}{|\,(1-S_{11}\Gamma_{\text{ant}})\,(1-S_{22}\Gamma_{\text{rcv}})-S_{12}S_{21}\Gamma_{\text{ant}}\Gamma_{\text{rcv}}|^2} \tag{2.20}$$

$$G_{\text{FE,load}} = \frac{(1-|\Gamma_{50\Omega}|^2)\,(1-|\Gamma_{\text{rcv}}|^2)\,|S_{21}|^2}{|\,(1-S_{11}\Gamma_{50\Omega})\,(1-S_{22}\Gamma_{\text{rcv}})-S_{12}S_{21}\Gamma_{50\Omega}\Gamma_{\text{rcv}}|^2} \tag{2.21}$$

where the output reflection coefficient $\Gamma_{\text{load}}(\nu)$ in was substituted by $\Gamma_{\text{rcv}}(\nu)$ for the reflection coefficient of the FE's output port when connected to the long coaxial cable and the receiver unit. This subtlety is acceptable for most general radio astronomy applications since their target of interest tend to be stronger and more defined than the weak 21-cm signal.

Based on the bicone measurement, $\Gamma_{\text{ant}}(\nu)$ is spectrally more complicated than the flat response of $\Gamma_{50\Omega}(\nu)$, as seen in Figure 2.7. Using the measured S-parameters for the active balun FE, the resulting difference in the transducer gain between two states can be large. Hence, simply measuring the gain in the laboratory and then applying this gain to the

antenna observation is insufficient for the stringent requirement for the global 21-cm science.

One way to confirm the accuracy of the calibration was to compared the calibrated spectrum to values published in the literature. In this experiment, a simple power-law parametrization was adopted (Rogers and Bowman, 2008),

$$\widehat{T}_{\rm fg}(\nu) = T_{\rm sky,150}\left(\frac{\nu}{150\ {\rm MHz}}\right)^{-\beta}, \tag{2.22}$$

where the normalization factor at 150 MHz is $T_{\rm sky,150} = 283.2$ K, and the foreground spectral index $\alpha = 2.47$. Figure 2.22 shows that this calibration was insufficient. The residual between the bicone measurement and the power-law fit is 10-100 K, with an RMS value across the band of ± 64 K. Such a large residual implies that the measurement is not sensitive to the required level for detecting the global 21-cm signal. This indicates that either the gain calibration we employed is not accurate enough, or there are other variations we need to constrain further. However, one of the biggest drawbacks of the on-off load approach is to rely on the transducer gain derived from power measured on a 50 Ω. As soon as the system switches back to the antenna, the derived gain from the load is no longer identical. It is more desirable if one can calibrate the gain using only the network-based S-parameters. Then the observer can have more control on constrain the FE's characteristics. In fact, this has inspired a new calibration scheme that we will present in Chapter 4.

2.4.2 Stability of the FE Calibration

The FE unit was exposed to the ambient environment during operation. To compensate for the gain change due to temperature fluctuations, extrapolation of the gain was computed using the fitting procedure in Section 2.3.1 based on the recorded temperature from the sensors placed in the FE.

There are at least two limitations to this approach. First, the gain fitting coefficients, $a_n(T)$ and b_{nm}, obtained were only applicable to the temperature range (17-31 °C) of our thermal control unit in the laboratory. However, the gain using these coefficients for $T_{\rm load}$

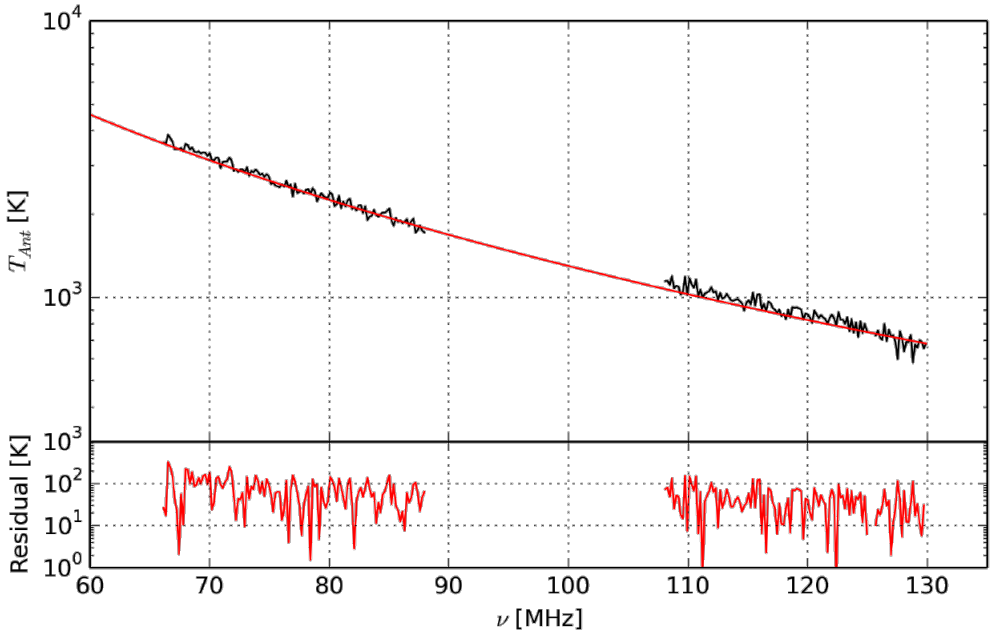

Figure 2.22: (Top) Comparison between calibrated spectrum (black) and foreground power-law model based on published values (red). Note the blanked region due to RFI excision of the FM band (88-108 MHz) and the digital TV (62-64 MHz). (Bottom) The residual between the measurement and the power law model. The large residual (> 10 K) indicates that the calibration, along with other systematics, were not sufficient yet for the global 21-cm signal.

has to be corrected for outside the reliable temperature range, which turned out was much larger than the lab range (0-15 °C during winter, and 18-35 °C during summer). As a result, there were large errors from the derived gain. The temperature variations of the FE and indoor BE rack are shown in Figure 2.23 along with the corresponding $T_{\rm ant}$ as a function of time over multiple days, at 68.97 MHz as an example.

Due to the motion of the Earth in the Milky Way, the apparent Galactic foreground at zenith for a ground observer will shift by about 4 minutes per day based on solar time. However, by definition, the observed foreground signal should repeat itself every 24 hours Local Sidereal Time (LST). One indicator used to check the data for stability is to align the spectra of multiple consecutive days in LST. Measurements were made during night time since there is minimal disturbance in the upper layers of the ionosphere without the presence

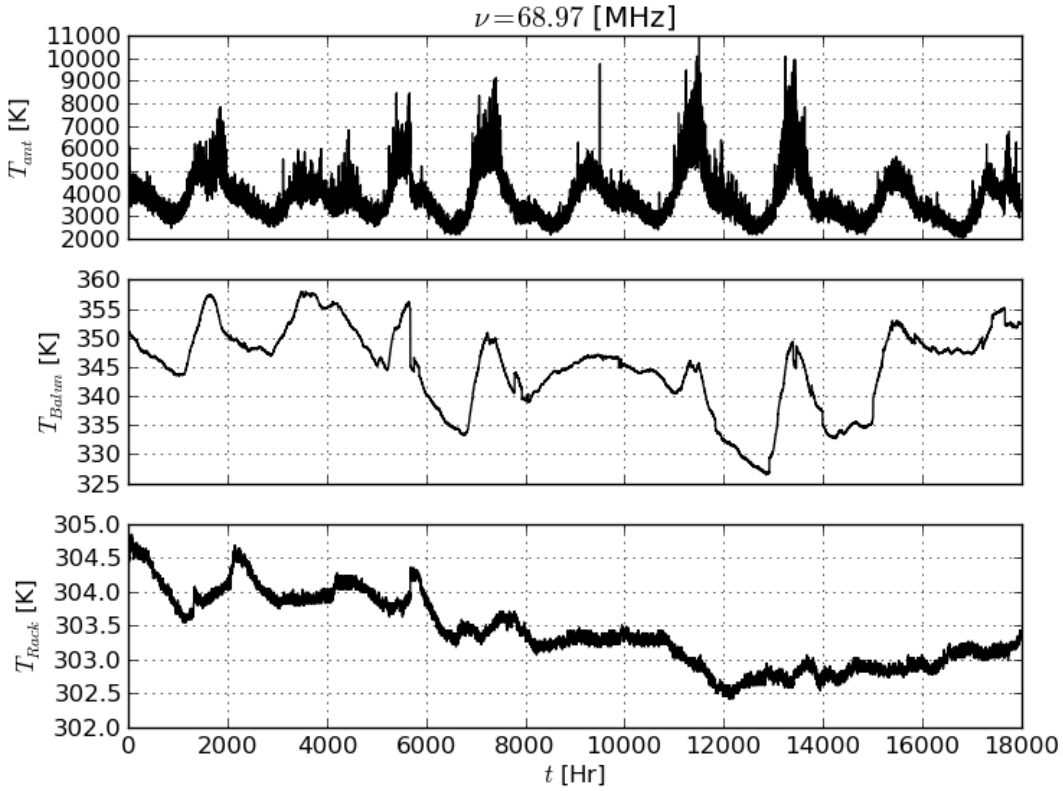

Figure 2.23: Calibrated $T_{\rm ant}$ at 68.97 MHz plotted as function of time over the course of nine days. The corresponding temperatures of the FE unit and indoor BE rack show large fluctuations in the ambient temperature (as large as 35 degrees in the field). This prevents the system from achieving the desired calibration accuracy.

of the Sun and there is a the reduction of RFI from aircraft telecommunication activities. Multiple days of the calibrated $T_{\rm ant}(\nu)$ over the course of 10 hours LST during night time observation are superimposed in Figure 2.24 to illustrate the large variations resulting from the calibration.

For empirical experiments, random and instrumental systematic errors bound the precision of the measurements. While long-term averaging can reduce random errors, systematic errors can only be removed through accurate calibration. In fact, systematic behaviors of radiometers are generally a function of both time and RF frequency. Effects from gain

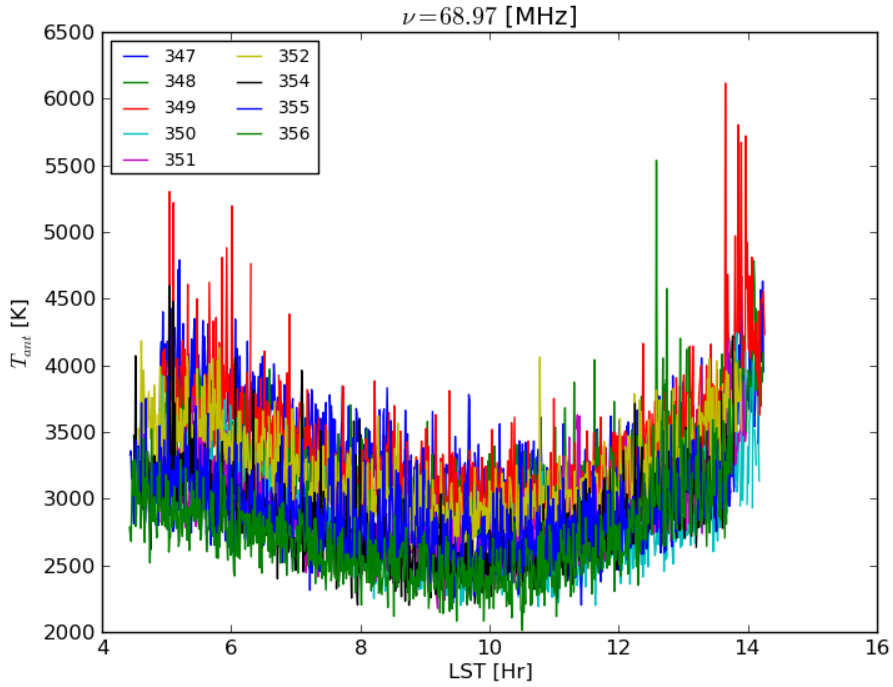

Figure 2.24: Calibrated spectrum at 68.97 MHz over 10 hours LST for nine consecutive days during night time observation.

fluctuation are apparent in the radiometer equation, which describes the contribution of different errors to the overall sensitivity of the radiometer. The sensitivity essentially is the root-mean-squared (RMS) value $\Delta T_{\rm min}(\nu)$ and is written as (),

$$\Delta T_{\rm min} = \sigma_{\rm RMS} = T_{\rm sys}\left[\frac{1}{\tau_{\rm int}\Delta\nu} + \left(\frac{\Delta G}{G}\right)^2 + \left(\frac{\Delta T_{\rm sys}}{T_{\rm sys}}\right)^2\right]^{1/2}, \tag{2.23}$$

where $T_{\rm sys}$ is the total system noise temperature, $\tau_{\rm int}$ is the integration time over the effective RBW $\Delta\nu$. If the gain variations ΔG is not corrected properly, the sensitivity of the system suffers. This is because the RMS eventually reaches a noise floor determined by the gain variation term in Equation 2.23, even after long-term integration to reduce the thermal noise term. Therefore, it is crucial to be able to calibrate the FE's gain fast enough before the any drifting occurs. Having the system exposed to ambient temperature does not help either, eventually we realized the importance of insulating the system. In fact, it would be better

to have an active thermal control system in place to regulate the operating temperature of the FE electronics.

2.4.3 Beam Chromatic Effect

As we have mentioned in the previous chapter, the antenna beam pattern, $F(\nu, \theta, \phi)$, is a function of frequency. Since $T_{\rm ant}(\nu)$ is a beam weighted value, the beam structures at different frequencies can produce a different power. This is what corrupts the spectral smoothness of the foreground spectrum $T_{\rm fg}(\nu)$ and preventing the log-log polynomial fit to remove it cleanly. Groups like SARAS and SARAS 2 have attempted to achieve a smooth antenna frequency response by designing antennas with unique shape and characteristic to compensate for the beam chromatic variations. For the biconical antenna, based on CST simulation, the frequency-dependent beams are apparent in angular plot of the E-plane ($\phi = 0°$) and the H-plane ($\phi = 90°$) as shown in Figure 2.25. To accentuate the frequency structure in the beams, we compute the spatial gradient of the CST beam pattern respect to the frequency, $\partial_\nu F(\nu, \theta, \phi)$. Comparison between the beam patterns and its gradient is shown in Figure 2.26.

2.4.4 Secondary Science

Besides the global 21-cm signal, a total-power experiment is also useful for secondary science, in particular for monitoring solar activities by measuring the disturbance in the upper layers of ionosphere. For example, during our observation in early Sep 2014 (Sep $10^{\rm th}$, 2014, 3:00 UTC), we were able to observe a X1.6 class[12] solar flare.

As shown in the waterfall plot in Figure 2.27 and spectra in Figure 2.28, the X-flares excited the ionosphere and completely corrupted the sky spectrum with strong flux. As shown the flare lasted for 6 hours before the sky returned to normal. More importantly, upon closer examination, there are ripple-like structures on the spectra of the flare. This

[12] X Class is designated for flare with peak flux range at 100-800 picometer $> 10^{-4}{\rm W/m}^2$.

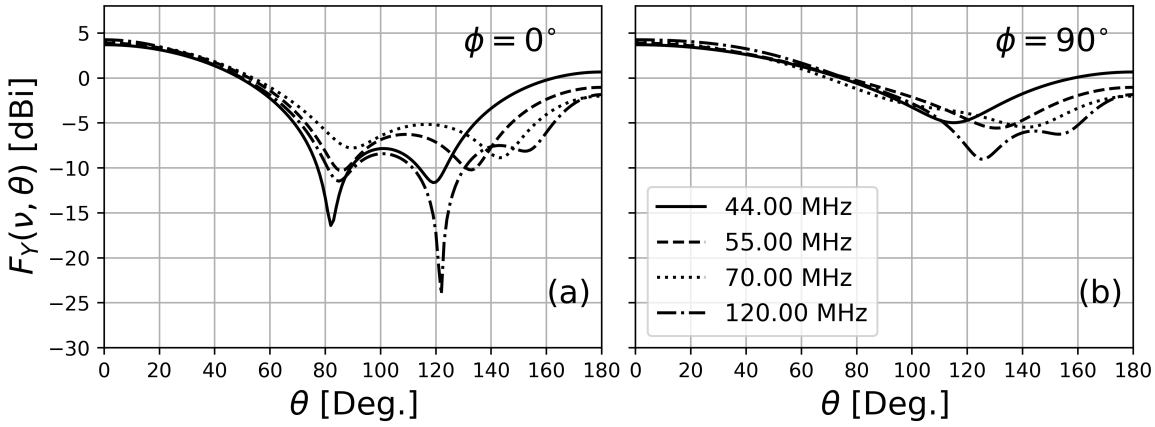

Figure 2.25: Angular plots for the CST beam of the biconical antenna. (Left) E-plane ($\phi = 0°$) and (Right) the H-plane ($\phi = 90°$) of the beams are smooth and symmetric. The chromaticity is apparent as the variations in the beam among different frequencies. Beam elongation, or ellipticity, is visible since the beam size are not identical between E- and H-planes.

flare has been confirmed by the data released[13] by the Solar Dynamics Observatory (SDO) as shown in Figure 2.29

2.5 Summary

In this chapter, we have presented the technical details and observational data from the bicone system. We have been able to adapt and convert existing hardware from the PAPER project to a functional system for the total-power measurement. Upon analyzing the data, we have identified multiple limitations that have prevented the bicone system to achieve the needed sensitive for a global 21-cm signal measurement. The precursor instrument has provided insights on redesigning the systems and potentially the entire approach of conducting global-signal measurement. We highlight some of the more important aspects:

- The "on-off" load calibration scheme is insufficient for high-accuracy measurement such as the global 21-cm signal. The premise of using gain derived from a 50 Ω load to correct for the gain when the FE is switched to antenna is inadequate since

[13] Data can be retrieved from
`https://hesperia.gsfc.nasa.gov/rhessi3/data/solar-data-browsing/index.html`

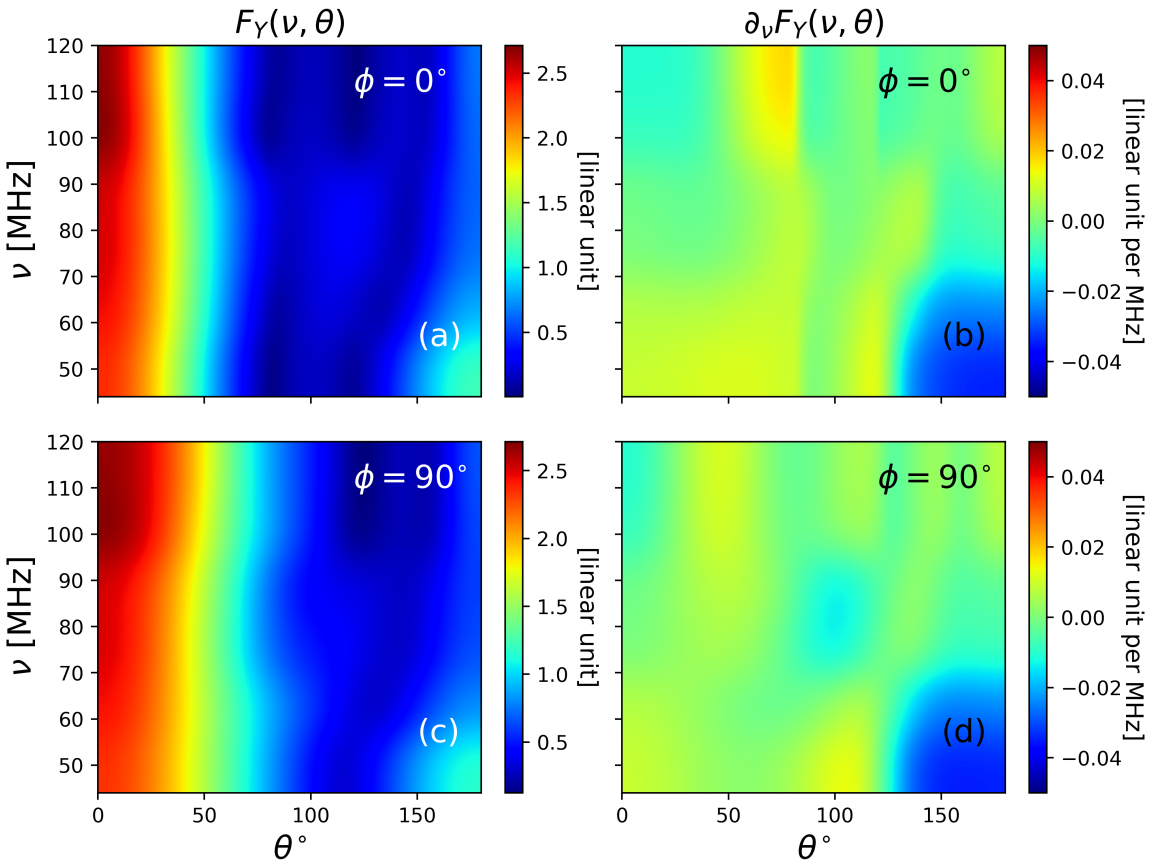

Figure 2.26: (Left) 2D plots of the E-plane ($\phi = 0°$) and the H-plane ($\phi = 90°$) for CST beam model, $F(\nu, \theta, \phi)$, of the biconical antenna. (Right) The 2D plots of the frequency gradient, $\partial_\nu F(\nu, \theta, \phi)$, of the beams on the left panels. Overall the beam gradient has spectral variations in the order of ± 0.02 per MHz close to the main lobe.

the input impedance, or reflection coefficient between the antenna and the load are different. $\Gamma(\nu)$ is a function of frequency when $\Gamma_{50\Omega}$ is constant. A more robust gain calibration scheme is needed.

- Exposing the FE system to the ambient environment introduces large temperature variations to the performance of the FE electronics. In combination with the slow cadence of the "on-off" load switching, the calibration cannot accurately correct the gain drifts. This can be improved by thermally stabilized the FE with active thermal control.

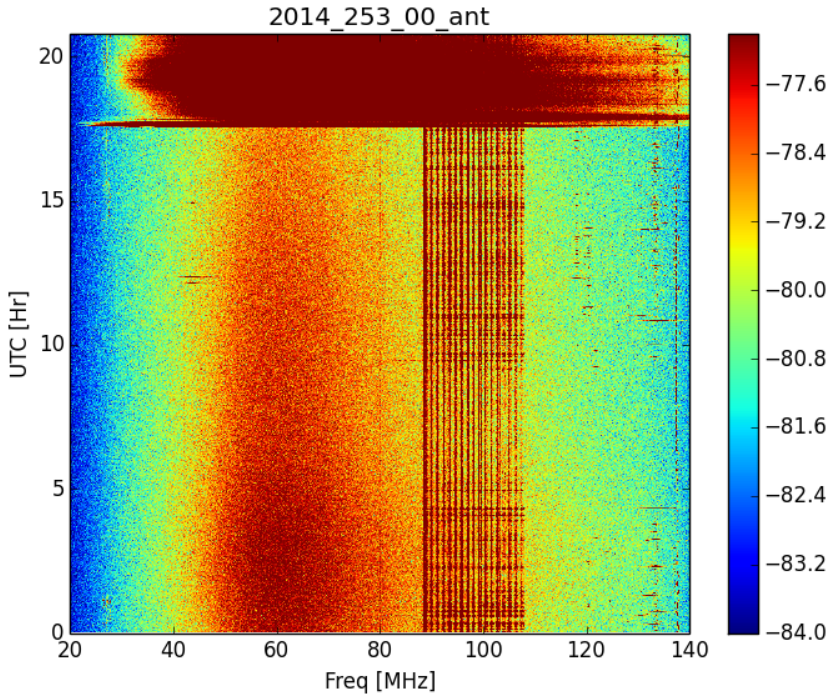

Figure 2.27: Waterfall plot for the day of the solar flare event on Sept 10^{th}, 2014 (Day of year 253). The color bar represent the calibrated T_{ant} in dB. The solar event started around 17:30 UTC. Noted the FM band and the Galactic disk (vertical orange blob) overhead peaked at around 03:00 UTC).

- By spending half the time in measuring the load, the radiometer can only observe the sky with 50% duty cycle. In addition, RFI and ionospheric disturbance such as that from solar activities, reduces the useful observation time even more. In other global experiments, the standard strategy is to only observe at night time to ensure minimal RFI and ionospheric effects.

- Although the total-power measurement is susceptible to variations in the sky spectrum, due to instrumental systematics or ionospheric conditions, one of the biggest challenges is to characterize the frequency-dependent antenna beam. It is difficult, if not impossible, to design an antenna that is broadband and has smooth frequency response. Any slight spectral structures from the beam or the RF chain can corrupt the foreground spectrum and complicate the foreground removal process.

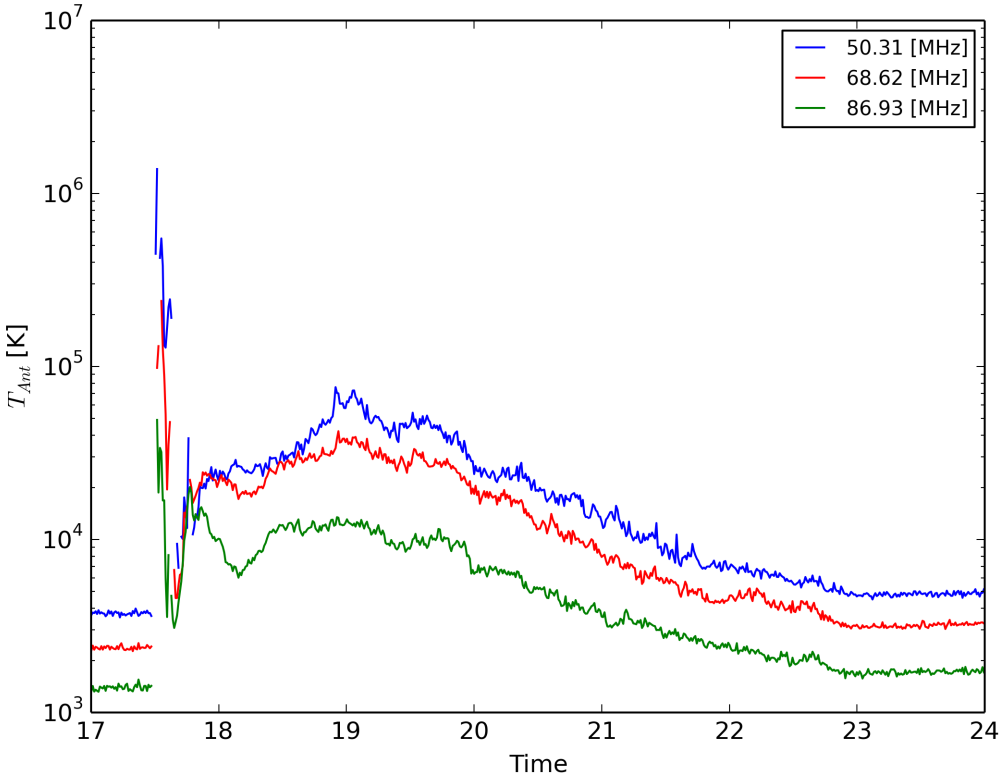

Figure 2.28: Measured antenna temperature plotted as a function of UTC in hour during the solar flare (rated class on Sept 10, 2014), plotted at three frequency channels [MHz]: 50.31 (blue), 68.62 (red), 86.93 (green). The flare has disturbed the sky spectrum for at least 6 hours. Upon closer inspection, ripple-like structures are visible on the spectra as a function of time.

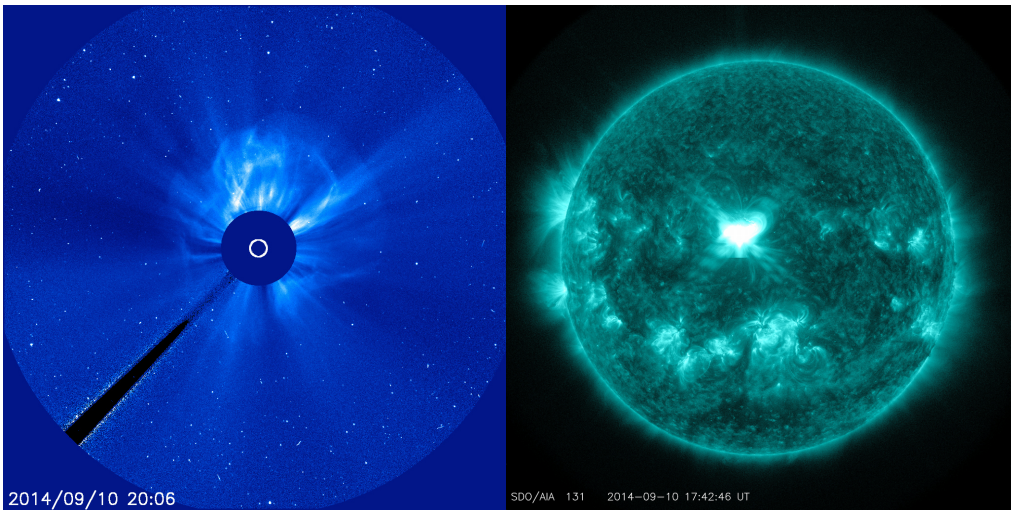

Figure 2.29: Archival data from the SDO recorded the X1.6 class flare on Sept 10^{th}, 2014 at 03:00 UTC. (Left) The image shows coronal mass ejection (CME) that correlated to the flare. (Right) The image shows a bright solar flare in the center. Credit: NASA SDO (Solar Dynamics Observatory)

Chapter 3

Projection-Induced Polarization Effect

> "I often say that research is a way of finding out what you are going to do when you can't keep on doing what you are doing now."
>
> — Charles F. Kettering (1876-1958), inventor and engineer

3.1 Introduction

Because of the large antenna beam width used in global 21-cm experiments, the 21-cm fluctuations on small angular scales ($< 2°$, Bittner and Loeb, 2011) are not resolvable compared to the foreground anisotropy on larger angular scales. Hence, as far as the global 21-cm experiment is concerned, the observed signal can be parametrized as a linear combination of the anisotropic foreground emission and a uniform 21-cm background.

As pointed out previously, there are two fundamental challenges in removing the strong foreground spectrum to reveal the cosmological 21-cm background. First, current observational attempts have so far demonstrated that artificially fitting the foreground with some form of parametric functions for the trend removal is only marginally effective when the smoothness of the foreground spectrum is corrupted by beam chromaticity and other frequency-dependent systematic errors.

Second, since the antenna in the conventional approach is pointed at the zenith of the local observer, the varying overhead sky imposes changes of the foreground spectrum in a period of 24 hours local sidereal time (LST). This is also known as the diurnal variation. In addition, ionospheric distortion (Vedantham et al., 2014; Datta et al., 2016; Sokolowski

et al., 2015b; Rogers et al., 2015) and radio-frequency interference (RFI) corruption (Offringa et al., 2013) can further compromise the accuracy of constraining the foreground spectrum during long-term observations, typically ranging from weeks to months. To mitigate these variations, conventional sky measurement is averaged over a small time window to obtain a mean total-power spectrum, typically over several sidereal hours of night-time observation for minimal ionospheric and RFI contamination. This drastically limits the fraction of useful sky data and thus the observation efficiency, especially when the system is only measuring the sky at most half of the time in the on-off load scheme.

It is extremely desirable to have a direct means to measure the foreground spectrum without confusion from the convoluted background signal as in a single total-power spectrum measurement. Better yet, there is a way to observe both spectra separately but simultaneously using the same instrument. In fact, our bicone system has inspired us to devise a new observational strategy that has potential to alleviate both aforementioned challenges. In this chapter, we will provide the general theory and simulation results for this model-independent scheme, which we referred to as the **projection-induced polarization effect** (PIPE). In essence, the PIPE uses polarimetry to exploit the dynamic nature of the foreground's spatial anisotropy to distinguish it from the 21-cm background.

Improvements to the shortcomings from the bicone system, regarding calibration and beam pattern effects, have been incorporated into the design of the Cosmic Twilight Polarimeter (CTP) and will be presented in the Chapter 4.

With the permission of AAS, the core material of this chapter was adapted from:
"A Polarimetric Approach for Constraining the Dynamic Foreground Spectrum for Cosmological Global 21 cm Measurements"
Nhan, B. D., Bradley, R. F., & Burns, J. O., 2017, ApJ, 836:90

3.2 Rationale

Spatially, a majority of the diffuse foreground emission is concentrated on the Galactic plane, with extragalactic sources sparsely distributed above and below it. By recognizing this the strong spatial anisotropy in the foreground in contrast to the much weaker 21-cm background, we proposed a polarimetric approach that helps to measure the foreground spectrum without relying on any presumed parametric sky models.

In brief, when a given sky region is projected onto a 2D antenna plane of a pair of crossed dipole, the coupling of asymmetric foreground signal to the crossed antenna pattern will produce a net composite polarization. Meanwhile, the uniform cosmological 21-cm background does not induce any of such polarization due to symmetry. If the antenna's field of view (FOV) is centered at a fixed point where the sky region can revolve about repeatedly every 24 hours LST, the induced net polarization will have a constant magnitude. As the sky revolves, the net polarization tracking the spatially averaged sky will be modulated by a periodic waveform. This modulation of the net projection-induced net polarization from the anisotropic foreground is what we referred to as the PIPE. Meanwhile, the uniform 21-cm background should produce zero net polarization. Our simplistic simulation results shown in Figure 3.1 illustrate how the revolution of asymmetric emission source in a constant field of view can give rise of the PIPE. Noting that the waveforms describing the net polarization contain two cycles within the 24-hour period.

Our proposed new technique is to exploit this dynamic characteristic in the induced polarization as a direct means to distinguish the foreground from the background. It is worth noting that this projection-induced polarization is distinct from the well-known linear polarization of the Galactic synchrotron emission (Westfold, 1959). The former is solely a geometric effect depending on the configuration of the observation. Meanwhile the latter is correlated to the intrinsic magnetic field of the Galaxy[1] , which is a considerably weaker

[1] A typical mean value for the magnetic field in the Milky Way is on the order of few to tens microGauss, (μG) (Beck and Wielebinski, 2013)

component than the PIPE.

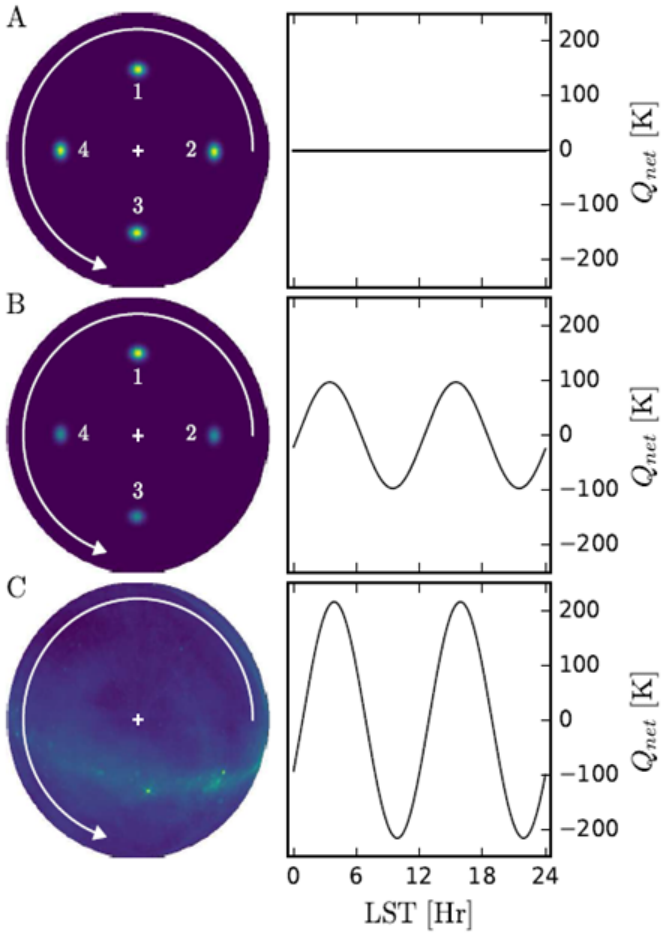

Figure 3.1: **(A)** As the four symmetric point sources of equal brightness revolve about a fixed point (left panel), their projection on the 2D antenna plane (right panel) does not induce a net polarization as a function of LST. **(B)** When source No. 1 is brighter than the other three, the asymmetry in this configuration imposes a net polarization as measured by the antenna and is periodic as the sources revolves about the fixed point. **(C)** Using the Haslam all-sky survey map at 408 MHz, the PIPE illustrates how the anisotropic foreground produces a periodic polarization, to be precise two cycles within 24 hours LST. Meanwhile the uniform 21-cm background should produce zero net polarization.

3.3 General Approach

The PIPE approach consists of pointing a stationary dual-polarized antenna, a pair of crossed dipoles above a finite ground plane, at a fixed reference point in the sky about which the same sky region is observed continuously. For a ground-based experiment, this unique sky pointing can either be the North Celestial Pole (NCP) for the northern hemisphere or the South Celestial Pole (SCP) for the southern, assuming the effects of precession of the equinoxes is negligible. Without loss of generality, as the Earth rotates, the FOV for the sky about the NCP is constant throughout the entire observation and the foreground regions appear to revolve about this fixed point.

The measured composite projection-induced polarization can be quantified in terms of a net Stokes vector $\mathbf{S}_{\text{net}}(\nu, t)$ as a function of time across the frequency range of interest, where $\mathbf{S}_{\text{net}}(\nu, t) = \{I_{\text{net}}(\nu, t), Q_{\text{net}}(\nu, t), U_{\text{net}}(\nu, t), V_{\text{net}}(\nu, t)\}$. The total sky intensity at each frequency, including both the background and foreground, is represented by the Stokes $I_{\text{net}}(\nu, t)$. This is equivalent to the total-power measured in the conventional global experiments. However, the Stokes $I_{\text{net}}(\nu, t)$ can be decomposed as a linear combination of the unpolarized ($I_u(\nu, y)$) and polarized ($I_p(\nu, t)$) portion of the beam-weighted sky signal, hence by definition $I_p(\nu, t) \leq I_{\text{net}}(\nu, t)$.

By convention, the latter three Stokes parameters, $\{Q_{\text{net}}(\nu, t), U_{\text{net}}(\nu, t), V_{\text{net}}(\nu, t)\}$, can be mapped in a 3-D Cartesian coordinate to form a sphere (Poincaré sphere) of a radius equals to the polarized intensity $I_p(\nu, t) = \sqrt{Q^2_{\text{net}}(\nu, t) + U^2_{\text{net}}(\nu, t) + V^2_{\text{net}}(\nu, t)}$. The Stokes $Q_{\text{net}}(\nu, t)$ measures linear polarizations at 0° and 90°, whereas the Stokes $U_{\text{net}}(\nu, t)$ measures linear polarizations at $\pm 45^\circ$ relative to the antenna's orientation as shown in Figure 3.2. The Stokes $V_{\text{net}}(\nu, t)$ can measure any existing circular polarization with positive and negative values for left-handed and right-handed orientation, respectively.

Because the same net foreground polarization is observed twice by the same dipole after the sky revolves by 180-degree apart, the linear Stokes $Q_{\text{net}}(\nu, t)$ and $U_{\text{net}}(\nu, t)$ are sinusoidal

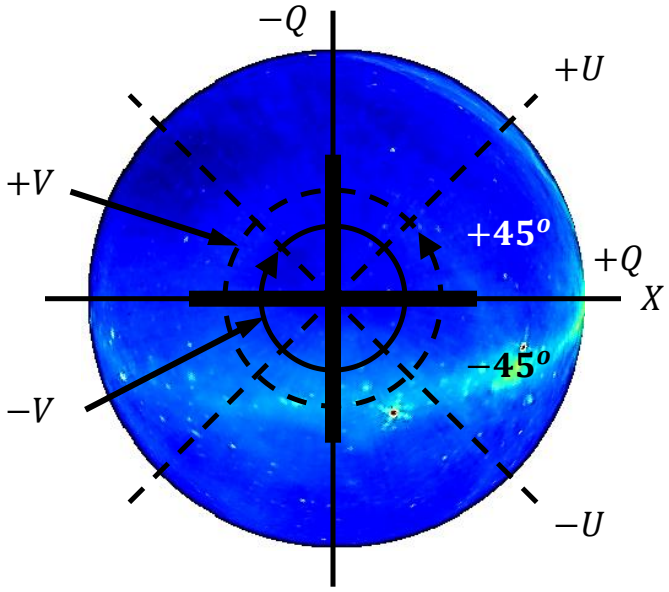

Figure 3.2: Aligning the crossed dipoles to the celestial pole, the projection-induced polarization from the foreground anisotropy can be characterized by a net composite Stokes vector in Poncairé space. The corresponding Stokes parameters Q, U, and V measure different orientations of the polarization: $\pm Q$ for 0° and 90°, $\pm U$ for ±45°, $+V$ for left-handed, and $-V$ for right-handed.

functions with an angular frequency of twice the sky revolution rate relative to the fixed antenna. This twice-angular frequency in the Stokes $Q_{\rm net}(\nu, t)$ and $U_{\rm net}(\nu, t)$ is precisely the dynamic feature that helps to distinguish the foreground component from the static 21-cm background as illustrated earlier in Figure 3.1.

By applying harmonic analysis such as Fourier transformation to estimate the power spectral density (PSD) of these two Stokes parameters for each of the observed frequency channels, a second harmonic associated with twice the angular frequency component can be determined. The amplitude of this second harmonic can be compiled together, channel by channel, to construct a replica of the foreground spectrum. I will refer this constructed spectrum as the second-harmonic Stokes spectrum hereafter.

Meanwhile, the constant total intensity $I_{\rm net}(\nu, t)$ contains both the background 21-cm signal and foreground emission, as in the case of the conventional total-power measurement

approach, is the zero-frequency component in the PSD. In a similar manner as above, the total power Stokes spectrum can be constructed. As a result, the zeroth harmonic Stokes spectrum contains both the background and foreground signal, whereas the second-harmonic Stokes spectrum only captures information about the foreground. In principle, scaling and subtracting the second-harmonic Stokes spectrum from the total-power spectrum can recover the embedded 21-cm signal. Mathematical details and simulations are presented in the following sections.

3.4 Constraining Foreground Spectrum with Projection-Induced Polarization

3.4.1 Stokes Formalism

Consider a coordinate system fixed to the sky and a pair of crossed-dipole antennas with their boresight aligned along the z-axis at $\theta = 0^\circ$ and the horizon is at $\theta = 90^\circ$ on the xy-plane for the antenna's coordinate system. I further assume that the sky coordinate is not observable below the horizon at $\theta \leq 90^\circ$, although the ionosphere can extend the visible sky below the horizon due to refraction in the low frequencies (e.g., Vedantham et al., 2014). From a given direction (θ, ϕ) in the sky at a given instant, the broadband incoming unpolarized radio signal can be represented as quasi-monochromatic electric field with polar and azimuthal components $\mathbf{E}_{\rm in}(\theta, \phi, \nu) = \{E_\theta(\theta, \phi, \nu)\widehat{\theta} + E_\phi(\theta, \phi, \nu)\widehat{\phi}\}$. The incoming E-field is projected and received by the crossed dipoles, which have an X and Y oriented E-fields that are orthogonal to each other. The observed field, $\mathbf{E}_{\rm out}(\theta, \phi, \nu)$ in Cartesian coordinates for such a system, is a product of the incoming field with a Jones matrix (Trippe, 2014),

$$\begin{aligned}
\mathbf{E}_{\rm out}(\theta, \phi, \nu) &= E_X(\theta, \phi, \nu)\widehat{\mathbf{x}} + E_Y(\theta, \phi, \nu)\widehat{\mathbf{y}} \\
&= \left[\mathbf{J}^X_{\rm ant}(\theta, \phi, \nu) + \mathbf{J}^Y_{\rm ant}(\theta, \phi, \nu)\right] \mathbf{E}_{\rm in}(\theta, \phi, \nu) \\
&= \mathbf{J}_{\rm ant}(\theta, \phi, \nu)\mathbf{E}_{\rm in}(\theta, \phi, \nu)
\end{aligned} \tag{3.1}$$

where the superscripts on the Jones matrices indicate the X and Y dipoles. In a realistic system, the Jones matrix also describes other instrumental systematics as well as external influences on the electric field such as ionospheric effects (Kraus, 1986; Heiles, 2002; Trippe, 2014). Here, I only consider the projection of the incoming E-field onto the dipole antennas, which is described by $\mathbf{J}_{\rm ant}$.

The antenna Jones matrix $\mathbf{J}_{\rm ant}$ is the composite far-field patterns of both crossed dipoles at each frequency, which is represented as,

$$\begin{aligned}\mathbf{J}_{\rm ant}(\theta,\phi,\nu) &= \begin{bmatrix} J_\theta^X & J_\phi^X \\ J_\theta^Y & J_\phi^Y \end{bmatrix}_{(\theta,\phi,\nu)} \\ &= \begin{bmatrix} |E_\theta^X| e^{j\Phi_\theta^X} & |E_\phi^X| e^{j\Phi_\phi^X} \\ |E_\theta^Y| e^{j\Phi_\theta^Y} & |E_\phi^Y| e^{j\Phi_\phi^Y} \end{bmatrix}_{(\theta,\phi,\nu)}\end{aligned} \tag{3.2}$$

where the complex far-field components for the X and Y oriented dipoles are given in terms of their magnitude $|E|$ and phase Φ for each direction (θ, ϕ).

Components of the Stokes vector at a given direction can be calculated as linear combinations of the observed E-field's autocorrelation and cross-correlation,

$$\begin{aligned} I^\nu_{\rm out}(\theta,\phi) &= \langle E_X E_X^* \rangle + \langle E_Y E_Y^* \rangle \\ Q^\nu_{\rm out}(\theta,\phi) &= \langle E_X E_X^* \rangle - \langle E_Y E_Y^* \rangle \\ U^\nu_{\rm out}(\theta,\phi) &= \langle E_X E_Y^* \rangle + \langle E_X^* E_Y \rangle \\ V^\nu_{\rm out}(\theta,\phi) &= j\left(\langle E_X E_Y^* \rangle - \langle E_X^* E_Y \rangle\right) \end{aligned} \tag{3.3}$$

where the bracket represents a time average of the product between the observed E-field components and their complex conjugates, with $j = \sqrt{-1}$. The spatial and frequency dependence on the E-field are suppressed for the ease of reading.

Assuming the E-fields from all directions add incoherently, the net composite field measured at the crossed dipoles are sums of squares instead of the square of sums of individual electric field. Hence, the Stokes vector representing the projection-induced polarization of

the foreground at a given instant is a vector summation of the individual Stokes vectors from each direction on the Poincaré sphere,

$$\begin{aligned} I^{\nu}_{\text{net}} &= \frac{1}{\Omega_{XY}} \sum_{\phi=0}^{2\pi} \sum_{\theta=0}^{\pi/2} I^{\nu}_{\text{out}}(\theta,\phi)\Delta\Omega \\ Q^{\nu}_{\text{net}} &= \frac{1}{\Omega_{XY}} \sum_{\phi=0}^{2\pi} \sum_{\theta=0}^{\pi/2} Q^{\nu}_{\text{out}}(\theta,\phi)\Delta\Omega \\ U^{\nu}_{\text{net}} &= \frac{1}{\Omega_{XY}} \sum_{\phi=0}^{2\pi} \sum_{\theta=0}^{\pi/2} U^{\nu}_{\text{out}}(\theta,\phi)\Delta\Omega \\ V^{\nu}_{\text{net}} &= \frac{1}{\Omega_{XY}} \sum_{\phi=0}^{2\pi} \sum_{\theta=0}^{\pi/2} V^{\nu}_{\text{out}}(\theta,\phi)\Delta\Omega \end{aligned} \tag{3.4}$$

where $\Omega_{XY} = \sum_{\phi=0}^{2\pi} \sum_{\theta=0}^{\pi/2} F(\theta,\phi,\nu)\Delta\Omega$ is the beam normalization factor of the averaged antenna radiation pattern $F(\theta,\phi,\nu) = (F^X + F^Y)/2$, where $F^{X,Y}(\theta,\phi,\nu) = |E^{X,Y}_{\theta}(\theta,\phi,\nu)|^2 + |E^{X,Y}_{\phi}(\theta,\phi,\nu)|^2$ are the radiation patterns of antenna X and Y, with the discrete differential solid angle element $\Delta\Omega = \sin\theta\Delta\theta\Delta\phi$.

3.4.2 Dynamic Characteristic of the Projection-induced Polarization

Since the sky revolves about the celestial pole periodically every sidereal day, this dynamic characteristic is also carried over to the resulting projection-induced polarization. To illustrate this, we simplify the projection by aligning the crossed dipoles' boresight with the NCP at $\theta = 0°$. This is analogous to placing the antenna at the Geographic North Pole (GNP, at latitude $\phi_{\oplus} = 90°$), such that the same sky revolves about the celestial pole continuously at an angular frequency ω_{sky}, where $\omega_{\text{sky}}/2\pi \ll \nu$.

Because the coordinate system we adopted that is fixed to the sky, the (θ,ϕ) coincide with the declination DEC and right ascension RA in the equatorial system, respectively. As the sky revolves relative to the fixed antennas on the ground, the net induced polarization reaches its maximal or minimal values when it is parallel or orthogonal to one of the dipoles. For the same dipole, the net induced polarization is detected twice per revolution, or twice

diurnal. This gives rise to the cyclic Stokes parameters $Q_{\text{net}}(\nu, t)$ and $U_{\text{net}}(\nu, t)$ with an angular frequency equaling twice the sky revolving rate, i.e., $2\omega_{\text{sky}}$.

In such a coordinate system, the observed E-field is produced as if having the antenna rotated relative to the fixed sky. By reciprocity, we can model the antenna response coupled to the incoming E-field from direction (θ, ϕ) as one emitted by an infinitesimal horizontal crossed dipoles placed at the origin of the coordinate system. For the dipole along x-axis, the complex farfield measured at distance r has components,

$$\begin{aligned} E_\theta^X(\theta, \phi, \nu) &\simeq -j\frac{\omega\mu I_0 l e^{-j\mathbf{k}\cdot\mathbf{r}}}{4\pi r}\cos\theta\cos\phi \\ E_\phi^X(\theta, \phi, \nu) &\simeq +j\frac{\omega\mu I_0 l e^{-j\mathbf{k}\cdot\mathbf{r}}}{4\pi r}\sin\phi \end{aligned} \tag{3.5}$$

where $\omega = 2\pi\nu$, $|\mathbf{k}| = 2\pi/\lambda$ is the wave number of the observed wavelength, μ is the permeability, and I_0 is the current excited across the infinitesimal dipole with length l by the source (Balanis, 2005). Similarly, for the y-oriented dipole, components of the corresponding farfield are,

$$\begin{aligned} E_\theta^Y(\theta, \phi, \nu) &\simeq -j\frac{\omega\mu I_0 l e^{-j\mathbf{k}\cdot\mathbf{r}}}{4\pi r}\cos\phi \\ E_\phi^Y(\theta, \phi, \nu) &\simeq -j\frac{\omega\mu I_0 l e^{-j\mathbf{k}\cdot\mathbf{r}}}{4\pi r}\cos\theta\sin\phi \end{aligned} \tag{3.6}$$

As the sky revolves about the boresight of the antenna over some time t, a sky emission from direction (θ_0, ϕ_0), that is originally coupled to the antenna response at (θ_0, ϕ_0), is now received to the antenna response $(\theta', \phi') = (\theta_0, \phi_0 + \omega_{\text{sky}}t)$. By substituting the fields from Eq. (3.6) into Eq. (3.1) to (3.3), the resulting Stokes parameters corresponding to (θ, ϕ) is a function of time and are written as,

$$\begin{aligned} I_{\text{out}}^\nu(\theta, \phi, t) =& g_0^2\left(E_\theta^2\cos^2\theta + E_\phi^2\right) \\ Q_{\text{out}}^\nu(\theta, \phi, t) =& g_0^2\left(E_\theta^2\cos^2\theta - E_\phi^2\right)\cos(2\omega_{\text{sky}}t) - \\ & 2g_0^2 E_\theta E_\phi\cos\theta\sin(2\omega_{\text{sky}}t) \\ U_{\text{out}}^\nu(\theta, \phi, t) =& g_0^2\left(E_\theta^2\cos^2\theta - E_\phi^2\right)\sin(2\omega_{\text{sky}}t) + \\ & 2g_0^2 E_\theta E_\phi\cos\theta\cos(2\omega_{\text{sky}}t) \\ V_{\text{out}}^\nu(\theta, \phi, t) =& 0 \end{aligned} \tag{3.7}$$

where $g_0 = \omega\mu I_0 l/4\pi r$, noting that the incoming E-field components are time independent. The net induced polarization, which is estimated by the vector sum of all Stokes vectors from all direction above the horizon as Eq. (3.4), subsequently consists of this twice-diurnal component as a function of time. This is the dynamic feature that we exploit to measure the foreground separately from the static background.

It is trivial that the net polarization can become relatively small, if not zero, when the overall foreground anisotropy decreases. For example, if the incoming E-field components are identical for all direction, the vector sum of the Stokes vectors reduces to zero. This is similar to the symmetry argument for the isotropic background signal. As a result, the magnitude of twice-diurnal component can be altered. However, this is very unlikely in a real observation except for some extreme cases, such as horizon obstruction at low latitude as discussed in Sec. 3.6.5. A more comprehensive analysis is elaborated through simulations with a realistic foreground map in Sec. 3.5 and discussions in Sec. 3.6.

3.4.3 Harmonic Analysis and Stokes Spectra

Since the net polarization from the PIPE is periodic and repeatable for every sidereal day, a robust method to quantify the magnitude and phase of the harmonic components in such a waveform is to compute its PSD for each observed frequency. For a continuous signal $g(t)$, its PSD can be estimated by the Fourier decomposition in the dynamical frequency, or harmonic, domain. For discrete signal data with length of N over sampling interval Δt, one of the optimized PSD estimates (Heinzel et al., 2002) is,

$$S_g^{\nu}(f) = \frac{(\Delta t)^2}{s_1^2} \left| \sum_{t=1}^{N} w(t) g(t) e^{-j2\pi f t} \right|^2 \tag{3.8}$$

where the window function $w(t)$ prevents spectral leakage between frequency channels in the PSD, and the normalization factor $s_1 = \sum_{t=0}^{N} w(t)$. In this study, we adopt the commonly used Blackman-Harris window function for the PSD calculations. At each observed frequency ν, a Stokes PSD can be estimated by replacing $g(t)$ with each of the net Stokes parameters.

Here we explicitly denote the dynamic frequency as f to distinguish it from the observed frequency ν. In the context of the sky rotation, $f = \omega_{\rm sky}/2\pi$. It is also worth noting that, in actual observation, this Fourier decomposition is a second FFT operation computed since the raw voltage from the antenna has been digitized and converted to complex spectra using the FFTW3 similar to the process described in Section 2.2.4.

Since the dynamical frequency f is a function of the sky rotation rate, it can also be converted to an dimensionless quantity as the order of harmonics n, where $n = 1/(fN\Delta t)$. Hence, the available power associated to the components of twice the angular frequency in Stokes $Q_{\rm net}(\nu, t)$ and $U_{\rm net}(\nu, t)$ can be estimated as $S^{\nu}_{Q}(n = 2)$ and $S^{\nu}_{U}(n = 2)$. Meanwhile, in case of the constant total intensity from $I_{\rm net}(\nu, t)$, the power is located at the zeroth harmonic $S^{\nu}_{I}(n = 0)$.

Since the ν-dependence of the Stokes parameters is not affected by the Fourier transformation, the spectral dependence of the sky measurement is carried over to the Stokes PSD. The measured Stokes spectra, $S^{\nu}_{Q}(n = 2)$ and $S^{\nu}_{U}(n = 2)$, originated from the PIPE are model-independent, high-fidelity, and scalable replicas of the foreground spectrum hidden in the total intensity $I_{\rm net}$. More importantly, the reconstructed foreground spectrum, using either $S^{\nu}_{Q}(n = 2)$ or $S^{\nu}_{U}(n = 2)$, does not contain any contribution from the 21-cm signal since the uniform background does not change as the sky revolves about the celestial pole. This satisfies the first desirable criteria that we emphasize in Section 3.1. Additionally, the PIPE approach also allow the foreground and 21-cm signal to be measured simultaneously since the zero-frequency component of the total intensity spectrum $S^{\nu}_{I}(n = 0)$ consists both the foreground and background together.

3.4.4 Simple Foreground Subtraction with Induced Stokes Spectra

Same as defined in Eq. (1.10), the beam-weighed sky signal measured as the equivalent antenna temperature $T_{\rm ant}(\nu)$ is defined as,

$$T_{\rm ant}(\nu) = \frac{\int_0^{2\pi}\int_0^{\pi/2} T_{\rm sky}(\nu,\theta,\phi)F(\theta,\phi,\nu)\sin\theta {\rm d}\theta{\rm d}\phi}{\int_0^{2\pi}\int_0^{\pi/2} F(\theta,\phi,\nu)\sin\theta {\rm d}\theta{\rm d}\phi} \tag{3.9}$$

where $T_{\rm sky}(\nu,\theta,\phi)$ is the brightness temperature distribution of the total sky (Kraus, 1986; Wilson et al., 2009). In an ideal case, the sky temperature is simply a linear combination of $T_{\rm fg}(\nu)$ and $\delta T_{\rm b,21cm}(\nu)$ as derived in Eq. 1.11. Hence, by assumption, the total-power spectrum at zero-frequency $S_I^\nu(n=0)$ is proportional to $T_{\rm ant}(\nu)$ and can be parametrized as,

$$S_{I,0}^\nu \equiv S_I^\nu(n=0) = A_1 k_B \left[T_{\rm fg}(\nu) + \delta T_{\rm b,21cm}(\nu)\right] + A_0 \tag{3.10}$$

Similarly, the second-harmonic Stokes spectra are,

$$\begin{aligned} S_{Q,2}^\nu &\equiv S_Q^\nu(n=2) = B_1 k_B T_{\rm fg}(\nu) + B_0 \\ S_{U,2}^\nu &\equiv S_U^\nu(n=2) = C_1 k_B T_{\rm fg}(\nu) + C_0 \end{aligned} \tag{3.11}$$

where the As, Bs, and Cs are the scaling factors and offsets. In practice, these scaling coefficients can corrupted by instrumental effects and become frequency-dependent unless further calibration is applied. By assuming optimal instrument calibration, the coefficients can be treated as constant for the purpose of this study.

Since all the Stokes spectra are measured simultaneously in the same observation, by solving for the scaling factors, the foreground spectrum ideally can be subtracted to recover the background signal, without the need of high-order polynomial fitting using, for instance, Eq. (6.1). Either equation in Eq. (3.11) can be used individually to solve for $T_{\rm fg}$ because both Stokes $Q_{\rm net}(t)$ and $U_{\rm net}(t)$ measure the same linear polarization with just a phase difference of 90°. However, using both measurements at the same time can improve the degrees of freedom in constraining the $n=2$ spectrum along with other potential instrumental systematics for the real data.

Without loss of generality, by substituting the Q-spectrum into Eq. (3.10) to solve for the background signal, we arrive,

$$\delta T_{\mathrm{b,21cm}}(\nu) = \frac{1}{k_B}\left(\frac{S^{\nu}_{I,0} - A_0}{A_1} - \frac{S^{\nu}_{Q,2} - B_0}{B_1}\right) \tag{3.12}$$

though utilizing both Stokes measurement, along with Stokes V measurement, is useful in practice. We can obtain a relation between A_1 and B_1 by taking the derivative on both sides of Eq. (3.12) as,

$$\frac{A_1}{B_1} = \left[\frac{\mathrm{d}S^{\nu}_{I,0}}{\mathrm{d}\nu} - A_1 k_B \frac{\mathrm{d}\delta T_{\mathrm{b,21cm}}(\nu)}{\mathrm{d}\nu}\right]\left(\frac{\mathrm{d}S^{\nu}_{Q,2}}{\mathrm{d}\nu}\right)^{-1} \tag{3.13}$$

If the global 21-cm spectrum consists of an absorption feature at ν_{min} as predicted by the models such as the two shown in Figure 3.3, there exists a global minimum at ν_{min} that can be determined by its first and second derivatives as shown in Figure 3.4.

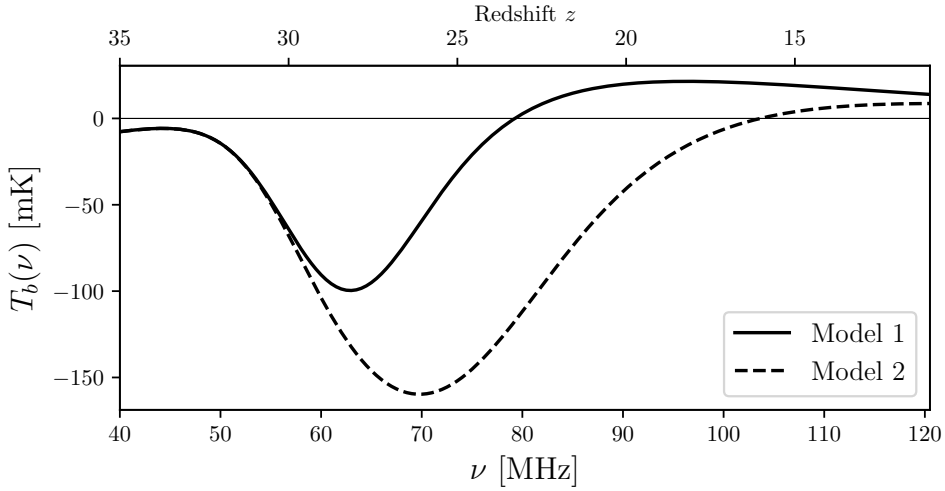

Figure 3.3: Two examples of simulated global 21-cm cosmology signal relative to the CMB. These models are generated using the Accelerated Reionization Era Simulations (ARES) code with fiducial model (solid curve, Model 1) and a factor of 10 less in the rate of X-ray heating (dashed curve, Model 2). Spectral structures of the 21-cm signal help to constrain the thermal history of the early universe between z of 35-11, which corresponds to observed frequencies of 40-120 MHz.

Hence, we can solve for A_1/B_1 based entirely on the derivatives of the measured Stokes

spectra since the derivative of $\delta T_{\mathrm{b,21cm}}(\nu)$ is zero if we evaluate Eq. (3.13) at ν_{min}

$$\frac{A_1}{B_1} = \frac{\mathrm{d}S^{\nu}_{I,0}}{\mathrm{d}\nu}\left(\frac{\mathrm{d}S^{\nu}_{Q,2}}{\mathrm{d}\nu}\right)^{-1}\Bigg|_{\nu=\nu_{\mathrm{min}}} \tag{3.14}$$

In principle, the first derivatives of the emission features at the higher end of the passband in Figure 3.3 also provide a zero crossing to constrain A_1/B_1. However, the emission feature is more likely to be outside the band since it is predicted to be broader and less prominent than the absorption one.

By comparing Eq. (3.13) and (3.14), it is apparent that the sources of error in solving for A_1/B_1 are the accuracy in estimating the derivatives of the measured Stokes spectra as well as determining ν_{min}. In general, there exists truncation error in numerical differentiation in the order of the frequency step size $\mathcal{O}(\Delta\nu)$ (Hamming, 1986). Hence, keeping the spectral resolution low can improve the accuracy of calculating the derivatives. However, determining the frequency of the absorption feature in the global 21-cm signal is not straightforward since the background signal is unknown. Possible ways helping to constrain ν_{min} and the sensitivity of this scheme are further discussed in Section 3.6.2 and Section 3.6.3. It is worth noting that the foreground removal discussed here only applies when the an absorption feature exists in the observing band as predicted by theory ($\sim 40 < \nu < 200$ MHz).

3.5 Simulations with a Realistic Foreground Map

3.5.1 Simulation Description

In this section, we illustrate how the projection-induced polarization from a realistic sky map can give rise to the second-harmonic spectrum and how a model global 21-cm spectrum can be recovered using the procedure presented in the previous section.

For simplicity, the broad farfield beam patterns of the crossed dipoles are approximated by circular Gaussian beams. Referencing from the typical antenna beam sizes from other global 21-cm experiments like EDGES (Mozdzen et al., 2016), we adopt a full width at half maximum (FWHM) of 60° for the Gaussian beams.

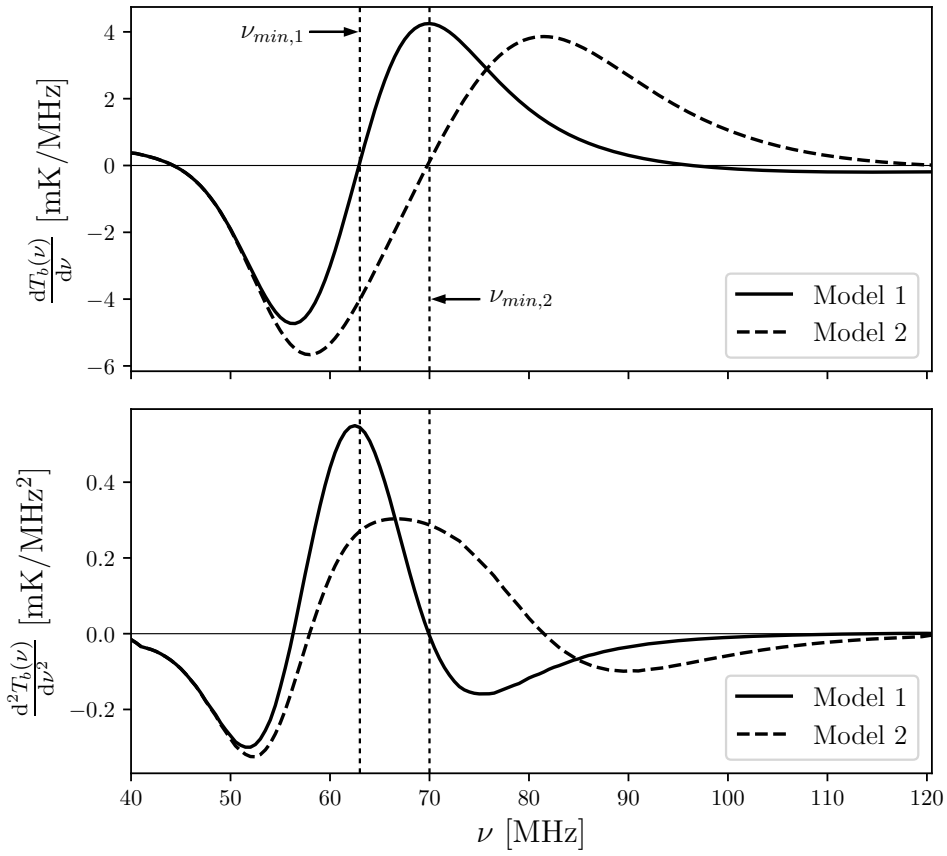

Figure 3.4: (Top) Zero crossings of the first derivatives of the ARES global 21-cm Model 1 (solid curve) and 2 (dashed curve) from Figure 3.3 help to determine their global minima at $\nu_{\rm min,1}$ and $\nu_{\rm min,2}$ (vertical dashed lines) respectively. These global minima help to obtain the coefficients to scale the second-harmonic spectrum $S^{\nu}_{Q,2}$ up to the total power spectrum $S^{\nu}_{I,0}$ for foreground subtraction. (Bottom) Magnitudes of the second derivatives of the models help to differentiate potential local minima from the global minima required for the scaling coefficients.

The Gaussian beams are centered at the NCP of a set of foreground maps which are extrapolated from the Haslam full-sky survey at 408 MHz, as shown in Figure 3.5 (Haslam et al., 1982), to 40-120 MHz using the same power-law function with a mean spectral index $\beta = 2.47$ as in Eq. (1.13),

$$T_{\rm fg}(\theta, \phi, \nu) = T_{\rm Haslam}(\theta, \phi) \left(\frac{\nu}{408\ {\rm MHz}}\right)^{-\beta} \tag{3.15}$$

For each of the ARES global 21-cm model, at each frequency, an isotropic 21-cm background

map of brightness temperature $\delta T_{\mathrm{b,21cm}}(\nu)$ for all directions is linearly combined with the foreground map $T_{\mathrm{fg}}(\nu, \theta, \phi)$. Since the spatial resolution is not critical in the global 21-cm measurement, it is sufficient to set the spatial resolution of both the beam patterns and the sky map to $1^\circ \times 1^\circ$ in our simulations. We also assume the Gaussian beams to be frequency independent across the passband, which is not necessarily true for the real antenna beams.

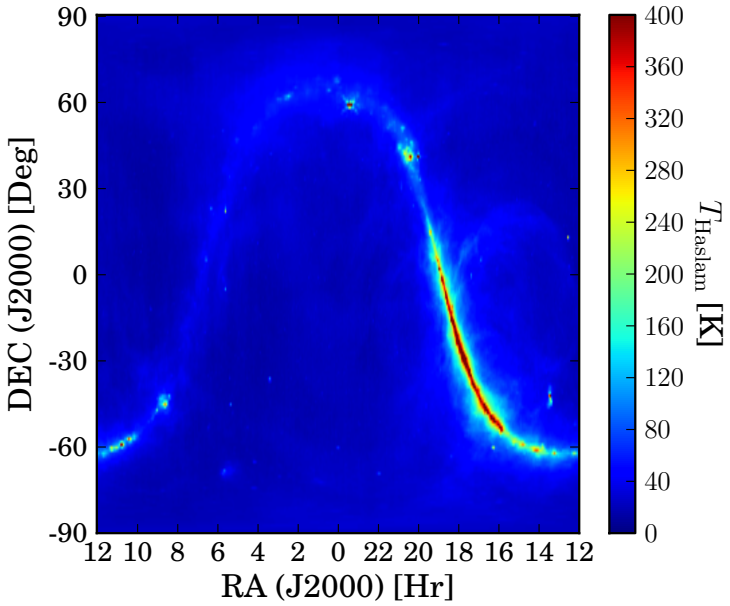

Figure 3.5: The realistic foreground between 40-120 MHz is extrapolated from the Haslam full-sky map at 408 MHz, as shown here, with a spectral index β of 2.47.

Although intrinsic linear polarization is known to exist in the Galactic synchrotron foreground, we assume the foreground itself to be unpolarized (or randomly polarized) in the simulations since the sky-averaged intrinsic polarization is expected to be less dominant than net projection-induced polarization. For completeness, both the chromatic beam effects and intrinsic polarization are elaborated in Section 3.6.

For an unpolarized foreground, half of the averaged total power is equally received by each of the antenna polarization. According to the formalism presented in Section 3.4.1, we estimate the incoming E-field from the foreground as $\mathbf{E}_{\mathrm{in}}(\theta, \phi, \nu) = \{E_0(\theta, \phi, \nu)\widehat{\theta} +$

$E_0(\theta, \phi, \nu)\widehat{\phi}\}$ where $E_0(\theta, \phi, \nu) = \sqrt{k_B T_{\rm fg}(\theta, \phi, \nu)/2}$ with the Boltzmann constant k_B.

3.5.2 Simulation Results

After the observed E-field is calculated as in Eq. (3.1), the net Stokes parameters are computed as the foreground revolves about the NCP at a rate of one cycle per 24 sidereal hours. The resulting Stokes parameters are Fourier transformed to compute the PSD. Zeroth- and second-harmonic spectra, $S^{\nu}_{I,0}$ and $S^{\nu}_{Q,2}$, are constructed by assembling the magnitude of the FFT output at $n = 0$ and $n = 2$ for all frequencies. Figure 3.6 summarizes the basic steps to produce the Stokes spectra.

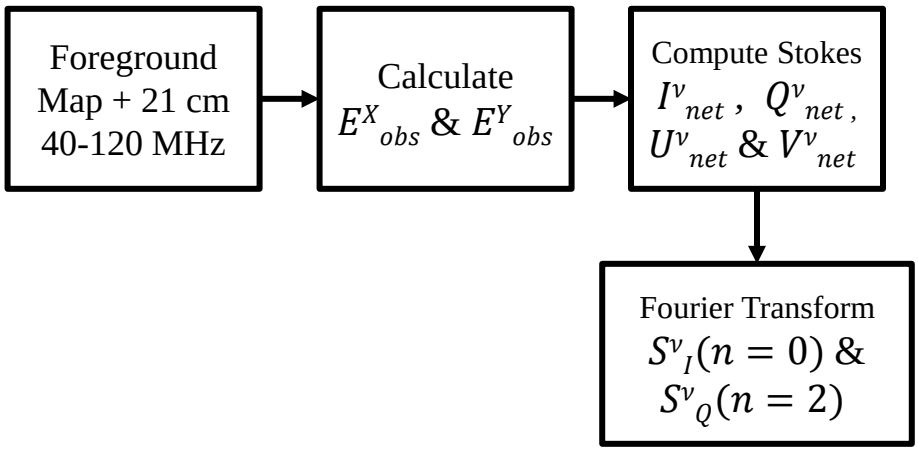

Figure 3.6: Summary for the simulations and analysis procedures that allows the foreground spectrum be separated from the isotropic 21-cm background by exploiting the dynamic characteristic in the projection-induced foreground polarization.

For a circular beam, the same sky region is observed continuously over time as the foreground revolves about the NCP, hence the $I_{\rm net}(\nu, t)$ is constant at each frequency as shown in Figure 3.7. This translates to a zero-frequency component in its periodogram as shown in Figure 3.8. In contrary, the linear net polarization represented by the Stokes $Q_{\rm net}(\nu, t)$ is a sinusoidal function with angular frequency that equals twice the sky's revolution rate, or

two cycles per 24 sidereal hours, as illustrated in Figure 3.9. Subsequently, its periodogram consists of only a harmonic at $n = 2$ in Figure 3.10. This second harmonic only arises from the anisotropy in the foreground map. Hence by constructing a second-harmonic spectrum $S^{\nu}_{Q,2}$ in a manner similar to $S^{\nu}_{I,0}$, we obtain a replica of the foreground spectrum, free from any isotropic background signal. This is confirmed by calculating the spectral index β recovered from the $S^{\nu}_{Q,2}$, which is found to be identical to the input β of 2.47 in Figure 3.11.

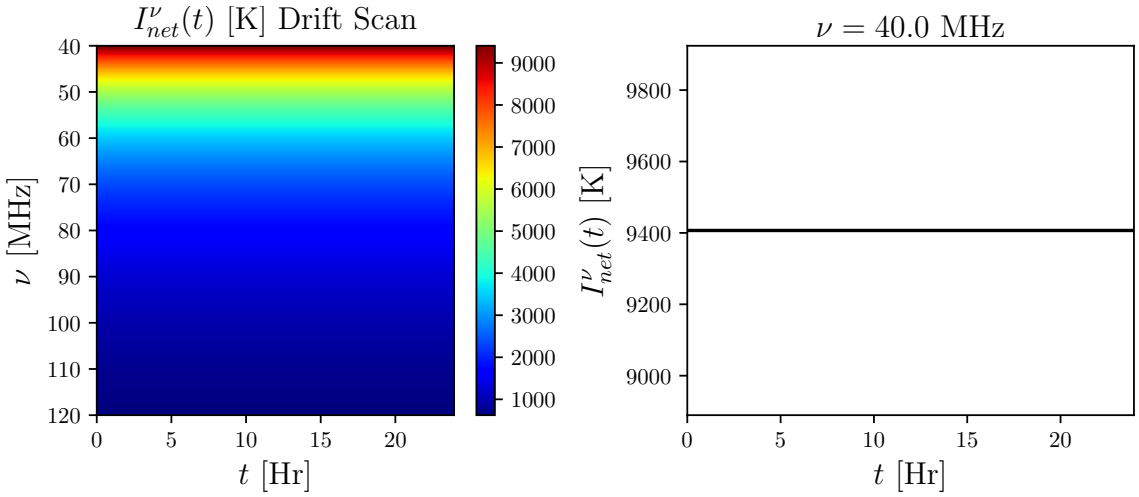

Figure 3.7: (Left) Stokes I_{net} drift scan for Haslam foreground example with circular Gaussian beams with the time on the x-axis and the observed frequencies on the y-axis. (Right) An example of the Stokes I_{net} which is constant for all time at $\nu = 40$ MHz. This total intensity measurement contains both the foreground and background signal.

In this ideal scenario, where instrumental systematics and other contaminations can be removed, the total power spectrum is identical to $S^{\nu}_{I,0}$ so A_1 is unity with zero offset A_0. Since $S^{\nu}_{Q,2}$ is a scalable replica of the the foreground spectrum, only the scaling coefficient B_1 is needed and no offset value B_0 is expected. After scaling the $S^{\nu}_{Q,2}$ up to the $S^{\nu}_{I,0}$ with B_1 as in Eq. (3.14), the foreground spectrum is subtracted to reveal the underlying global 21-cm model with Eq. (3.12), as shown in Figure 3.11 and Figure 3.12.

In this simulation, we assume that the Stokes measurements have been integrated long enough to achieve a minimal measurement precision and the only remaining error in the

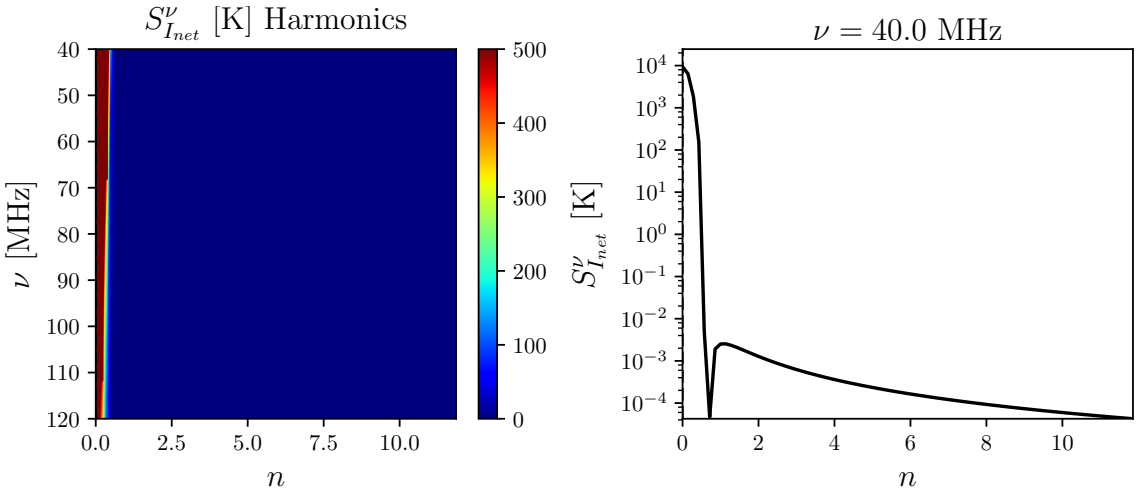

Figure 3.8: (Left) The FFT of the Stokes $I_{\rm net}$ are shown in terms of harmonic order n as a function of observed frequencies. (Right) The total available power for the constant Stokes $I_{\rm net}$ can be find at harmonic $n = 0$. The zeroth-harmonic Stokes spectrum $S^{\nu}_{I,0}$ is constructed by assembling the magnitude at $n = 0$ across the 40-120 MHz band.

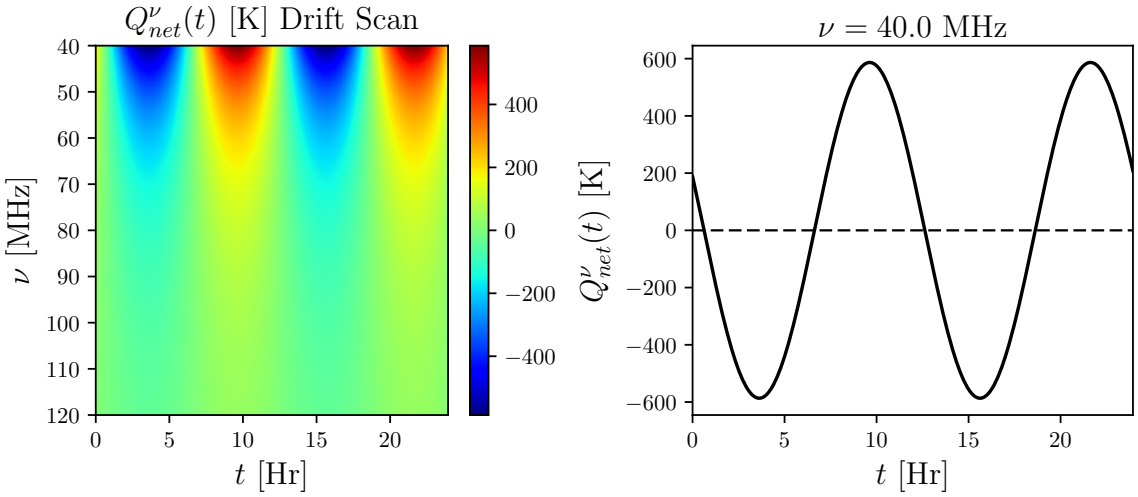

Figure 3.9: (Left) Stokes $Q_{\rm net}$ drift scan for Haslam foreground example with circular Gaussian beams with the time on the x-axis and the observed frequencies on the y-axis. (Right) The projection-induced polarization is modulated by a sinusoidal waveform with angular frequency of twice the sky rotation rate at each observed frequency, as shown here for $\nu = 40$ MHz. This dynamic characteristic is unique to the foreground and can be used to separate it from the static background so the spectral structures of the foreground spectrum can be constrained without assuming any sky model.

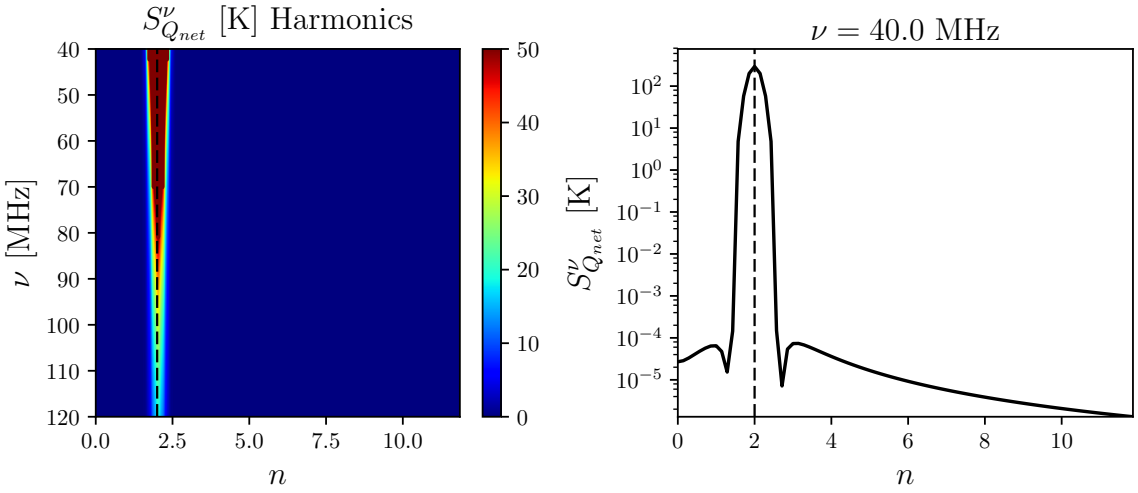

Figure 3.10: (Left) Similar to the total intensity measurement, FFT of the Stokes $Q_{\rm net}$ helps to distinguish different harmonic components function of observed frequencies. (Right) The second-harmonic Stokes spectrum $S^{\nu}_{Q,2}$ can be constructed by assembling the magnitude at $n = 2$ across the band of interest. This resulting spectrum contains only the foreground but not the background 21-cm signal.

extracted 21-cm model is the uncertainty σ_{AB} from determining the scaling factor A_1/B_1, or $1/B_1$ in this case. Details on error propagation is elaborated in following section.

3.6 Implementation Aspects

3.6.1 Foreground subtraction error propagation

As mentioned in Section 3.4.4, the dominant sources of error originate from estimating the derivatives of the Stokes spectra as well as determining the $\nu_{\rm min}$ at which the first derivative of absorption feature in the background signal vanishes. Because both errors are functions of the frequency resolution, the confidence levels on the extracted Model 1 and Model 2 as shown above are attributed to the resolution chosen for this simulation, i.e., $\Delta\nu = 1$ MHz.

Assuming the absorption feature exists at $\nu_{\rm min}$ within the instrument's passband, but the estimated $\nu'_{\rm min} = \nu_{\rm min} \pm \Delta\nu$ with error $\Delta\nu$ is used for Eq. (3.13), then a non-zero

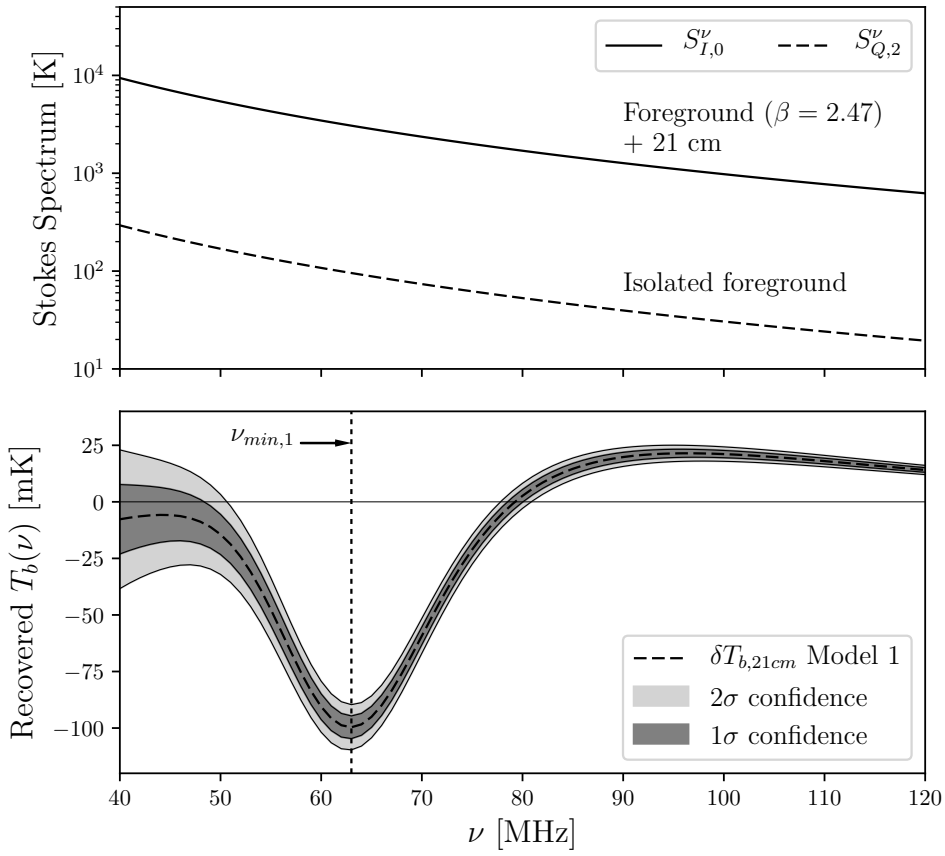

Figure 3.11: (Top) The Stokes spectrum $S^{\nu}_{Q,2}$ (dashed curve) is shown to have a spectral index identical to the input value β of 2.47. By scaling and subtracting this spectrum from the total intensity spectrum $S^{\nu}_{I,0}$ (solid curve), the background 21-cm signal can be retrieved. (Bottom) 1σ and 2σ confidence levels of the extracted 21-cm spectrum is compared to the input ARES spectrum for Model 1 (dashed curve). The primary uncertainty in this result is due to error in estimating $\nu_{\rm min,1}$ (vertical dashed line) for the first derivative of Model 1 to compute the scaling factor $1/B_1$ of Eq. (3.14).

$\mathrm{d}\delta T_{\rm b,21cm}/\mathrm{d}\nu$ is unknowingly assumed to be zero when computing A_1/B_1 with Eq. (3.14). In fact, when evaluating Eq. (3.13) at $\nu'_{\rm min} \neq \nu_{\rm min}$, we obtain a non-zero value on the right-hand side (RHS) in the following equation,

$$\frac{A_1}{B_1} - \frac{\mathrm{d}S^{\nu}_{I,0}}{\mathrm{d}\nu}\left(\frac{\mathrm{d}S^{\nu}_{Q,2}}{\mathrm{d}\nu}\right)^{-1} = A_1 k_B \frac{\mathrm{d}\delta T_{\rm b,21cm}(\nu)}{\mathrm{d}\nu}\left(\frac{\mathrm{d}S^{\nu}_{Q,2}}{\mathrm{d}\nu}\right)^{-1} \tag{3.16}$$

Since the frequency resolution of the simulations is set to 1 MHz, the first derivative of $\delta T_{\rm b,21cm}$ does not equal to zero exactly at the estimated $\nu'_{\rm min}$. So we estimate the σ_{AB} to be

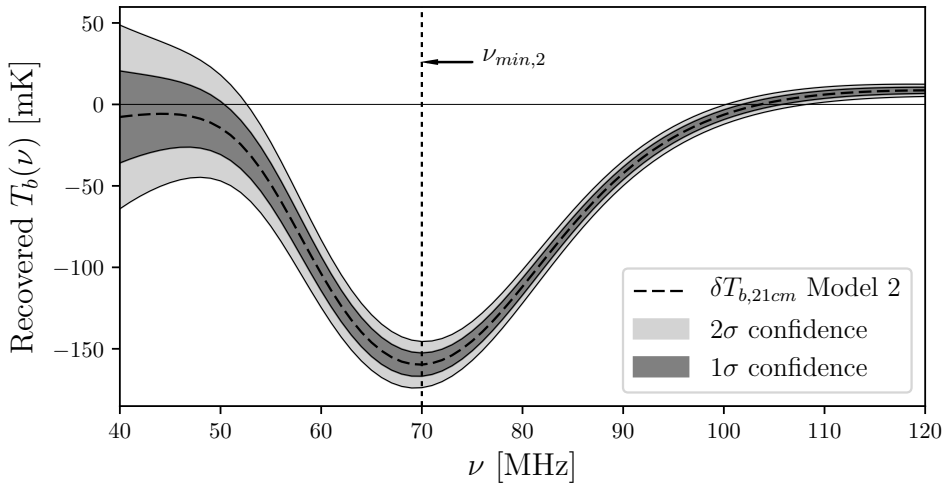

Figure 3.12: 1σ and 2σ confidence levels of the extracted 21-cm spectrum is compared to the input ARES spectrum for Model 2 (dashed curve). The primary uncertainty in this result is due to error in estimating $\nu_{\rm min,2}$ (vertical dashed line) for the first derivative of Model 2 to compute the scaling factor $1/B_1$ of Eq. (3.14).

the unknown difference between the values of A_1/B_1 at the correct $\nu_{\rm min,1}$ and at the $\nu'_{\rm min}$. This error is essentially the term on the RHS but we are not using the derivative of our input Model 1 directly.

By applying a basic error propagation to Eq. (3.12), the uncertainty of the extracted 21-cm signal $\sigma_{\rm 21cm}$ can be estimated as,

$$\sigma_{\rm 21cm}(\nu) = \frac{1}{k_B A_1}\left[\sigma^2_{I,0}(\nu) + \left(\frac{A_1}{B_1}\right)^2 \sigma^2_{Q,2}(\nu) \ + (S^\nu_{Q,2} - B_0)^2\sigma^2_{AB}\right]^{1/2} \tag{3.17}$$

where $\sigma_{I,0}$ and $\sigma_{Q,2}$ are the measurement uncertainties of the Stokes spectra $S^\nu_{I,0}$ and $S^\nu_{Q,2}$ defined by the radiometer equation in Eq. (3.19). In the simulations above, we assume the measurement uncertainty of the Stokes spectra have been reduced to a minimal level after longterm integration, so the overall uncertainty of the extracted signal which defines the confidence levels reduces to,

$$\sigma_{\rm 21cm}(\nu) = (S^\nu_{Q,2} - B_0)\sigma_{AB} = S^\nu_{Q,2}\sigma_{AB} \tag{3.18}$$

3.6.2 Searching for $\nu_{\rm min}$

Except for the derivatives of the Stokes spectra on the left-hand side (LHS) of Eq. (3.16), the scaling factor and the background signal's first derivative are unknowns. As an observer, we are simply searching for a frequency of the absorption feature in the background so that the second terms on the RHS vanishes even without knowing where it is. We here propose a blind search to determine an optimal $\nu_{\rm min}$ during the foreground subtraction. After an initial foreground subtraction by choosing a random frequency as $\nu_{\rm min}$ in the passband, the process of scaling and subtracting $S^{\nu}_{Q,2}$ from $S^{\nu}_{I,0}$ can be refined iteratively (ideally from one end of the passband to the other) until potential spectral structures may appear in the residual spectrum, as illustrated in Figure 3.13.

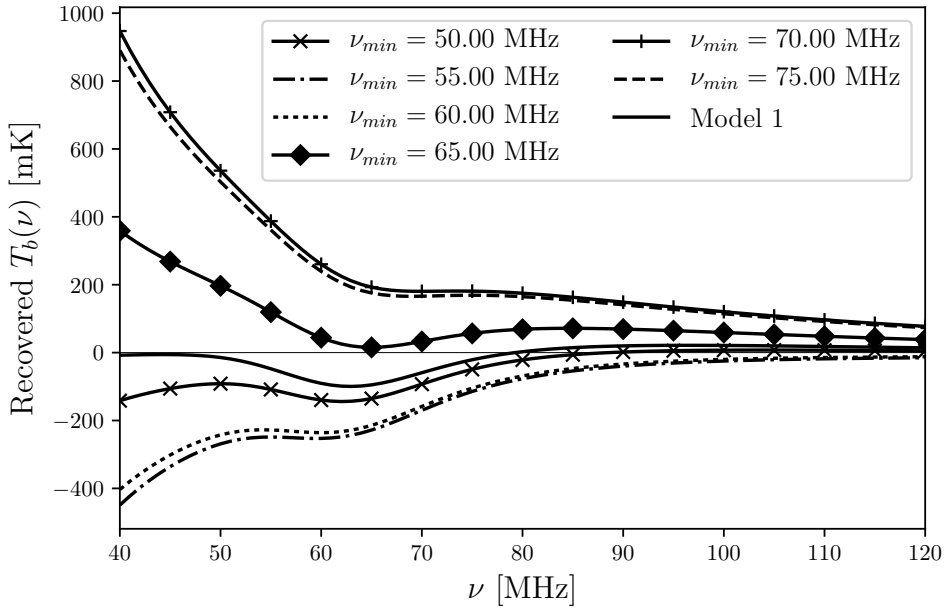

Figure 3.13: Illustration on how the scaling factor A_1/B_1 can be refined iteratively by a blind search for frequency $\nu_{\rm min}$ of the global 21-cm absorption feature, at which its first derivative equals to zero. Shown here is a series of recovered candidates for the input 21-cm model spectrum. Each of the curve is estimated by scaling and subtracting the second-harmonic spectrum from the total-power spectrum using a A_1/B_1 factor computed at an assumed $\nu_{\rm min}$ as shown in the legend, without using any information from the input Model 1.

Without the background signal and its absorption feature as a priori information, the iterative scaling process only converges when it locates a zero crossing in the global 21-cm spectrum's derivative. By assuming that each of the chosen $\nu_{\min}$ can potentially be the desired value, we can simply calculate A_1/B_1 by ignoring the extra term on the RHS of Eq. (3.16). Figure 3.14 shows how A_1/B_1 varies as a function of $\nu_{\min}$. By the formulation of Eq. (3.16), it is not surprising that the curve is proportional to the negative value of Model 1's first derivative in Figure 3.4. More importantly, since local and global minima can be distinguished by the magnitude of the second derivative, we can determine the desired $\nu_{\min,1}$ simply by taking the first derivative of A_1/B_1 respect to $\nu_{\min}$, as shown in Figure 3.14, without any knowledge of the background signal.

It is worth noting that the approach presented here only applies to an idealized instrument with optimized calibration, which is free from any spurious contamination and unwanted distortion. Presence of realistic instrumental systematics and other measurement uncertainties can complicate this foreground subtraction procedure. More sophisticated estimation algorithms, which utilize theoretical constraints from the 21-cm physics and instrument models in terms of the Bayesian statistics such as the Monte Carlo Markov Chain (MCMC, Harker et al., 2012; Mirocha et al., 2015) and SVD, are needed in parallel. This will be investigated in future work.

3.6.3 Stokes spectra measurement sensitivity

In the full sky simulations above, the Stokes spectra are assumed to have been integrated long enough to achieve an optimal measurement precision such that only σ_{AB} dominates the overall error in extracting the 21-cm models as shown in Figure 3.11 and Figure 3.12. By considering only the contribution of thermal noise after other systematics have been corrected and treating σ_{AB} as a second-order effect, we estimate the required integration time to achieve a $\sigma_{I,0}/k_B$ of at least 10 part per million (ppm) of the expected sky noise temperature with the radiometer equation.

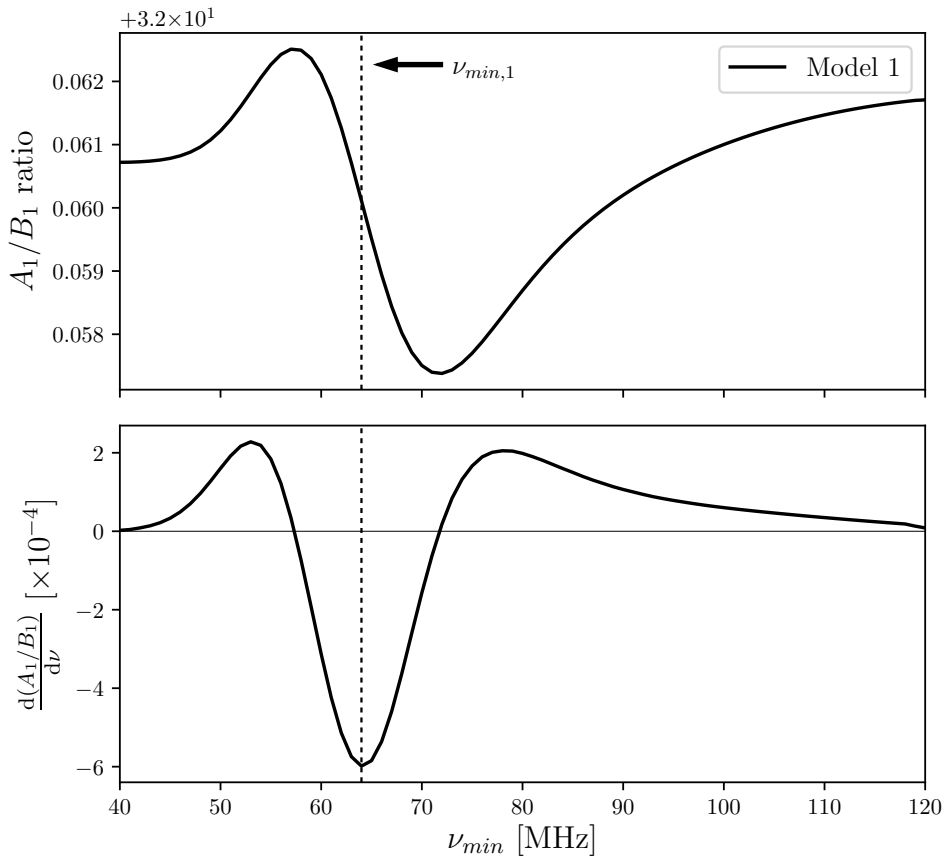

Figure 3.14: (Top) This illustrates how the factor A_1/B_1 varies a function of the chosen $\nu_{\rm min}$ during the blind search procedure. Since each chosen $\nu_{\rm min}$ is used by assuming it is the frequency of the absorption feature, A_1/B_1 represents the unknown error contributed by the term on the RHS of Eq. (3.16). Hence it is proportional to the negative value of the global 21-cm spectrum's first derivative. (Bottom) Since the magnitude of a second derivative helps to distinguish a local minimum from a global one, taking the first derivative of A_1/B_1 respect to $\nu_{\rm min}$ provides an additional information to allow the iterative process to converge onto the desired $\nu_{\rm min,1}$ (as shown in the dashed line).

The generic radiometer equation in Eq. (3.19) suggests the measuring uncertainty (or minimal detectable temperature change) at each frequency channel $\Delta T_{\rm min}(\nu)$ is dictated by the systematic noise temperature $T_{\rm sys}(\nu)$ and decreases as a function of the overall integration time $\tau_{\rm int}$ and the available bandwidth $\Delta\nu$ in the absence of any receiver gain variations.

$$\Delta T_{\rm min}(\nu) = \frac{T_{\rm sys}(\nu)}{\sqrt{\tau_{\rm int}\Delta\nu}} \tag{3.19}$$

From the simulation, at 40 MHz, the total sky temperature is about 9400 K. By assuming a receiver noise temperature $T_{\rm rcv} = 300$ K, the total system noise temperature $T_{\rm sys} \sim 9,700$ K. For different bandwidth value, using the radiometer equation, a rudimentary estimates of integration time are calculated. As shown in Table 3.1, a reasonably short integration time

Table 3.1: Integration time estimates for different spectral resolution

$\Delta\nu$ [Hz]	$\tau_{\rm int}$ [Hr]
1.0×10^4	2.46×10^4
5.0×10^4	4.92×10^3
1.0×10^5	2.46×10^3
5.0×10^5	4.92×10^2
1.0×10^6	2.46×10^2

is needed for $\Delta\nu > 100$ kHz to achieve the required sensitivity under the given assumptions.

3.6.4 Ground effects on the antenna beams

Our simulations assume a pair of crossed-dipole antennas located at the GNP (at latitude $\phi_\oplus = 90°$) to have a full FOV the northern sky centered at the NCP. For practical and logistical reasons, such an instrument can only be deployed at locations of latitude between $0° < \phi_\oplus < 90°$, where the Equator is at $\phi_\oplus = 0°$. The antenna will be pointing toward the NCP at a tilt angle δ which is a function of the observer's latitude.

From simple image theory formulation, it is shown that the farfield antenna beams for a horizontal dipole above a finite ground plane at height h are smooth pattern resembling the Gaussian beams (Balanis, 2005). However, as the antenna and its ground plane are being tilted to point at the celestial pole, instead of a single image, multiple images of the dipole are reflected across the ground screen as well as the actual ground as illustrated in Figure 3.15. The different images from different propagation distances result in phase delays such that interferometric fringes are introduced into the beams. These ground effects can be mitigated by situating the antenna system on a slope instead of on the flat ground as

in Figure 3.16. The slope angle needs to be consistent with the tilt angle δ. Given the proposed configuration, any potential ground effects on the antenna beam will be present in the measured Stokes parameters as constant with time. It is worth noting that such beam distortion due to the ground can very likely impose a $n = 1$ harmonic ,if not at higher orders ($n > 4$), to the Stokes measurement instead of at $n = 2$ due to the relative geometry of the antenna and the sky.

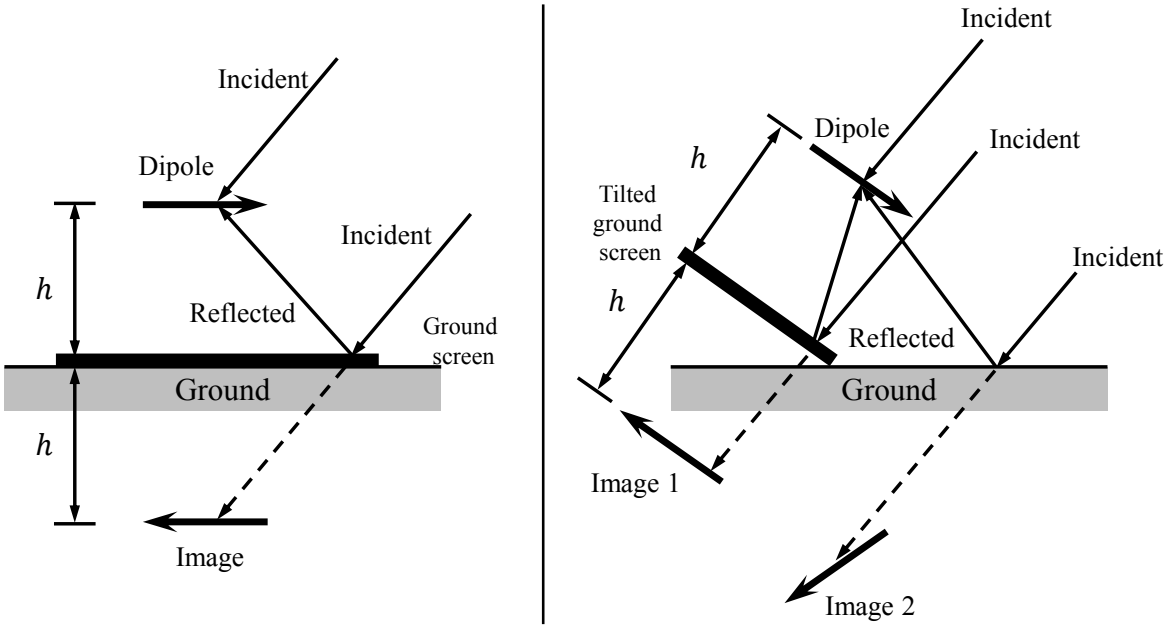

Figure 3.15: (Left) There is a single image when the horizontal dipole is above the ground plane at a height of h. (Right) Multiple images are present when the dipole are tilted relative to the flat ground. This introduces unwanted interferometric fringes that distort the smooth dipole beams.

3.6.5 Horizon obstruction

As the latitude decreases toward the Equator, the FOV is partially obstructed by the horizon thus the visible sky can be separated into two parts. Only the inner region of the sky about the boresight, as shown within the dashed circle in Figure 3.17, is observable the entire time, whereas the sky region outside the dashed circle rises and sets once per revolution.

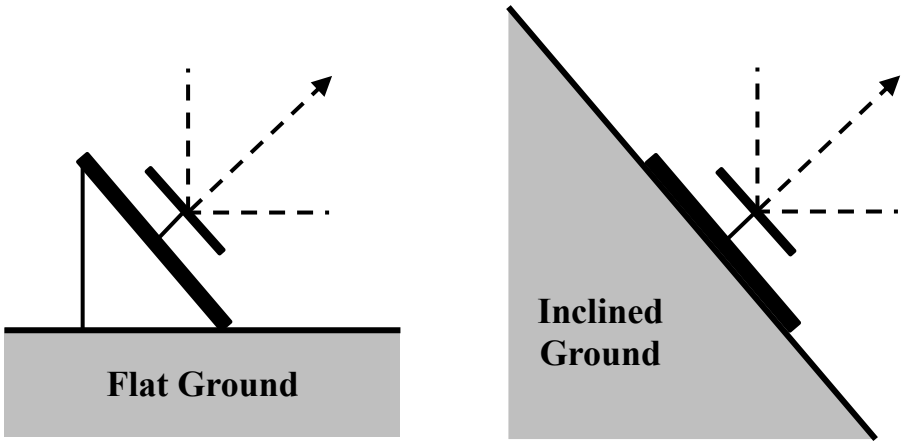

Figure 3.16: To mitigate the ground effects on the beams, the tilted dipole can be situated on an inclined ground (Right) with a slope similar to the tilt angle δ instead of a flat ground (Left), depends on the observer's latitude.

As pointed out in previous sections, the magnitude of the second harmonic in projection-induced polarization depends on the overall anisotropy of the sky region which can be observed the entire time continuously. Hence, with the presence of the horizon, the sky region that contributes to the second harmonic in $S^{\nu}_{Q,2}$ and $S^{\nu}_{U,2}$ is this inner sky region within the dashed circle. As a result, smaller radii of the inner sky region at lower latitudes imply lower accuracy of the second harmonics relative to overall system noise. Additionally, as the outer sky region rises and sets, it contributes additional terms to the projection-induced polarization with angular frequency of at least once per revolution to produce a $n = 1$ harmonic. Meanwhile, the sharp cutoff of the horizon will also introduce high-frequency components to the periodic waveforms in the Stokes parameters which can be identified at $n > 4$ in the PSD. Similar to other effects mentioned above, although these additional harmonics can take over the power from the second harmonic and lower its sensitivity, their effects are attenuated because the antenna gain decreases at larger angles away from the boresight for the outer sky region.

By incorporating the observer's latitude, effects of the horizon obstruction on the Stokes measurement can be characterized and corrected if needed. A balance is also needed between

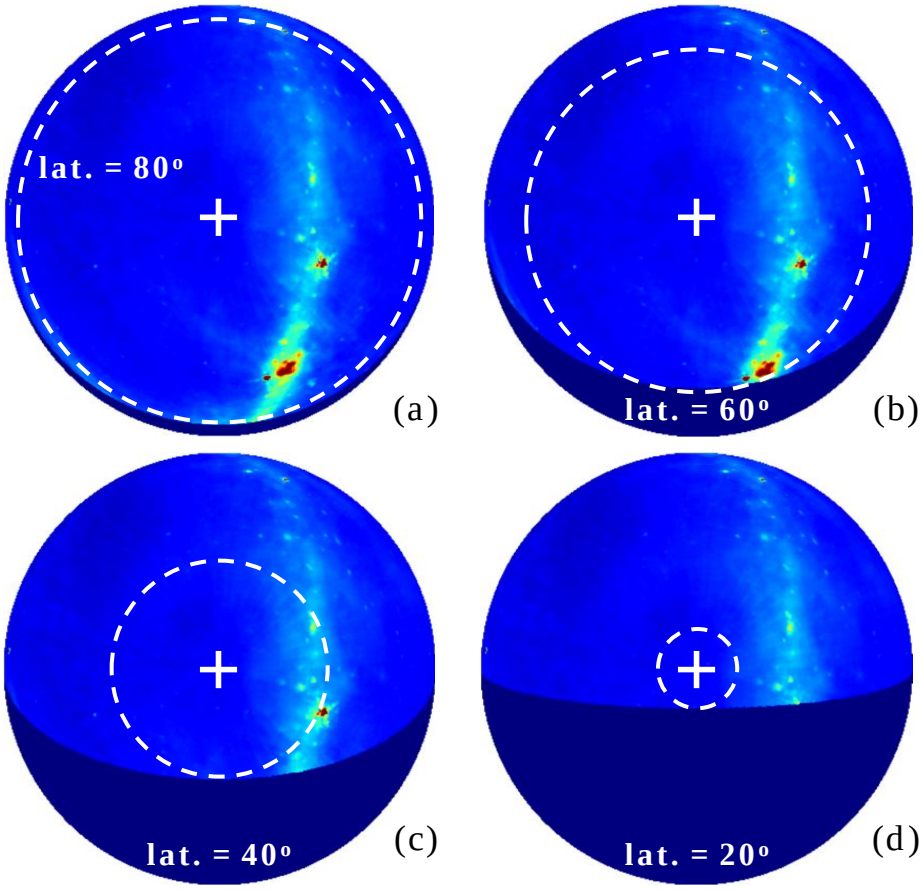

Figure 3.17: The observable sky centered at the NCP is partially obstructed by the horizon as the latitude of the observation site decreases: (a) $\phi_{\oplus} = 80°$, (b) $\phi_{\oplus} = 60°$, (c) $\phi_{\oplus} = 40°$, and (d) $\phi_{\oplus} = 20°$. As a result, the inner sky region is observable the entire time (inside the white dashed circle), whereas the outer region rises and sets once per revolution. As the inner sky region shrinks, so do the amplitude hence the S/N of the second-harmonic spectrum. A first-order harmonic is introduced to the linear Stokes parameters due to the rising an setting of the outer sky region.

site selection, RFI prevention, S/N of the projection-induced Stokes parameters, as well as minimal ionospheric disturbance. For example, selecting a radio-quiet zone with a latitude range that can accommodate a minimal horizon obstruction yet not close to the Earth's magnetic poles, at which strong interaction between the ionosphere and cosmic rays is well

known (Newell et al., 2001). An alternative to avoid the Earth's horizon effect is to adapt this technique into a space-based instrument, such as what is being proposed for DARE (Dark Age Radio Explorer, Burns et al., 2012).

3.6.6 Beam pointing error

By design, the accuracy of measuring the second harmonic component in the projection-induced polarization relies on the antenna pointing. If the antenna boresight is not aligned with the celestial poles, the foreground region centered at the celestial pole is not concentric with the antenna beams, as illustrated in Figure 3.18. As the sky revolves around, the foreground appears to "wobble" about the off-centered pointing.

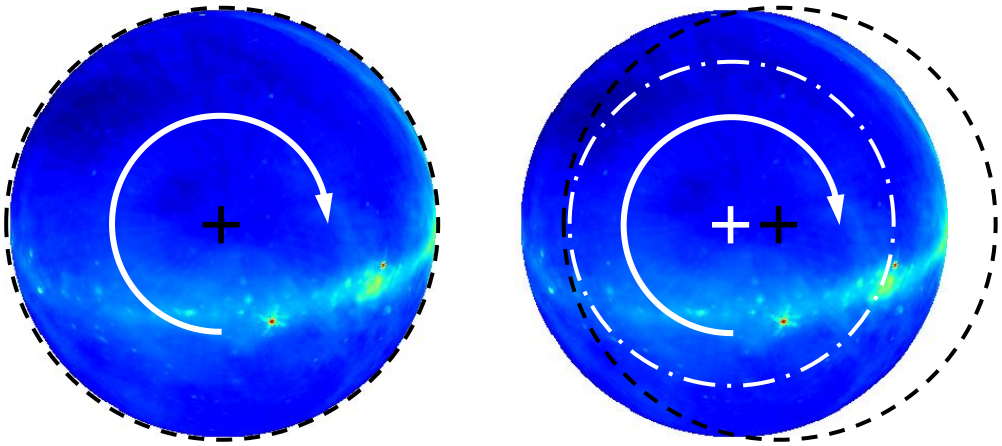

Figure 3.18: (Left) The antenna pointing is aligned to the NCP hence the sky revolution is concentric to the antenna's field of view. (Right) Misalignment between the antenna's boresight (black cross) and the NCP (white cross) results in only a portion of the visible sky (within the white dot-dashed circle) that is observable continuously the entire time. The white arrow indicates the orientation of the sky rotation relative to the observer.

Similar to the horizon obstruction, the effective sky region that produces the $n = 2$ component (within the dot-dashed circle) is reduced which decreases the power of the second harmonic spectrum thus limits the accuracy of the Stokes measurements. As the off-centered sky revolves around, amplitudes and angular frequencies of the Stokes parameters

are modulated such that additional harmonics are introduced in their PDS, for example an additional $n = 4$ component can be introduced to the measured intensity I and I_p. These modulations depend on the frequency-dependent beam sizes, hence they will also cause unwanted spectral structures to appear in the measured sky spectrum because the modulations correlate to the frequency-dependent beam sizes. Being said, these effects can easily be mitigated by improving the pointing accuracy. Based on our simulations, we find that the error is acceptable for a pointing error of 1° or less relative to the celestial pole based.

3.6.7 Effects of intrinsic foreground polarization

Synchrotron emission Galactic foreground is well known to have a linearly polarized component. As an example, Figure 3.19 illustrates the spatial distribution of the intrinsic foreground polarized brightness temperature observed from the DROO 1.4 GHz sky survey (Wolleben et al., 2006).

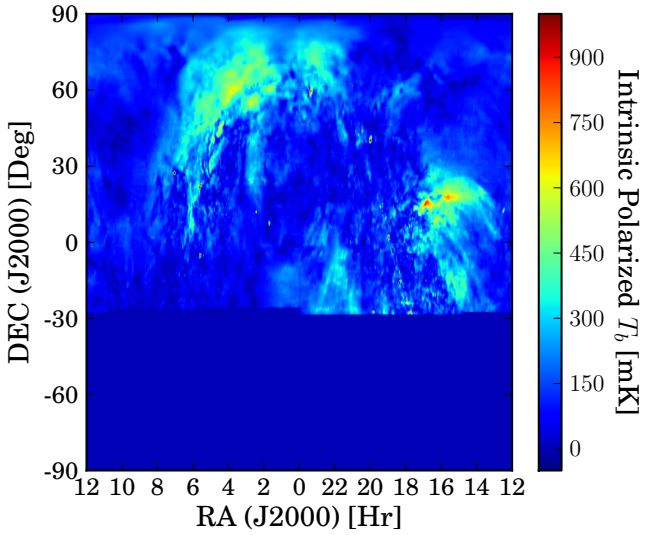

Figure 3.19: Intrinsic foreground polarized temperature map obtained from the DRAO sky survey at 1.4 GHz.

As the polarized incoming signal propagates through the magnetized interstellar medium

(ISM), the polarization angle of the signal rotates, which is known as Faraday rotation. In Gaussian cgs units, the change in propagation phase angle is given as (Wilson et al., 2009),

$$\Delta\psi = \lambda^2 \mathrm{RM} = \frac{e^2}{2\pi m_e^2 c^2} \frac{1}{\nu^2} \int_0^L B_{\parallel}(l) n_e(l) \mathrm{d}l \tag{3.20}$$

where the rotation measure RM is defined to be the integration of the electron number density $n_e(l)$ with the ISM magnetic field component that is parallel to the direction of propagation $B_{\parallel}(l)$ at each distance increment $\mathrm{d}l$ along the path of the medium with thickness of L. The other physical constants are the charge of an electron e, electron mass m_e, and the speed of light in vacuum c.

Due to irregular distribution of electron density in the ISM as well as the Galactic magnetic field, the frequency-dependent Faraday rotation of the incoming polarized foreground emission will be different across the band. Hence, unwanted spectral structures can also be introduced to the measured spectrum. In fact, the intrinsic foreground polarization has been identified as the main cause of the polarization leakage which complicates the instrument calibration in the interferometric EoR experiments (Jelić et al., 2014, 2015; Asad et al., 2015).

A single polarization dipole system in conventional global experiment may be insensitive to linearly polarized portion of the foreground emission if the antenna is not aligned with the orientation of the foreground polarization. On the other hand, a full-Stokes measurement as proposed in this study can measure the intrinsically polarized portion of the foreground and improves the accuracy of the foreground spectrum measurement. Since the intrinsic polarization follows the apparent foreground rotation relative to the antenna on the ground, its contribution to the net projection-induced polarization can be represented as a vector summation between the projection Stokes vector $\mathbf{S}_{\mathrm{net}}$ and the intrinsic Stokes vector $\mathbf{S}_{\mathrm{intr}}$. As a result, the total measured polarization $\mathbf{S}_{\mathrm{tot}}$ also contains a component of twice the sky revolution rate. A total-power spectrum and a second harmonic spectrum can be reconstructed as before. Assuming only the polarizations are linear, Figure 3.20 illustrates

the vector summation between Stokes vectors can be represented by a 2-D version of the Poincaré sphere with the Q and U axes.

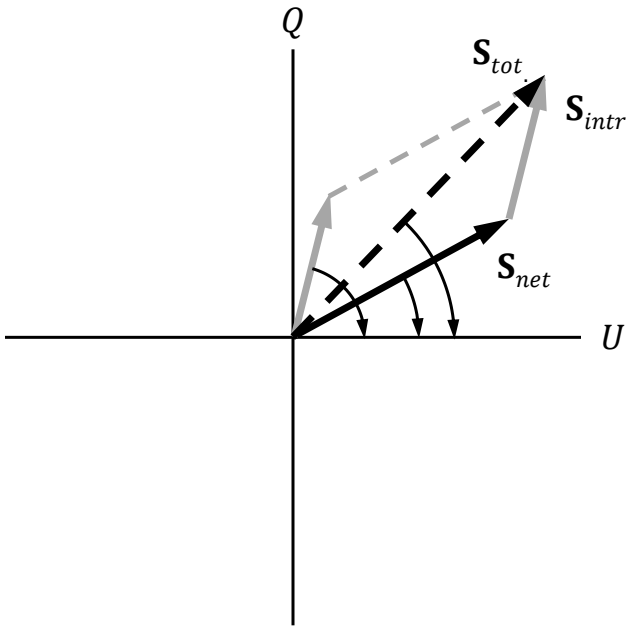

Figure 3.20: Intrinsic foreground polarization $\mathbf{S}_{\rm intr}$ (solid gray) contributes to the projection-induced polarization $\mathbf{S}_{\rm net}$ (solid black) as a vector summation. Since the intrinsic polarization follows the foreground rotation, the resulting total measured polarization $\mathbf{S}_{\rm tot}$ (dashed black) also contains a second harmonic component which can be used to constrain the foreground spectrum.

3.6.8 Foreground spectral index variations and detection validation

The foreground continuum emission has been observed to have a direction-dependent spectral index β depending on the pointing, i.e., $\beta = \beta(\theta, \phi)$. The spectral index distribution can be estimated by extrapolating from a power law between the Haslam all-sky survey at 408 MHz and a 45 MHz map (Guzmán et al., 2011) as shown in Figure 3.21. This may potentially complicate the foreground measurement using the second-harmonic Stokes spectrum. By writing Eq. (3.21) with a non-constant β as

$$T_{\rm fg}(\theta, \phi, \nu) = T_{\rm Haslam}(\theta, \phi) \left(\frac{\nu}{408\ {\rm MHz}} \right)^{-\beta(\theta,\phi)} \tag{3.21}$$

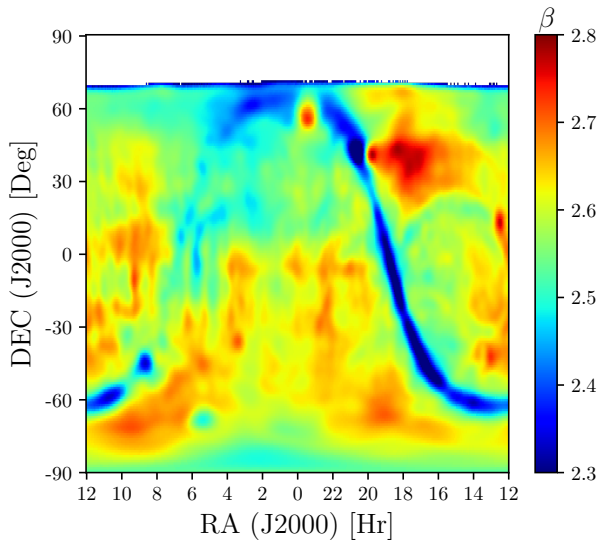

Figure 3.21: Foreground spectral index distribution is obtained from extrapolating between the Haslam all-sky survey at 408 MHz and a 45 MHz map. The missing data around the NCP represents $\sim 4\%$ of the whole sky in the 45-MHz map.

it is apparent the chromatic antenna beam pattern can couple to the sky differently at different frequencies. As a result, the net projection-induced polarization can vary and contribute some unwanted spectral feature to the Stokes spectra, especially the second-harmonic one, if the antenna beam is not corrected.

However, since the induced-polarization approach measures both the total-power spectrum and the second harmonic spectrum simultaneously from the same sky region, as the simulations suggested, the measured mean spectral index of $S^{\nu}_{Q,2}$ is still identical to the foreground spectral index in $S^{\nu}_{I,0}$ for any given mean value of β averaged over the sky. In fact, one of the biggest challenges for the global signal experiment is to ensure such any spectral structures detected in the residual are indeed from the background signal. This degeneracy can be broken by carrying out multiple observation at different sky regions. For example, on the ground, if the residual spectral features measured at the NCP and SCP are consistent, they are very likely originated from the same source, and possibly the background itself.

Table 3.2: Summary of harmonic analysis for the projection-induced Stokes spectra.

Signal Sources	Harmonic Order n					2*Notes
Stokes Spectrum:	S_I^ν	$S_{I_p}^\nu$	S_Q^ν	S_U^ν	S_V^ν	
21-cm background	0	...	...	...	...	for circular Gaussian beams
Projection-induced polarization	...	...	2	2	...	for circular Gaussian beams
Beam gain distortion & elongation	0, 4	4	H^2	H	H	need correction with beam models
Horizon obstruction	0, 1	1	1	1	1	latitude & sky dependent
Boresight pointing error	4	4	H	H	H	
RFI	0	H	H	H	H	location & time dependent
Ionospheric distortion	0	H	H	H	H	time & latitude dependent, pseudo-periodic

3.6.9 RFI and ionospheric distortion

One of the major sources of contamination is RFI. Traditionally, radio-quiet sites, such as South Africa's Karoo desert and Murchison Radio-Astronomy Observatory in Western Australia, are chosen for minimal contamination. Recently, DARE proposed to carry out observations on the lunar farside when the spacecraft orbits around the Moon (Burns et al., 2012). Nonetheless, regardless how quiet a site is, there is always low-level RFI which is either reflected or scattered from satellites, space debris, and the ionosphere (Offringa et al., 2013).

A common practice is to utilize RFI excision algorithm, such as one based on kurtosis of the incoming signal's statistics (Antoni, 2004; de Roo, 2009; Nita and Gary, 2010), to remove the corrupted signal channels. This approach is more effective to detect the strong instead of the low-level RFI, especially ones that are equivalent to the system's noise level. Hence, unknown spectral structures can also be introduced to the measured spectrum. However, since most of the incoming RFI are direction-dependent, they do not necessarily introduce any dynamic variations to the measured linear Stokes parameters, unless they are affected by the ionosphere during propagation. More importantly, the RFI does not contain a $n = 2$

component, hence does not have a major effect on the second-harmonic spectrum used to constrain the foreground spectrum.

The ionosphere has been well known for causing refraction, absorption, and self-emission to radio propagation. Not until recently that careful studies have started investigating the effects of ionospheric distortion to the ground-based 21-cm measurements (Vedantham et al., 2014; Datta et al., 2016; Sokolowski et al., 2015b; Rogers et al., 2015). The ionosphere consists of plasma layers with complex structures whose characteristics are position and time dependent. The total electron content (TEC), which represents the total electron column density for a given direction, varies throughout the day. These variations are pseudo-periodic from one day to another, but not repeatable and difficult to quantify. Current total-power global 21-cm experiments (Sokolowski et al., 2015b; Rogers et al., 2015) have only provided limited understanding on how these ionospheric effects can impact the accuracy and precision of the global 21-cm signal. Attempts to utilize Global Positioning System (GPS) ionospheric measurements are considered insufficient to calibrate the ionospheric effect (Datta et al., 2016). However, by measuring the dynamic ionospheric variations, our polarimetric approach may provide some constraints on their influence on the overall sky measurement as a function of time and observed frequency. A more thorough study in this area will be conducted in future work.

3.7 Summary

In this chapter, we have shown that the harmonic decomposition of the dynamic Stokes parameters provides additional information on different types of measurement and systematic uncertainties. In most cases, the experiment can be designed and configured to modulate the foreground measurement in attempt to distinguish these perturbations from the signal of interest. Based on our simulations and analysis, Table 3.2 provides a rudimentary list of harmonic components that can potentially be used to identify different signal sources and bound the uncertainty in constraining the foreground spectrum. Harmonics at higher orders

($n > 4$) are indicated as "H" for reference.

In analogy to the CMB anisotropy studies (i.e., Tegmark and Efstathiou, 1996; Ichiki, 2014), the foreground spatial anisotropy and hence its induced-polarization can also be decomposed into spherical harmonic $Y_l^m(\theta, \phi, \nu)$ with different modes $l = 0, 1, 2, \ldots$ and $m = 0, \ldots, l$. We speculate that such decomposition is complementary to the harmonic analysis. In fact, by combining the two, it may be possible to characterize different contribution and systematics in the measurement by mapping out different modes and harmonics, similar to Table 3.2. This is outside the scope of the current study.

By assuming an idealized instrument with a Gaussian beam, free from RFI and ionospheric distortion, and the absorption feature of the 21-cm spectrum is present in the instrument passband, some of the key aspects we found are:

- The spectral dependence of the foreground spectrum can be robustly measured in terms of the second-harmonic Stokes spectra $S^{\nu}_{Q,2}$ and $S^{\nu}_{U,2}$ retrieved from the frequency-dependent cyclic signature in the projection-induced polarization when the FOV is centered at a celestial pole.

- The blind search for zero-crossing from the first derivative of the background 21-cm spectrum provides a unique initial condition in solving for the scaling factor between the Stokes spectra to be used for foreground subtraction, even without any knowledge of the background signal.

- Chromatic distortion from the frequency-dependent antenna beam is one of the main instrumental effects that introduced unwanted spectral structures to confuse the foreground and the global 21-cm spectra. Careful beam calibration procedures, such as using beam models generated by sophisticated electromagnetic propagation simulation software and direct beam measurement, are required.

- Environment factors and observation configuration, like ground effects and pointing

error, contribute variations and confusions to the measurements in this polarimetric approach. Realistic assessment on instrument design and setup will help increasing the measurement sensitivity for the Stokes spectra.

- As long as the foreground spectra from different sky regions, such as ones about the NCP and SCP, can be measured and subtracted independently, recovered global spectral structures will be consistent to a common homogeneous 21-cm background. This helps eliminating observational ambiguity and increases detection likelihood of the global 21-cm signal.

This study established a framework for development of a proof-of-concept instrument, the CTP, which is described in the next chapter. In Chapter 6, we explore some of the implementation aspects listed above to further evaluate our approach.

Chapter 4

The Cosmic Twilight Polarimeter Experiment

> "It doesn't matter how beautiful your theory is, it doesn't matter how smart you are. If it doesn't agree with experiment, it's wrong."
>
> — Richard P. Feynman (1918-1988), physicist

In the previous chapter, our simulation demonstrated that, with an idealized antenna beam and foreground map, the projection-induced polarization effect (PIPE) provides a direct means, namely the twice-diurnal spectrum, to constrain the spectral shape of the foreground spectrum without the need of arbitrary parametric foreground models. In this chapter, we will present the details of a proof-of-concept instrument, the Cosmic Twilight Polarimeter (CTP). The CTP was developed between summer 2016 to late 2017, and then deployed at the Equinox Farm, LLC in Troy, VA. The CTP is used to evaluate the feasibility of the PIPE approach for ground-based global 21-cm cosmology. The concept for the CTP is summarized in Section 4.1. Instrumentation details are described in Section 4.2, along with its new network-based parameter tracking calibration scheme in Section 4.3. The CTP site is about 120 miles southeast of the Green Bank Observatory (GBO) and 100 miles southwest of the Washington metropolitan area and the Dulles International Airport (IAD). Their relative locations are illustrated in Figure 4.1.

4.1 Overview

As described in the previous chapter, the PIPE relies on exploiting the dynamic nature of the foreground's spatial anisotropy. To achieve this with a ground-based experiment, the

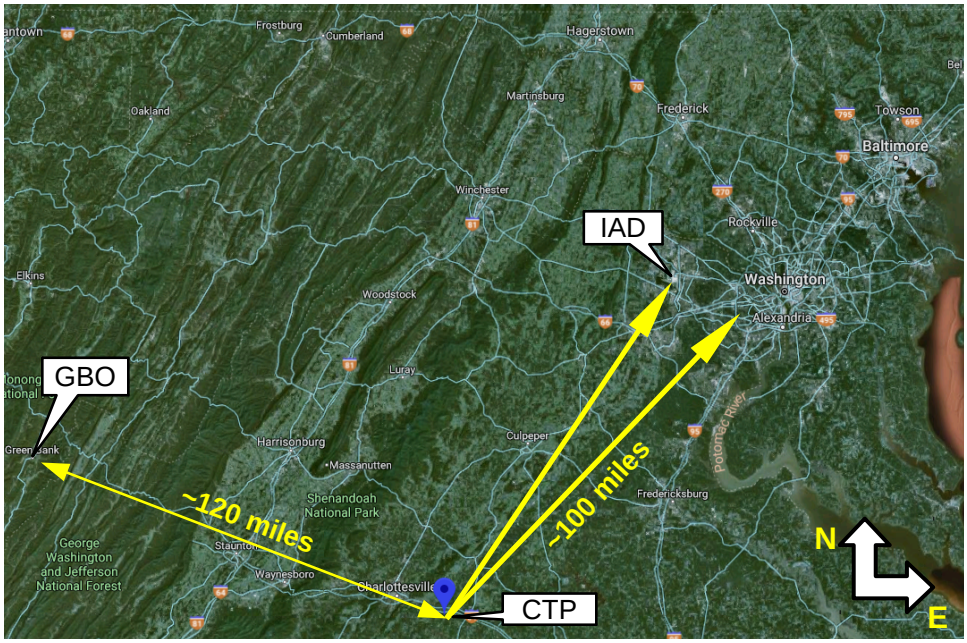

Figure 4.1: The deployment site of the CTP is located at the Equinox Farm, about 120 miles southeast of the GBO and 100 miles southwest of the Washington metropolitan and the IAD.

PIPE needs a constant field of view (FOV) within which the apparent observed sky region would revolve about a fixed pointing position. On the ground, there are only two such locations in the sky, namely the North Celestial Pole (NCP) and South Celestial Pole (SCP). The CTP is configured by pointing a stationary dual-polarized antenna toward the NCP and conducting continuous observations as the sky revolves about the celestial pole due to the Earth's rotation. The general instrument layout is illustrated in Figure 4.2. In contrast to conventional zenith-pointing, drift-scan global experiments, the CTP can observe a constant FOV of the same sky region about the NCP, continuously.

In addition to the new observational configuration, to address the shortcomings from the previous bicone prototype in Chapter 2, four main improvements have been adopted. First, to apply polarimetry and achieve a smoother frequency response, a sleeved dipole antenna design is used. Second, to mitigate variability in the front-end (FE) characteristics due to temperature fluctuations, the FE electronics are stabilized by a dual-stage active thermal

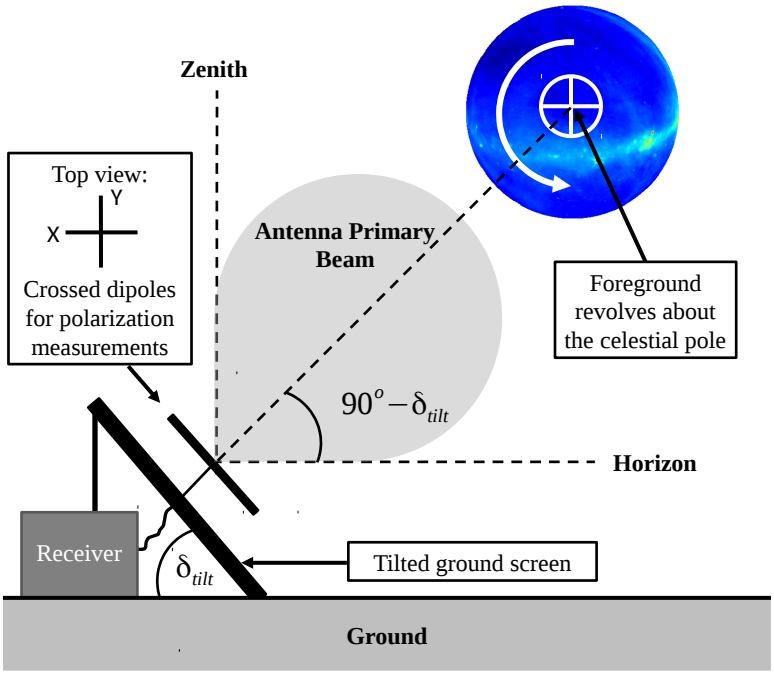

Figure 4.2: Schematic for the ground-based CTP, which consists of a pair of tilted crossed-dipoles pointing at a celestial pole. The primary differences between this polarimetric approach and other global 21-cm experiments are full-Stokes measurements and its configuration to separate the foreground from the static background. The tilt angle $\delta_{\rm tilt}$ corresponds to the observer's latitude, i.e, $\delta_{\rm tilt} = 90^\circ - (\text{Obs. Lat.})$.

control unit. Third, by recognizing the limitations of the previous on-off load calibration, a more robust frequency-tone calibration scheme is adopted to track the transducer gain variations. Lastly, instead of constraining the noise temperature, which depends on the input source impedance, the network-based noise parameters, in combination with numerical circuit simulations, are used to characterize the noise in the signal chain.

4.2 CTP Instrumentation

The CTP consists of a sleeved dipole antenna with two orthogonal polarizations Figure 4.4. Each polarization has its own signal chain made of a FE RF module that amplifies and filters the primary incoming signal. A second FE module is the tone module that couples

and measure the injected calibration tone from a synthesizer to the main RF signal path. All four FE modules are housed in a two-stage thermally controlled environment. The output RF signal, metadata, and control lines are transmitted through 15 feet of cables to the back-end (BE) data-acquisition (DAQ) system located in a weatherproof enclosure beneath the ground screen. Reduced raw data are stored to a local indoor data storage server through a Ethernet link for post-processing. These four main stages for the overall data pipeline are illustrated by the block diagram in Figure 4.3.

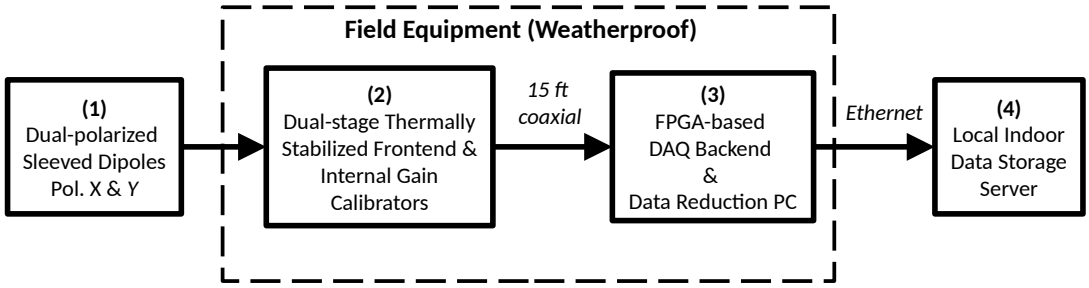

Figure 4.3: Block diagram showing the four main stages of the CTP system: (1) The dual-polarized sleeved dipole antenna with two polarizations (X & Y), (2) The thermally stabilized FE, and (3) the BE instrument rack connected to (4) local server where the data are processed and stored.

4.2.1 Sleeved Dipole Antenna

The CTP's sleeved dipole is a scaled version of the PAPER antenna. The larger structure allows the CTP antenna to receive signals at lower frequencies, by shifting PAPER's 100-200 MHz band lower to 60-120 MHz. Instead of being a traveling wave antenna like the finite bicone described in Chapter 2 which works as a fat dipole, the sleeved dipole antenna is a double-resonant antenna.

A generic resonant antenna is a type of antenna that transmits (or receives) RF radiation by turning the signal into a standing wave along the antenna elements, such as a dipole. By definition, an antenna is resonant when its input impedance has zero reactance, or $Z_{\rm ant} = R + j0$ is pure real at its feed outputs, so that the excited voltage and current are

in phase at the antenna output terminals. In practice, due to the fixed physical dimension, the antenna is only resonant over a narrow band as the reactance becomes larger outside the resonant frequency. Thus, a simple dipole is not ideal for broadband applications.

A sleeved dipole can provide a broader bandwidth by imposing a second resonance. This is achieved by placing the crossed dipoles centered between two conductive disks which act as a coaxial resonator. The second resonant frequency is determined by the spacing between the two disks, the diameters and thickness of the disks. Based on our analysis on beam size coverage for the foreground to achieve an optimal measurement sensitivity for the twice-diurnal component of the PIPE, it suggests that beam symmetry is crucial. Through iterative study with CST simulation designs, we have determined that a symmetric beam can be achieved by installing a conductive external cylindrical wall (or skirt) around the sleeved dipole. The mesh skirt force the E-field of the RF radiation to zero at the boundary (Neben et al., 2016a; Ewall-Wice et al., 2016). The final physical dimensions of the CTP's sleeved dipole are provided in Figure 4.4.

Nonetheless, the sleeved dipole also suffers from the beam chromaticity, as shown in the angular plots for the the E-plane ($\phi = 0°$) and H-plane ($\phi = 90°$) of the CST beam patterns, $F(\nu, \theta, \phi)$, in Figure 4.5. Note that no beam bifurcation is visible after the skirt was installed. Another way to quantify the beam chromaticity is to compute the spatial gradient of the CST beam pattern respect to the frequency, $\partial_\nu F(\nu, \theta, \phi)$. By comparing $\partial_\nu F(\nu, \theta, \phi)$ between Figures 4.5 and 2.26, it shows that the sleeved dipole has a more chromatic structures comparing to the bicone's beam. However, comparing to the elongated bicone beam, the mesh skirt on the sleeved dipole helps to produce a more symmetric beam, as evidenced by how the E- and H-planes of the beam overlap each other in the angular beam sizes between 60 and 120 MHz in Figure 4.6.

To cross check with the simulation, the antenna reflection coefficient $\Gamma_{\rm ant}(\nu)$ is measured with a VNA after deployment. The double resonance features are visible as the two dips in the magnitude of the measured antenna's reflection coefficient $\Gamma_{\rm ant}(\nu)$ shown in Figure 4.7.

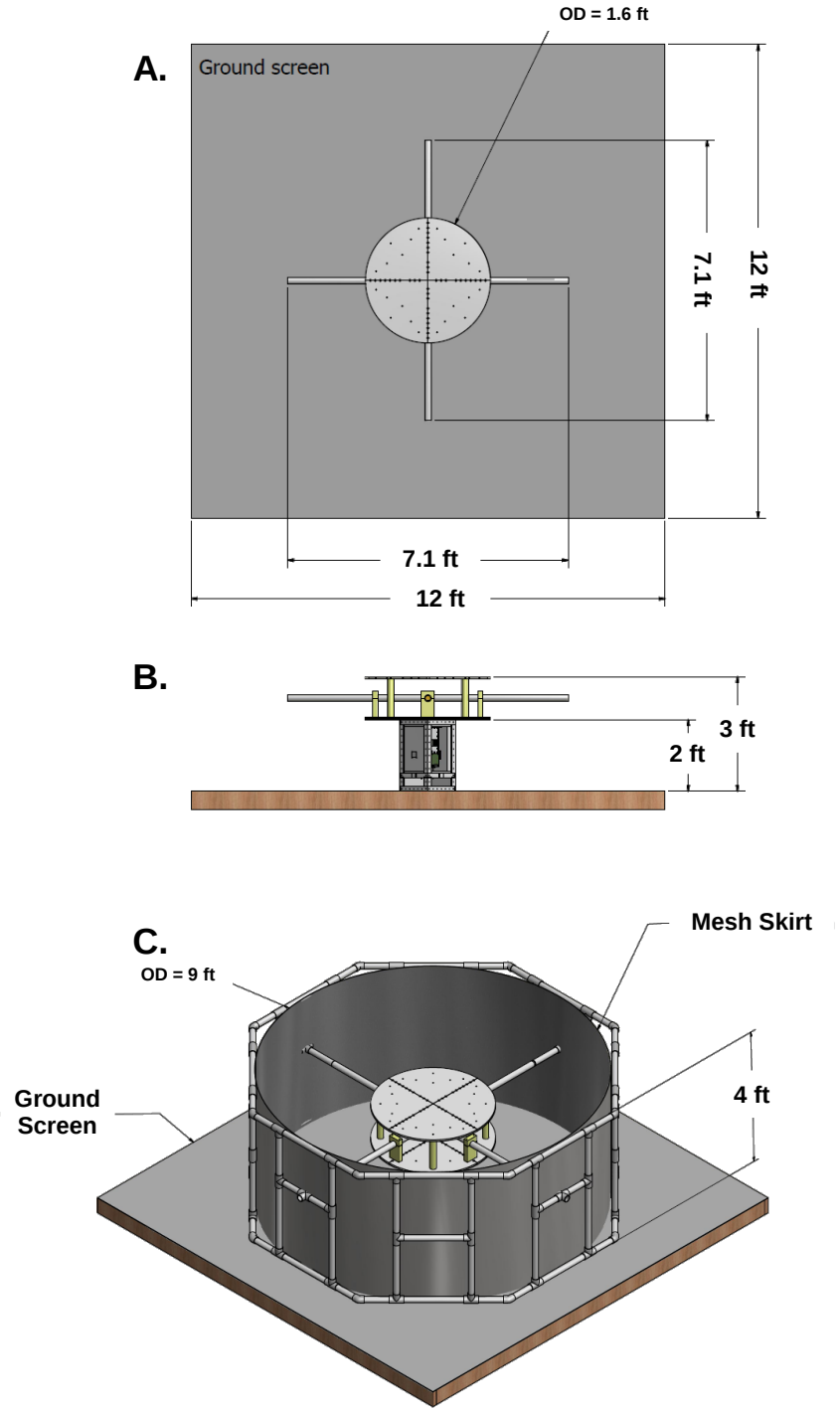

Figure 4.4: 3D rendering of the sleeved dipole antenna for the CTP, which consists of four main components: a pair crossed dipoles between two circular disks, a housing for the FE electronics under the antenna, a mesh screen as ground plane, and a cylindrical mesh skirt.

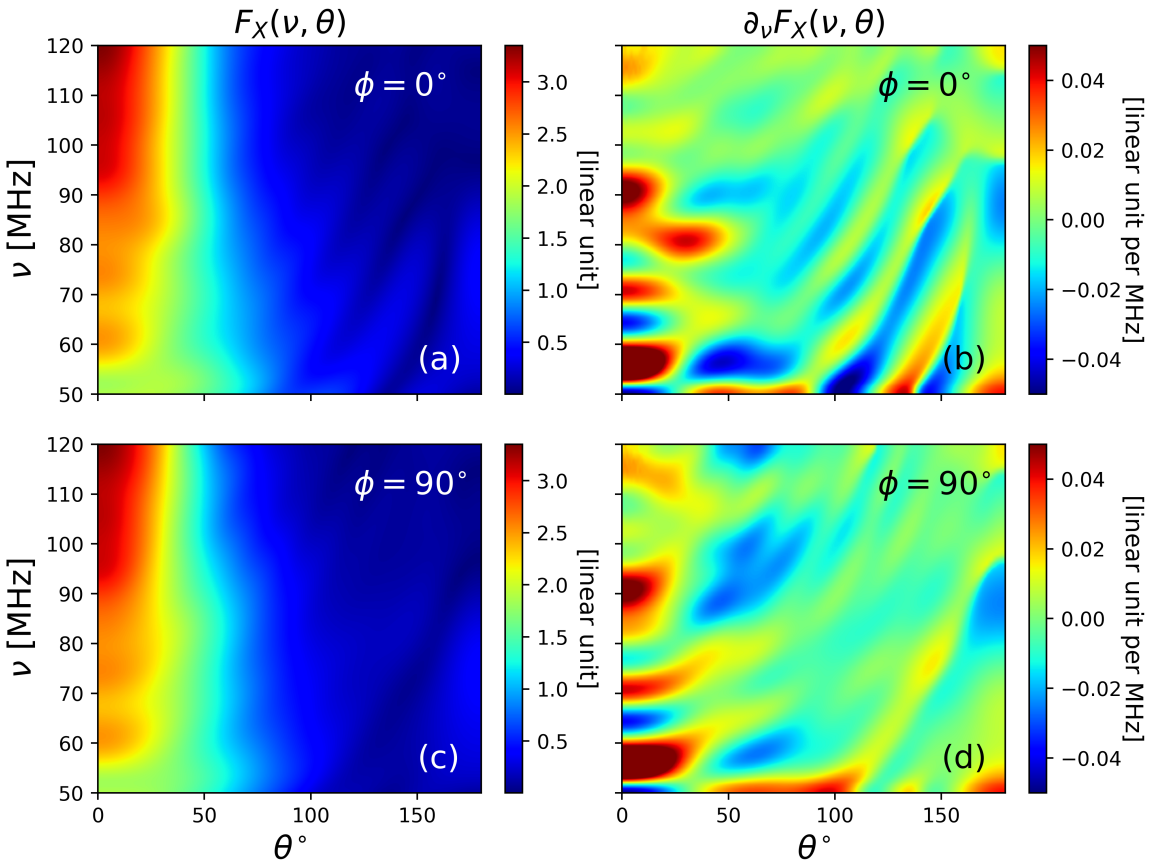

Figure 4.5: (Left) 2D plots of the E-plane ($\phi = 0°$) and the H-plane ($\phi = 90°$) for polarization X of the CST beam model, $F_X(\nu, \theta, \phi)$, of the sleeved dipole with ground screen parallel to the ground soil. (Right) The 2D plots of the frequency gradient, $\partial_\nu F_X(\nu, \theta, \phi)$, of the beams on the left panels. The strong fringing structures due to interactions between the beam and ground are more apparent in the gradient plots. Due to symmetry, the polarization Y beam, $F_Y(\nu, \theta, \phi)$, share similar patterns and frequency structures.

In the case of the sleeved dipoles, since a passive balun is used instead of the active balun as in the bicone system, the reference plane for the VNA measurement is set at the output of the balun instead of at the ends of the dipoles. This minor difference can result in some discrepancy between the VNA measurement and the CST's reflection coefficient unless proper model of the balun is included in the simulation. Since modeling the balun circuitry properly in complex and time-consuming, we have foregone the balun modeling and only focus on the consistency in the VNA measurements for the antenna reflection coefficient,

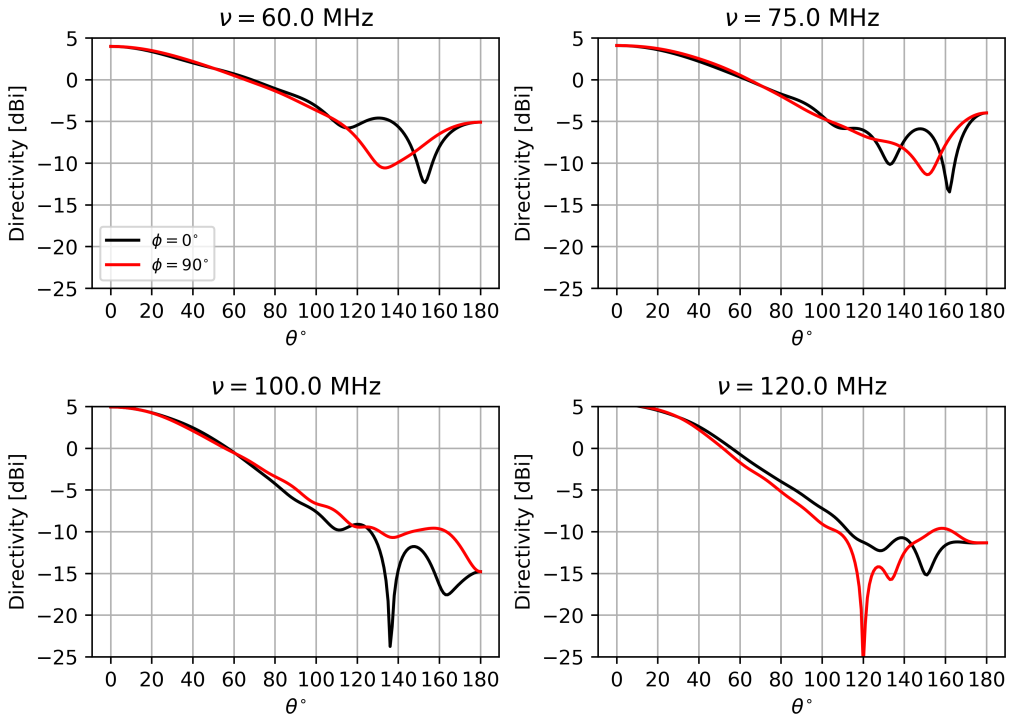

Figure 4.6: Angular beam size comparison for CTP's sleeved dipole, for the E-plane ($\phi = 0$, black) and H-plane ($\phi =$, red), obtained from the CST simulation.

$\Gamma_{\text{ant}}(\nu)$. This suffices for the purpose of this study since both gain and noise calibration are based on the actual measured values of $\Gamma_{\text{ant}}(\nu)$ from the VNA. Connection between the antenna feed lines and the balun, along with the reference plane for the VNA measurement, is shown in Figure 4.8.

4.2.2 FE System

According to our findings from the bicone system, we conclude that its on-off load switching calibration is inadequate to correct the transducer gain due to temperature variations. In that scheme, the available sky observation time is reduced at least 50% since half of the time is spent on the 50 Ω load. The limitations from RFI and ionosphere in day time further reduce the useful data to the night-time observation only. As a result, both the gain fluctuations and the limited integration time have compromised the system's sensitiv-

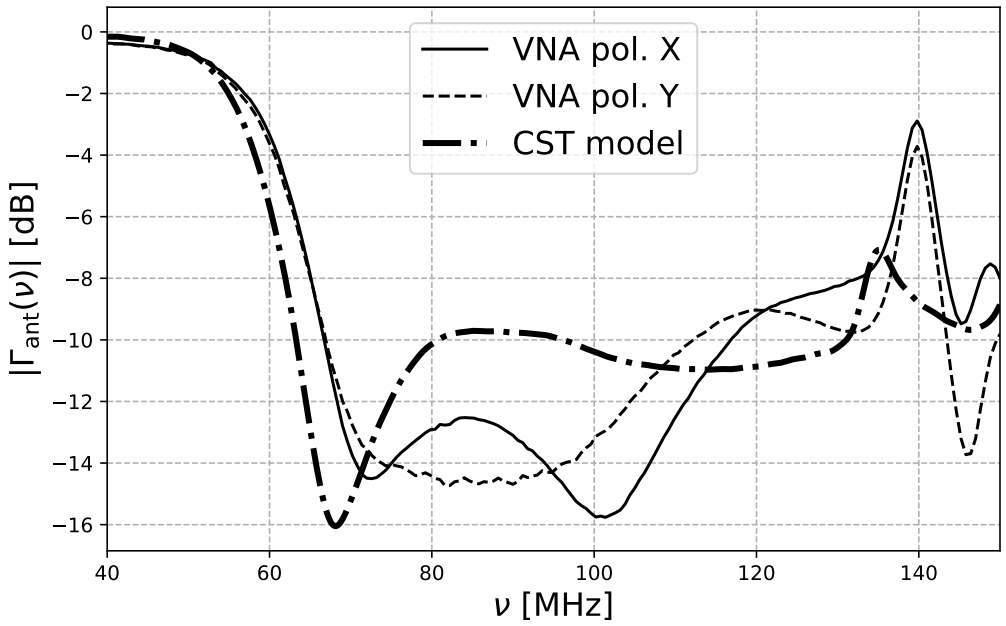

Figure 4.7: VNA measurement of the antenna reflection coefficients $\Gamma_{\text{ant}}(\nu)$ of the CTP sleeved dipole for polarization X (solid) and Y (dashed) are compared to the CST model (dot-dashed). The double resonant features are apparent between 60 and 120 MHz. The difference between VNA measurements of the two polarizations is due to variations in the fabrication of the toroidal inductors used at the passive balun. Due to complexity in modeling the ground soils and detailed structures on the antenna, we don't expect the small features of the CST model align with the VNA measurement. Nonetheless, the model does reflect characteristics of the double resonance.

ity, as suggested by the radiometer equation in Eq. (2.23). To circumvent these limitations, we have completely redesigned the FE system along with a new network-parameter based calibration scheme for the transducer gain and noise temperature.

Dual-stage Active Thermal Control: To address the temperature variations, instead of exposing the FE electronics to the outdoor ambient temperature, the CTP's FE modules are housed in a thermally-regulated weatherproof enclosure which is equipped with an active thermal control system Figure 4.9. To compensate for the large temperature swings between day and night time ($\gtrsim 40$ °C), the thermal control system stabilizes the temperature of the FE electronics through two individual stages. The FE electronic modules are contained in

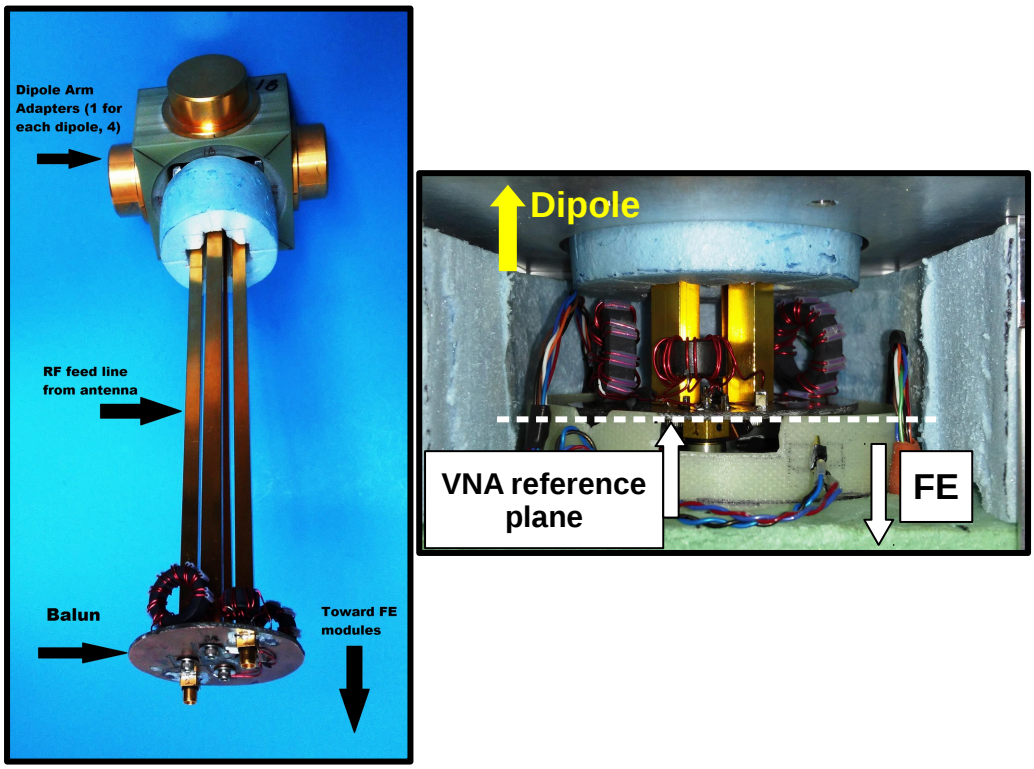

Figure 4.8: CTP's passive balun for each polarization consists of two toroidal transformers that convert the balanced signal into unbalanced one before entering the FE system. (Left) Attachment between dipoles arms' adapter in the top and the balun circuit board in the bottom by four RF feedlines, one pair for each polarization. (Right) Close-up picture of the balun board after connected to the FE modules inside the thermal control unit Stage 1. The VNA reference plane used for the VNA calibration and antenna measurement is shown (white dashed).

the inner stage (Stage 2), which in return is regulated by an outer stage (Stage 1).

Each stage is insulated with closed-cell extruded polystyrene (XPS) foam and regulated by four thermoelectric heat pumps, one on each side of the housing. The heat pumps are controlled by a proportional-integral-derivative (PID) unit using a negative temperature coefficient (NTC) thermistor as thermal feedback. The general layout of this FE enclosure is shown in Figure 4.9. In essence, the PID controller maintains the internal temperature of the enclosure to within uncertainty of the set value. For example, if the outside temperature is lower than the interior, the PID will draw current in a direction such that the heat pumps

can remove the internal heat, and vice versa.

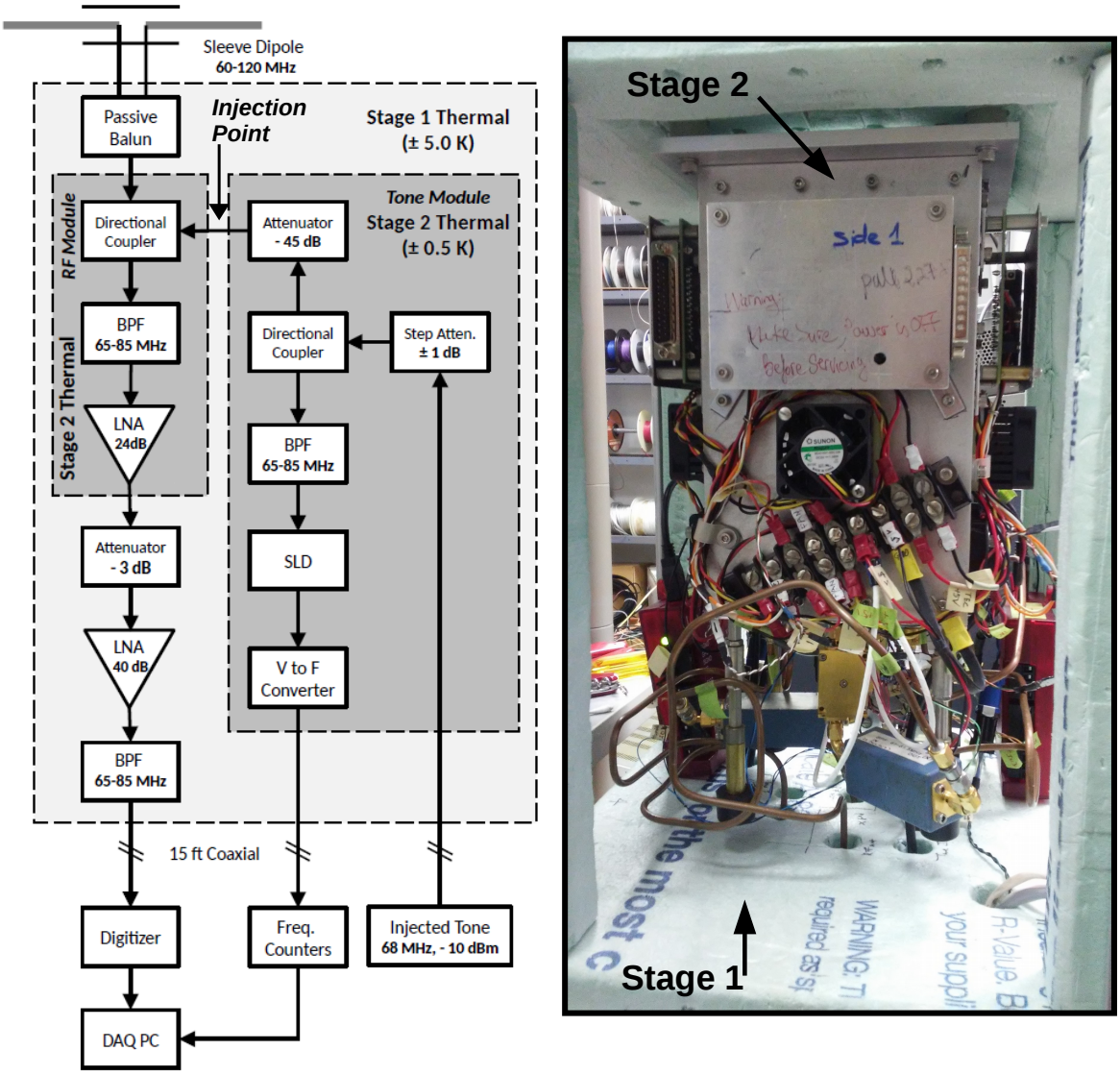

Figure 4.9: (Left) FE block diagram for one of the polarizations, which consists of one RF module and one tone module for the injected calibration tone at 68 MHz. Both FE modules are enclosed within the dual-stage active thermal control unit. (Right) Dual-stage FE Thermal Control.

Since it is more effective to heat an enclosed space than cooling it with thermoelectric devices, each thermal control stage is set to a higher temperature than its respective ambient temperature. For example, the outer stage is kept at an temperature warmer than the outdoor ambient, meanwhile the inner Stage 2 containing the FE electronics is set to be

warmer than Stage 1. As a result, Stage 1 is able to maintain the temperature within ±5 K, and Stage 2 holds within ±0.5 K, as illustrated in Figure 4.10. It is worth noting that, since the global 21-cm experiment is sky noise dominated ($\sim 10^3 - 10^4$K), it is more important to keep the FE stabilized thermally than to have them operating in low temperature like other microwave devices. Hence no cryogenic cooling is required. This also significantly reduces the operating cost.

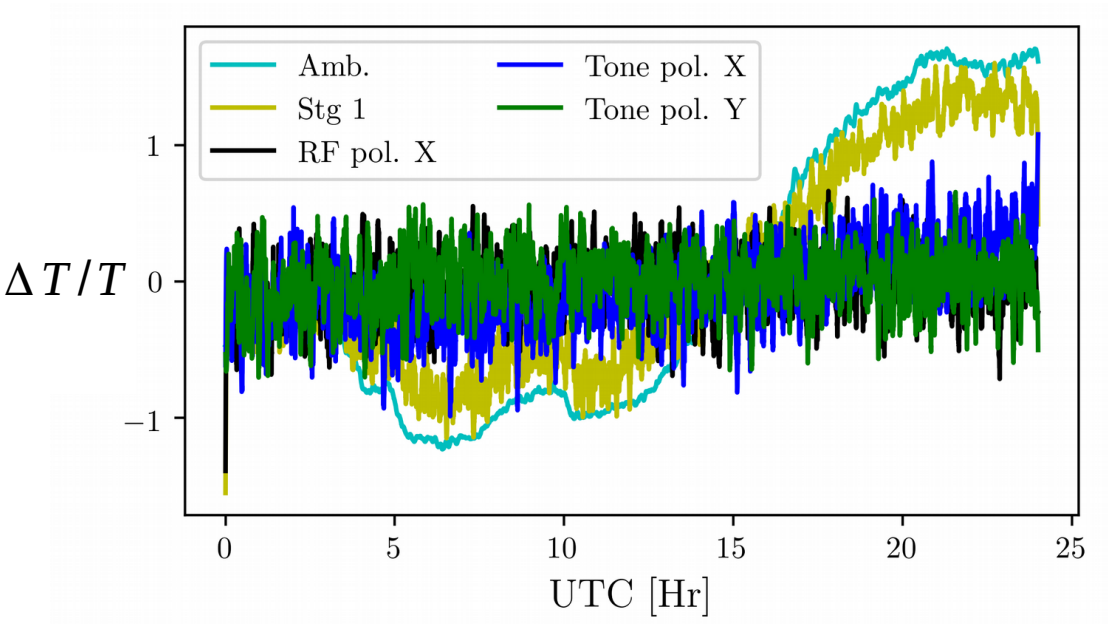

Figure 4.10: Comparison of the normalized temperature sensor reading over 24 hours of observation for the external ambient (cyan), the interior temperature of Stage 1 (yellow), and the FE modules inside Stage 2 (remaining curves). The smaller variations of the sensors on the inner FE modules in relative to the ambient and Stage 1 temperature illustrate the effectiveness of the dual-stage thermal control in suppressing large temperature fluctuations. Nonetheless, there are still room for future improvement on the stability.

FE with Built-in Frequency-Tone Calibration:

Instead of relying on the on-off load switching to correct for the transducer gain as in the bicone system, we have developed a new calibration scheme that does not involve switching. It utilizes a strong reference tone at a fixed frequency (68 MHz), which is injected into the main RF signal chain in the FE, to track the gain variations in real time. Doing

so allows the CTP to observe the sky for the entire time without losing integration time for switching to a load.

Because of the strong amplitude of the tone, a high signal-to-noise ratio (S/N) measurement of the gain variations can be obtained within the given short observing interval. In contrast, a broadband noise reference would have had to integrate over much longer time to achieve an similar level of sensitivity. Since the reference tone only measures the gain variations at the tone frequency, ν_{tone}, the frequency response of the transducer gain is obtained with the help of extrapolation between lab measured S-parameters and the network model. The detail of this tone-based calibration is described below in Section 4.3.1.

As suggested by the block diagram in Figure 4.9, the FE unit of each polarization is composed of two separate FE modules: one RF module and one tone module. This time, the FE electronics are housed in RFI-tight brass modules which are contained inside the thermal control Stage 2, as described above. The FE is designed such that each of the four FE modules is thermally insulated and regulated independently from each other to minimize thermal coupling among themselves. The layout configuration of the FE modules inside the Stage 2 enclosure is shown in Figure 4.11.

Main RF Signal Chain Module:

The CTP's RF module consists of three main components, as illustrated in Figure 4.12. When the RF signal enters the device, it passes through the directional coupler to combine with the injected tone from the tone module. The sky signal and the reference tone both pass through a custom-made 4-pole inverse-ChebyshevInverse Chebyshev filter is used instead of the more common Butterworth filter because we have to achieve sharper cutoff for the filter response. The compromise for using the former design is inducing potentially unwanted ripple across the passband. However, since only a 20 MHz band is needed, the ripples induced by a 4-pole inverse Chebyshev is acceptable for the CTP prototype. band-pass filter (BPF1) before being amplified by a monolithic microwave integrated circuit (MMIC) low-noise amplifier (LNA) (TriQuint TQP3M9009).

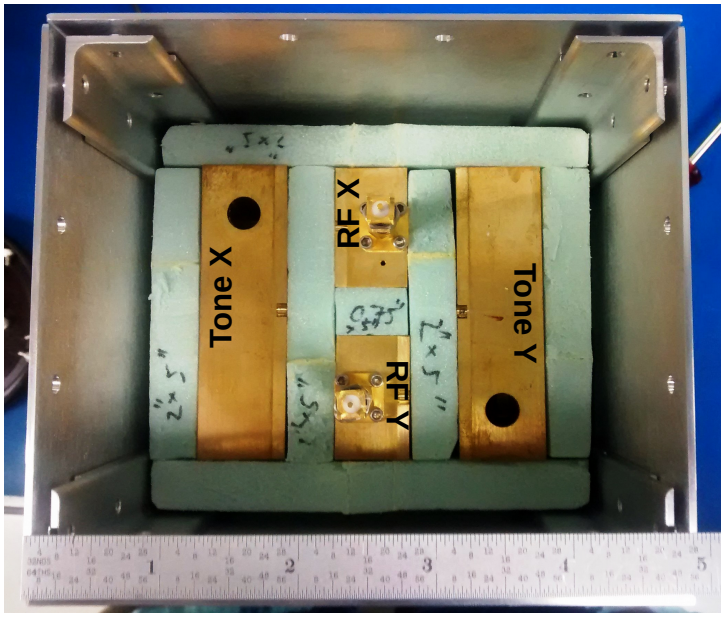

Figure 4.11: The layout of the FE modules within the Stage 2 of the active thermal control. For each polarization, there is one RF module and one tone module. Each of the modules is thermally regulated and insulated independently to minimize thermal coupling.

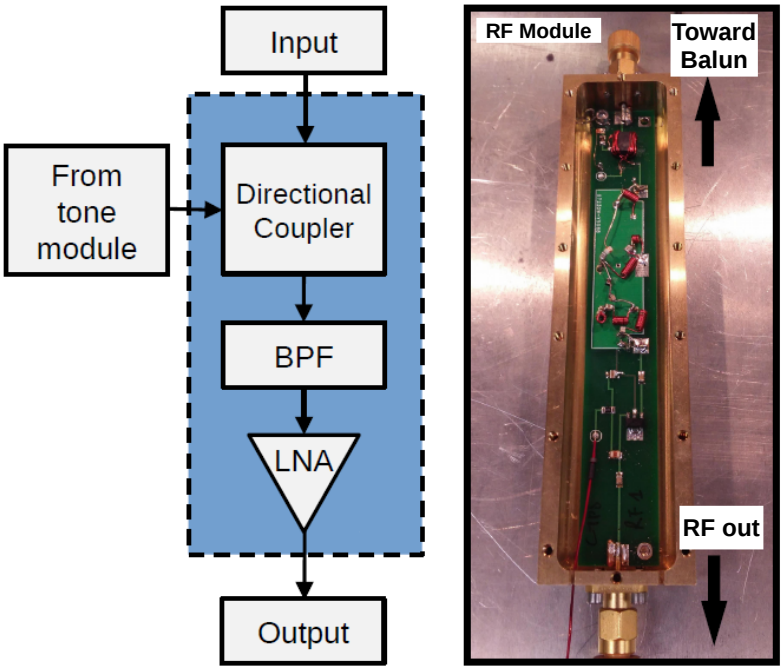

Figure 4.12: RF module block diagram (left) and picture (right).

In the bicone system, multiple stages of LNAs are used to amplify the incoming signal in the earlier stages before the signal enters the BPF in the last stage inside the receiver box. The rationale for such design is to ensure that the sky signal is sufficiently amplified before being corrupted by the electronic noise and before it passes through the BPF. Our results demonstrate that strong RFI, especially from FM transmissions (88-108 MHz), can saturate an LNA in the receiver module after they are amplified by the active balun. This causes gain compression to occur when the active device has entered a nonlinear operating regime from being overdriven. To mitigate this, we have placed a BPF up front of the RF signal chain to suppress out-of-band signal.

For the CTP to be deployed at the Equinox Farm, a less radio-quiet environment than the GBO, the BPF is designed for the 65-85 MHz band to suppress the local digital TV band around (62-64 MHz) and the FM stations (88-108 MHz). As a result, this has reduced the useful bandwidth within 20 MHz. Although it is a bit narrow for the ultimate global 21-cm signal, it should suffice as a proof of concept for the PIPE technique.

Tone Calibration Module:

Two fundamental criteria are needed to improve the gain measurement: one is to be able to measure the change (or drift) in the gain within a short time interval, and second is to be able to measure that change accurately. We have developed a means to track the differential gain change using a high S/N injected tracking frequency tone. This allows us to measure the change on the tone power with high precision.

In brief, the tone-based system involves two main steps to track the system's gain variations. The injected tone[1] at $\nu_{\text{tone}} = 68$ MHz, which is supplied by an external synthesizer, enters the FE tone module through a step attenuator before being split into two directions by a directional coupler. One part of the tone is coupled to the main RF module as described above. This tone along with the sky signal are digitized by the Signatec DAQ card.

[1] The tone frequency can be arbitrary as long as it is within the passband of the FE. We chose ν_{tone} to be 68 MHz for the tone resides close to the low band edge so the center of the band is not interrupted.

Meanwhile, the second part of the tone signal is passed through a second BPF, a square-law detector (SLD), and a voltage-to-frequency (V-to-F) converter which converts the tone power into low frequency pulse wave ($\sim$ 100 kHz). The count frequency is recorded by a universal frequency counter (HP 5335A). The overall layout of the tone module is presented in Figure 4.13.

The step attenuator is the key component in this scheme. It modulates the tone power by lowering it 1 dB and then resumes to the original value for every other acquisition scan. For example, if the first scan has tone set to -10 dB then the second scan is -11 dB, and so forth. By simply modulating the tone power by 1 dB, any potential gain drift on the main RF signal chain will reflect on the differential change in the 1 dB difference of the tone coupled to the RF module. Meanwhile, the frequency counter of the second part of the tone power measures the uncorrupted tone power independent of the RF modules. In principle, the gain variations of the FE RF module can be derived indirectly by comparing the differential change in tone power between the frequency counter and the tone measured through the RF module itself. Details of this tone calibration is further described in Section 4.3.1.

4.2.3 BE Instruments and Deployment

Due to the more complex instrument configuration than the bicone precursor, the BE system of the CTP consists of a variety of instruments mounted on a rack. The entire rack is stored in a weatherproof outdoor enclosure which is thermally regulated by an external AC unit. As illustrated in Figure 4.14, the rack contains: a main PC for acquiring the RF and metadata with the same Signatec PX14400A digitizer card from the bicone system, a secondary PC designated to perform Fourier transformation from raw RF voltages into spectra, two universal frequency counters to measure the tone power for each polarization, a synthesizer to provide the 68 MHz tone, the PID controller for Stage 1 thermal control unit, a Rubidium clock to synchronize all the instruments to a common cadence, DC power

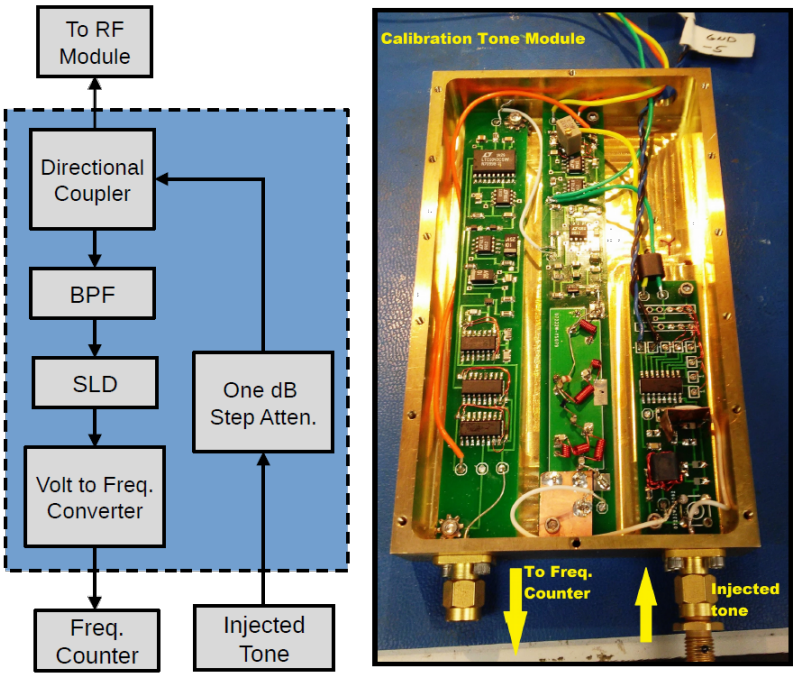

Figure 4.13: Tone Module Block Diagram and Picture.

supplies, and a UPS unit to prevent any power glitches. The BE instrument rack is connected to the FE unit with 15 feet of coaxial and power cables. The shorter cable helps to reduce the potential signal attenuation through the transmission, as was the case of the 120 feet cable for the bicone system.

The deployment site was prepped in early fall of 2017. Due to the lack of azimuthal rotation of the supporting structure, proper alignment is crucial so that the CTP's meridian coincide to the NCP. During the deployment, to minimize the pointing error, we have been meticulous when aligning the CTP ground screen with the NCP using a segment of PVC pipe attached to the center of the ground screen as a view finder for the Polaris during night time as illustrated in Figure 4.15.

As shown in panels A-C in Figure 4.16, once a square grid was laid out, four supporting posts were installed before the ground screen was placed on them. As shown in panels E and F, a pair of winches with static rope were used to tilt of the ground plane to a desired

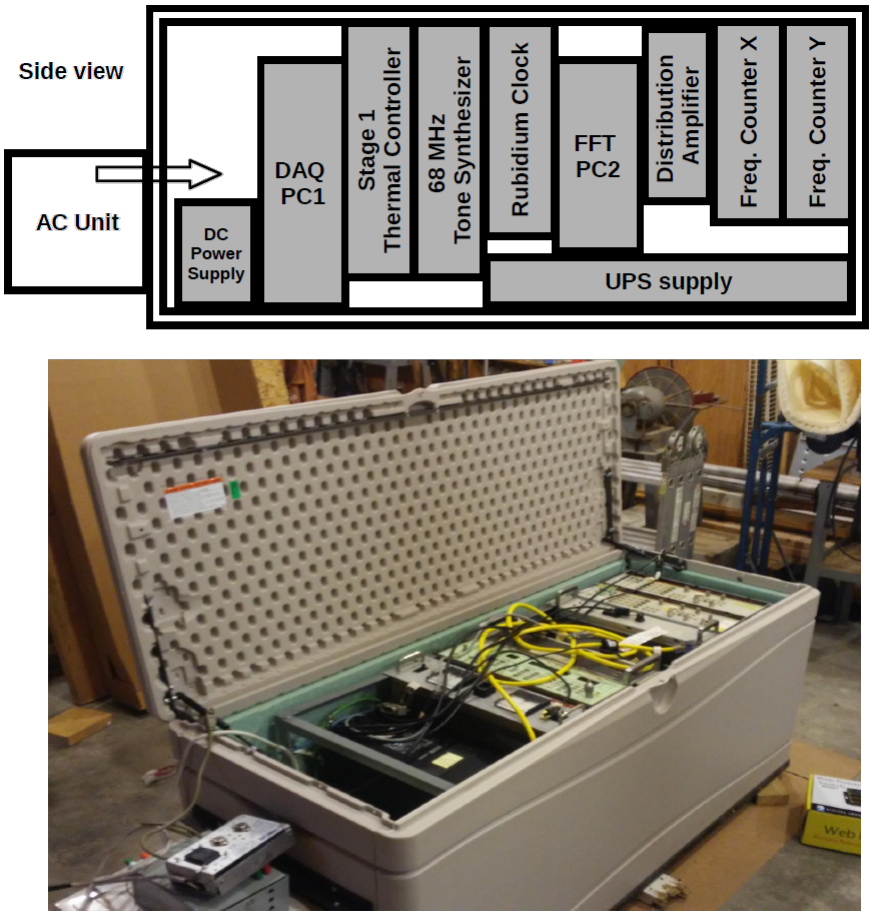

Figure 4.14: The BE instrument rack contains the DAQ PCs, the frequency counters, the synthesizer for the 68 MHz reference tone, thermal controller for the outer thermal stage of the FE housing, and the rubidium clock for system synchronization. The BE rack inside a weatherproof housing is thermally regulated by an external thermal control unit.

angle. The titling angle relative to the ground for a local observer equals 90° minus the observer's latitude. At the Equinox Farm in Troy, VA, the latitude is about 38°, hence the ground plane was titled at 52°. Once the ground plane was secured in place, the skirt and the sleeved antenna were relocated and assembled on site. The final deployed system is shown in Figure 4.18. The BE rack situated below the antenna is also shown in Figure 4.17.

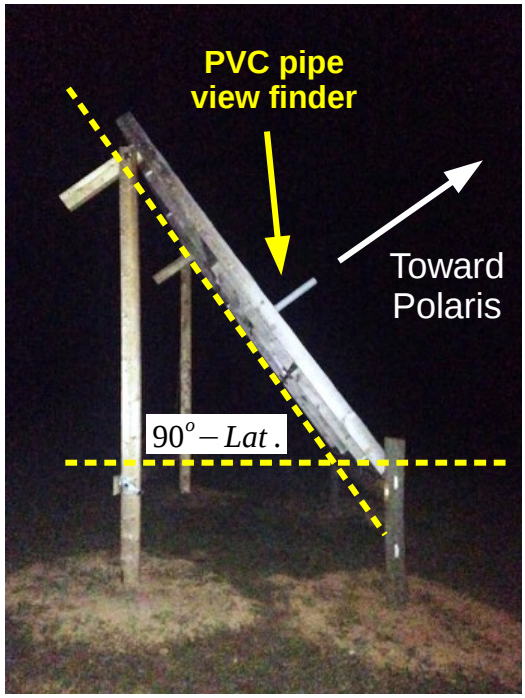

Figure 4.15: We use a segment of PVC attached to the center of the ground screen and adjust the tilting angles until the Polaris is centered in the PVC view finder.

4.3 Instrument Calibration

In general, two-port network theory is applied to a device under test (DUT) such as an LNA. There are two ways to characterize a multi-stage signal chain, either by measuring the gain and noise of an individual stage or by assuming the entire signal chain is one composite two-port network. In principle, these two approaches are equivalent as long as the system consists of devices operating in the linear regime (Engberg and Larsen, 1995).

As seen from above, the CTP consists of primarily linear devices like LNAs and passive BPFs. To simplify the measurement, we treat the entire FE signal chain (from the input of the RF module to the end of the coaxial cable) as a single DUT. In such a configuration, in terms of the two-port network terminology, the source reflection coefficient $\Gamma_{\rm src}(\nu)$ corresponds to the impedance of the device $Z_{\rm src}(\nu)$ attached to the input port the RF module. The output load reflection coefficient $\Gamma_{\rm load}(\nu)$ refers to the reflection due to impedance mis-

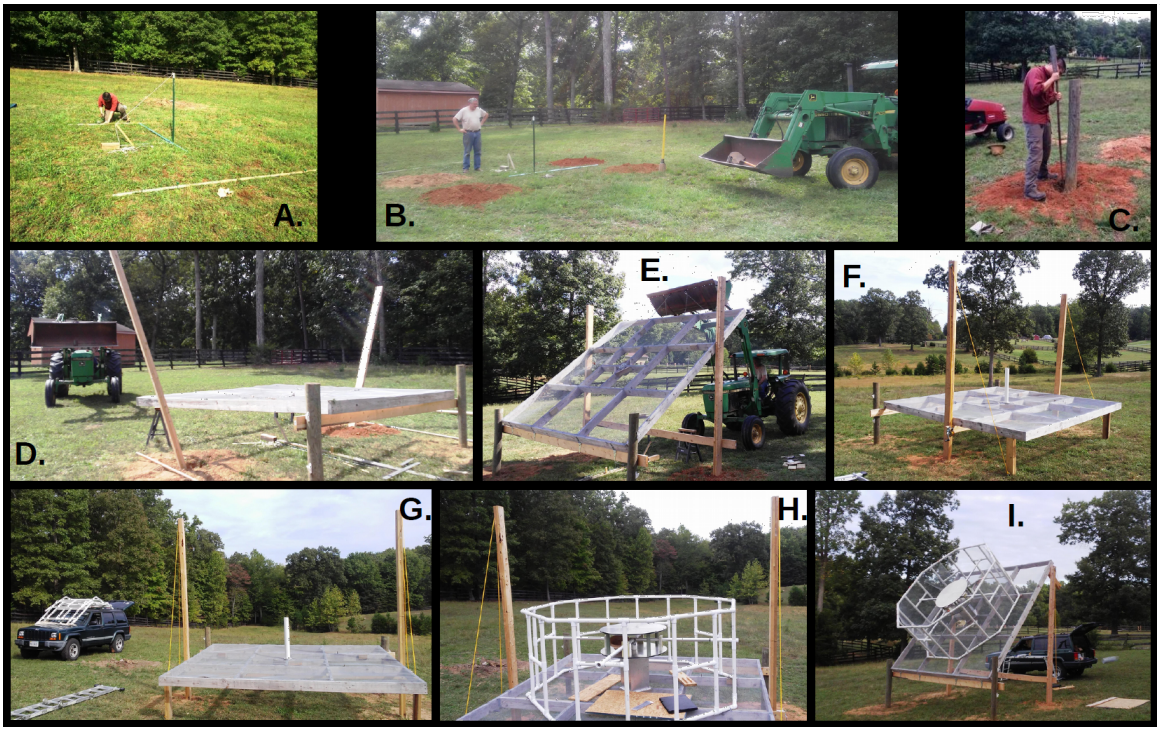

Figure 4.16: Construction and deployment of the CTP at the Equinox Farm. (Panel A.-C.) Surveying and installing the four supporting fence posts for the ground screen. These steps are crucial in having the north-pointing alignment since the antenna is unable to rotate azimuthally. (Panel D.-F.) Transporting and installing ground screen onto the supporting posts. Mechanical winches were added on each side of the vertical posts for raising the antenna to the proper pointing angle at the NCP. (Panel G.-I.) Assembling sleeved dipole and skirt (PVC frame and conductive mesh) onto the ground plane.

match of the device connected to the end of the 15-foot coaxial cable, thus the reflection coefficient of the input port of the Signatec ADC card.

4.3.1 High-Precision Injected Tone Gain Calibration

The measured power at $\nu_{\rm tone}$ for the two, high and low, states can be written as,

$$\begin{aligned} P_{\rm hi}(\nu_{\rm tone}) &= P_{\rm tone,hi} + P_n(\nu_{\rm tone}) = G_{T,\rm hi}(\nu_{\rm tone}) \left[P^0_{\rm tone,hi} + k_B \Delta\nu T_{\rm sys}(\nu_{\rm tone})\right] , \\ P_{\rm lo}(\nu_{\rm tone}) &= P_{\rm tone,lo} + P_n(\nu_{\rm tone}) = G_{T,\rm lo}(\nu_{\rm tone}) \left[P^0_{\rm tone,lo} + k_B \Delta\nu T_{\rm sys}(\nu_{\rm tone})\right] , \end{aligned} \tag{4.1}$$

Figure 4.17: The BE instrument rack is placed behind the antenna underneath the ground plane. The antenna is connected to the BE rack with 15 feet of coaxial cables.

where the second term in the brackets is the system[2] noise temperature $T_{\rm sys}(\nu_{\rm tone})$ over the channel bandwidth $\Delta\nu$, is assumed constant over the time interval of the measurement between high and low tone-stepping states. $P^0_{\rm tone,hi}$ and $P^0_{\rm tone,lo}$ are the measured tone powers at the tone module before being coupled to the RF module (at the injection point on the left panel of Figure 4.9). By solving for the power difference between the two tone states as illustrated in Figure 4.19, we arrive at,

$$\begin{aligned} \Delta P_{\rm obs}(\nu_{\rm tone}) &\equiv P_{\rm hi}(\nu_{\rm tone}) - P_{\rm lo}(\nu_{\rm tone}) \\ &= G_T(\nu_{\rm tone})(P^0_{\rm tone,hi} - P^0_{\rm tone,lo}), \end{aligned} \tag{4.2}$$

where we have substituted $G_{T,\rm hi}(\nu) = G_{T,\rm lo}(\nu) = G_T(\nu)$ since the system is assumed to be stable over the short interval between the high and low states. This is reasonable since the FE is thermally stabilized and the time interval is short.

To determine the change in the transducer gain as a function of temperature over the course of observation, we first define the difference in the calculated $G_T(\nu_{\rm tone})$ of the reference

[2] Using the standard convention, system temperature includes both the antenna temperature and the receiver noise temperature, i.e., $T_{\rm sys}(\nu) = T_{\rm ant}(\nu) + T_{\rm rcv}(\nu)$

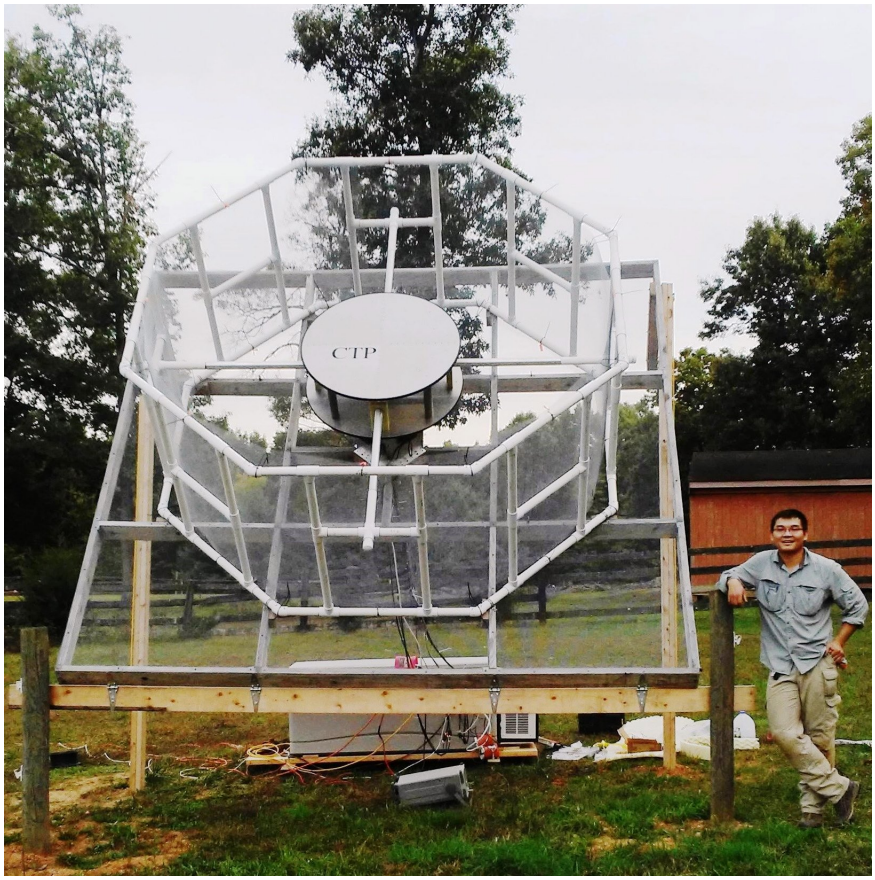

Figure 4.18: Final configuration of the deployed CTP at the Equinox Farm, LLC in Troy, VA, at a latitude of about 38° in early October of 2017.

tone between two time stamps t_i and t_{i+1} as,

$$\Delta G_T(\nu_{\text{tone}}, t_i) = G_T(\nu_{\text{tone}}, t_{i+1}) - G_T(\nu_{\text{tone}}, t_i) \tag{4.3}$$

where $G_T(\nu_{\text{tone}}, t_i)$ is the transducer gain derived from each pair of high-low (or low-high) states. By substituting Eq. (4.2) in (4.3), we obtain,

$$\Delta G_T(\nu_{\text{tone}}, t_i) = \frac{\Delta P_{\text{obs}}(\nu_{\text{tone}}, t_{i+1})}{\Delta P_{\text{tone}}(t_{i+1})} - \frac{\Delta P_{\text{obs}}(\nu_{\text{tone}}, t_i)}{\Delta P_{\text{tone}}(t_i)}, \tag{4.4}$$

where $\Delta P_{\text{tone}}(t_i) = [P_{\text{tone,hi}}(t_i) - P_{\text{tone,lo}}(t_i)]$ is the tone power difference between the high and low states. This implies that for each $\Delta G_T(\nu_{\text{tone}}, t_i)$, one need two consecutive sets of high-low (and low-high) measurements.

Recall that the injected tone is split into two parts in the tone module. One part is

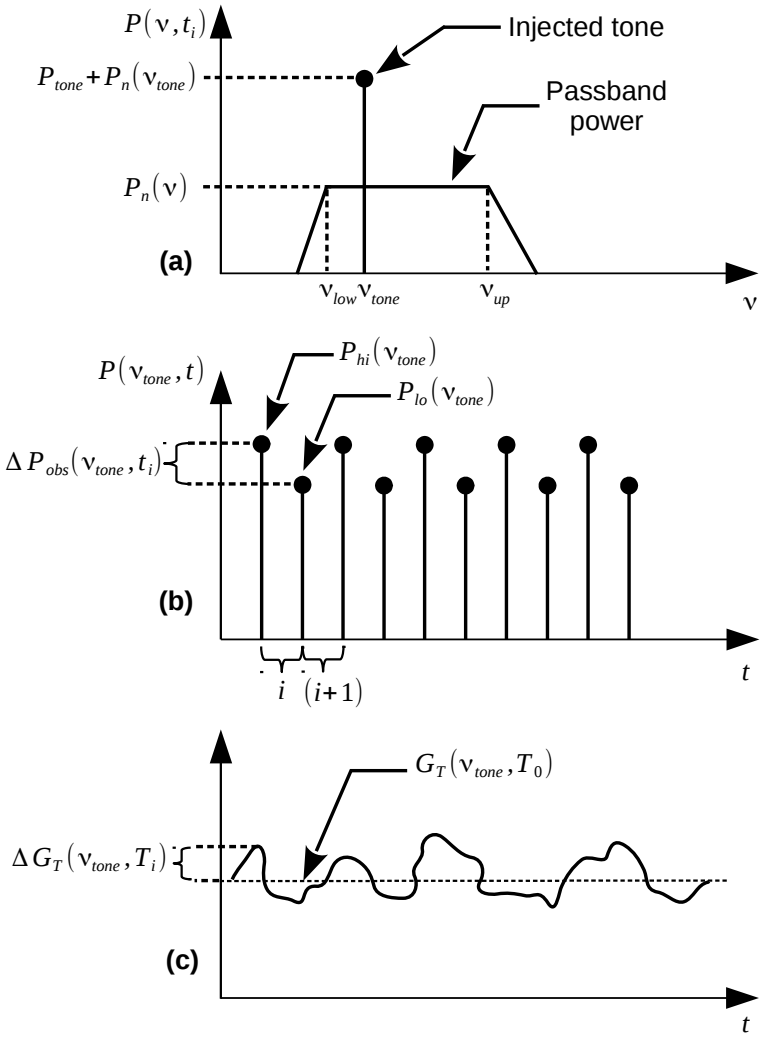

Figure 4.19: Injected tone stepping to track the change in the transducer gain. **(a)** Illustration of the passband noise power with the injected tone power at ν_{tone} at time stamp t_i. **(b)** Illustration for how stepping the tone power between high and low states allows us to calculate the $\Delta P_{\text{obs}}(\nu_{\text{tone}}, t_i)$ for a given time stamp t_i. **(c)** Illustration for the differential gain deviation at temperature T_i, $\Delta G_T(\nu_{\text{tone}}, T_i)$, that deviates from the reference transducer gain calculated for T_0. By design, for every $\Delta G_T(\nu_{\text{tone}}, T_i)$, two $\Delta P_{\text{obs}}(\nu_{\text{tone}}, t)$ from two different time steps are needed as described in Eq. (4.3). Note that the time stamp t_i and temperature recorded at that instance, T_i, is used interchangeably in this study.

coupled to the main RF module, whereas the other part of the tone passes through a SLD and a V-to-F converter (see Figure 4.13). By design, this output counting frequency from the

V-to-F converter is linearly proportional to the magnitude of the corresponding tone power which is also coupled to the RF module (similar methods have been used in continuum power measurement in radio astronomy, e.g., Kraus, 1986; Wilson et al., 2009). As a result, if we define the counts measured by the frequency counter at time stamp t_i for the high state as $\mathrm{Count}_{\mathrm{hi}}(t_i)$ and $\mathrm{Count}_{\mathrm{lo}}(t_i)$, the unknown tone power difference $\Delta P_{\mathrm{tone}}(t_i)$ can be estimated as the difference in counts as,

$$\Delta P_{\mathrm{tone}}(t_i) = C_0 \Delta \mathrm{Count}(t_i) = C_0 \left[\mathrm{Count}_{\mathrm{hi}}(t_i) - \mathrm{Count}_{\mathrm{lo}}(t_i)\right], \tag{4.5}$$

where C_0 is defined as the scaling constant in $P_{\mathrm{tone}}(t_i) = C_0 \mathrm{Count} + C_1$, and C_1 is an offset constant that cancels out. Although this scaling factor is susceptible to changes at different operating temperature, we assume they are constant under thermal control.

Subsequently, the gain change $\Delta G_T(\nu_{\mathrm{tone}}, t_i)$ can be solved by substituting Eq. (4.5) into (4.4) as,

$$\begin{aligned} \Delta G_T(\nu_{\mathrm{tone}}, t_i) &= \frac{\Delta P_{\mathrm{obs}}(\nu_{\mathrm{tone}}, t_{i+1})}{C_0 \Delta \mathrm{Count}(t_{i+1})} - \frac{\Delta P_{\mathrm{obs}}(\nu_{\mathrm{tone}}, t_i)}{C_0 \Delta \mathrm{Count}(t_i)} \\ &= \frac{1}{C_0}\left[\frac{\Delta P_{\mathrm{obs}}(\nu_{\mathrm{tone}}, t_{i+1})}{\Delta \mathrm{Count}(t_{i+1})} - \frac{\Delta P_{\mathrm{obs}}(\nu_{\mathrm{tone}}, t_i)}{\Delta \mathrm{Count}(t_i)}\right] \end{aligned} \tag{4.6}$$

where $\Delta P_{\mathrm{obs}}(\nu_{\mathrm{tone}}, t_i)$ are measured by the Signatec card and $\Delta \mathrm{Count}(t_i)$ are computed from the values acquired by the HP frequency counters over the short time interval (about 8 seconds since it takes 4 s for each tone state to be recorded). More importantly, the high S/N tone power provides a direct and fast means to determine gain variations $\Delta G_T(\nu_{\mathrm{tone}}, t_i)$. In fact, the precision of $\Delta G_T(\nu_{\mathrm{tone}}, t_i)$ is the relative S/N of the tone power and the effective passband noise power. For example, if the tone is at least 40 dB stronger than the effective noise power over $\Delta\nu$, the standard deviation of $\Delta G_T(\nu_{\mathrm{tone}}, t_i)$ is at least four orders of magnitude smaller than its mean value.

Recalling from Eq. (2.15), the transducer gain of a two-port DUT for a given temperature T_i at time stamp t_i is defined as,

$$G_T(\nu, T_i) = \frac{\left(1 - |\Gamma_{\mathrm{src}}|^2\right)\left(1 - |\Gamma_{\mathrm{load}}|^2\right)|S_{21}|^2}{\left|\left(1 - S_{11}\Gamma_{\mathrm{src}}\right)\left(1 - S_{22}\Gamma_{\mathrm{load}}\right) - S_{12}S_{21}\Gamma_{\mathrm{src}}\Gamma_{\mathrm{load}}\right|^2}, \tag{4.7}$$

where the four S-parameters describe the intrinsic characteristic of the DUT and are independent of the input source $\Gamma_{\rm src}$ and output load $\Gamma_{\rm load}$ impedances. The time and temperature variable are interchangeable since at each time stamp t_i, a corresponding temperature T_i is recorded with the sensor, assuming the delayed response is negligible.

To apply the gain calibration for the CTP observation, we first calculate the transducer gain in Eq. (4.7) using the S-parameters acquired from the laboratory VNA measurement, which is evaluated at temperature T_i using the fourth degree polynomial parametrization similar to Eq. (2.19) as,

$$\begin{aligned} S_{kl}(\nu, T_i) &= \left[\sum_{n=0}^{4} a_n(T)\nu^n\right]_{kl} \\ &= \left[\sum_{n=0}^{4}\left(\sum_{m=0}^{4} b_{nm}T^m\right)\nu^n\right]_{kl}\Bigg|_{T=T_i}, \end{aligned} \tag{4.8}$$

where $k, l \in \{1, 2\}$ for each of the four S-parameters. The source reflection coefficient is the measured antenna reflection $\Gamma_{\rm ant}(\nu)$ coefficient using the VNA in the field. $\Gamma_{\rm load}(\nu)$ is the reflection coefficient at the input port of the Signatec ADC card which is also acquired by the VNA. Analysis from the CST simulation suggests that the temperature dependence on the antenna structure is negligible, hence the reflection coefficient is assumed to be independent of temperature variations. As operating under thermal control and in the linear regime, it is reasonable to assume that the gain varies equally across the relatively narrow 65-85 MHz band[3] . Hence, the gain variations derived from the tone frequency can be applied for all frequencies across band, i.e., $\Delta G_T(\nu_{\rm tone}, T_i) \approx \Delta G_T(\nu, T_i)$.

Residuals from the temperature variations are still present even if the FE is stabilized under thermal control. The effectiveness of the tone calibration on long-term integration of the CTP's FE in the lab is apparent in Figure 4.20 when comparing to a fixed transducer gain calibration only without tracking. Without applying the tone tracking (solid curve), the smaller gain variations limits the system's sensitivity to about 100 ± 10 K.

[3] A more rigorous estimation may be needed for correcting a wider band, such as 60-120 MHz.

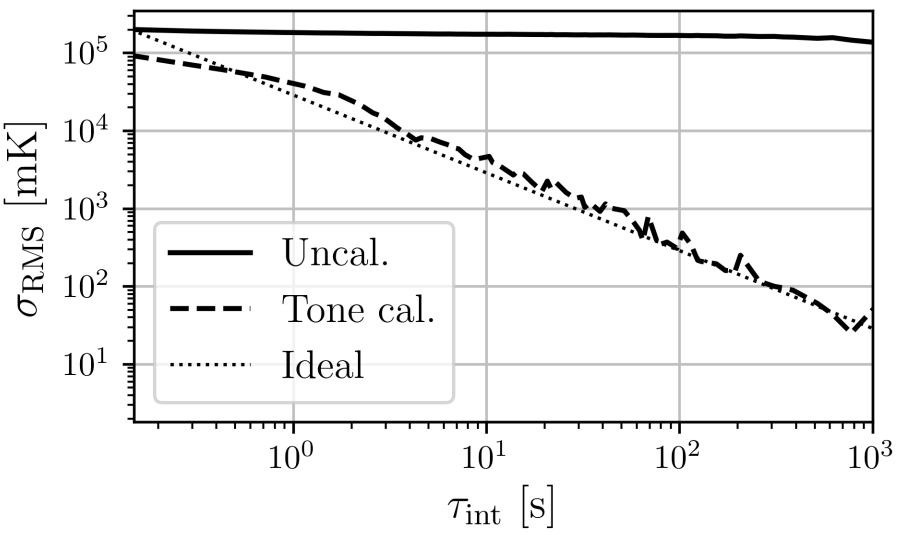

Figure 4.20: Comparison of the CTP's FE sensitivity in the lab when integrating a 50 Ω termination at the input. The over RMS error of the uncalibrated data settles about 100 ± 10 K (solid). Meanwhile, the tone-calibrated data (dashed) allows the system to reach a sensitivity close to an ideal radiometer (dotted).

Combining the FE thermal control system, the tone-based calibration this provides a robust and fast way to track the gain with much better precision than the previous on-off load scheme. In summary, these are the steps we have devised to estimate and correct the transducer gain $G_T(\nu)$ by using an injected tone and network-based parameters as the operating temperate drifts over time:

(1) Obtain the high and low state power from the ADC digitizer for $P_{\mathrm{hi}}(\nu_{\mathrm{tone}})$ and $P_{\mathrm{lo}}(\nu_{\mathrm{tone}})$ to compute $\Delta P_{\mathrm{obs}}(\nu_{\mathrm{tone}})$ for time stamps t_i and t_{i+1},

(2) Obtain the counts from the frequency counter for high and low states to compute ΔCount for time stamps t_i and t_{i+1},

(3) Substitute $\Delta P_{\mathrm{obs}}(\nu_{\mathrm{tone}})$ and the difference in counts ΔCount into Eq. (4.6) to calculate the gain change at ν_{tone} for temperature T_i, $\Delta G_T(\nu_{\mathrm{tone}}, T_i)$,

(4) Extrapolate the transducer gain $G_T(\nu, T_0)$ in Eq. 4.7 to a reference T_0, preferably

the initial temperature reading after the FE has reached thermal stability at time t_0, using polynomial fits the S-parameters $S_{kl}(\nu, T_i)$ in Eq. (4.8), the field measured $\Gamma_{\rm ant}(\nu)$, and $\Gamma_{\rm load}(\nu)$ from the Signatec ADC card,

(5) Assume $\Delta G_T(\nu_{\rm tone}, T_i)$ to be the same across the band for a calculated $G_T(\nu, T_i)$ and apply the appropriate gain correction for a measured T_i relative to the reference $G_T(\nu, T_0)$ at T_0.

4.3.2 Circuit-model Based Noise Correction

Unlike the on-off load scheme described in Chapter 2, the noise temperature $T_n(\nu)$ of the system does not cancel out during the tone-based calibration process as in Eq. (2.14), not to mention the inaccuracy of assuming $T_n(\nu)$ to be identical for the on and off states. Hence, besides calibrating $G_T(\nu, T)$ of the CTP's signal chain, it is also crucial to determine and remove the electronic receiver noise temperature, $T_n(\nu, T)$, of the system before revealing the underlying sky signal.

The noise temperature of an active device, like an LNA, is typically measured in the laboratory with direct means such as using a Noise Figure Analyzer (NFA). For many applications in radio astronomy and telecommunication, the noise figure NF or the effective noise temperature T_n (sometimes denoted as T_e) of the DUT measured by an NFA is adequate to characterize the internal noise behavior of the system. Similarly, conventional global 21-cm experiments have employed different schemes to constrain this noise temperature of their system, such as the three-load switching scheme from EDGES (Bowman et al., 2008; Bowman and Rogers, 2010). However, T_n is intrinsically a function of input impedance like $G_T(\nu)$. In other words, the noise temperature measured in the laboratory or under a different input reference source is not equivalent to the noise temperature needed to calibrate during observation, when the antenna is attached to the system.

Nevertheless, in noise theory, there exists a set of four parameters called noise pa-

rameters that can provide a more robust way to calculate T_n (Engberg and Larsen, 1995). They are intrinsic to the DUT and independent of the input impedance. This is analogous to the S-parameters for the transducer gain. In fact, network simulation software, such as ADS[4] (Advanced Design System) and AWR[5] (Applied Wave Research), commonly requires information for both the noise parameters and S-parameters to estimate T_n of a device.

For the CTP, we used a network-theory based formulation to constrain and correct the noise of the system based on the noise parameters instead of just attempting to determine $T_n(\nu)$ on the fly as in load-switching schemes. For a two-port device with a complex source impedance $Z_{\rm src}(\nu)$, its effective noise temperature can be expressed as the noise factor[6] $F_n(\nu) = 1 + T_n(\nu)/T_{\rm ref}$, where $T_{\rm ref} = 290$ K is the standard noise temperature conventionally chosen so that $k_B T_{\rm ref} = 4.00 \times 10^{-21}$ W. In principle, if the source impedance can be matched to an optimal value $Z_{\rm opt}(\nu)$, then a minimum noise value $T_{\rm min}(\nu)$can be obtained. With the assumption of linearity, the noise factor can be parametrized as

$$F_n(\nu) = F_{\rm min}(\nu) + \frac{4 r_n(\nu) |\Gamma_{\rm src}(\nu) - \Gamma_{\rm opt}(\nu)|^2}{|1 + \Gamma_{\rm opt}(\nu)|^2 \left(1 - |\Gamma_{\rm src}(\nu)|^2\right)}, \tag{4.9}$$

where the minimum noise factor $F_{\rm min}(\nu) = 1 + T_{\rm min}(\nu)/T_{\rm ref}$, and the normalized equivalent noise resistance $r_n(\nu) = R_n(\nu)/Z_0$. The complex reflection coefficient of the source and optimal impedances are defined as $\Gamma_{\rm src}(\nu)$ and $\Gamma_{\rm opt}(\nu)$ respectively, where $\Gamma_i = (Z_i - Z_0)/(Z_i + Z_0)$ with $Z_0 = 50\Omega$. Including the real and imaginary part of $\Gamma_{\rm opt}(\nu)$, the set of four noise parameters needed to determine $T_n(\nu)$ for the CTP system is $\Big\{ F_{\rm min}(\nu),\ {\rm Re}\left[\Gamma_{\rm opt}(\nu)\right],\ {\rm Im}\left[\Gamma_{\rm opt}(\nu)\right], r_n(\nu) \Big\}$. The noise figure is a multivariable function that can be graphically represented as Figure 4.21, where $F_{\rm min}(\nu)$ is the minimum value of the $F_n(\nu)$ surface.

To calculate these parameters, we measure the system with a combination of different input reference impedance $Z_{\rm src}(\nu)$. The input reference set consists of $25\Omega,\ 50\Omega,\ 75\Omega$ loads with RC and RL in series. Each of the inputs is made of surface mount passive components,

[4] By Keysight, `https://www.keysight.com/en/pc-1297113/advanced-design-system-ads`
[5] By National Instrument (NI), `http://www.awrcorp.com/`
[6] The noise factor is the linear value of the noise figure as $NF = 10 \log_{10}(F_n)$.

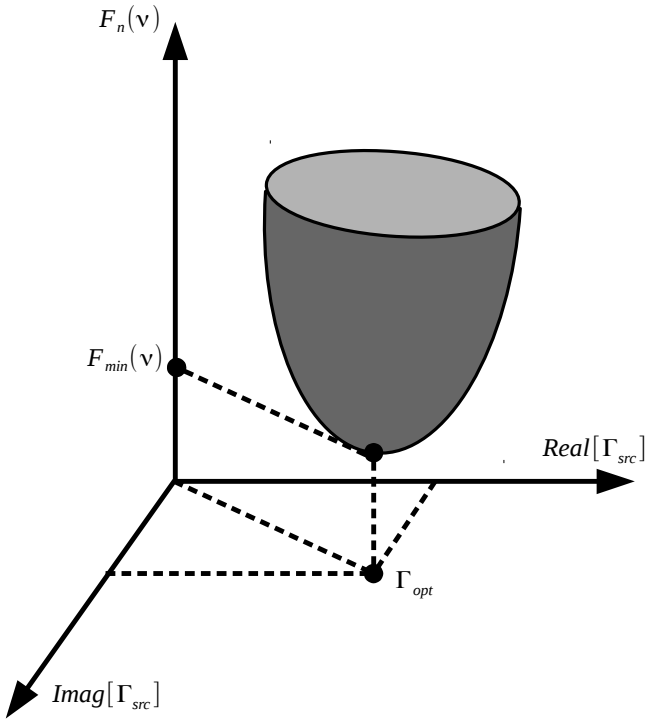

Figure 4.21: Graphical representation of the noise figure function, where $F_{\min}(\nu)$ is the minimum noise level when the source impedance reaches an optimal level $\Gamma_{\text{opt}}(\nu)$. The xy-plane represents the real and imaginary terms of $\Gamma_{\text{src}}(\nu)$, and the z-axis represent the $F_n(\nu)$.

which are housed in a RF-tight module with a SMA (SubMinature version A) connector for connecting to the CTP's main RF module, as shown in Figure 4.22. Since the four noise parameters are unique to the CTP system by definition, they can be determined by fitting the set of $F_n(\nu)$ for the five different input sources $\Gamma_{\text{src}}(\nu)$ as shown in Figure 4.23. We utilized an optimize Markov Chain Monte Carlo (MCMC) algorithm, the `emcee` (Foreman-Mackey et al., 2013), to fit measured $F_n(\nu)$ and $\Gamma_{\text{src}}(\nu)$ to Eq. (4.9). However, later analysis shows that the MCMC fit does not converge on unique solutions unless the offset $F_{\min}(\nu)$ in Eq. (4.9) is determined.

In practice, there are ways to determine $F_{\min}(\nu)$ such as using an NFA and a VNA combining an impedance tuner to painstakingly determine the minimum noise value of the DUT at each frequency. This process can be time-consuming and expensive (Caruso and

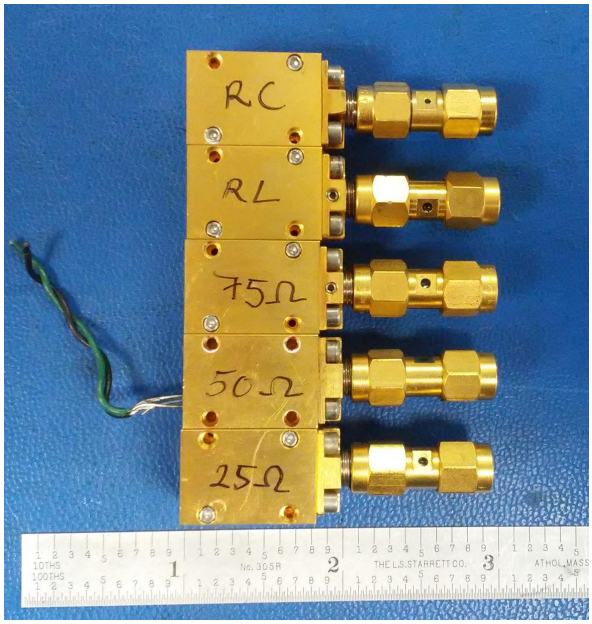

Figure 4.22: Input impedance sets for determining the noise parameters of the CTP system in the laboratory before applying the MCMC fit for the set of four noise parameters. The input loads are (in descending order): *RC* in series, *RL* in series, 75 Ω, 50 Ω, and 25 Ω.

Sannino, 1978; Mitama and Katoh, 1979; Simpson et al., 2008). Instead, we utilize the ADS software to model the electronic circuit for the RF module. Although it is not optimal, the ADS simulation provides a quantitative estimate of the $F_{\min}(\nu)$ of the FE RF signal path. This is a reasonable assumption since the noise in the measured signal is dominated by the earlier amplification stage according to Friis formula[7] (Engberg and Larsen, 1995), which states that the noise contributed by latter stages is less significant because the noise of the first stage becomes dominant when it is amplified by the first LNA. After acquiring the $F_{\min}(\nu)$ from the ADS model, we refit the remaining three noise parameters with the lab measured $F_n(\nu)$ for each of the $\Gamma_{\text{src}}(\nu)$ from the input test set. The MCMC results for both polarization are shown in Figure 4.24.

Similar to the gain calibration procedure, we characterize the noise temperature of the system using the network-based noise parameters. In combination with lab measurement of

[7] For a multistage amplification, the total noise factor $F_{\text{total}} = F_1 + \frac{F_2-1}{G_1} + \frac{F_3-1}{G_1 G_2} + \cdots$, where F_i and G_i are the noise factor and gain for each corresponding stage.

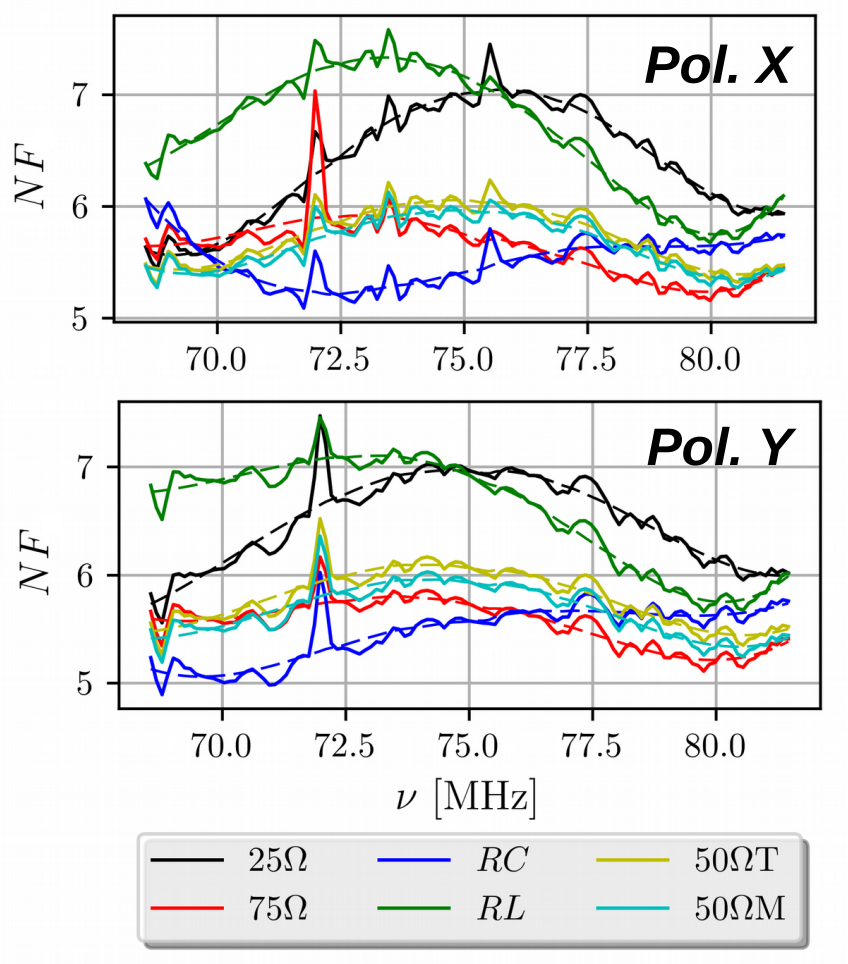

Figure 4.23: The noise figures for polarization X (upper panel) and Y (lower panel) of the CTP system (except the sleeved antenna) measured for different input impedance modules, including 25Ω, 50Ω, 75, RC, and RL loads (solid). Two types of 50Ω load are used for the comparison test and there is a slight difference between the SMA terminal type (50ΩT, yellow) and surface mount type (50M, cyan). The best fit values of these NF are superimposed (dashed). These NF are used to help constraining the noise parameters of the CTP system.

the $F_n(\nu)$ for different input impedances and the ADS circuit modeling, these are the steps we have devised to estimate noise temperature of the CTP during observation:

(1) For each of the input impedance test source, measure the noise factor $F_n(\nu)$ of the CTP FE system in the lab with the Signatec ADC,

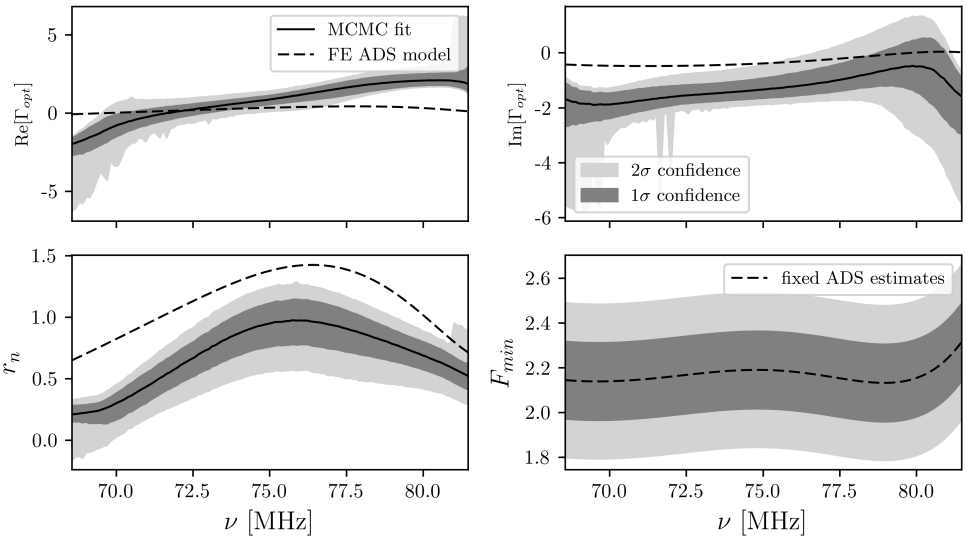

Figure 4.24: MCMC fit of the noise parameters based on the lab measured $F_n(\nu)$ and $\Gamma_{\rm src}(\nu)$, along with the ADS estimation of $F_{\rm min}(\nu)$ for the FE RF module. Since $F_{\rm min}(\nu$ is a free constant, the MCMC fit does not converge unless it is constrained. Normally, a tedious lab-measurement process is needed to accuracy determine $F_{\rm min}$. To the first order accuracy, we have utilize a network model to give us an estimate of the minimum noise temperature.

(2) Measure the reflection coefficient $\Gamma_{\rm src}(\nu)$ of each of input source with the VNA,

(3) Obtained the ADS model value for the $F_{\rm min}(\nu)$ for the FE RF module,

(4) Using `emcee` to best fit Eq. (4.9) for the three remaining noise parameters: Re $[\Gamma_{\rm opt}(\nu)]$, Im $[\Gamma_{\rm opt}(\nu)]$, and $r_n(\nu)$,

(5) Obtain the antenna reflection coefficient $\Gamma_{\rm ant}(\nu)$ for the sleeved dipole with the VNA,

(6) Substitute $\Gamma_{\rm ant}(\nu)$ as $\Gamma_{\rm src}(\nu)$ into Eq. (4.9) to solve the $F_n(\nu)$ for the observation using the noise parameters derived from step (4).

4.4 Summary

In this chapter, we have presented the technical and calibration details of the CTP experiment which is developed as a proof-of-concept instrument for the PIPE approach.

Derived from the experience with the bicone precursor, we have made four fundamental improvements on the CTP radiometer:

- In order to configure a ground-based observation to measure the projection-induced polarization from the foreground onto the antenna plane, the CTP is tilted such that the antenna's boresight is aligned to the NCP. By having a constant FOV about the NCP, this also reduces the diurnal variation from zenith pointing.

- To improve the circularity of the antenna beam for the sensitivity of measuring the PIPE, a sleeved dipole antenna with the addition of a conductive skirt is adopted for polarimetry. The improved antenna design provides a good match (with $|\Gamma_{\rm ant}(\nu| \leq -10$ dB) for 60-120 MHz, where one of the strongest absorption features of the global 21-cm signal is predicted to be present.

- To achieve gain calibration with a high dynamic range, a tone-tracking scheme is implemented in place of the on-off load switching. The temperature dependence of the FE electronics have been mitigated by the dual-stage thermal control system. By eliminating the switch, the impedance mismatch between input source impedances (antenna and 50 Ω load) is avoided. Furthermore, the strong tone provides a high S/N measurement of the gain variations $\Delta G_T(\nu, T)$ to calibrate the CTP's transducer gain with the help of the lab measured S-parameters as described in Section 4.3.1.

- Last but not least, to characterize the source of noise in the CTP instrument, instead of constraining the noise temperature $T_n(\nu)$, we adopted a network-based noise parameters approach to derive $T_n(\nu)$ for the observation directly from the measured antenna impedance. Since $T_n(\nu)$ is dependent on the input source impedance of the device, measuring the noise temperature from a reference calibrator or an NFA in the lab does not correct the frequency-dependent noise accurately. On the other hand, $\{F_{\rm min}(\nu),\ {\rm Re}\left[\Gamma_{\rm opt}(\nu)\right],\ {\rm Im}\left[\Gamma_{\rm opt}(\nu)\right],\ r_n(\nu)\}$ are intrinsic to the system's network, so

they provide a more reliable means to derive $T_n(\nu)$ for the appropriate $Z_{\text{ant}}(\nu)$ once the noise parameters are determined.

Analysis and evaluation for the preliminary data collected by the CTP during its short deployment are presented in the next chapter.

Chapter 5

CTP Data Reduction and System Evaluation

> "The first principle is that you must not fool yourself and you are the easiest person to fool."
>
> — Richard P. Feynman (1918-1988), physicist

In this chapter, we discuss data reduction and analysis procedures used to derive the Stokes measurement of the composite projection-induced polarization measured by the CTP. The data acquisition (DAQ) system is configured to satisfy multiple aspects of the system, such as data quality, requirements for implementing the tone-tracking calibration scheme, feasibility of managing the data on limited hardware, etc. We begin the chapter by describing the DAQ pipeline and how the data are processed to the final Stokes spectra used to constrain any potential twice-diurnal component from the projection induced polarization effect (PIPE). We conclude with an evaluation for the CTP by comparing its result to simulations through a series of statistical tests. This provides insights to address some of the major challenges discussed in the next chapter.

5.1 DAQ and Reduction Pipelines

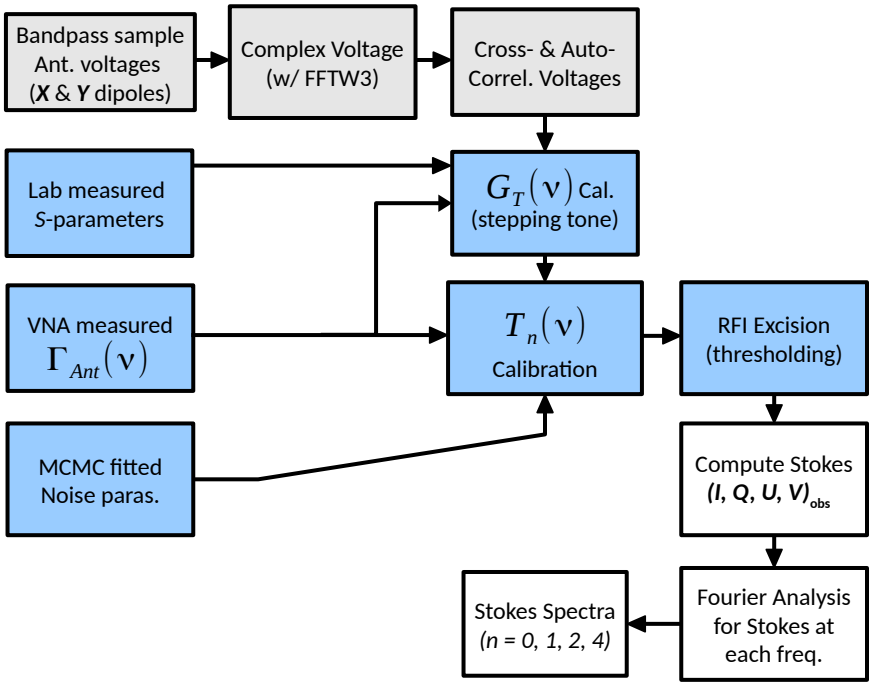

Figure 5.1: CTP data pipeline consists of three main phases. The DAQ pipeline samples and converts antenna voltages into correlated voltages as part of the (grey shaded). The reduction pipeline includes: 1) Calibrate transducer gain and noise temperatures for the correlated spectra along with excising RFI (blue), 2) Compute Stokes parameters and harmonic decomposition to construct the Stokes spectra, mainly for $n = \{0, 1, 2, 4\}$ (white).

The CTP also uses the 14-bit Signatec PX14400A FPGA-based digitizer mounted on a PC (PC1) to sample the antenna voltage data. For polarimetry, both of the digitizer's channels are used for polarization X and Y. Signals from both polarizations, after passing through the front-end (FE) system described in the last chapter, are sampled and stored on hard disk drives (HDDs) on PC1 before being transferred[1] to a second PC (PC2) for computing their fast Fourier transformation (FFT). The FFT decomposes the raw signal voltages into complex coefficients in the spectral space. Instead of saving the averaged total

[1] Due to the high sampling rate and the limited computational resource on PC1, it is impossible to sample the data and compute the FFT simultaneously on the same workstation. Hence, we resort to accumulating the raw data on PC1 and transfer them to PC2 via a local network before carrying out the FFT computation.

power for the signals as in the bicone experiment, their auto-correlation and cross-correlation are computed and averaged separately.

As illustrated in Figure 5.1, the averaged correlation data are stored on the data server for post processing. The data reduction process[2] begins with flagging and excising frequency channels corrupted by radio frequency interference (RFI) before calibrating the transducer gain (G_T) and noise temperature (T_n) for the auto-spectra and cross-spectra. Subsequently, the Stokes parameters are computed using these correlated spectra before applying the Fourier harmonic analysis to constrain the twice-diurnal component arising from the projection-induced polarization.

To compute the correlated spectra, complex sampling is needed to preserve the phase of the input signals from both polarizations. To do so, the real temporal antenna voltages from the X and Y dipoles at time stamp t_i, $V_X(N_t, t_i)$ and $V_Y(N_t, t_i)$, are Fourier transformed into the complex voltages, $\widetilde{V}_X(\nu, t_i)$ and $\widetilde{V}_Y(\nu, t_i)$, using the same FFTW3 software library as for the bicone system. Similar to the bicone system, to balance between preserving the signal power and suppressing spectral side lobes, a four-term Blackman-Harris (BH4) window function, $w_{\rm bh4}(N_t)$, is also used here to prevent spectral power leaking from one frequency channel to another when transforming a finite segment of time stream data of length N_t.

To balance between the accuracy in tracking the transducer gain drift and the minimal required integration time, the DAQ system is configured for the CTP's 65-85 MHz band by bandpass sampling[3] the signal at sampling rate f_s of 58.5 Ms/s. Similar to that described in Section 2.2.4, at each time stamp t_i, a timestream data burst of size $N_{\rm buff}$ is acquired by the digitizer. The data burst is then divided up into $N_{\rm FFT}$ segments, each has a data length of $N_{\rm 1seg} = N_t = 2N_{\rm chan}$. Each of the data segments are then Fourier transformed in to complex

[2] To accommodate for hardware drivers of the digitizer, the DAQ pipeline is written in C language. Meanwhile, the data reduction and analysis are carried out with Python.

[3] Opposite to oversampling, bandpass sampling allows a bandpass-filtered signal to be sampled at a rate lower than its Nyquist rate but still sufficient to reconstruct the signal. Bandpass sampling utilizes aliasing to record the signal image from the passband $[\nu_{\rm low}, \nu_{\rm up}]$ to baseband $[0, 3f_s/2]$. The ideal range of f_s for the given passband signal is $\left[\frac{2\nu_{\rm up}}{n}, \frac{2\nu_{\rm low}}{n-1}\right]$ where $1 \leq n \leq \frac{\nu_{\rm up}}{\nu_{\rm up}-\nu_{\rm low}}$.

values and averaged over $N_{\rm FFT}$ segments. Due to the data input/output capacity of PC1, the sample buffer size is set at,

$$N_{\rm buff} = N_{\rm FFT} \times N_{\rm 1seg} = N_{\rm FFT} \times (2N_{\rm chan}) = 2^{14} \times 1024 = 2^{24} \tag{5.1}$$

This produces a resolution bandwidth (RBW) of $\Delta\nu = f_s/N_t \approx 57.12$ kHz, and an integration time interval for each data burst of $\Delta\tau_{\rm int} = N_{\rm FFT}/(2\Delta\nu) \approx 0.143$ s for the complex $\widetilde{V}_X(\nu, t_i)$ and $\widetilde{V}_Y(\nu, t_i)$ with 512 channels. Due to overhead delay in the system when reading the frequency counts from the two general frequency counters with the general purpose interface bus (GPIB), the system can only acquired one data burst for every four seconds on average. This limits the DAQ efficiency to $\eta_s \approx (\Delta\tau_{\rm int}/4 \text{ s}) \times 100\% \ \approx 3.6\%$.

This efficiency seems low, but according to the radiometer equation, after correcting $\Delta G_T(\nu)$ and removing $T_n(\nu)$, to integrate the sky noise[4] of 2,722 K at 60 MHz to the minimal detectable temperature[5] of $\Delta T_{\rm min} = 50$ mK, the total integration time needed is,

$$\begin{aligned} \tau_{\rm int,total} &= \frac{1}{\eta_s}\left[\frac{T_{sys}(60 \text{ MHz})}{\Delta T_{\rm min}(60 \text{ MHz})\sqrt{\Delta\nu}}\right]^2 \\ &= \frac{1}{3.6\%}\left(\frac{2.72\times10^6 \text{ mK}}{50 \text{ mK}\sqrt{57.12 \text{ kHz}}}\right)^2 \approx 16.70 \text{ days} \end{aligned} \tag{5.2}$$

In principle, to reach a sensitivity of 50 mK at 60 MHz, it takes less than about two weeks of continuous observation even operating at the limit capacity of the CTP's DAQ system.

For a continuous observation session, the total raw complex voltage data being stored on the local HDD on PC1 is about 1.4 TB per day. With the limited HDD space for the available system ($\sim$ 9 TB) and the slow data transfer rate ($\sim$ 10 MB/s) between PC1 and PC2 on the Ethernet link, the system's disk capacity can only accumulate and process the raw data for two weeks continuously. A new observation session does not start until the disks

[4] Extrapolated from the foreground power law in Eq. (3.15) with $\alpha = 2.47$ and $T_{150} = 283.2$ K.

[5] The average magnitude of models for the global 21-cm signal $\delta T_{\rm b,21cm}(\nu)$ ranges between 10-100 mK. The statistical significant level to confirm a 3σ detection for the 21-cm signal should technically be at least an order of magnitude lower, i.e., 10^{-2}-10^{-1} mK. However, since the CTP only targets the foreground spectrum, it is sufficient to relax the sensitivity requirement to the detectable level of the twice-diurnal harmonics. Hence, by comparing the magnitude of harmonics in the simulation to the expected noise value, 50 mK is a sensible sensitivity limit to choose for analysis.

are cleared. We acknowledge that such data flow is not the most efficient, yet it provides a sufficient system for prototyping. The reduced correlation spectra and metadata are then transferred to a local server for long-term storage with a Wifi local access data link system, which consists of an internet modem and a Yagi antenna tuned at 2.4 GHz. The data management along with the datalink setup are shown in Figure 5.2. The DAQ configuration parameters for the CTP system is also summarized in Table 5.1.

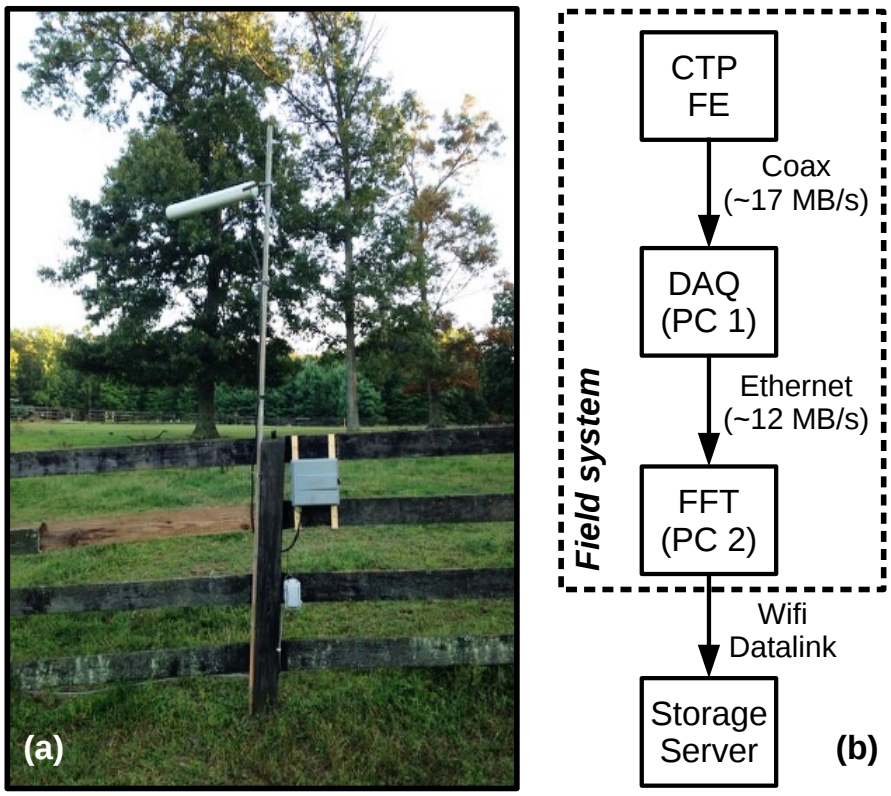

Figure 5.2: CTP's data management: (a) The Wifi datalink system consisting of a modem and a Yagi antenna tuned at 2.4 GHz provides an access point between the field system and the indoor server. (b) Block diagram for the CTP data management.

Table 5.1: Summary of the CTP data pipeline parameters.

Effective passband	B_{eff}	65-85 MHz
Sampling frequency	f_s	58.5 MHz
Sampling buffer size per scan	N_{buff}	2^{24}
Number of FFT segments averaged per scan	N_{FFT}	2^{14}
Number of spectral channel	N_{chan}	512
Resolution bandwidth (RBW)	$\Delta\nu$	57.12 kHz
Integration interval	$\Delta\tau_{\text{int}}$	0.143 s
Sampling efficiency	η_s	3.6%
Raw voltage data size (per day)		1.4 TB
Reduced correlation data size (per day)		337 MB

5.2 Data Products

5.2.1 Correlation Spectra and Stokes Parameters

To calculate the Stokes vector $\mathbf{S}_{\text{obs}} = (I, Q, U, V)_{\text{obs}}$ for the net projection-induced polarization of the foreground onto the antenna plane, we need to compute the complex auto-correlation and cross-correlation of the sampled voltage from both polarizations. This is typically written in terms of coherency matrix $\mathbf{C}(\nu, t)$ as,

$$\mathbf{C}(\nu,t) = \begin{pmatrix} \langle \widetilde{V}_X \widetilde{V}_X^* \rangle & \langle \widetilde{V}_X \widetilde{V}_Y^* \rangle \\ \langle \widetilde{V}_Y \widetilde{V}_X^* \rangle & \langle \widetilde{V}_Y \widetilde{V}_Y^* \rangle \end{pmatrix}_{\nu,t} \tag{5.3}$$

Using Ergodic theory, the brackets can be estimated as ensemble average of the products of the complex voltages and their complex conjugates. These quantities subsequently are converted to temperature units representing the antenna temperature $T_{\text{ant}}(\nu)$ for the sky signal, after $G_T(\nu)$ and $T_n(\nu)$ of the CTP system are corrected.

As described in the previous chapter, the calibration procedures for the CTP's $G_T(\nu)$ and $T_n(\nu)$ are formulated based on two sets of network-based parameters, i.e., S-parameters $\Big\{S_{11}(\nu),\ S_{12}(\nu),\ S_{21}(\nu),\ S_{22}(\nu)\Big\}$ and noise parameters $\Big\{F_{\text{min}}(\nu),\ \text{Re}\left[\Gamma_{\text{opt}}(\nu)\right],\ \text{Im}\left[\Gamma_{\text{opt}}(\nu)\right],\ r_n(\nu)\Big\}$ respectively. Unlike $G_T(\nu)$ and $T_n(\nu)$, these two sets of parameters are intrinsic to the two-port system itself and independent of the impedance of the input source $\Gamma_{\text{src}}(\nu)$, and

output load $\Gamma_{\rm load}(\nu)$ as in Eq. (4.7) and (4.9). Hence, it is more feasible to measure them directly under a controlled environment in the laboratory before applying them to correct the field observation, by simply substituting $\Gamma_{\rm src}(\nu)$ with the VNA measurement of the antenna reflection coefficient $\Gamma_{\rm ant}(\nu)$ for the input source.

We first calibrate $G_T(\nu, t)$ with the tone-tracking procedure described in Section 4.3.1. We choose an initial time stamp t_0, after ensuring the system has been in equilibrium by checking the temperature sensors readouts, so that a temperature reading at T_0 is used as the reference point for correcting the subsequent gain variations. We calculate the $G_T(\nu, T_0)$ at T_0, then use the recorded tone power from the frequency counters and the measured valued in the auto-spectra, combining with the VNA measurement of $\Gamma_{\rm ant}(\nu)$, to correct for the gain drift as,

$$G_T(\nu, T_i) = G_T(\nu, T_0) + \Delta G_T(\nu, T_i) \tag{5.4}$$

where $\Delta G_T(\nu, T_i)$ is derived based on the count difference between the two different tone-stepping levels as in Eq. (4.4). Its value can be negative or positive relative to the reference $G_T(\nu, T_0)$ depending on the direction of the drift, and recalling that that time stamp t_i and temperature T_i are interchangeable. This gain calibration is applied separately for each of the X and Y polarizations since the frequency responses of their signal paths are slightly different.

With the set of noise parameters, extracted from the MCMC fitting using the lab measurements as described in Section 4.3.2, and the field-measured $\Gamma_{ant}(\nu)$, $T_n(\nu)$ of the FE system during observation is derived. Although the noise temperature is also a function of temperature as the transducer gain, it is a bit more complicated to keep track of the temperature dependence of the noise parameters without a proper ADS (Advanced Design Software) model for the FE electronics. Since the change in $T_n(\nu)$ is less significant than the gain change in terms of relative magnitude between sky noise and receiver noise, we assume $T_n(\nu)$ to be constant for both polarizations during the observation, with a fixed uncertainty

based on the errors from the four extracted noise parameters from the MCMC algorithm.

After correcting for the gain drift in $G_T(\nu, t_i)$ and removing $T_n(\nu, t_i)$ of each polarization from the correlated spectra in the coherence matrix $\mathbf{C}(\nu, t_i)$, we arrive at a set of auto-correlated and cross-correlated antenna temperatures, $\Big\{T_{\mathrm{ant},XX}(\nu, t_i),\, T_{\mathrm{ant},YY}(\nu, t_i),\, T_{\mathrm{ant},XY}(\nu, t_i),\, T_{\mathrm{ant},YX}(\nu, t_i)\Big\}$. Details for converting the raw antenna voltage to these temperatures are provided in Appendix D. These antenna temperatures are used to compute the four Stokes parameters for the observed composite projection-induced polarization as,

$$\begin{aligned} I_{\mathrm{obs}}(\nu, t_i) &= T_{\mathrm{ant},XX} + T_{\mathrm{ant},YY} \\ &= \frac{1}{k_B \Delta\nu}\left[\left(\frac{\langle \widetilde{V}_X \widetilde{V}_X^* \rangle}{G_{T,X}} + \frac{\langle \widetilde{V}_Y \widetilde{V}_Y^* \rangle}{G_{T,Y}}\right) - (T_{n,X} + T_{n,Y})\right], \end{aligned} \tag{5.5}$$

$$\begin{aligned} Q_{\mathrm{obs}}(\nu, t_i) &= T_{\mathrm{ant},XX} - T_{\mathrm{ant},YY} \\ &= \frac{1}{k_B \Delta\nu}\left[\left(\frac{\langle \widetilde{V}_X \widetilde{V}_X^* \rangle}{G_{T,X}} - \frac{\langle \widetilde{V}_Y \widetilde{V}_Y^* \rangle}{G_{T,Y}}\right) - (T_{n,X} - T_{n,Y})\right], \end{aligned} \tag{5.6}$$

$$U_{\mathrm{obs}}(\nu, t_i) = T_{\mathrm{ant},XY} + T_{\mathrm{ant},YX} = \frac{2}{k_B \Delta\nu} \frac{\mathrm{Re}\left(\langle \widetilde{V}_X \widetilde{V}_Y^* \rangle\right)}{\sqrt{G_{T,X} G_{T,Y}}}, \tag{5.7}$$

$$V_{\mathrm{obs}}(\nu, t_i) = j(T_{\mathrm{ant},XY} - T_{\mathrm{ant},YX}) = \frac{-2}{k_B \Delta\nu} \frac{\mathrm{Im}\left(\langle \widetilde{V}_X \widetilde{V}_Y^* \rangle\right)}{\sqrt{G_{T,X} G_{T,Y}}}, \tag{5.8}$$

where $j = \sqrt{-1}$. The details of the derivation, under the assumption that some of cross terms between two polarizations are negligible, are also provided in Appendix D.

Before the correlated antenna temperatures are converted to Stokes parameters, we remove data channels that are flagged to have been corrupted by RFI. For the bicone system, a kurtosis-based figure of merit (FOM), the spectral kurtosis estimator $\widehat{SK}$ (Nita and Gary, 2010), was used for excising RFI in the averaged total-power spectrum. If the distribution of the sampled power of a certain channel within the short interval deviates from a Gaussian distribution, $\widehat{SK}(\nu)$ of that distribution can be used to discriminate whether it is corrupted by RFI. However, since the correlated temperatures are computed with the complex voltages $\widetilde{V}(\nu, t_i)$, a different RFI excision FOM is needed.

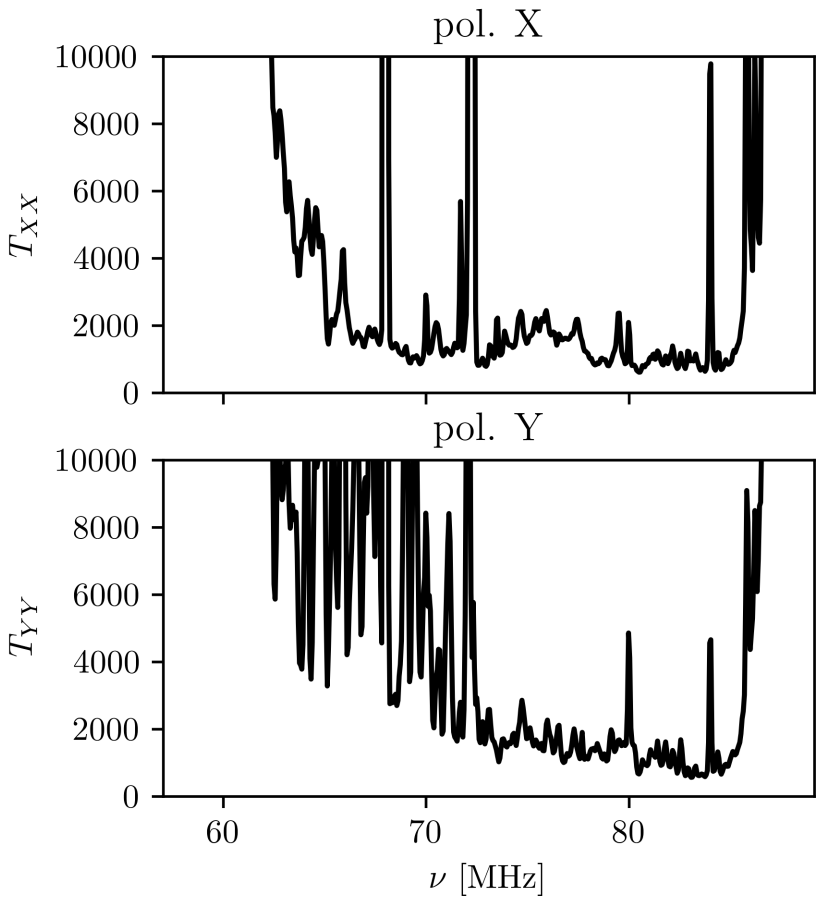

Figure 5.3: An example of the calibrated spectra for $T_{\mathrm{ant},XX}$ and $T_{\mathrm{ant},YY}$ before RFI excision. This shows that the RFI on the dipole Y (horizontal to the ground) is stronger than dipole X, which suggests the RFI can be polarized. However, this is not complete show stopper as discussed in Section 5.3.3.

There are several FOMs that are designed to screen RFI for complex samples, such as the complex signal kurtosis (CSK) designed to improve the sensitivity in detecting RFI in complex signals (Bradley et al., 2015; Schoenwald et al., 2016). However, for these FOMs to work, they need to be computed with the raw complex voltages in real time before the data are averaged and stored in HDDs. Since computing the CSK in real time would significantly compromise the DAQ sampling efficiency and thus the sensitivity of the CTP, we have resorted to using a basic thresholding method and flagging channels with power greater than a given thresholding value from the mean. The mean value is estimated by averaging the

power at a given frequency over a short interval of 5-10 minutes. We set the threshold to be two standard deviations from the samples averaged within that 5-10 minute interval.

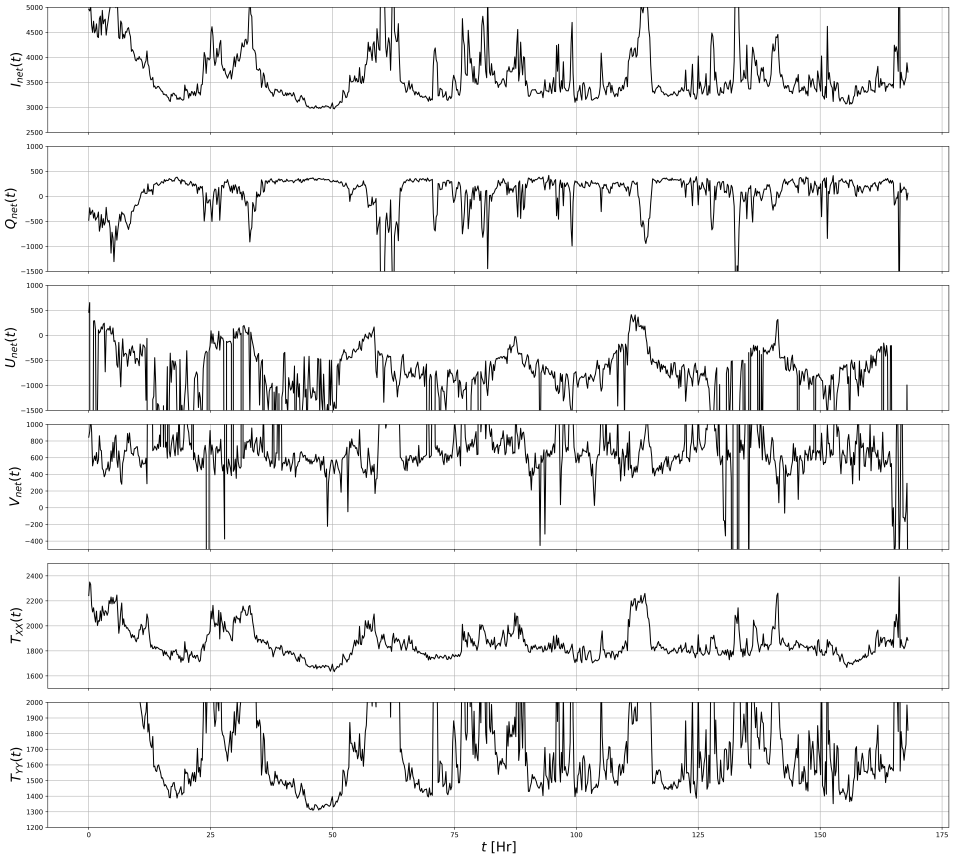

Figure 5.4: Stokes parameters at 81.98 MHz after being concatenated for 7 consecutive days, from Nov 27$^{\text{th}}$ to Dec 4$^{\text{th}}$, 2017. The strong diurnal component in the waveform corresponds to the Galaxy being the strongest when its is above the horizon.

It is clear from Figure 5.3 that the data are heavily contaminated by the RFI. Nonetheless, with the best attempt, we have managed to extract few frequency channels of the calibrated Stokes parameters with the least corruption around 82 MHz for further harmonic analysis. As an example, after rudimentary RFI excision, the Stokes parameters and the auto-correlation of the antenna temperature at 81.98 MHz are plotted over the course of 7 consecutive days (from Nov 27$^{\text{th}}$ to Dec 4$^{\text{th}}$, 2017) from our best observation run[6] in

[6] After deployment, we had three observation sessions in Fall 2017. Due to technical problems and trouble

Figure 5.4.

5.2.2 Stokes Harmonic Analysis and Stokes Spectra

After applying the RFI excision and choosing the channels that are least corrupted, harmonic decomposition is applied to the Stokes parameters in these channels. As suggested by the PIPE simulation as described in Section 3.5, the twice-diurnal ($n = 2$) components in the waveforms of Stokes $Q_{\rm obs}(\nu)$ and $V_{\rm obs}(\nu)$ are expected to have a period of 12 hours LST. The Fourier decomposition needs at least several cycles of the waveform to resolve the low-order harmonics ($n \leq 5$).The FFT is computed for the 10 consecutive days of the calibrated Stokes parameters to recover the low-order harmonics. For this procedure, we use the optimized Python script `numpy.fft.rfft` and another BH4 window function $w'_{\rm bh4}(t_i)$ to transform the real Stokes parameters into complex coefficients in the harmonic space. Using similar notations as in Section 3.4.3, the power spectral density (PSD) of the Stokes parameters can be written as,

$$S_I^\nu(f) = \left[\frac{4}{s_1^2}\left|\sum_{t_i=1}^{N} w'_{\rm bh4}(t_i) I_{\rm obs}(\nu,t_i) e^{-j2\pi f t_i}\right|^2\right]^{1/2} \tag{5.9}$$

$$S_Q^\nu(f) = \left[\frac{4}{s_1^2}\left|\sum_{t_i=1}^{N} w'_{\rm bh4}(t_i) Q_{\rm obs}(\nu,t_i) e^{-j2\pi f t_i}\right|^2\right]^{1/2} \tag{5.10}$$

$$S_U^\nu(f) = \left[\frac{4}{s_1^2}\left|\sum_{t_i=1}^{N} w'_{\rm bh4}(t_i) U_{\rm obs}(\nu,t_i) e^{-j2\pi f t_i}\right|^2\right]^{1/2} \tag{5.11}$$

$$S_V^\nu(f) = \left[\frac{4}{s_1^2}\left|\sum_{t_i=1}^{N} w'_{\rm bh4}(t_i) V_{\rm obs}(\nu,t_i) e^{-j2\pi f t_i}\right|^2\right]^{1/2} \tag{5.12}$$

where f is the dynamical frequency that is related to the harmonic order as, $n = 1/(fN\Delta t)$, Δt is the integration time interval for data, and N is the total number of data sample for all the concatenated days ($\sim 21,600$ data bursts per day, for 1 burst for every 4 s). The

shooting during the first two sessions, we have acquired a final batch of data for the evaluation presented in this chapter.

normalization factor for the window function is $s_1 = \sum_{t_i}^{N} w'_{\mathrm{bh4}}(t_i)$. There are two factors of 2 in the numerator. One is for converting the double-sided complex spectrum into single-sided real spectrum. The other factor of 2 is from the $\sqrt{2}$ for the RMS voltage. It is worthwhile to mention that this second FFT computation applied to the Stokes data are different from the initial FFT described in Section 5.1. The second FFT computes the harmonics of the Stokes parameters that have been averaged over N_{FFT} and calibrated for each time stamp t_i, whereas the first FFT converts the raw antenna voltage $V(N_t, t_i)$ to observed frequency space $\widetilde{V}(\nu, t_i)$. As an example, the derived harmonic decomposition for the Stokes parameters at 80 MHz is shown in Figure 5.5.

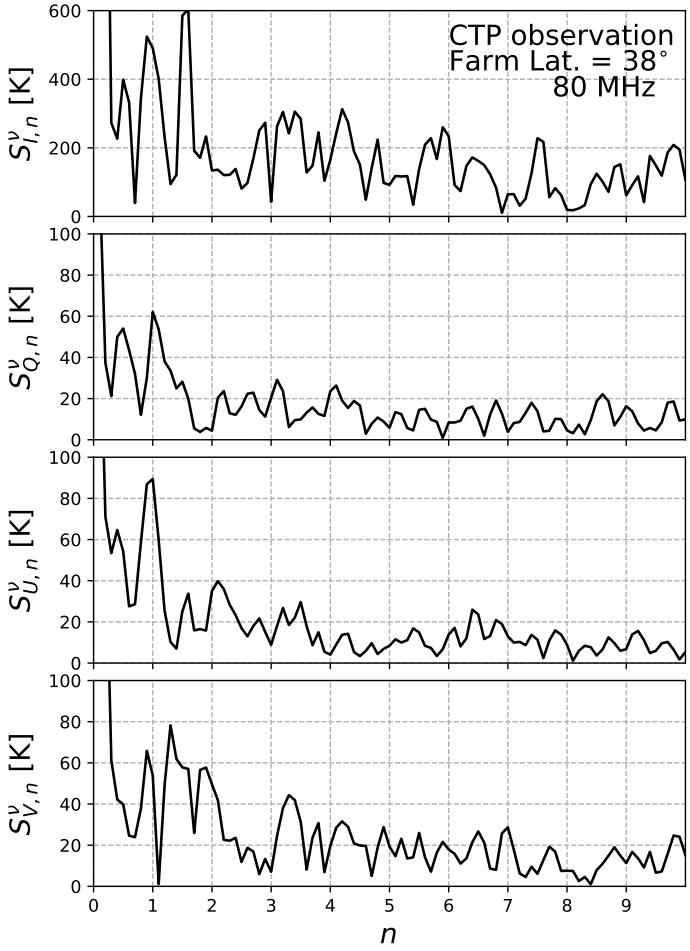

Figure 5.5: Stokes Harmonics for 80 MHz

5.3 Data Analysis and Interpretation

Our system has suffered from multiple challenges including ground distortions on the antenna beam, significant RFI, and horizon obstruction at our current latitude. Nonetheless, the development of the CTP, with a tight time schedule and limited resources, has provided valuable information on improving the system for the next generation of instrument. In this section, we use simulations for PIPE with more realistic beam models to help interpret the results from the CTP data.

5.3.1 Effects of Strong RFI and Intermodulation

Although we have designed our BPF (65-85 MHz) to minimize strong RFI from the local digital TV stations (62-64 MHz) and FM band (88-108 MHz) from entering the CTP, upon reviewing the raw power spectra from the X and Y polarizations in Figure 5.3, it is apparent that multiple channels have been corrupted by RFI. The data also indicate that the RFI is polarized since the RFI in dipole Y is stronger than dipole X as shown in Figure 5.3.

There are several possible sources of RFI contamination, primarily due to the north-pointing configuration and the site situating outside the radio-quiet zone. The CTP is pointing toward the north and thus is susceptible to air traffic telecommunication from the Dulles International Airport (IAD) and other transmissions from the Washington metropolitan area at about 100 miles northeast from the CTP as shown in Figure 4.1. There is also the possibility of self-generating RFI internally emitted by the instrument rack stored beneath the ground screen.

As a result, the strong RFI could have overdriven the FE electronics into the nonlinear regime causing intermodulation distortion (IMDs) across the band. For example, upon closer inspection, intermods can appear as the evenly spaced harmonic spikes in neighboring frequency channels, as shown in the waterfall plot of the correlated antenna temperatures between 80-85 MHz (Figure 5.6) and the corresponding Stokes parameters (Figure 5.7).

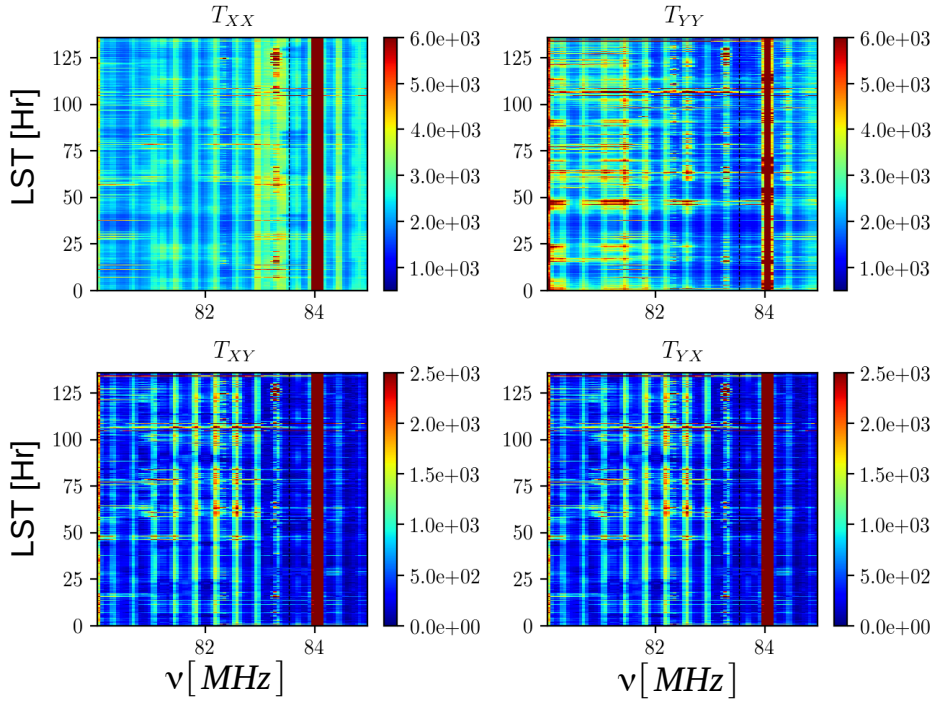

Figure 5.6: Waterfall plot of the correlated spectra over 80-85 mHz region of the CTP. Evenly spaced harmonics along the frequency axis over all time are possibly the intermodulation created by exposing the front end to strong RFI.

5.3.2 Ground Effects on Antenna Beam

In Section 3.6.4, we speculated that the antenna beam can be affected by simply tilting it toward the ground. From image theory, in the tilted configuration, besides the image-dipole produced behind the antenna's ground plane, the ground soil acts as a second reflection plane for a second image of the dipole. This second image-dipole acts as a second element for an interferometer and hence distorts the beams with fringes. In an attempt to mitigate some of this ground effect, we deployed the CTP on a shallow slope (about $-10°$ from horizon). Additionally, we have checked this by comparing the VNA measurements of $\Gamma_{\text{ant}}(\nu)$ for the sleeved dipole at zenith-pointing and NCP-pointing. As Figure 5.8 suggests, since the variations are small between tilting and laying the antenna parallel to the ground, we did not expect the antenna beam to be changed much.

Upon rerunning the CST simulations with a larger ground soil coverage under the sleeve

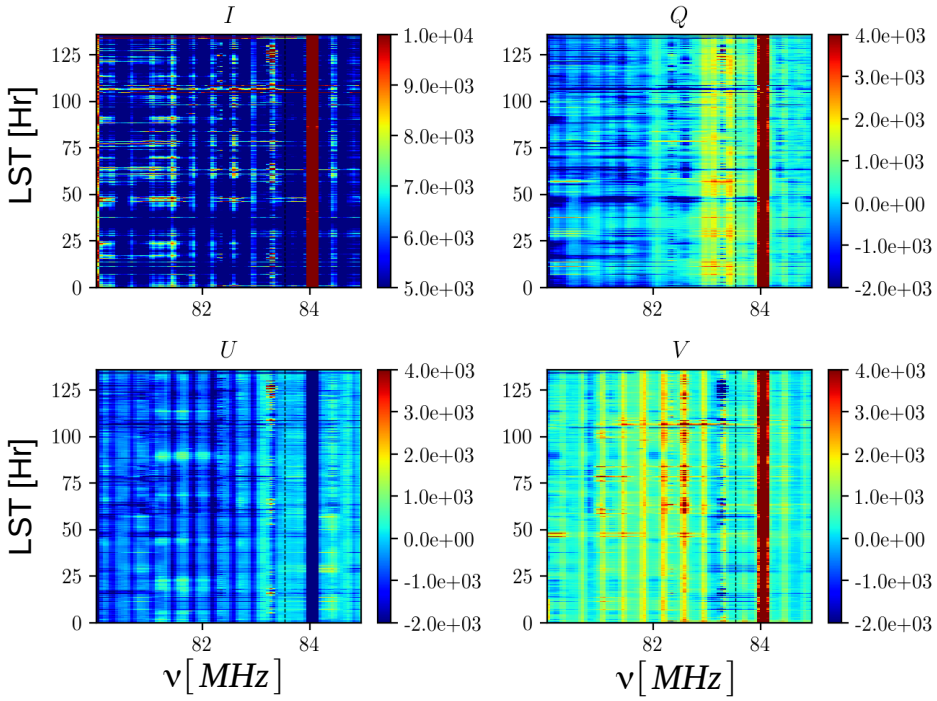

Figure 5.7: Waterfall plot of the calibrated Stokes parameters

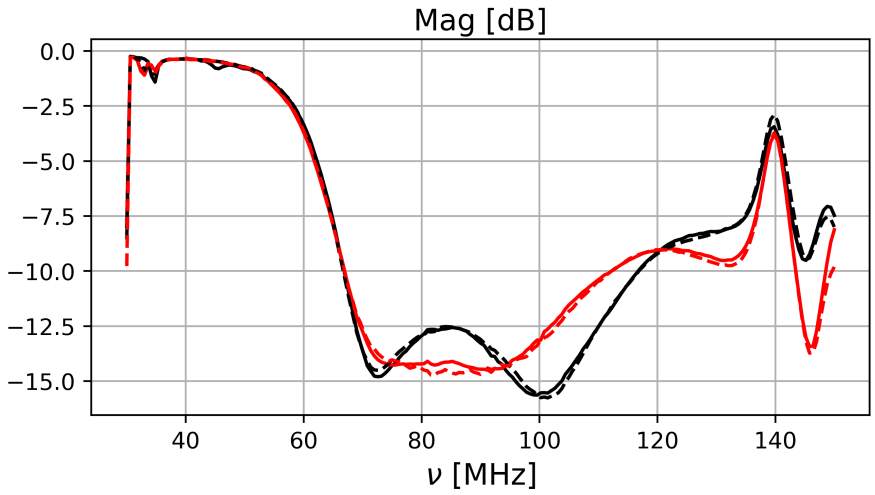

Figure 5.8: VNA measurement of the antenna reflection coefficients $\Gamma_{\text{ant}}(\nu)$ of the CTP sleeved dipole for polarization X (black) and Y (red). The double resonant features are apparent between 60 and 120 MHz. The $\Gamma_{\text{ant}}(\nu)$ are measured in both configurations for the sleeved antenna: zenith pointing (solid), and NCP pointing (dashed). The difference between the two polarizations is due to variations in the fabrication of the toroidal inductors used at the passive balun.

dipole and setting the antenna with tilting angle of $\delta_{\text{tilt}} = 90° - \text{Obs. Lat.} = 52°$, we have determined that the antenna beams are indeed corrupted by strong fringing structures. This is evidenced by comparing the E-plane ($\phi = 0°$) and the H-plane ($\phi = 90°$) of the zenith-pointing beam (Figure 5.9) to the tilted beam (Figure 5.10). In addition, due to different offset positions between two dipoles relative to the ground, the propagation path length for the reflect signal off the ground to each of the dipoles is not identical. This produces distinct fringing structures between the X (Figure 5.10) and Y (Figure 5.11) dipoles.

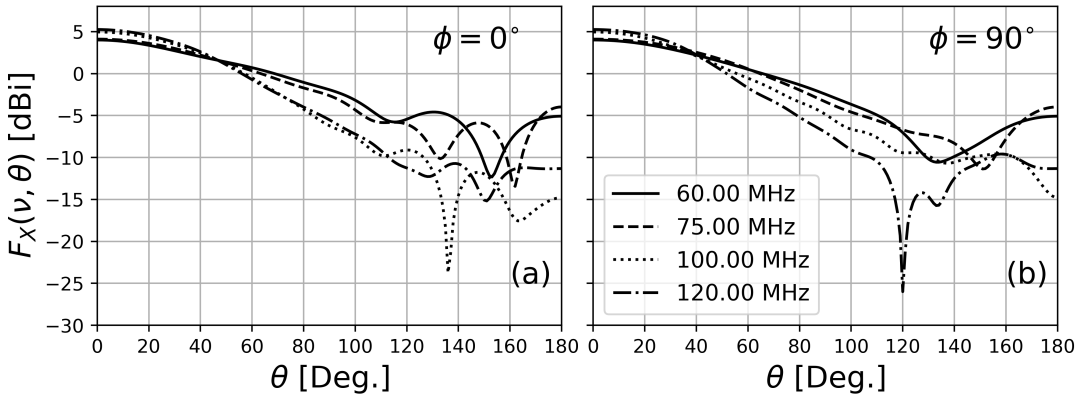

Figure 5.9: Angular plots for the CST beam of the sleeved dipole when the antenna is set at parallel to the ground. Hence the E-plane ($\phi = 0°$) and the H-plane ($\phi = 90°$) of the beams are smooth and symmetric. The chromaticity is apparent as the variations in the beam among different frequencies.

As before, the fringing structures that corrupts the tilting beam can be characterized by comparing the spatial gradient of the CST beam pattern respect to the frequency, $\partial_\nu F_X(\nu, \theta, \phi)$ for dipole X (Figure 5.12) and Y (Figure 5.13) to the non-tilting sleeved dipole beam from Figure 4.5, on the same colorbar scale with a range of ± 0.04 per MHz.

5.3.3 Twice-diurnal Component Validation

Based on the idealized PIPE simulation discussed in Chapter 3, which used a frequency-independent Gaussian beam and situated on the GNP, the $n = 0$ components represent the DC constant offsets of the waveforms in the Stokes parameters. In particular, $S_I^\nu(n = 0)$

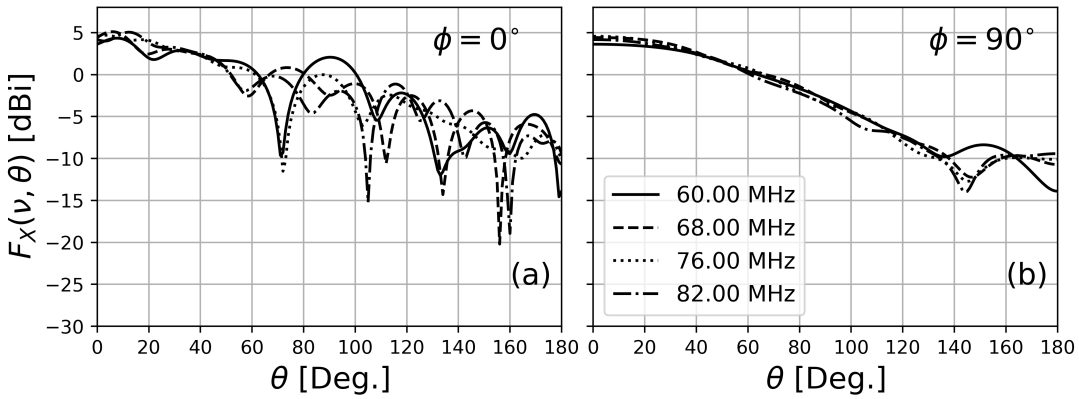

Figure 5.10: Angular plots for the CST beam of the sleeved dipole at polarization X when the antenna is tilted toward the NCP. As a result, the E-plane ($\phi = 0^\circ$) and the H-plane ($\phi = 90^\circ$) of the beam are corrupted with fringing structures due to the interferometric effect from interacting with the ground when the antena is tilted.

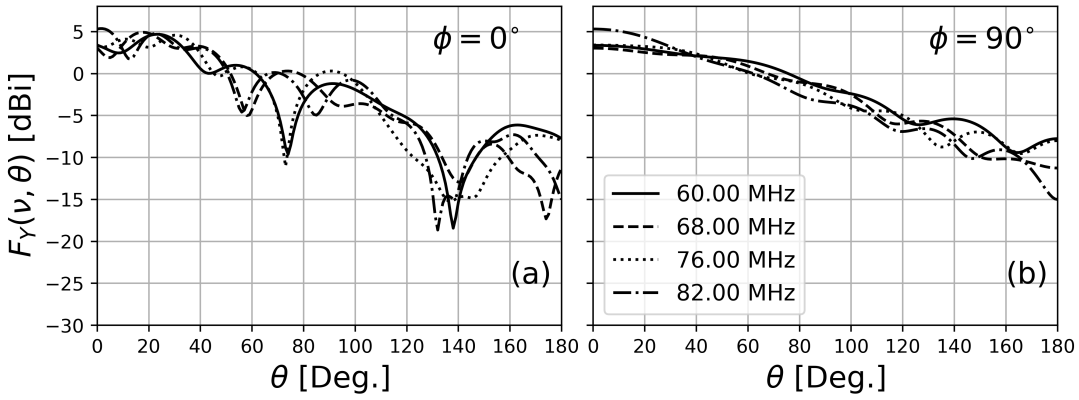

Figure 5.11: Similar to the previous plot, but for the polarization Y. Due the different path lengths the reflected signals have to travel to each of the dipoles, the fringing structures are different between the two polarizations.

is equivalent to the total intensity of the sky-averaged signal, hence containing in principle both the global 21-cm background $\delta T_{\mathrm{b,21cm}}(\nu)$ and foreground $T_{\mathrm{fg}}(\nu)$. Meanwhile, the diurnal component in Stokes I, $S_I^\nu(n = 1)$, results from the diurnal cycle of the foreground portion that rises and sets above the horizon once a day. However, this diurnal component is not necessarily a unique measure for the foreground spectrum since there are other systematics with diurnal characteristics in a real measurement. From our analysis, the twice-diurnal

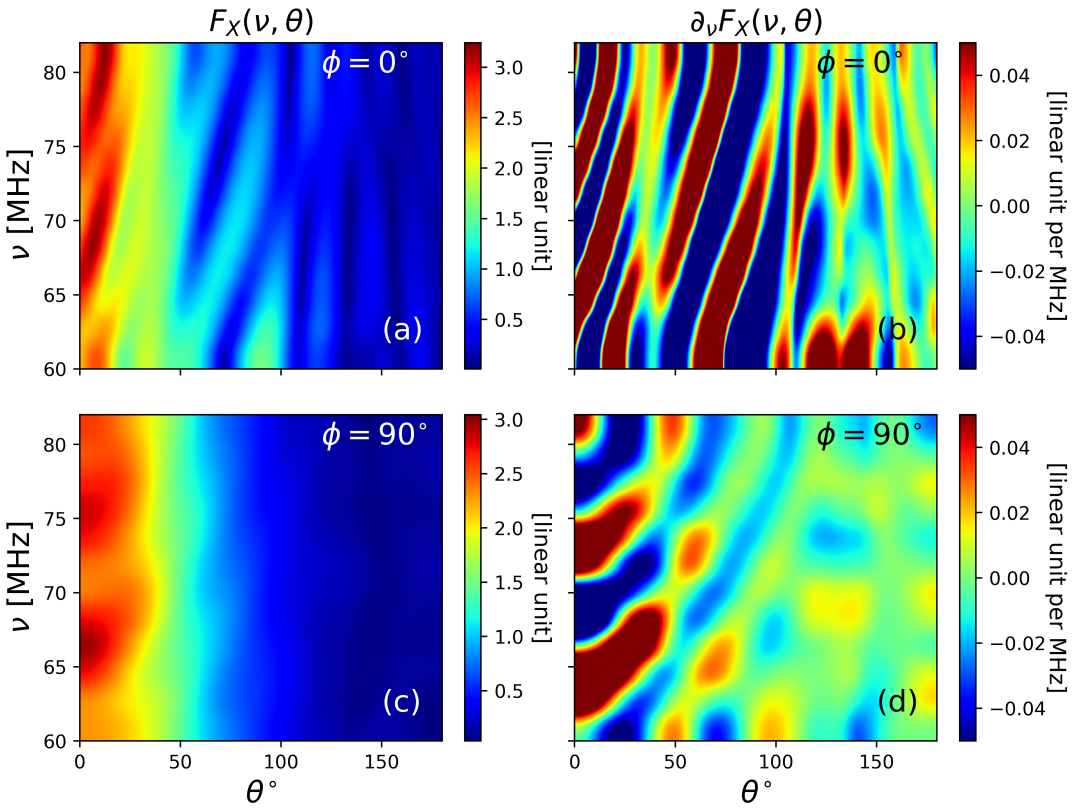

Figure 5.12: (Left) 2D plots of the E-plane ($\phi = 0°$) and the H-plane ($\phi = 90°$) for polarization X CST beam model, $F_X(\nu, \theta, \phi)$, of the sleeved dipole when tilted toward NCP. (Right) The 2D plots of the frequency gradient, $\partial_\nu F_X(\nu, \theta, \phi)$, of the beams on the left panels. The strong fringing structures due to interactions between the beam and ground are more apparent in the gradient plots.

signature from the PIPE, as measured in the Stokes spectra[7] $S^\nu_{Q,2}$ and $S^\nu_{U,2}$, is a more reliable representation for the foreground since it arises from the foreground portion observed continuously for the entire 24 hours LST by the design of the PIPE approach.

However, the harmonic decomposition of the Stokes $Q_{\rm obs}$ and $U_{\rm obs}$ derived from the CTP measurement (such as at 81.98 MHz in Figure 5.5) shows multiple low-order harmonics. Although the CTP results show that there exists an $S^\nu_{I,0}$ and $S^\nu_{I,1}$ terms as expected, there is no apparent signal at $S^\nu_{Q,2}$ term and a tentative detection of $S^\nu_{U,2}$. More importantly, the observation does not appear to contain the $S^\nu_{Q,2}$ and $S^\nu_{U,2}$ components as strong as predicted

[7] Recall the shorthand of $S^\nu_{i,n} = S^\nu_i(n)$, where i is the Stokes parameters, and n is the harmonic order.

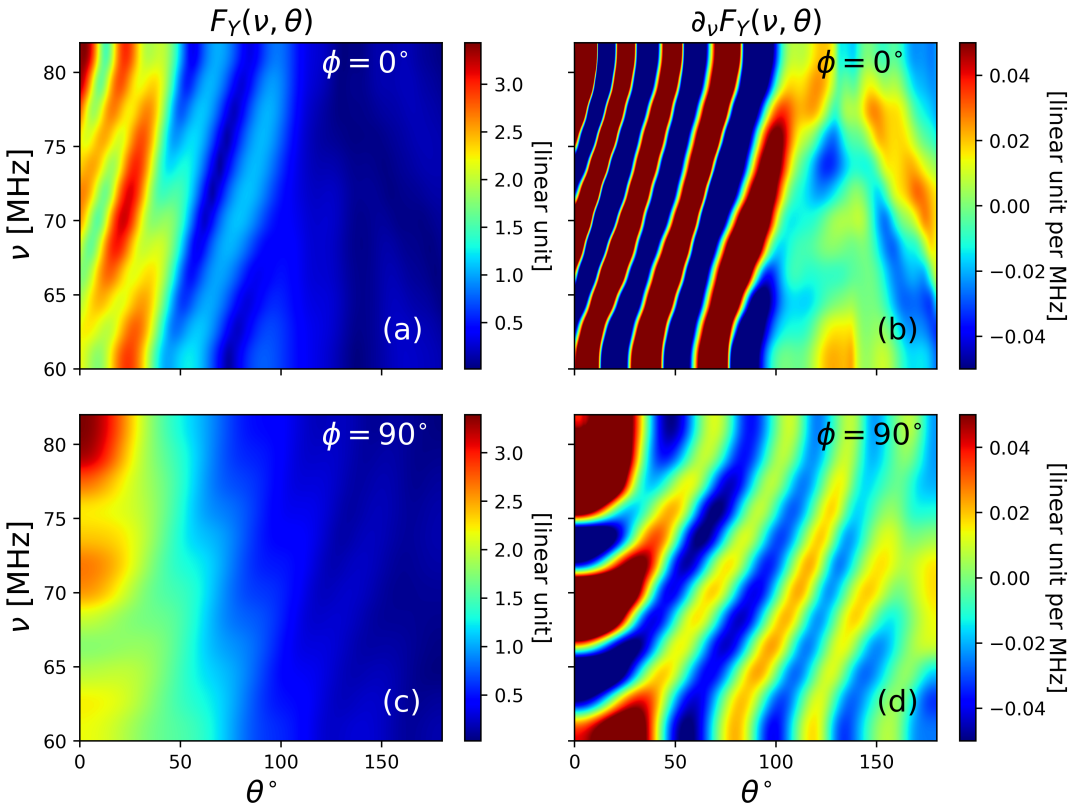

Figure 5.13: Similar plot as Figure 5.12, for the Y polarization. Note that the difference between the fringing structures of the two polarizations. This difference could have been caused the power offset between the two polarizations and compromises the phase coherency needed for polarimetry. Hence, it corrupts the waveforms of the Stokes parameters.

by the idealized PIPE simulation.

The first of these two discrepancies can be explained by the imbalance power measured by the X and Y polarization. Regardless of the gain and noise temperature calibration we have applied, the overall signal power observed by antenna Y is stronger relative to antenna X. This is most likely caused by distortion from the polarized RFI as discussed in Section 5.3.1 and the two beams being distorted differently. In principle, both polarizations should have received an equal amount for flux from the sky since any intrinsic polarization from the foreground synchrotron emission itself is expected to be small relative to the projection-induced polarization. As a result, the sum and difference of the auto-correlation T_{XX} and

T_{YY} produce offsets which can corrupt the temporal waveforms of Stokes $I_{\rm obs}$ and $Q_{\rm obs}$. On the other hand, these offsets are likely canceled out when computing the cross-correlation T_{XY} and T_{YX} for Stokes $U_{\rm obs}$ and $V_{\rm obs}$ because the extra power in the Y-polarization is distributed equally in the XY and YX terms. Hence, the measurement of $S_U^\nu(n)$ seems to be more reliable for further analysis.

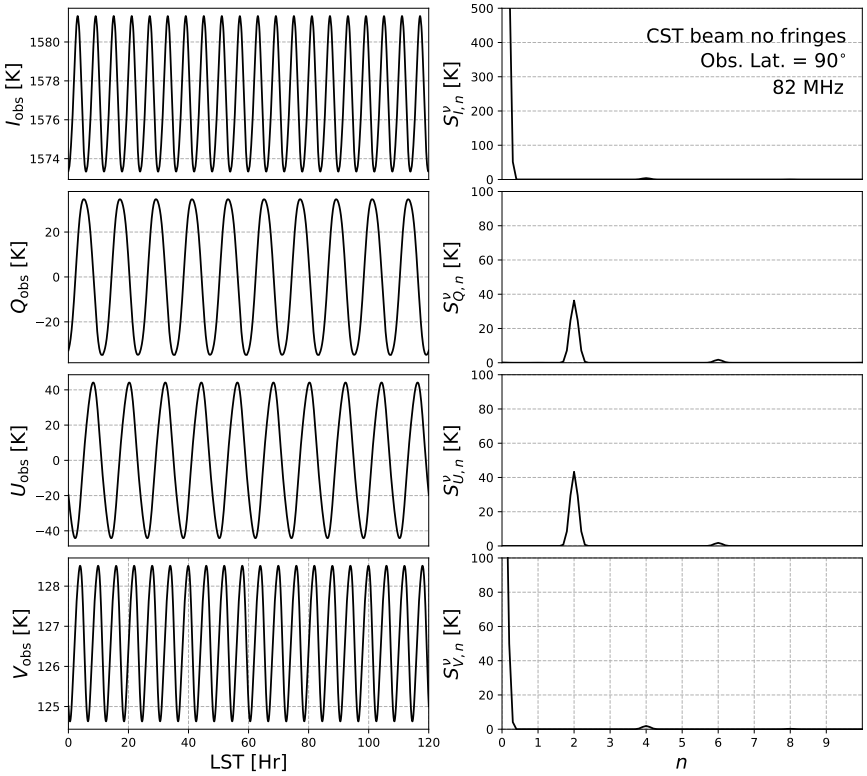

Figure 5.14: PIPE simulation result for idealized antenna beam at 82 MHz located at North Pole. (Left) Waveforms of the Stokes parameter for multiple days of observation. (Right) Harmonic decomposition for the corresponding Stokes parameters on the left, note the strong twice-diurnal ($n = 2$) component for Stokes $Q_{\rm obs}$ and $U_{\rm obs}$.

To qualitatively address the second discrepancy regarding the amplitude of the twice-diurnal components in Stokes $Q_{\rm obs}$ and $U_{\rm obs}$, we incorporate the realistic CST beams with the ground fringing effects into the our simulation. Furthermore, since the previous idealized simulation assumes the antenna is located in the Geographic North Pole (GNP), we also include a proper horizon obstruction for the latitude of the CTP at 38°. By assuming a

perfect system calibration, without any RFI and ionospheric corruption, the PIPE simulation produces the Stokes parameters with waveforms (Figure 5.15) that are quite different from the former ideal case (Figure 5.14).

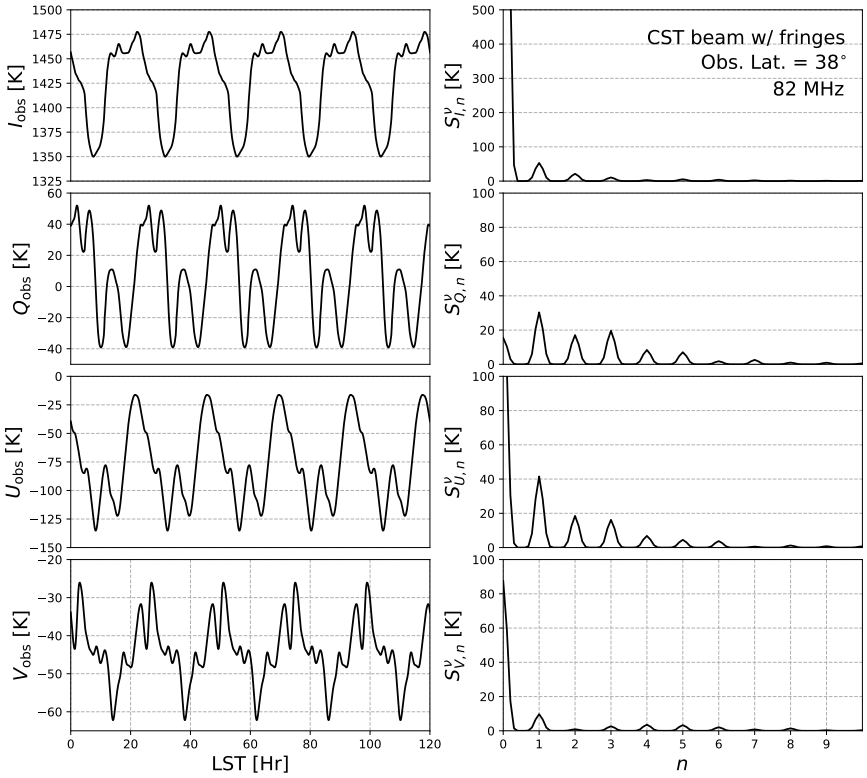

Figure 5.15: PIPE Simulation result for CST antenna beam at 82 MHz located at latitude of 38° which produces the horizon cutoff of the northern sky. (Left) Waveforms of the Stokes parameter for multiple days of observation, note that the beam fringing effects and horizon cutoff have corrupted the symmetric sinusoidal waveforms from the idealized case. Instead they impose discontinuities and high-order harmonics to the waveforms. (Right) Fourier decomposition of the corresponding Stokes parameters from the left, note the strong twice-diurnal components have been compromised by other high-order terms. This is more consistent to the CTP observation we have analyzed.

As discussed in Section 3.6.5, with the horizon present in the field of view (FOV) of the CTP, the observed foreground becomes two components. One of the foreground components above horizon along the beam's boresight is observed continuously 24 hours LST. Meanwhile, the second foreground component is the broader region of the foreground observed by the

outer edge of the beam which rises and sets every sidereal day. The latter part imposes a discontinuity onto the Stokes waveforms as it gives rise to the diurnal components as seen in the harmonic decomposition of the simulation results shown in Figure 5.15. This essentially corrupts the smooth sinusoidal waveforms from the idealized case. Additionally, because the antenna beams have been partially distorted by the ground when tilting the antenna, the fringing effects also compromised the phase coherency of the antenna beams to accurately measure the induced polarization. Consequently, the expected strong twice-diurnal components in Stokes $Q_{\rm obs}$ and $U_{\rm obs}$ have been diminished and corrupted by the high-order harmonics.The Stokes spectra from the same simulation is shown in Figure 5.16.

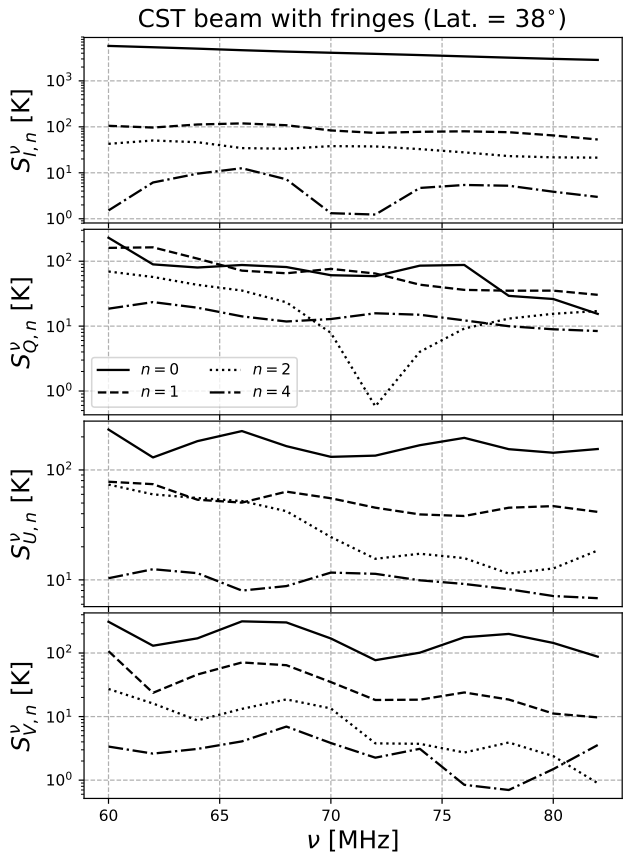

Figure 5.16: Stokes spectra for the PIPE simulation at 82 MHz using the corrupted CST beam and including horizon obstruction, for $n = \{0, 1, 2, 4\}$.

As noted above, the power offset between two polarizations have made Stokes $Q_{\rm obs}$ less reliable than $U_{\rm obs}$ for accessing the twice-diurnal component. Upon closer examination, there seems to be a harmonic at $S^{\nu}_{U,2}$. By computing the ratio of the magnitude of the $S^{\nu}_{U,2}$ relative to the noise floor of the $S^{\nu}_{U}(n)$, we arrive an S/N of 4.95 for the twice-diurnal component in Stokes U at 81.98 MHz. We define the noise floor in the PSD of Stokes U as the mean value of the spectral power of order n for $n \in [n_{\rm min}, n_{\rm max}]$, i.e., $\mu_i = \frac{1}{(n_{\rm max}-n_{\rm min})} \sum_{n=n_{\rm min}}^{n_{\rm max}} S^{\nu}_{i}(n)$, where $[n_{\rm min}, n_{\rm max}]$ are the range of components in $S^{\nu}_{U}(n)$ that only contain the noise of the PSD. Our simulation suggests that no significant harmonics are observed for $n \geq 10$, hence we have chosen $[n_{\rm min}, n_{\rm max}] = [10, 15]$.

Table 5.2: Harmonic ratio test for $S^{\nu}_{Q}(n)$ and $S^{\nu}_{U}(n)$ between observed data and simulation at 81.98 MHz.

Stokes PSD	n-ratio	Obs [$\pm$0.5]	Sim
$S^{\nu}_{Q}(n)$	1:2	9.58	1.77
	2:3	1.11	0.87
	2:4	1.51	2.03
$S^{\nu}_{U}(n)$	1:2	1.83	2.24
	2:3	3.21	1.14
	2:4	2.14	2.72

With such a S/N, we can confirm the detection of a harmonic as at $n = 2$ only at 81.98 MHz and few neighboring channels. Yet, we need to verify whether these harmonics created by the PIPE or other measurement artifacts. Hence we conduct two additional tests for the data. First we compare the relative magnitude ratios of between the low-order harmonics $n = \{0, 1, 2, 4\}$ in Stokes $Q_{\rm obs}$ and $U_{\rm obs}$ between the observation and the simulated result at 82 MHz, as shown in Figure 5.17. From the simulation, the ratio of $S_{U,1}/S_{U,2} \approx 2.24$. This is consistent with the ratio measured in the CTP data (1.83 ± 0.5) regardless of the difference in the scaling between the simulated and observation data. Meanwhile, the ratios $S_{U,2}/S_{U,3}$) are 1.14 (for simulation) and 3.21 ± 0.5 (for CTP data). A more complete power ratio between harmonics for both Stokes $Q_{\rm obs}$ and $U_{\rm obs}$ are listed in Table 5.2. By simply

checking the relative power of the harmonics at 81.98, it suggests that, at least for the first 4 harmonics, the relative powers from the measurement in Stokes $U_{\rm obs}$ are more consistent to our simulation than Stokes $Q_{\rm obs}$. This seems to be consistent to what we pointed out above that Stokes $Q_{\rm obs}$ is more corrupted than Stokes $U_{\rm obs}$ due to the imbalance RFI contamination between the two polarizations.

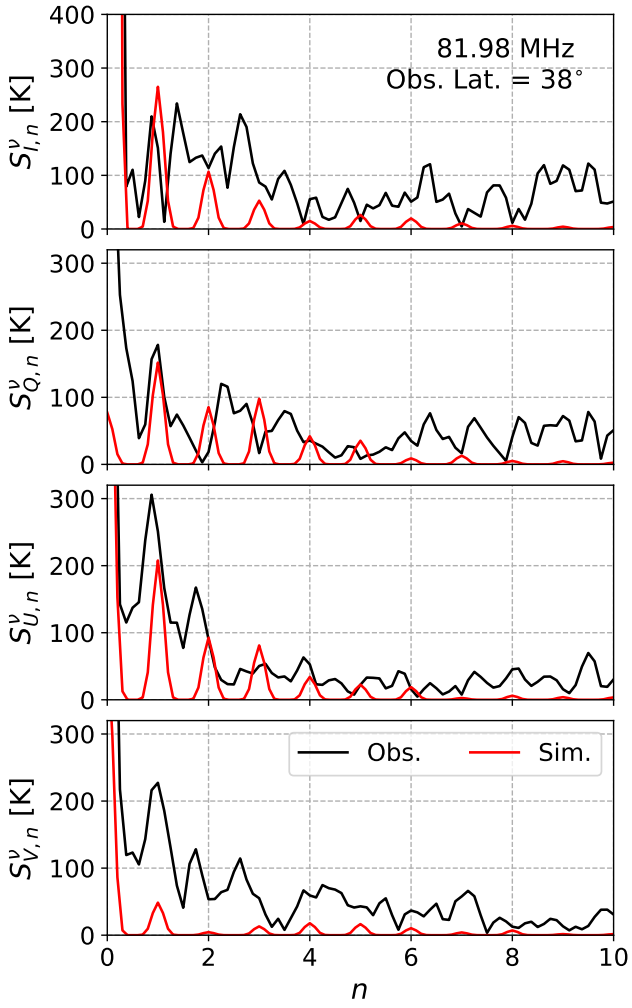

Figure 5.17: Comparison of the harmonic decomposition of the observed data (black) with the PIPE simulation (red) at 81.98 MHz.

We have also performed a consistency test among frequency channels, however due to the limited data and the present of the strong RFI, we can only confirm the a few neighboring channels of 81.98 MHz that exhibits similar result of power-ratio test. We are

unable to perform similar test for the lower end of our band due to the strong corruption in the polarization Y as seen in Figure 5.3. For completeness, although most of the channels have been corrupted by RFI, we superimpose the expected Stokes spectra on the observed data for $n = \{0, 1\}$ in Figure 5.18 and $n = \{2, 4\}$ in Figure 5.19. Since the observation have only passed two of the three tests, conservatively it is only a marginal detection for the PIPE. Further study and improvement are needed.

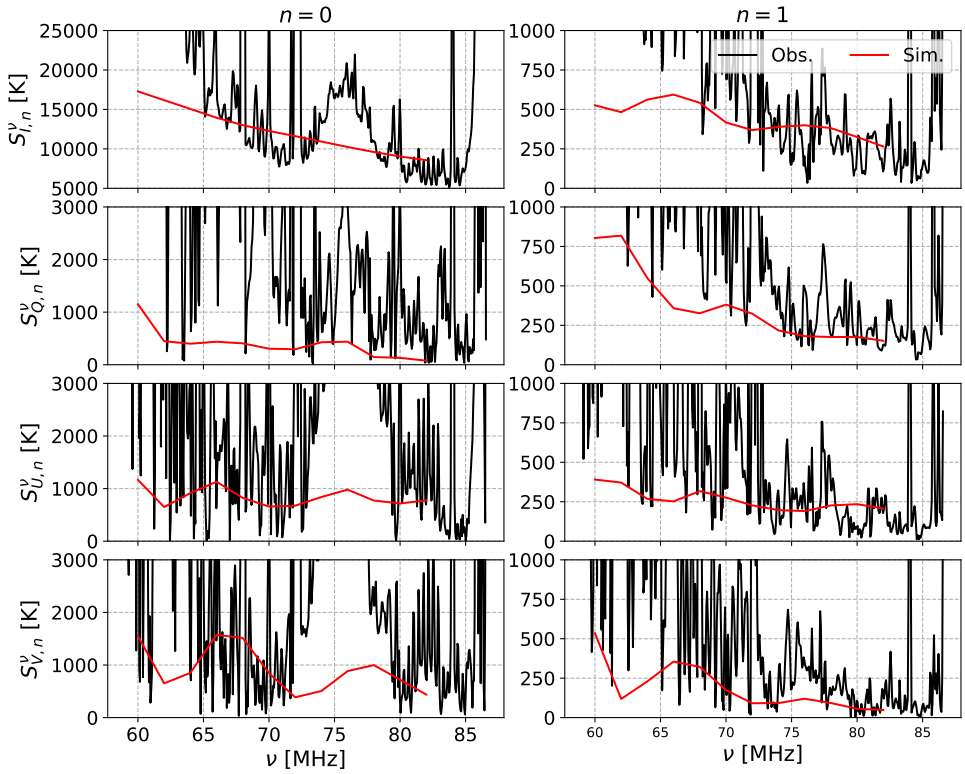

Figure 5.18: Comparison between observed Stokes spectra and simulation, for $n = 0$ (left) and 1 (right) at 81.98 MHz. Note the broadband RFI emission between 70-80 MHz.

5.3.4 Antenna Beam Pointing Error

Since the PIPE observation relies on centering the antenna at the NCP to measure the asymmetry in the foreground sources in terms of the twice-diurnal components in Stokes Q_{obs} and U_{obs}, the alignment of the antenna's boresight at the celestial pole determines the

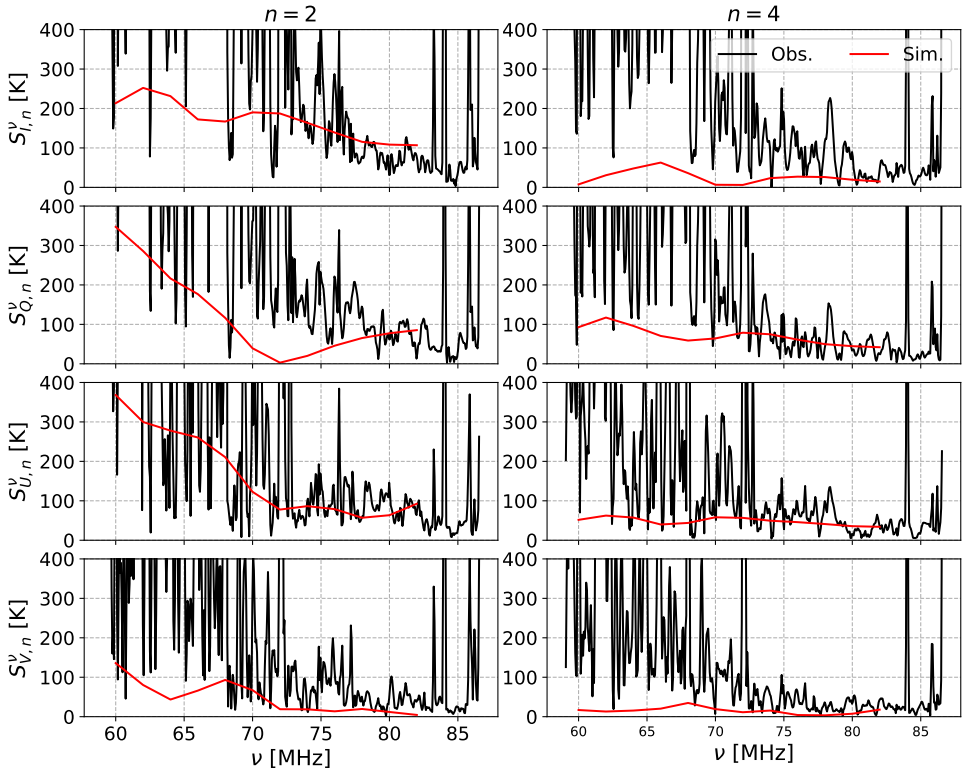

Figure 5.19: Comparison between observed Stokes spectra and simulation, for $n = 2$ (left) and 4 (right) at 81.98 MHz.

accuracy of the $n = 2$ terms. If the antenna beam is not concentric to the foreground region centered at the NCP, the detected waveforms for the net foreground polarization can appear to be "wobbling" about the boresight, as discussed in Section 3.6.6.

Although we have taken extreme care in aligning the CTP to the NCP during the deployment, to further quantify the effects of pointing error, we have simulated the PIPE for different off-boresight pointing angles. We compare simulation results of the Stokes spectra for $n = \{0, 1, 2, 4\}$ at different off-boresight angles in Figure 5.21, ranging from $-10°$ to $30°$ with $0°$ to be the perfect alignment with the NCP, negative angles when the antenna pointing approaches the horizon, and positive angles when the pointing approaches the zenith as illustrated in Figure 5.20.

According to simulation results of $S^{\nu}_{Q}(n)$ and $S^{\nu}_{U}(n)$ in Figure 5.21, within a range

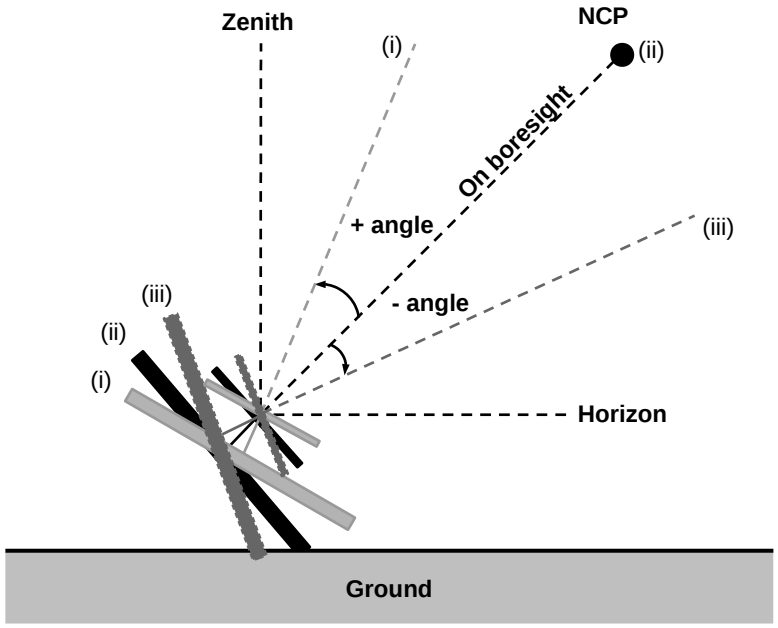

Figure 5.20: CTP simulation for different pointing angles relative to the NCP: (i) Positive off-boresight angle when the antenna pointing approaches to zenith, (ii) when boresight aligned to the NCP, and (iii) negative off-boresight angle when the antenna pointing approaches the horizon.

of $\pm 5^\circ$ about boresight, the $n = 1$ (dashed) and $n = 2$ (dotted) Stokes spectra are distinguishable. Meanwhile, as the antenna's off-boresight pointing angle approach zenith, the twice-diurnal curves blend in with the diurnal Stokes spectra. In another words, this analysis suggests that the antenna is still sensitive to the PIPE for pointing accuracy of within $\pm 5^\circ$. Since the Polaris has a declination (DEC) of $+89.25^\circ$, which is less than 1° off from the NCP (DEC = $+90^\circ$) in the equatorial coordinate system, our alignment procedure is justified.

5.4 Summary

In this chapter, we have presented the data products observed by the CTP prototype. According to our analysis from the data, we have concluded that the CTP has suffered primarily from three main technical challenges: 1) RFI from telecommunication transmission and self-generated interference by our instrument rack, 2) Beam corruptions due to the ground fringing effect, and 3) Horizon obstructions at a low latitude. In combination, these

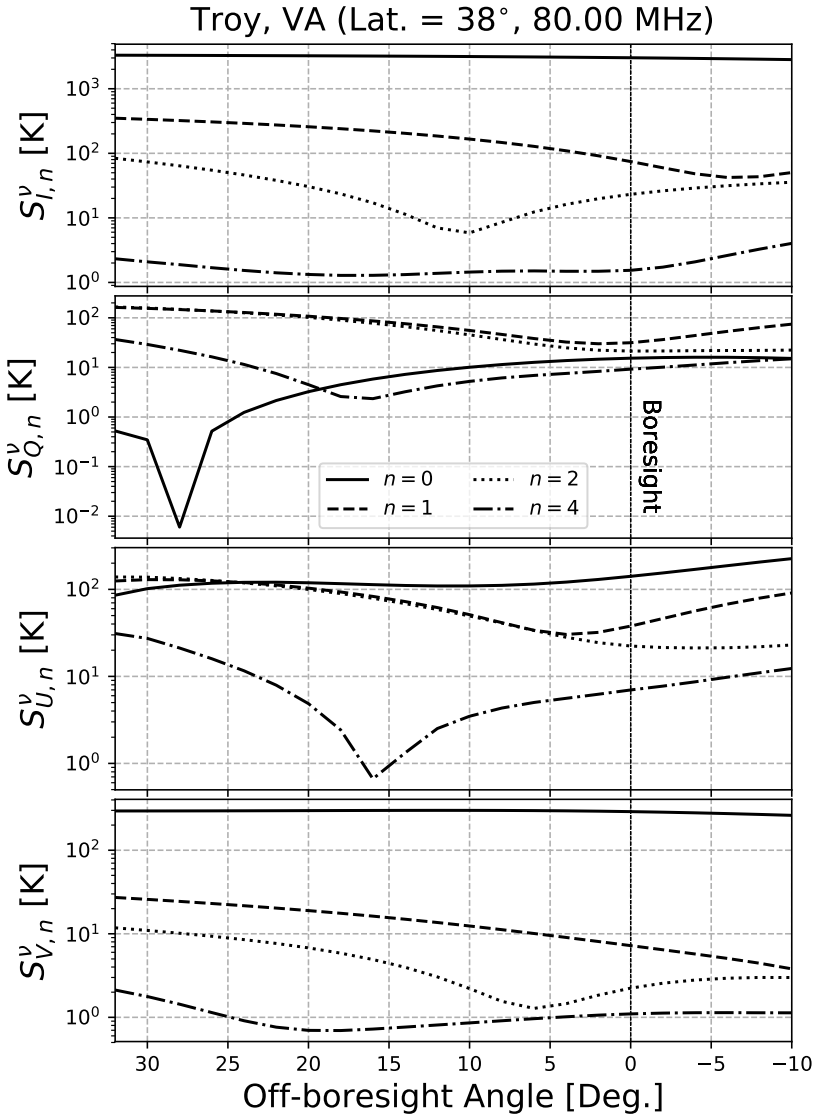

Figure 5.21: Simulation result for the PIPE as a function of off-boresight pointing angles using the idealized CST beam for the sleeved dipole at 82 MHz. The antenna is situated at the latitude of the Equinox Farm in Troy, VA at 38°. The $n = 2$ and $n = 1$ components become distinguishable within $\pm 5°$ about boresight indicating that using Polaris as our alignment for the NCP is sufficient.

effects have reduced the significance level of confirmation the PIPE effect to be marginal, primarily based on the assessment of the twice-diurnal harmonic components in the $S^{\nu}_{Q}(n)$ and $S^{\nu}_{U}(n)$.

Nonetheless, the deployment of the CTP prototype has provided valuable information

to improve the current instrumentation and observation techniques. In fact, preparation works and new strategies for the next generation of the CTP are underway and summarized in the next chapter.

- In Section 5.3.3, we obtain a S/N of 4.95 for the $S^{\nu}_{U,2}$ relative to the noise floor of the PSD, and comparing the harmonic ratios between the measurement and the semi-realistic simulation. However, without definitive consistency test across the band, especially for lower frequencies other than 81.98 MHz, we can only marginally confirm our detection of the twice-diurnal component due to the PIPE. Conservatively, we conclude that this result can be improved and confirm with the next deployment after we can address all the major systematics in the current CTP.

- The tilting antenna configuration relative to the flat ground has created an interferometric effect that severely corrupts the smooth antenna beams with fringes. As a result, this compromises the beam's phase coherency needed to measure the projection-induce polarization. This fringing effect can be mitigated by either placing the antenna on a slope or on top of a tall structure.

- The horizon cutoff of a local observer at latitude below the geographic poles obstructs the FOV of the CTP. This reduces the effective region of sky that can be continuously observed to produce the PIPE. The horizon causes part of the foreground region rise and set daily. This imposes diurnal component to the Stokes parameters and hence reducing the sensitivity of the twice-diurnal components of $S^{\nu}_{Q}(n)$ and $S^{\nu}_{U}(n)$. This can elevated by moving the instrument to a site with latitude closer to the poles.

- By reallocating the instrument to a radio-quiet site and repackaging our instrument rack, we are confident that most of the RFI can be suppressed.

- The temperature reading of the FE system has also shown that the stability for gain calibration is sufficient, except for few occasional abnormality due to large

temperature swing in field. A minor improvement on the thermal control system will be needed.

- Due to the suboptimal quality of the data, the system has not been sensitive to detect any major effects from ionospheric variations, and potential polarization leakage (both from the instrument and the intrinsic foreground). Since we have not been able to confirm the foreground spectrum across the band, we have not been able to analyze the effect of varying spectral index in the foreground as suggested in Section 3.6.8.

Chapter 6

Discussion and Future Works

> "However difficult life may seem, there is always something you can do, and succeed at. It matters that you don't just give up."
>
> — Stephen Hawking (1942-2018), cosmologist

In the last two chapters, instrumentation details and observation results for the CTP prototype were presented. Overall system evaluation in the last chapter has identified several major technical limitations on CTP's current instrument design and observational strategy. Although the data have been heavily corrupted by the RFI and the antenna beams distorted by ground effects, we were able to determine a marginal detection of the projection-induced polarization for the anisotropic foreground. With the help of the PIPE simulation, we have devised several improvements on the instrumentation and observation strategy to improve the feasibility of applying the PIPE approach to constrain the foreground in global 21-cm measurements. In this chapter, we discuss the feasibility of the PIPE approach in detecting the global 21-cm signal, as well as some of the aspects that can significantly improve the performance of the CTP in the near future.

6.1 Discussion

The primary objective of the PIPE approach is to develop a direct and model-independent means to constrain the spectrum of synchrotron emission from the Galactic and extragalactic foreground, $T_{\rm fg}(\nu)$. In the conventional global 21-cm approach, due to the expected smoothness of the foreground spectrum, it is parametrized in terms of a polynomial function before

being subtracted to recover the underlying global 21-cm spectrum, $\delta T_{\rm b,21cm}(\nu)$. One of the more commonly used functions is a polynomial in log-log space as mentioned in Chapter 1,

$$\log \widehat{T}_{\rm fg}(\nu) = \sum_{m=0}^{M>0} c_m \left(\log \nu\right)^m , \tag{6.1}$$

where $\widehat{T}_{\rm fg}(\nu)$ is the estimated foreground spectrum with polynomial coefficient c_m of order m up to some order $M > 0$. Previous studies have suggested that low-order fitting may be sufficient in characterizing the foreground spectrum for the global experiments (Bernardi et al., 2015). However, as pointed out in Section 1.3.2, the polynomial fit approach is insufficient unless the measured spectrum is free of instrumental distortions, especially beam chromaticity. In this section, we discuss inherent limitation on the PIPE approach for a ground-based instrument like CTP.

6.1.1 Beam Chromatic Effects on the PIPE's Accuracy

From the idealized PIPE simulation presented in Chapter 3, with a frequency-independent Gaussian beam, we have illustrated that the PIPE approach can indeed help to constrain the spectral shape of the foreground spectrum without presuming any parametrization or model. By centering the field of view (FOV) of the polarimeter at the North Celestial Pole (NCP), one can measure a net polarization originating from the projection of the anisotropic foreground on the antenna plane. Modulation of this net polarization gives rise a unique twice-diurnal periodic signature on the waveforms of the measured Stokes parameters, in particular the Stokes $Q_{\rm obs}$ and $U_{\rm obs}$. By measuring the magnitude of this second harmonic at each frequency channel, in principle the Stokes spectra[1] $S^{\nu}_{Q,2}$ and $S^{\nu}_{U,2}$ can trace out the exact spectral shape of the $T_{\rm fg}(\nu)$.

In practice, the observed Stokes spectra are also corrupted by the chromatic antenna beams which impose unwanted spectral structures on the Stokes spectra as in the conventional total-power spectrum. Correction for the beams' chromaticity is crucial, especially

[1] Recall the shorthand of $S^{\nu}_{i,n} = S^{\nu}_{i}(n)$, where i is the Stokes parameters, and n is the harmonic order.

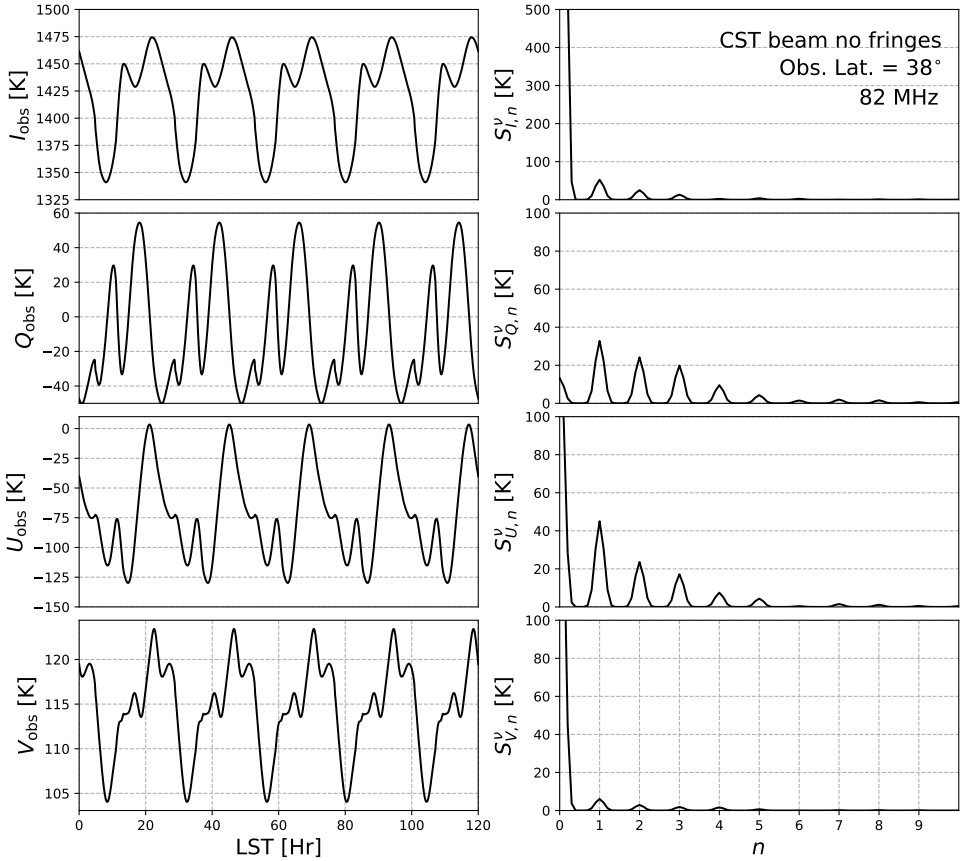

Figure 6.1: PIPE simulation result for CST antenna beam at 82 MHz located at NGP. By placing the antenna parallel to the ground soil, the fringing effects have been removed. As a result, many of the high-frequency structures are removed from the waveforms of the Stokes parameters on the left. However, due to horizon obstruction at low latitude (38°), the sensitivity of the twice-diurnal components in Stokes $Q_{\rm obs}$ and $U_{\rm obs}$ are diminished.

if the antenna beams do not have a smooth frequency response. By assuming the beam fringing distortion from the ground has been removed by placing the antenna on a slope or high off the ground, we simulate at the same latitude as the CPT prototype with the realistic CST beams for the ground-parallel sleeved dipole. The results for the beam at 82 MHz (We chose 82 MHz to be close to the clean channel we have observed for the ease of comparison) in Figure 6.1 suggests that the majority of the high-order structures on the waveforms of the Stokes parameters have disappeared because of the improvement in the beam. However, due to the low latitude, power of the twice-diurnal components in S^{ν}_{Q} and S^{ν}_{U} are still diminished

by the horizon obstruction.

This is apparent in the corresponding Stokes spectra for $n = \{0,\ 1,\ 2,\ 4\}$ that are plotted in Figure 6.2. $S^{\nu}_{Q,2}$ and $S^{\nu}_{U,2}$ (dotted curves) are weaker than the diurnal component (dashed curves). Similar to the scenario described in the previous chapter, although we have used an improved antenna beam, the horizon obstruction does play a dominant role in suppressing the twice-diurnal terms.

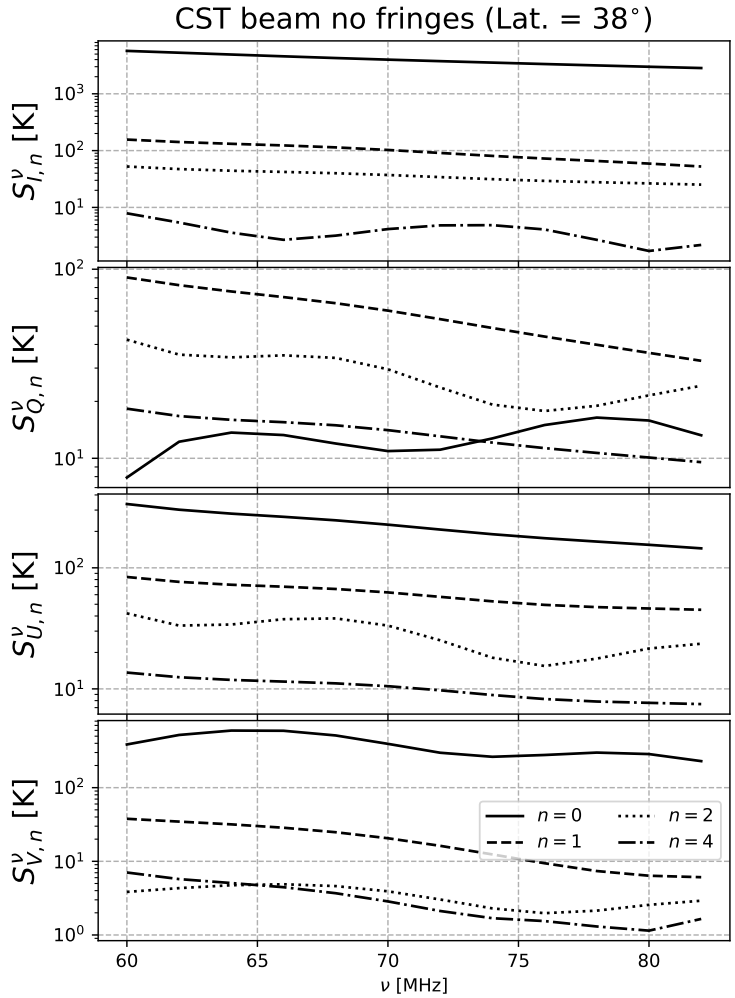

Figure 6.2: Simulated Stokes spectra for $n = \{0,\ 1,\ 2,\ 4\}$ from the ground-parallel sleeved dipole CST beams at latitude of 38°. Due to horizon obstruction, the twice-diurnal components ($n = 2$, dotted) in the Stokes spectra are diminished and the diurnal curves ($n = 1$, dashed) becomes dominant.

Therefore, we examine the accuracy of the PIPE approach in the best-case scenario

by removing the horizon obstruction in the simulation using the same ground-parallel CST beams. As the antenna is positioned at the North Geographic Pole (NGP), $S^{\nu}_{Q,2}$ and $S^{\nu}_{U,2}$ (dotted curves) in Figure 6.3 are dominant over other harmonics, including the $n = 1$ curves (dashed). This is consistent to the expected property of the PIPE.

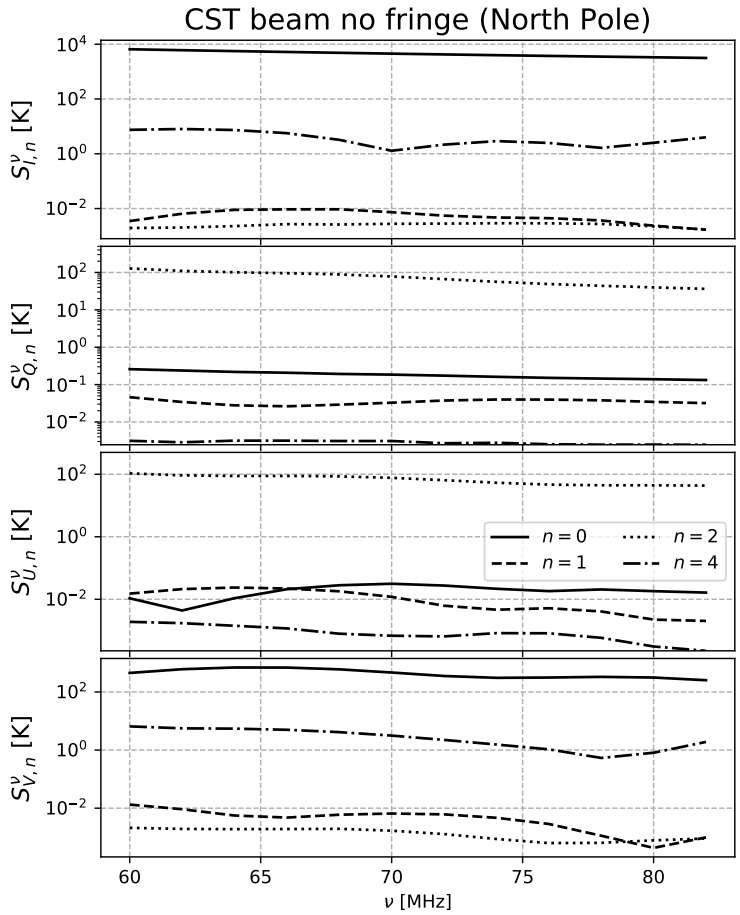

Figure 6.3: Simulated Stokes spectra for $n = \{0,\ 1,\ 2,\ 4\}$ from the ground-parallel sleeved dipole CST beams at the NGP. In the absence of the horizon obstruction, the strong twice-diurnal components ($n = 2$, dotted) in the Stokes spectra for $Q_{\rm obs}$ and $U_{\rm obs}$ have become more dominant than other harmonics and can be used to constrain the foreground spectrum as proposed by the PIPE approach.

Additionally, we quantify the accuracy of the spectral shape for the foreground spectra, derived from the Stokes spectra $S^{\nu}_{Q,2}$ and $S^{\nu}_{U,2}$, with the RMS value across the band relative

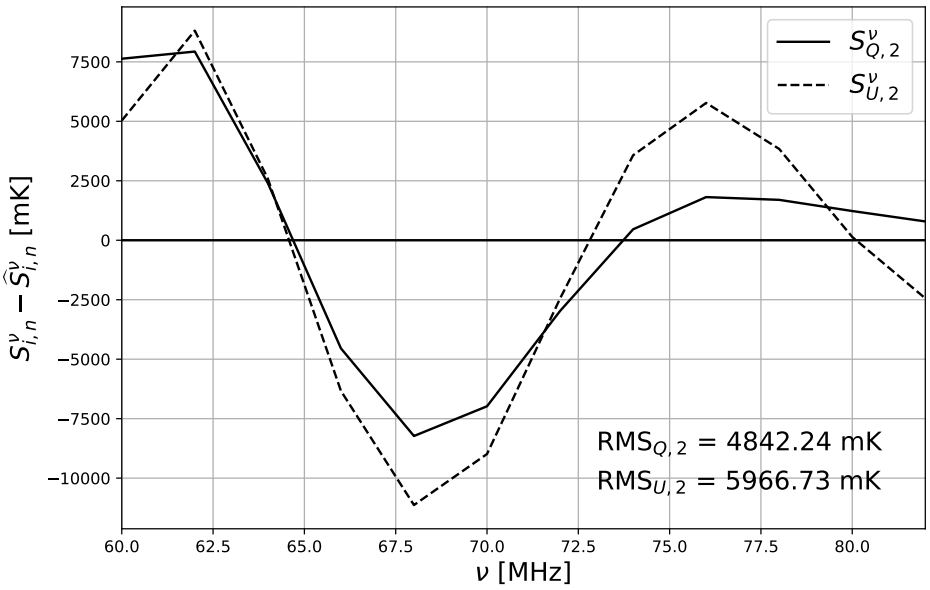

Figure 6.4: Residual temperatures between the simulated Stokes spectra and the fitted power law with $\beta = 2.47$. Spectral structures in the residual plot indicate strong corruption beam chromaticity on the recover twice-diurnal Stokes spectra relative to the ideal power law simulation input for the foreground. Noting the close resemblance between the beam chromatic structures and the global 21-cm signal. The priority for CTP, and other global 21-cm experiments, is to ensure similar types of systematics do not result in a false detection for the cosmological signal.

to the power law with $\beta = 2.47$ used as the input for the simulation as

$$\mathrm{RMS}_{i,n} = \sqrt{\sum_{\nu=\nu_{\mathrm{low}}}^{\nu_{\mathrm{hi}}} \left[S^{\nu}_{i,n} - \widehat{S}^{\nu}_{i,n} \right]^2} \tag{6.2}$$

where $i = \{Q,\ U\}$, $n = 2$ for the twice-diurnal components, and $[\nu_{\mathrm{low}}, \nu_{\mathrm{hi}}]$ are the lower and upper frequencies of the spectra. Meanwhile, $\widehat{S}^{\nu}_{i,n}$ is the least-squares fitting of the Stokes spectra $S^{\nu}_{i,n}$ to a power law $S_0 \left(\nu/\nu_0\right)^{-\beta}$.

In Figure 6.4, the residuals between the simulated Stokes spectra with beam chromaticity and the power-law fits contain spectral structures across the band. We obtain $\mathrm{RMS}_{Q,2} \approx 4,800$ mK and $\mathrm{RMS}_{U,2} \approx 6,000$ mK, which are much larger than the desired value for foreground subtraction. This is mainly due to the large frequency structures present in the residuals. More importantly, these residual spectra contain spectral features that re-

semble to ones expected in the global 21-cm signal. Although this analysis has suggested that the PIPE approach is also susceptible to the antenna beam structures like other global 21-cm experiments, the PIPE approach does provide extra degrees of freedom to constrain the beam and other instrumental systematics by being a full-Stokes measurement. The variations on the beam structures are no longer confined to just a single total-power spectrum. In principle, their distortion can be characterized simultaneously with all Stokes spectra if detailed beam maps are known.

Until now, the most reliable approach to measure an antenna beam at low frequency is to estimate it with the ORBCOMM[2] satellite constellation at 137 MHz (Neben et al., 2016b,a). Besides being limited to a single frequency, the dynamic range of this approach ($\sim$ 30 dB) is still not high enough to correct the smaller beam structures in the foreground spectrum for the global 21-cm signal. We need an accuracy of at least $\sim$ 40 dB for beam correction since the foreground is at least four orders of magnitude larger than the background signal.

A drone-based technique, such as the ECHO (External Calibrator for Hydrogen Observatories Jacobs et al., 2017), has been developed recently to map the antenna beam at low frequency with a transmitter mounted on a remote-controlled drone. In principle, it is invaluable to have a series of transmitters at frequencies lowers than 137 MHz to probe the beam. Yet, so far, this has only been a proof-of-concept experiment and development is still underway before it can be sensitive enough to apply for 21-cm experiments. For now, numerical simulation software, such as CST, are the best tools to characterize the beams with some limitations such as long computational time and inaccuracies for simulating highly detailed antenna structures and the surrounding environment properties.

[2] `https://www.orbcomm.com/en/networks/satellite/orbcomm-og2`

6.1.2 Future Site Selection

As pointed out in the last section, horizon obstruction of the sky at low latitude reduces the sensitivity of the projection-induced polarization. Intuitively, by moving the CTP closer to the geographic poles to increase the measurable foreground region, centered at celestial poles, can improve the sensitivity and accuracy of using the twice-diurnal components induced in Stokes $Q_{\rm obs}$ and $U_{\rm obs}$ to constrain the spectral shape of the foreground spectrum, $T_{\rm fg}(\nu)$.

We have run a series of simulations with the instrument placed at different latitudes (as illustrated by the diagram in Figure 6.5), the resulting Stokes spectra with their magnitudes at harmonics of $n = 0,\ 1,\ 2,\ 4$ are measured as a function of latitude. For completeness, observations on both northern and southern hemispheres are simulated and compared, as shown in Figure 6.6 using the CST beam model at 80 MHz for the same ground-parallel sleeved dipole.

As expected, the magnitudes of the $S^{\nu}_{Q,2}$ and $S^{\nu}_{U,2}$ become more dominant as the latitude approaches either geographic pole, and eventually flattens out when the peak sensitivity is reached. One way to determine the latitude value at which the sensitivity of the twice-diurnal components becomes dominant is to search for the region where the ratios of $S^{\nu}_{i,2}/S^{\nu}_{i,1} \geq 2$, for both Stokes $Q_{\rm obs}$ and $U_{\rm obs}$. The cross-over point, namely where the dotted curves intersects with dashed curve in Figure 6.6, indicates a latitude at which the twice-diurnal components have surpassed the diurnal terms. As seen in Figure 6.6, the northern and southern hemisphere produce different levels of PIPE measurements, hence the cross-over points are not identical. This distinction is primarily due to the different net anisotropy projected by the different sky regions as illustrated by the orthographic projection plot of the Haslam map at 408 MHz in Figure 6.7. The foreground component in the southern sky is at least an order of magnitude stronger than the northern one.

We have compared the latitudes of several radio astronomy sites available for future

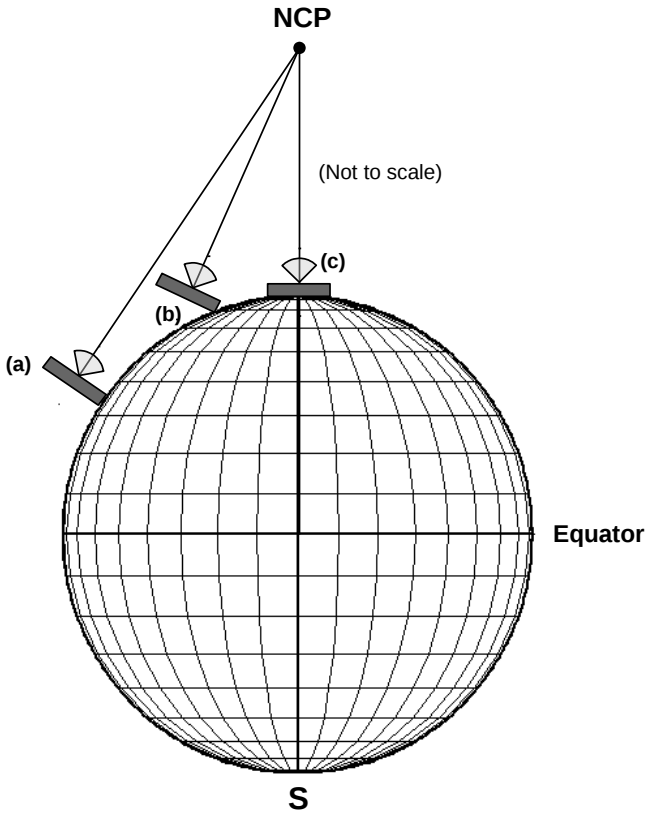

Figure 6.5: Illustration for placement of antenna as a function of latitude on the northern hemisphere: (a) At low latitude (e.g, 38°), horizon obstruction diminishes the sensitivity of the twice-diurnal component of the induced polarization, (b) Simulation for antenna placed at mid-latitude, and (c) at the NGP. The symbol with a small wedge on a rectangle represent the antenna beam on the ground plane.

deployment on both hemispheres. Besides the South Pole, most southern sites (like the Atacama Desert in Chile, the Murchison Radio Observatory in Western Australia, and the Karoo region in South Africa) situate between latitude of 20°-30°. The best option is the Karoo region since its latitude meets the criteria for $S^{\nu}_{i,2}/S^{\nu}_{i,1}2$. On the other hand, for northern hemisphere, we have compared the Dominion Radio Astrophysical Observatory (DRAO) in British Columbia of Canada and the Thule Air Base in Greenland, along with the latitude of the current CTP prototype. The DRAO is at latitude of about 49° so only provides a marginal latitude to measure the PIPE. Meanwhile, based on the simulation,

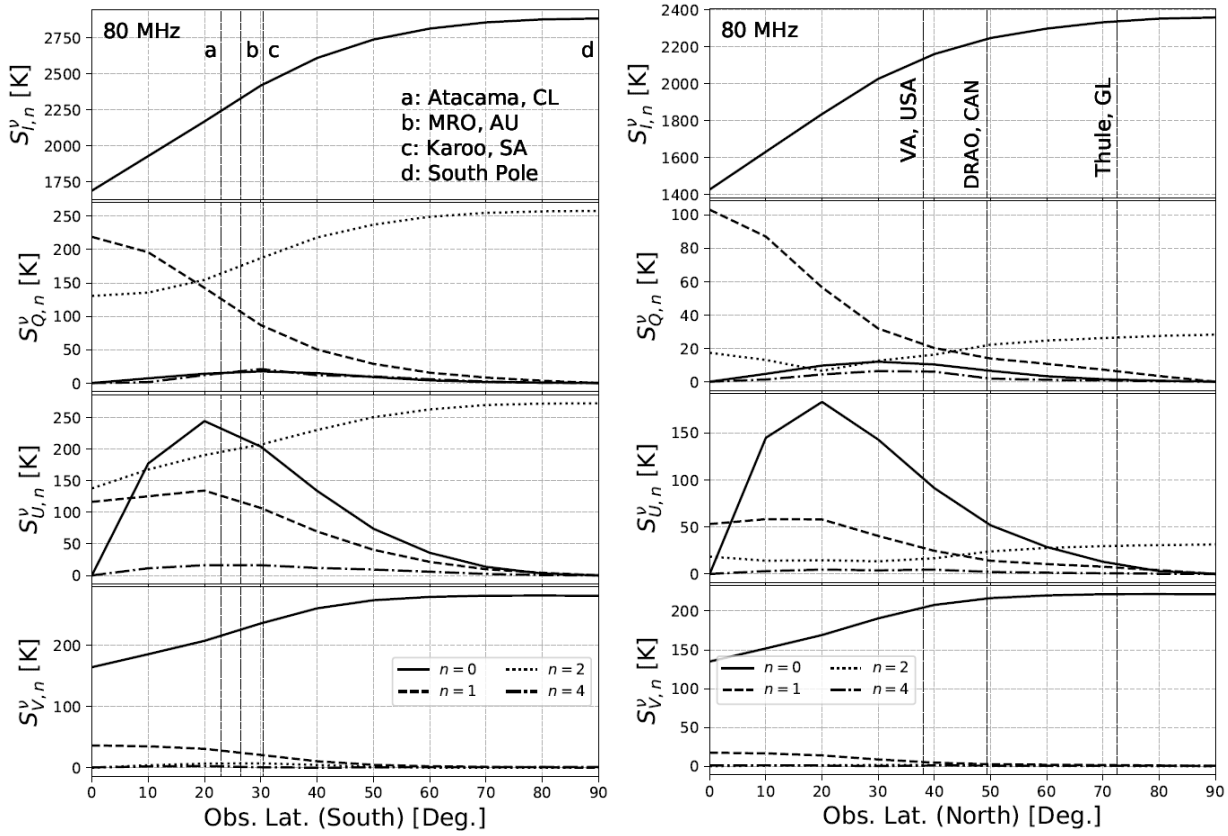

Figure 6.6: Simulation results, using the ground-parallel beam at 80 MHz, for the sensitivity for the induced polarization as a function of latitude: (Left) Potential observation sites on the southern hemisphere, with the South Pole as the optimal choice. (Right) Potential sites on the northern hemisphere, with Thule Air Base in Greenland as the optimal choice.

Thule at latitude of 72°, home of the Greenland Telescope Project[3] , provides the best option for future deployment in the northern sky. Nonetheless, we so far have received verbal confirmation of support from the staff of both northern sites for future collaboration. Further inquiry will be needed to determine an optimal site.

The EDGES experiment recently announced a first detection of the global signal at 78 MHz (Bowman et al., 2018). Due to the discrepancies in the magnitude and flatness at the bottom of the observed absorption feature compared to theoretical expectations, it is important to confirm this detection with an instrument that has different systematics.

[3] `https://www.cfa.harvard.edu/greenland12m/`

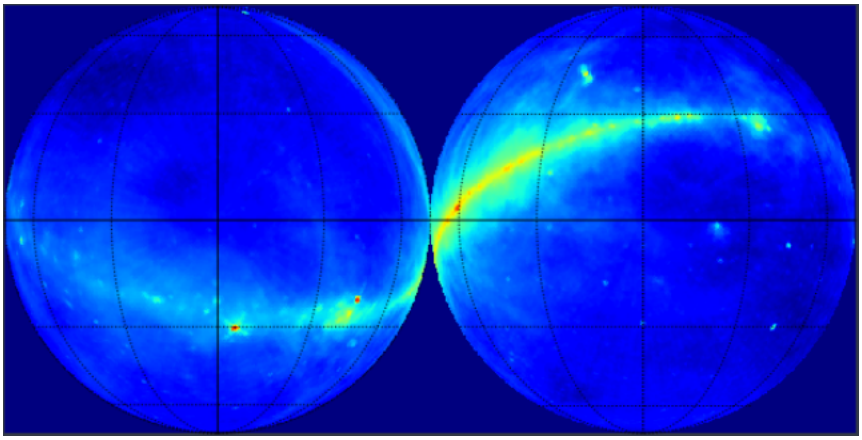

Figure 6.7: Illustration of the northern (left) and southern (right) sky using the Haslam map at 408 MHz plotted in orthographic projection. The distinction in the two sky regions produces a different net anisotropy for the PIPE of each respective sky.

Hence, it is critical to have an independent follow-up observation with a different instrument or technique. The CTP provides such a means to validate the global 21-cm measurement, especially the measured absorption signal is centered at 78 MHz which is within the CTP's passband. Furthermore, the CTP will be an invaluable to confirm the global 21-cm signal independently from both hemispheres, either using the same instrument or a second copy of it.

6.1.3 Ionospheric Effects

Some of the previous studies have suggested that the ionosphere fluctuations in the total electron content (TEC) does not pose a significant problem for ground-based global 21-cm experiments (Sokolowski et al., 2015b). Yet other studies have also pointed out that the ionospheric refraction and absorption can have long-term effects on the sensitivity of the observations (Vedantham et al., 2014; Datta et al., 2016). Nonetheless, the errors contributed by the TEC fluctuations are expected to be less dominant than signal attenuation in the ionosphere during strong solar activities at $\nu \sim 80$ MHz. As we moving closer to the geographic poles and to lower frequencies, attenuation from the ionosphere becomes

significant, especially during strong solar activities such as flares and coronal mass ejections (CME). By comparing the archival TEC data[4] along with the attenuation maps[5] between a normal day (Sept 01, 2017 at 00:00 UTC, Figure 6.8[6]) and a day with strong flare (Sept 09, 2017 at 23:00 UTC, Figure 6.9), it is clear that during the flare day, the majority of the ionosphere in pole regions is saturated, which leads to complete attenuation of the sky signal. Additionally, there is also ionospheric scintillation which causes rapid disruptions on the RF signal's phase coherency (van Bemmel, 2007). Nonetheless, due to the infrequency of these events, dates with corrupted data in the event of strong solar activity can be removed from the analysis.

6.2 Future Work

6.2.1 Follow-up Experiment: CTP v2.0

Before we deploy the CTP to a remote site, we have planned to transfer the CTP (v2.0) to the Green Bank Observatory (GBO) later in 2018. One of the major improvements is to relocate the sleeved dipole off the ground by mounting it on top of a 45-foot dish as shown in Figure 6.10. The antenna will be at least 50 feet off the ground, CST simulations have suggested that such a distance from the ground soil can significantly mitigate the interferometric fringing effects in the current CTP. Careful modeling of the dish and feed supports will also be required to capture a more realistic beam model.

By operating in the radio quiet zone, this will substantially suppress the RFI and drastically improve the CTP performance. However, as observed from the bicone data, the FM stations between 88-108 MHz are still visible in GBO, hence the CTP v2.0 will continue

[4] Data provided by the Center for Orbit Determination in Europe (CODE), fetched by the Python script `radioion` provided by Prof. James Aguirre from the University of Pennsylvania,
`https://github.com/UPennEoR/radionopy`

[5] Attentuation maps is based on Sauer and Wilkinson (2008), data acquired from the National Oceanic and Atmospheric Administration (NOAA)
`https://www.swpc.noaa.gov/content/global-d-region-absorption-prediction-documentation`

[6] I would like to thank David Bordenave for providing the Python script to produce these comparison plots.

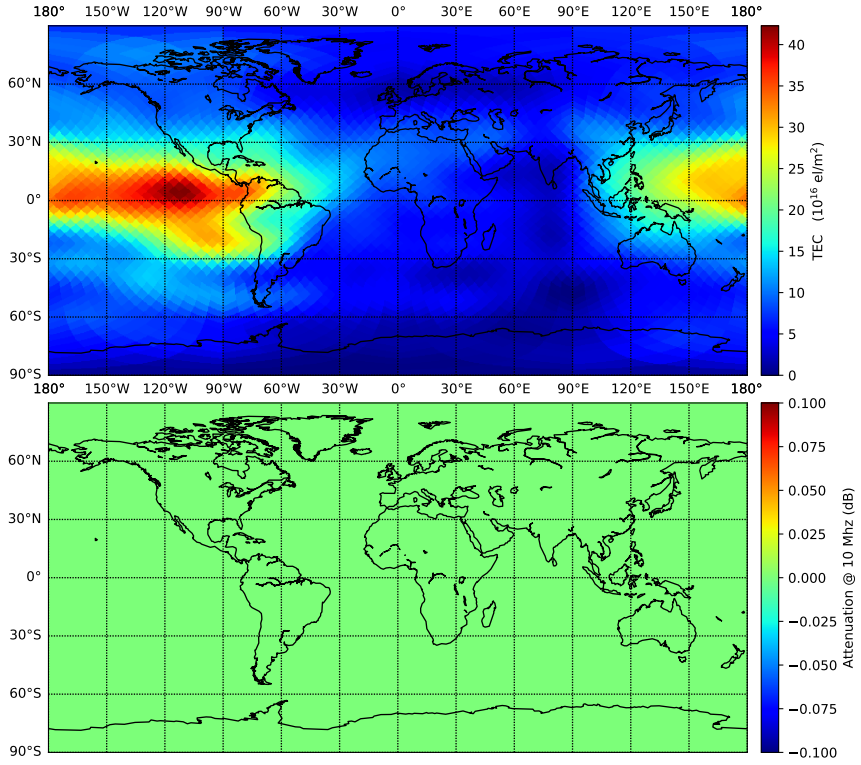

Figure 6.8: TEC (top) and attenuation (bottom) maps for the ionosphere conditions on normal day (Sept 01, 2017 at 00:00 UTC). Although there are large variations TEC close to the Equator, which is typical, no significant attenuation is observed. Source: CODE and NOAA.

to operate at 65-85 MHz. We have planned to upgrade and reduce the back end (BE) of the v2.0 to improve DAQ efficiency and frequency resolution. It will be useful to decrease the resolution bandwidth (RBW) from the current value of $\Delta\nu = 57.12$ kHz by another factor of 10 to prepare the data for a more sophisticated RFI excision algorithm such as the complex signal kurtosis (CSK) as described in the last chapter (Bradley et al., 2015; Schoenwald et al., 2016). More importantly, developing the CTP V2.0 allows us to upgrade the instrument to a more portable version so that we can deploy it at remote sites, without the need of major infrastructure to be in place.

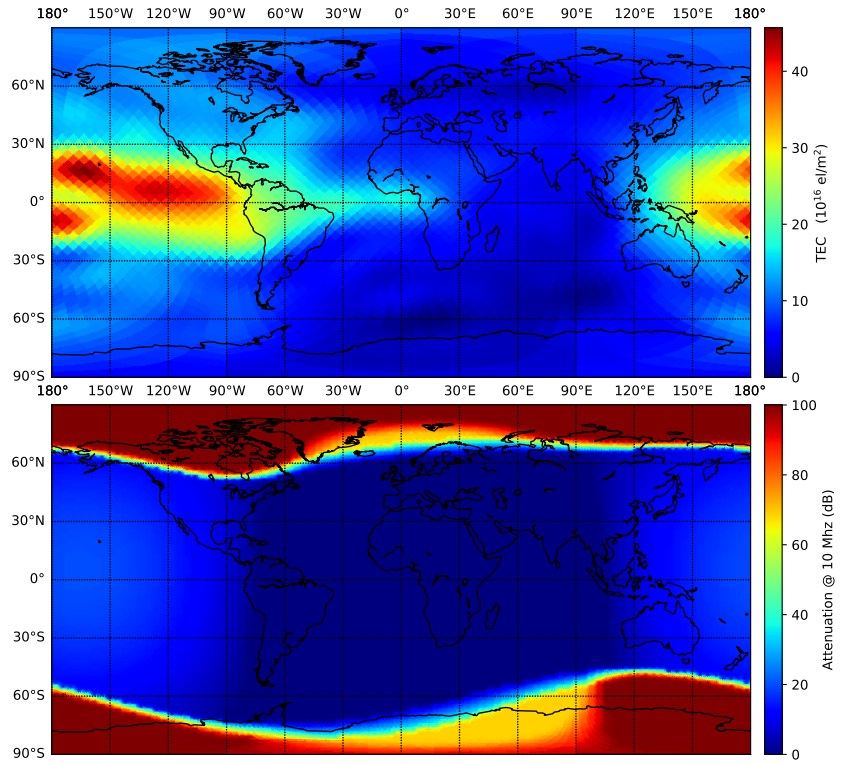

Figure 6.9: TEC (top) and attenuation (bottom) maps for the ionosphere conditions on the day with a strong solar flare (Sept 09, 2017 at 23:00 UTC). During the active period, ionosphere in both polar regions (latitude 60°) are saturated with high energy particles so that the signal are large attenuated. Although this is not ideal for any experiments located at those latitudes, these solar activities are not frequent nor long-lasting. Hence, it is not a major threat for any ground-based experiments. Source: CODE and NOAA

6.2.2 Testbed for SVD-based Algorithm Development

Due to limitations of the current CTP, we have not been able to attempt a background 21-cm signal measurement. However, there is an urgency within the global 21-cm community to make a second measurement of the global 21-cm signal to confirm the EDGES's result published earlier this year. So far, the most mature astrophysical parameter extraction tools for the global 21-cm signal are based on Markov Chain Monte Carlo (MCMC) fitting (e.g., Harker et al., 2012; Harker, 2015). However, these algorithms all suffer from the lack of information for the foreground and instrumental systematics.

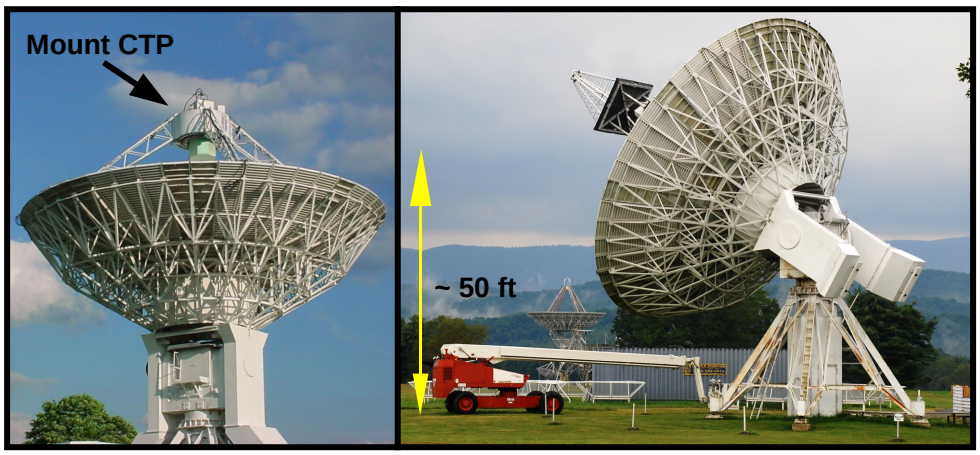

Figure 6.10: 45-foot dish located at the GBO, where the CTP v2.0 will be mounted at the feed point. By moving the antenna to height of $\sim$ 50 feet, the fringing effects on the beams can be removed, as suggested by simulations.

Another important aspect of continuing the development effort for the CTP v2.0 is to provide a realistic testbed for parameter-inference algorithms based on singular value decomposition (SVD), such as the `pylinex` program currently being developed by our collaborators (Tauscher et al., 2018). The SVD-based `pylinex`, in conjunction with the MCMC technique, relies on large training sets, which are made up with numerical models for the global 21-cm signal along with measurements of the foreground and instrumental effects, to constrain the background 21-cm signal. For example, using idealized beam patterns along with sky survey maps such as the Haslam map at 408 MHz, `pylinex` has illustrated the power of utilizing full-Stokes measurements, as in the PIPE approach, in extracting the background signal comparing to the traditional total-power experiment, as shown in Figure 6.11. Hence, the CTP v2.0 can provide valuable data to further develop the SVD pipeline for real observational data.

6.2.3 Technology Transfer for Space-based Missions

Another important aspect of developing the CTP is to eventually apply the PIPE approach for a space-based global 21-cm mission, such as SmallSats mission concepts like

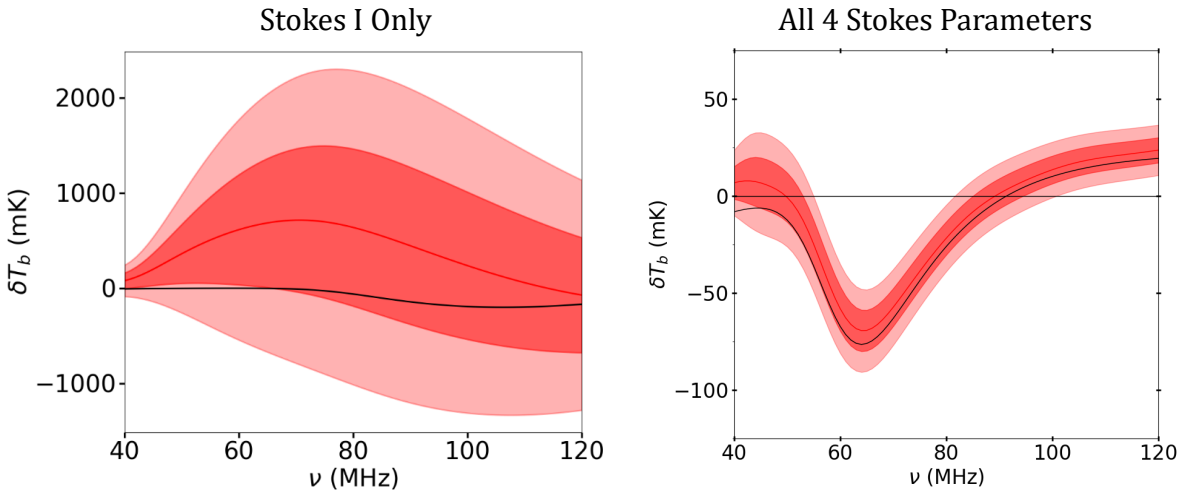

Figure 6.11: By utilizing a large training sets for global 21-cm models, beam models, and foreground maps, the SVD-based `pylinex` demonstrates the power the PIPE approach when simultaneously constraining all four Stokes parameters (right) instead of just the total-power spectrum in conventional approach (left). The two uncertainty bands are 1σ (dark red) and 2σ (light red) of the recovered signal, overplotted on top of the input global 21-cm model (solid black curve). Source: Figure is provided by the authors of Tauscher et al. (2018).

DAPPER (Dark Ages Polarimeter PathfindER) currently being proposed by the NASA-funded NESS (Network for Exploration and Space Science) collaboration at CU Boulder under PI Prof. Jack O. Burns. Due to limitations in the observer's horizon, ground effects on the beams, ionosphere, and RFI, a space-based radiometer carrying out observation on the far side of the Moon can alleviate the majority of these problems. DAPPER's science can address one of NASA's astrophysics science goals to "explore how (the Universe) began and evolved" and the SMD's (Science Mission Directorate) goal to "explore the origin and evolution of galaxies, stars." More importantly, DAPPER will be a pathfinder for a mission recommended in the NASA Astrophysics Roadmap (Kouveliotou et al., 2014).

6.3 Summary

Finally, in this chapter, we have concluded this thesis with a wide array of topics that address the inherent limitations of the PIPE approach. The CTP prototype described in the last two chapters have provided us an enormous amount of information to better understand the instrumentation requirements and potential shortcomings of the PIPE technique. Nonetheless, simulation studies have encouraged us to further develop a CTP v2.0 to retire some of the major problems, including reallocating the system to the GBO for lower RFI contamination as well as removing the beam fringing effects by mounting the antenna on top of the GBO's 45-foot dish.

The sensitivity of measuring the PIPE to constrain the foreground spectrum improves significantly when the experiment is conducted closer to the geographic poles, hence reallocating the CTP v2.0 to a new observation site is necessary to fully realize this technique. Although the CTP is susceptible to beam chromatic effects, as other global 21-cm experiments, the CTP and the PIPE approach provides unique advantages including:

- Full-Stokes measurement to increase the degrees of freedom in constraining the foreground and instrumental systematics. The SVD-based analysis in Figure 6.11 has illustrated the power of the PIPE approach under idealized conditions.

- Pole-pointing allows the CTP to modulate the net projection-induced polarization and provide a direct measurement of the foreground characteristics without artificially fitting the foreground spectrum with any parametric models as in conventional global 21-cm experiments.

- Furthermore, a pole-pointing observation can maximize the efficiency and integration time because it can in principle observe the same sky region continuously unlike drift-scan observing from zenith-pointing experiments.

- Our network-based calibration approach for the transducer gain (with the tone step-

ping and S-parameters tracking) and the noise temperature (with combination of lab measurement and network model for the noise parameters), along with a thermal-controlled front-end design, provide a high dynamic-range and low-cost calibration for the CTP measurement.

We believe that the beam chromatic distortion is not a show stopper. It can be addressed with the current technology development, such as the drone-based beam mapping and detailed numerical simulation on faster computers. After all, the CTP is a much more affordable instrument than the large interferometric arrays that consist of hundreds, if not thousands, of antennas. At such a low cost, the CTP is a low risk experiment that is worthwhile to continue the development effort. Especially when there is a chance the PIPE technique can be adapted to a space-based mission like DAPPER. The CTP and the PIPE approach are promising, perhaps to confirm EDGES's detection or even uncover new mysteries from the early Universe.

Bibliography

Abel, T., Bryan, G. L., and Norman, M. L. (2002). The Formation of the First Star in the Universe. Science, 295:93–98.

Antoni, J. (2004). The spectral kurtosis of nonstationary signals: Formalisation, some properties, and application. In 2004 12th European Signal Processing Conference, pages 1167–1170. Vienna: IEEE.

Antoni, J. (2006). The spectral kurtosis: A useful tool for characterising non-stationary signals. Mechanical Systems and Signal Processing, 20(2):282–307.

Asad, K. M. B., Koopmans, L. V. E., Jelić, V., Pandey, V. N., Ghosh, A., Abdalla, F. B., Bernardi, G., Brentjens, M. A., de Bruyn, A. G., Bus, S., Ciardi, B., Chapman, E., Daiboo, S., Fernandez, E. R., Harker, G., Iliev, I. T., Jensen, H., Martinez-Rubi, O., Mellema, G., Mevius, M., Offringa, A. R., Patil, A. H., Schaye, J., Thomas, R. M., van der Tol, S., Vedantham, H. K., Yatawatta, S., and Zaroubi, S. (2015). Polarization Leakage in Epoch of Eeionization Windows - I. Low Frequency Array Observations of the 3C196 Field. , 451:3709–3727.

Balanis, C. A. (2005). Antenna Theory: Analysis and Design. 3rd ed.; Hoboken, NJ: John Wiley & Sons.

Baldwin, J. E. (1986). TESTING Searches for primordial pancakes. Highlights of Astronomy, 7:333–339.

Barkana, R. (2018). Possible interaction between baryons and dark-matter particles revealed by the first stars. Nature, 555:71 EP –.

Barkana, R. and Loeb, A. (2001). In the Beginning: the First Sources of Light and the Reionization of the Universe. , 349:125–238.

Beck, R. and Wielebinski, R. (2013). Planets, Stars and Stellar Systems. Volume 5: Magnetic Fields in Galaxies, page 641.

Bennett, C. L., Bay, M., Halpern, M., Hinshaw, G., Jackson, C., Jarosik, N., Kogut, A., Limon, M., Meyer, S. S., Page, L., Spergel, D. N., Tucker, G. S., Wilkinson, D. T., Wollack, E., and Wright, E. L. (2003). The Microwave Anisotropy Probe Mission. Astrophys. J., 583:1–23.

Bernardi, G., McQuinn, M., and Greenhill, L. J. (2015). Foreground Model and Antenna Calibration Errors in the Measurement of the Sky-averaged λ 21 cm Signal at $z \sim 20$. Astrophys. J., 799:90.

Bittner, J. M. and Loeb, A. (2011). Measuring the Redshift of Reionization with a Modest Array of Low-frequency Dipoles. Journal of Cosmology and Astroparticle Physics, 4:38.

Bouwens, R. J., Illingworth, G. D., Labbe, I., Oesch, P. A., Trenti, M., Carollo, C. M., van Dokkum, P. G., Franx, M., Stiavelli, M., González, V., Magee, D., and Bradley, L. (2011). A Candidate Redshift $z \sim 10$ Galaxy and Rapid Changes in that Population at an Age of 500 Myr. Nature, 469:504–507.

Bowman, J. D., Cairns, I., Kaplan, D. L., Murphy, T., Oberoi, D., Staveley-Smith, L., Arcus, W., Barnes, D. G., Bernardi, G., Briggs, F. H., Brown, S., Bunton, J. D., Burgasser, A. J., Cappallo, R. J., Chatterjee, S., Corey, B. E., Coster, A., Deshpande, A., deSouza, L., Emrich, D., Erickson, P., Goeke, R. F., Gaensler, B. M., Greenhill, L. J., Harvey-Smith, L., Hazelton, B. J., Herne, D., Hewitt, J. N., Johnston-Hollitt, M., Kasper, J. C., Kincaid, B. B., Koenig, R., Kratzenberg, E., Lonsdale, C. J., Lynch, M. J., Matthews, L. D., McWhirter, S. R., Mitchell, D. A., Morales, M. F., Morgan, E. H., Ord, S. M., Pathikulangara, J., Prabu, T., Remillard, R. A., Robishaw, T., Rogers, A. E. E., Roshi, A. A., Salah, J. E., Sault, R. J., Shankar, N. U., Srivani, K. S., Stevens, J. B., Subrahmanyan, R., Tingay, S. J., Wayth, R. B., Waterson, M., Webster, R. L., Whitney, A. R., Williams, A. J., Williams, C. L., and Wyithe, J. S. B. (2013). Science with the Murchison Widefield Array. Proc. Astron. Soc. Aust., 30:e031.

Bowman, J. D. and Rogers, A. E. E. (2010). A Lower Limit of $\Delta z > 0.06$ for the Duration of the Reionization Epoch. Nature, 468:796–798.

Bowman, J. D., Rogers, A. E. E., and Hewitt, J. N. (2008). Toward Empirical Constraints on the Global Redshifted 21 cm Brightness Temperature During the Epoch of Reionization. , 676:1–9.

Bowman, J. D., Rogers, A. E. E., Monsalve, R. A., Mozdzen, T. J., and Mahesh, N. (2018). An Absorption Profile Centred at 78 Megahertz in the Sky-averaged Spectrum. Nature, 555:67 EP –.

Bradley, D. C., Schoenwald, A. J., Wong, M., Mohammed, P. N., and Piepmeier, J. R. (2015). Wideband digital signal processing test-bed for radiometric rfi mitigation. In Geoscience and Remote Sensing Symposium (IGARSS), 2015 IEEE International, pages 3489–3492. IEEE.

Bromm, V., Coppi, P. S., and Larson, R. B. (1999). Forming the First Stars in the Universe: The Fragmentation of Primordial Gas. Astrophys. J., Lett., 527:L5–L8.

Burns, J. O., Bradley, R., Tauscher, K., Furlanetto, S., Mirocha, J., Monsalve, R., Rapetti, D., Purcell, W., Newell, D., Draper, D., MacDowall, R., Bowman, J., Nhan, B., Wollack, E. J., Fialkov, A., Jones, D., Kasper, J. C., Loeb, A., Datta, A., Pritchard, J., Switzer, E.,

and Bicay, M. (2017). A Space-based Observational Strategy for Characterizing the First Stars and Galaxies Using the Redshifted 21 cm Global Spectrum. Astrophys. J., 844:33.

Burns, J. O., Lazio, J., Bale, S., Bowman, J., Bradley, R., Carilli, C., Furlanetto, S., Harker, G., Loeb, A., and Pritchard, J. (2012). Probing the First Stars and Black Holes in the Early Universe with the Dark Ages Radio Explorer (DARE). Advances in Space Research, 49:433–450.

Carozzi, T. and Woan, G. (2011). A fundamental figure of merit for radio polarimeters. IEEE Transactions on Antennas and Propagation, 59(6):2058–2065.

Caruso, G. and Sannino, M. (1978). Computer-aided Determination of Microwave Two-port Noise Parameters. IEEE Transactions on Microwave Theory Techniques, 26:639–642.

Collin, R. E. (2007). Foundations for Microwave Engineering. John Wiley & Sons.

Datta, A., Bradley, R., Burns, J. O., Harker, G., Komjathy, A., and Lazio, T. J. W. (2016). The Effects of the Ionosphere on Ground-based Detection of the Global 21 cm Signal from the Cosmic Dawn and the Dark Ages. , 831:6.

de Roo, R. D. (2009). A Simplified Calculation of the Kurtosis for RFI Detection. IEEE Transactions on Geoscience and Remote Sensing, 47:3755–3760.

De Roo, R. D. (2009). A simplified calculation of the kurtosis for rfi detection. Geoscience and Remote Sensing, IEEE Transactions on, 47(11):3755–3760.

Dicke, R. H. (1982). 1946, The Measurement of Thermal Radiation at Microwave Frequencies, page 106.

Dwyer, R. (1983). Detection of non-gaussian signals by frequency domain kurtosis estimation. In Acoustics, Speech, and Signal Processing, IEEE International Conference on ICASSP'83., volume 8, pages 607–610. IEEE.

Ellis, R. S., McLure, R. J., Dunlop, J. S., Robertson, B. E., Ono, Y., Schenker, M. A., Koekemoer, A., Bowler, R. A. A., Ouchi, M., Rogers, A. B., Curtis-Lake, E., Schneider, E., Charlot, S., Stark, D. P., Furlanetto, S. R., and Cirasuolo, M. (2013). The Abundance of Star-forming Galaxies in the Redshift Range 8.5-12: New Results from the 2012 Hubble Ultra Deep Field Campaign. Astrophys. J., Lett., 763:L7.

Engberg, J. and Larsen, T. (1995). Noise Theory of Linear and Nonlinear Circuits. John Wiley & Sons.

Ewall-Wice, A., Bradley, R., Deboer, D., Hewitt, J., Parsons, A., Aguirre, J., Ali, Z. S., Bowman, J., Cheng, C., Neben, A. R., Patra, N., Thyagarajan, N., Venter, M., de Lera Acedo, E., Dillon, J. S., Dickenson, R., Doolittle, P., Egan, D., Hedrick, M., Klima, P., Kohn, S., Schaffner, P., Shelton, J., Saliwanchik, B., Taylor, H. A., Taylor, R., Tegmark, M., and Wirt, B. (2016). The Hydrogen Epoch of Reionization Array Dish. II. Characterization of Spectral Structure with Electromagnetic Simulations and Its Science Implications. , 831:196.

Ewen, H. I. and Purcell, E. M. (1951). Observation of a Line in the Galactic Radio Spectrum: Radiation from Galactic Hydrogen at 1,420 Mc./sec. Nature, 168:356.

Fan, X., Carilli, C. L., and Keating, B. (2006). Observational Constraints on Cosmic Reionization. Ann. Rev. Astron. Astrophys., 44:415–462.

Field, G. B. (1958). Excitation of the Hydrogen 21-CM Line. Proceedings of the IRE, 46:240–250.

Fiori, A. M. and Zenga, M. (2009). Karl pearson and the origin of kurtosis. International Statistical Review, 77(1):40–50.

Foreman-Mackey, D., Hogg, D. W., Lang, D., and Goodman, J. (2013). emcee: The MCMC Hammer. , 125:306.

Frigo, M. and Johnson, S. G. (2005). The design and implementation of fftw3. In PROCEEDINGS OF THE IEEE, pages 216–231.

Furlanetto, S. R. (2006). The global 21-centimeter background from high redshifts. Mon. Not. R. Astron. Soc., 371:867–878.

Furlanetto, S. R., Oh, S. P., and Briggs, F. H. (2006). Cosmology at Low Frequencies: The 21 cm Transition and the High-redshift Universe. Phys. Rep., 433:181–301.

Gilfanov, M., Grimm, H.-J., and Sunyaev, R. (2004). L_X-SFR Relation in Star-forming Galaxies. Mon. Not. R. Astron. Soc., 347:L57–L60.

Greenhill, L. J. and LEDA Collaboration (2015). Constraining the Thermal State of the IGM at $z \sim 20$. In American Astronomical Society Meeting Abstracts #225, volume 225 of American Astronomical Society Meeting Abstracts, page 403.07.

Grimm, H.-J., Gilfanov, M., and Sunyaev, R. (2003). High Mass X-ray Binaries as a SFR Indicator. Astronomische Nachrichten, 324:171.

Guzmán, A. E., May, J., Alvarez, H., and Maeda, K. (2011). All-sky Galactic Radiation at 45 MHz and Spectral Index between 45 and 408 MHz. , 525:A138.

Haiman, Z., Thoul, A. A., and Loeb, A. (1996). Cosmological Formation of Low-Mass Objects. Astrophys. J., 464:523.

Hamming, R. W. (1986). Numerical Methods for Scientists and Engineers. 2nd ed.; NY: Dover Publications.

Harker, G. J. A. (2015). Selection between Foreground Models for Global 21-cm Experiments. Mon. Not. R. Astron. Soc., 449:L21–L25.

Harker, G. J. A., Pritchard, J. R., Burns, J. O., and Bowman, J. D. (2012). An MCMC Approach to Extracting the Global 21-cm Signal During the Cosmic Dawn from Sky-averaged Radio Observations. Mon. Not. R. Astron. Soc., 419:1070–1084.

Haslam, C. G. T., Salter, C. J., Stoffel, H., and Wilson, W. E. (1982). A 408 MHz All-sky Continuum Survey. II - The Atlas of Contour Maps. 47:1.

Heiles, C. (2002). A Heuristic Introduction to Radioastronomical Polarization. In Stanimirovic, S., Altschuler, D., Goldsmith, P., and Salter, C., editors, Single-Dish Radio Astronomy: Techniques and Applications, volume 278 of Astronomical Society of the Pacific Conference Series, pages 131–152. San Francisco, CA: Astronmical Society of the Pacific.

Heinzel, G., Rüdiger, A., and Schilling, R. (2002). Spectrum and spectral density estimation by the Discrete Fourier transform (DFT), including a comprehensive list of window functions and some new at-top windows. Technical report, Max Planck Institute for Gravitational Physics.

Hinshaw, G., Larson, D., Komatsu, E., Spergel, D. N., Bennett, C. L., Dunkley, J., Nolta, M. R., Halpern, M., Hill, R. S., Odegard, N., Page, L., Smith, K. M., Weiland, J. L., Gold, B., Jarosik, N., Kogut, A., Limon, M., Meyer, S. S., Tucker, G. S., Wollack, E., and Wright, E. L. (2013). Nine-year Wilkinson Microwave Anisotropy Probe (WMAP) Observations: Cosmological Parameter Results. Astrophys. J., Suppl. Ser., 208:19.

Hogan, C. J. and Rees, M. J. (1979). Spectral Appearance of Non-uniform Gas at High z. Mon. Not. R. Astron. Soc., 188:791–798.

Hogg, D. W. (1999). Distance Measures in Cosmology. ArXiv Astrophysics e-prints.

Ichiki, K. (2014). CMB Foreground: A Concise Review. Progress of Theoretical and Experimental Physics, 2014(6):06B109.

Ifeachor, E. C. and Jervis, B. W. (2002). Digital Signal Processing: A Practical Approach. Pearson Education.

Jacobs, D. C., Burba, J., Bowman, J. D., Neben, A. R., Stinnett, B., Turner, L., Johnson, K., Busch, M., Allison, J., Leatham, M., Serrano Rodriguez, V., Denney, M., and Nelson, D. (2017). First Demonstration of ECHO: an External Calibrator for Hydrogen Observatories. , 129(3):035002.

Jelić, V., de Bruyn, A. G., Mevius, M., Abdalla, F. B., Asad, K. M. B., Bernardi, G., Brentjens, M. A., Bus, S., Chapman, E., Ciardi, B., Daiboo, S., Fernandez, E. R., Ghosh, A., Harker, G., Jensen, H., Kazemi, S., Koopmans, L. V. E., Labropoulos, P., Martinez-Rubi, O., Mellema, G., Offringa, A. R., Pandey, V. N., Patil, A. H., Thomas, R. M., Vedantham, H. K., Veligatla, V., Yatawatta, S., Zaroubi, S., Alexov, A., Anderson, J., Avruch, I. M., Beck, R., Bell, M. E., Bentum, M. J., Best, P., Bonafede, A., Bregman, J., Breitling, F., Broderick, J., Brouw, W. N., Brüggen, M., Butcher, H. R., Conway, J. E., de Gasperin, F., de Geus, E., Deller, A., Dettmar, R.-J., Duscha, S., Eislöffel, J., Engels, D., Falcke, H., Fallows, R. A., Fender, R., Ferrari, C., Frieswijk, W., Garrett, M. A., Grießmeier, J., Gunst, A. W., Hamaker, J. P., Hassall, T. E., Haverkorn, M., Heald, G., Hessels, J. W. T., Hoeft, M., Hörandel, J., Horneffer, A., van der Horst, A.,

Iacobelli, M., Juette, E., Karastergiou, A., Kondratiev, V. I., Kramer, M., Kuniyoshi, M., Kuper, G., van Leeuwen, J., Maat, P., Mann, G., McKay-Bukowski, D., McKean, J. P., Munk, H., Nelles, A., Norden, M. J., Paas, H., Pandey-Pommier, M., Pietka, G., Pizzo, R., Polatidis, A. G., Reich, W., Röttgering, H., Rowlinson, A., Scaife, A. M. M., Schwarz, D., Serylak, M., Smirnov, O., Steinmetz, M., Stewart, A., Tagger, M., Tang, Y., Tasse, C., ter Veen, S., Thoudam, S., Toribio, C., Vermeulen, R., Vocks, C., van Weeren, R. J., Wijers, R. A. M. J., Wijnholds, S. J., Wucknitz, O., and Zarka, P. (2014). Initial LOFAR Observations of Epoch of Reionization Windows. II. Diffuse Polarized Emission in the ELAIS-N1 Field. , 568:A101.

Jelić, V., de Bruyn, A. G., Pandey, V. N., Mevius, M., Haverkorn, M., Brentjens, M. A., Koopmans, L. V. E., Zaroubi, S., Abdalla, F. B., Asad, K. M. B., Bus, S., Chapman, E., Ciardi, B., Fernandez, E. R., Ghosh, A., Harker, G., Iliev, I. T., Jensen, H., Kazemi, S., Mellema, G., Offringa, A. R., Patil, A. H., Vedantham, H. K., and Yatawatta, S. (2015). Linear Polarization Structures in LOFAR Observations of the Interstellar Medium in the 3C 196 Field. , 583:A137.

Kaiser, N. (1987). Clustering in Real Space and in Redshift Space. Mon. Not. R. Astron. Soc., 227:1–21.

Kogut, A. (2012). Synchrotron Spectral Curvature from 22 MHz to 23 GHz. Astrophys. J., 753:110.

Komatsu, E., Dunkley, J., Nolta, M. R., Bennett, C. L., Gold, B., Hinshaw, G., Jarosik, N., Larson, D., Limon, M., Page, L., Spergel, D. N., Halpern, M., Hill, R. S., Kogut, A., Meyer, S. S., Tucker, G. S., Weiland, J. L., Wollack, E., and Wright, E. L. (2009). Five-Year Wilkinson Microwave Anisotropy Probe Observations: Cosmological Interpretation. Astrophys. J., Suppl. Ser., 180:330–376.

Komatsu, E., Smith, K. M., Dunkley, J., Bennett, C. L., Gold, B., Hinshaw, G., Jarosik, N., Larson, D., Nolta, M. R., Page, L., Spergel, D. N., Halpern, M., Hill, R. S., Kogut, A., Limon, M., Meyer, S. S., Odegard, N., Tucker, G. S., Weiland, J. L., Wollack, E., and Wright, E. L. (2011). Seven-year Wilkinson Microwave Anisotropy Probe (WMAP) Observations: Cosmological Interpretation. Astrophys. J., Suppl. Ser., 192:18.

Kouveliotou, C., Agol, E., Batalha, N., Bean, J., Bentz, M., Cornish, N., Dressler, A., Figueroa-Feliciano, E., Gaudi, S., Guyon, O., Hartmann, D., Kalirai, J., Niemack, M., Ozel, F., Reynolds, C., Roberge, A., Straughn, K. S. A., Weinberg, D., and Zmuidzinas, J. (2014). Enduring Quests-Daring Visions (NASA Astrophysics in the Next Three Decades). ArXiv e-prints.

Kraus, J. D. (1966). Radio astronomy. McGraw-Hill.

Kraus, J. D. (1986). Radio Astronomy. 2nd ed.; Powell, OH: Cygnus-Quasar Books.

Lepp, S. and Shull, J. M. (1984). Molecules in the Early Universe. , 280:465–469.

Loeb, A. (2006). First Light. ArXiv Astrophysics e-prints.

Loeb, A. and Furlanetto, S. R. (2013). The First Galaxies in the Universe.

Madau, P., Meiksin, A., and Rees, M. J. (1997). 21 Centimeter Tomography of the Intergalactic Medium at High Redshift. Astrophys. J., 475:429–444.

Mellema, G., Koopmans, L. V. E., Abdalla, F. A., Bernardi, G., Ciardi, B., Daiboo, S., de Bruyn, A. G., Datta, K. K., Falcke, H., Ferrara, A., Iliev, I. T., Iocco, F., Jelić, V., Jensen, H., Joseph, R., Labroupoulos, P., Meiksin, A., Mesinger, A., Offringa, A. R., Pandey, V. N., Pritchard, J. R., Santos, M. G., Schwarz, D. J., Semelin, B., Vedantham, H., Yatawatta, S., and Zaroubi, S. (2013). Reionization and the Cosmic Dawn with the Square Kilometre Array. Experimental Astronomy, 36:235–318.

Mesinger, A., Furlanetto, S., and Cen, R. (2011). 21CMFAST: A Fast, Seminumerical Simulation of the High-redshift 21-cm Signal. Mon. Not. R. Astron. Soc., 411:955–972.

Mineo, S., Gilfanov, M., and Sunyaev, R. (2012). X-ray Emission from Star-forming Galaxies - I. High-mass X-ray Binaries. Mon. Not. R. Astron. Soc., 419:2095–2115.

Mirocha, J. and Furlanetto, S. R. (2018). What does the First Highly-redshifted 21-cm Detection Tell Us about Early Galaxies? ArXiv e-prints.

Mirocha, J., Harker, G. J. A., and Burns, J. O. (2015). Interpreting the Global 21-cm Signal from High Redshifts. II. Parameter Estimation for Models of Galaxy Formation. Astrophys. J., 813:11.

Mitama, M. and Katoh, H. (1979). An improved computational method for noise parameter measurement. IEEE Transactions on Microwave Theory and Techniques, 27(6):612–615.

Monsalve, R. A., Rogers, A. E. E., Bowman, J. D., and Mozdzen, T. J. (2017a). Calibration of the EDGES High-band Receiver to Observe the Global 21 cm Signature from the Epoch of Reionization. , 835:49.

Monsalve, R. A., Rogers, A. E. E., Bowman, J. D., and Mozdzen, T. J. (2017b). Results from EDGES High-band. I. Constraints on Phenomenological Models for the Global 21 cm Signal. , 847:64.

Mozdzen, T. J., Bowman, J. D., Monsalve, R. A., and Rogers, A. E. E. (2016). Limits on Foreground Subtraction from Chromatic Beam Effects in Global Redshifted 21 cm Measurements. Mon. Not. R. Astron. Soc., 455:3890–3900.

Muller, C. A. and Oort, J. H. (1951). Observation of a Line in the Galactic Radio Spectrum: The Interstellar Hydrogen Line at 1,420 Mc./sec., and an Estimate of Galactic Rotation. Nature, 168:357–358.

National Research Council (2010). New Worlds, New Horizons in Astronomy and Astrophysics. The National Academies Press, Washington, DC. pg. 46.

Neben, A. R., Bradley, R. F., Hewitt, J. N., DeBoer, D. R., Parsons, A. R., Aguirre, J. E., Ali, Z. S., Cheng, C., Ewall-Wice, A., Patra, N., Thyagarajan, N., Bowman, J., Dickenson, R., Dillon, J. S., Doolittle, P., Egan, D., Hedrick, M., Jacobs, D. C., Kohn, S. A., Klima, P. J., Moodley, K., Saliwanchik, B. R. B., Schaffner, P., Shelton, J., Taylor, H. A., Taylor, R., Tegmark, M., Wirt, B., and Zheng, H. (2016a). The Hydrogen Epoch of Reionization Array Dish. I. Beam Pattern Measurements and Science Implications. , 826:199.

Neben, A. R., Hewitt, J. N., Bradley, R. F., Dillon, J. S., Bernardi, G., Bowman, J. D., Briggs, F., Cappallo, R. J., Corey, B. E., Deshpande, A. A., Goeke, R., Greenhill, L. J., Hazelton, B. J., Johnston-Hollitt, M., Kaplan, D. L., Lonsdale, C. J., McWhirter, S. R., Mitchell, D. A., Morales, M. F., Morgan, E., Oberoi, D., Ord, S. M., Prabu, T., Udaya Shankar, N., Srivani, K. S., Subrahmanyan, R., Tingay, S. J., Wayth, R. B., Webster, R. L., Williams, A., and Williams, C. L. (2016b). Beam-forming Errors in Murchison Widefield Array Phased Array Antennas and their Effects on Epoch of Reionization Science. , 820:44.

Newell, P. T., Greenwald, R. A., and Ruohoniemi, J. M. (2001). The Role of the Ionosphere in Aurora and Space Weather. Reviews of Geophysics, 39:137–149.

Nita, G. M. and Gary, D. E. (2010). The Generalized Spectral Kurtosis Estimator. , 406:L60–L64.

Nita, G. M., Gary, D. E., Liu, Z., Hurford, G. J., and White, S. M. (2007). Radioq frequency interference excision using spectral-domain statistics. Publications of the Astronomical Society of the Pacific, 119(857):805–827.

Norton, D. E. and Podell, A. F. (1975). Transistor amplifier with impedance matching transformer. US Patent 3,891,934.

Oesch, P. A., Bouwens, R. J., Illingworth, G. D., Labbé, I., Trenti, M., Gonzalez, V., Carollo, C. M., Franx, M., van Dokkum, P. G., and Magee, D. (2012). Expanded Search for $z \sim 10$ Galaxies from HUDF09, ERS, and CANDELS Data: Evidence for Accelerated Evolution at $z > 8$? Astrophys. J., 745:110.

Oesch, P. A., Brammer, G., van Dokkum, P. G., Illingworth, G. D., Bouwens, R. J., Labbé, I., Franx, M., Momcheva, I., Ashby, M. L. N., Fazio, G. G., Gonzalez, V., Holden, B., Magee, D., Skelton, R. E., Smit, R., Spitler, L. R., Trenti, M., and Willner, S. P. (2016). A Remarkably Luminous Galaxy at $z = 11.1$ Measured with Hubble Space Telescope Grism Spectroscopy. Astrophys. J., 819:129.

Offringa, A. R., de Bruyn, A. G., Zaroubi, S., Koopmans, L. V. E., Wijnholds, S. J., Abdalla, F. B., Brouw, W. N., Ciardi, B., Iliev, I. T., Harker, G. J. A., Mellema, G., Bernardi, G., Zarka, P., Ghosh, A., Alexov, A., Anderson, J., Asgekar, A., Avruch, I. M., Beck, R., Bell, M. E., Bell, M. R., Bentum, M. J., Best, P., Bîrzan, L., Breitling, F., Broderick, J., Brüggen, M., Butcher, H. R., de Gasperin, F., de Geus, E., de Vos, M., Duscha, S., Eislöffel, J., Fallows, R. A., Ferrari, C., Frieswijk, W., Garrett, M. A., Grießmeier, J., Hassall, T. E., Horneffer, A., Iacobelli, M., Juette, E., Karastergiou, A., Klijn, W., Kondratiev, V. I., Kuniyoshi, M., Kuper, G., van Leeuwen, J., Loose, M., Maat, P.,

Macario, G., Mann, G., McKean, J. P., Meulman, H., Norden, M. J., Orru, E., Paas, H., Pandey-Pommier, M., Pizzo, R., Polatidis, A. G., Rafferty, D., Reich, W., van Nieuwpoort, R., Röttgering, H., Scaife, A. M. M., Sluman, J., Smirnov, O., Sobey, C., Tagger, M., Tang, Y., Tasse, C., Veen, S. t., Toribio, C., Vermeulen, R., Vocks, C., van Weeren, R. J., Wise, M. W., and Wucknitz, O. (2013). The Brightness and Spatial Distributions of Terrestrial Radio Sources. Mon. Not. R. Astron. Soc., 435:584–596.

Oort, J. H. (1984). Superclusters at Large Redshifts - Can Protosuperclusters and the Birth of 'Pancakes' be Observed? Astron. Astrophys., 139:211–214.

Ottonello, C. and Pagnan, S. (1994). Modified frequency domain kurtosis for signal processing. Electronics Letters, 30(14):1117–1118.

Paciga, G., Chang, T.-C., Gupta, Y., Nityanada, R., Odegova, J., Pen, U.-L., Peterson, J. B., Roy, J., and Sigurdson, K. (2011). The GMRT Epoch of Reionization Experiment: A New Upper Limit on the Neutral Hydrogen Power Spectrum at $z \sim 8.6$. Mon. Not. R. Astron. Soc., 413:1174–1183.

Parashare, C. and Bradley, R. F. (2005). Instrument development for paper: A precision array to probe the epoch of reionization. Technical report.

Parsons, A. R., Backer, D. C., Foster, G. S., Wright, M. C. H., Bradley, R. F., Gugliucci, N. E., Parashare, C. R., Benoit, E. E., Aguirre, J. E., Jacobs, D. C., Carilli, C. L., Herne, D., Lynch, M. J., Manley, J. R., and Werthimer, D. J. (2010). The Precision Array for Probing the Epoch of Re-ionization: Eight Station Results. Astron. J., 139:1468–1480.

Parsons, A. R., Pober, J. C., Aguirre, J. E., Carilli, C. L., Jacobs, D. C., and Moore, D. F. (2012). A Per-baseline, Delay-spectrum Technique for Accessing the 21 cm Cosmic Reionization Signature. , 756:165.

Patra, N., Subrahmanyan, R., Raghunathan, A., and Udaya Shankar, N. (2013). SARAS: A Precision System for Measurement of the Cosmic Radio Background and Signatures from the Epoch of Reionization. Experimental Astronomy, 36:319–370.

Petrovic, N. and Oh, S. P. (2011). Systematic Effects of Foreground Removal in 21-cm Surveys of Reionization. Mon. Not. R. Astron. Soc., 413:2103–2120.

Planck Collaboration, Ade, P. A. R., Aghanim, N., Alves, M. I. R., Armitage-Caplan, C., Arnaud, M., Ashdown, M., Atrio-Barandela, F., Aumont, J., Aussel, H., and et al. (2014). Planck 2013 Results. I. Overview of Products and Scientific Results. 571:A1.

Planck Collaboration, Ade, P. A. R., Aghanim, N., Arnaud, M., Ashdown, M., Aumont, J., Baccigalupi, C., Banday, A. J., Barreiro, R. B., Bartlett, J. G., and et al. (2016). Planck 2015 Results. XIII. Cosmological Parameters. Astron. Astrophys., 594:A13.

Pober, J. C., Liu, A., Dillon, J. S., Aguirre, J. E., Bowman, J. D., Bradley, R. F., Carilli, C. L., DeBoer, D. R., Hewitt, J. N., Jacobs, D. C., McQuinn, M., Morales, M. F., Parsons, A. R., Tegmark, M., and Werthimer, D. J. (2014). What Next-generation 21 cm Power

Spectrum Measurements can Teach us About the Epoch of Reionization. Astrophys. J., 782:66.

Pritchard, J. R. and Furlanetto, S. R. (2007). 21-cm Fluctuations from Inhomogeneous X-ray Heating Before Reionization. Mon. Not. R. Astron. Soc., 376:1680–1694.

Pritchard, J. R. and Loeb, A. (2010). Constraining the Unexplored Period between the Dark Ages and Reionization with Observations of the Global 21 cm Signal. Phys. Rev. D, 82(2):023006.

Pritchard, J. R. and Loeb, A. (2012). 21 cm Cosmology in the 21st Century. Reports on Progress in Physics, 75(8):086901.

Purcell, E. M. and Field, G. B. (1956). Influence of Collisions upon Population of Hyperfine States in Hydrogen. Astrophys. J., 124:542.

Rogers, A. E. E. and Bowman, J. D. (2008). Spectral Index of the Diffuse Radio Background Measured from 100 to 200 MHz. Astron. J., 136:641–648.

Rogers, A. E. E., Bowman, J. D., Vierinen, J., Monsalve, R., and Mozdzen, T. (2015). Radiometric Measurements of Electron Temperature and Opacity of Ionospheric Perturbations. Radio Science, 50:130–137.

Sauer, H. H. and Wilkinson, D. C. (2008). Global mapping of ionospheric hf/vhf radio wave absorption due to solar energetic protons. Space Weather, 6(12).

Schoenwald, A. J., Bradley, D. C., Mohammed, P. N., Piepmeier, J. R., and Wong, M. (2016). Performance Analysis of a Hardware Implemented Complex Signal Kurtosis Radio-frequency Interference Detector. In Microwave Radiometry and Remote Sensing of the Environment (MicroRad), 2016 14th Specialist Meeting on, pages 71–75. IEEE.

Scott, D. and Rees, M. J. (1990). The 21-cm Line at High Redshift: a Diagnostic for the Origin of Large Scale Structure. Mon. Not. R. Astron. Soc., 247:510.

Shaver, P. A., Windhorst, R. A., Madau, P., and de Bruyn, A. G. (1999). Can the Reionization Epoch be Detected as a Global Signature in the Cosmic Background? Astron. Astrophys., 345:380–390.

Simpson, G., Ballo, D., Dunsmore, J., and Ganwani, A. (2008). A new noise parameter measurement method results in more than 100x speed improvement and enhanced measurement accuracy. In 2008 72nd ARFTG Microwave Measurement Symposium, pages 119–127.

Singh, S., Subrahmanyan, R., Udaya Shankar, N., Sathyanarayana Rao, M., Fialkov, A., Cohen, A., Barkana, R., Girish, B. S., Raghunathan, A., Somashekar, R., and Srivani, K. S. (2017). SARAS 2 Constraints on Global 21-cm Signals from the Epoch of Reionization. ArXiv e-prints.

Smith, F. J. (1966). Spin-change in O-H Collisions. Planet. Space Sci., 14:937–946.

Smoot, G., Bennett, C., Weber, R., Maruschak, J., Ratliff, R., Janssen, M., Chitwood, J., Hilliard, L., Lecha, M., Mills, R., Patschke, R., Richards, C., Backus, C., Mather, J., Hauser, M., Weiss, R., Wilkinson, D., Gulkis, S., Boggess, N., Cheng, E., Kelsall, T., Lubin, P., Meyer, S., Moseley, H., Murdock, T., Shafer, R., Silverberg, R., and Wright, E. (1990). COBE Differential Microwave Radiometers - Instrument Design and Implementation. Astrophys. J., 360:685–695.

Sokolowski, M., Tremblay, S. E., Wayth, R. B., Tingay, S. J., Clarke, N., Roberts, P., Waterson, M., Ekers, R. D., Hall, P., Lewis, M., Mossammaparast, M., Padhi, S., Schlagenhauferq, F., Sutinjo, A., and Tickner, J. (2015a). BIGHORNS - Broadband Instrument for Global HydrOgen ReioNisation Signal. , 32:e004.

Sokolowski, M., Wayth, R. B., Tremblay, S. E., Tingay, S. J., Waterson, M., Tickner, J., Emrich, D., Schlagenhaufer, F., Kenney, D., and Padhi, S. (2015b). The Impact of the Ionosphere on Ground-based Detection of the Global Epoch of Reionization Signal. , 813:18.

Spergel, D. N., Bean, R., Doré, O., Nolta, M. R., Bennett, C. L., Dunkley, J., Hinshaw, G., Jarosik, N., Komatsu, E., Page, L., Peiris, H. V., Verde, L., Halpern, M., Hill, R. S., Kogut, A., Limon, M., Meyer, S. S., Odegard, N., Tucker, G. S., Weiland, J. L., Wollack, E., and Wright, E. L. (2007). Three-Year Wilkinson Microwave Anisotropy Probe (WMAP) Observations: Implications for Cosmology. Astrophys. J., Suppl. Ser., 170:377–408.

Spergel, D. N., Verde, L., Peiris, H. V., Komatsu, E., Nolta, M. R., Bennett, C. L., Halpern, M., Hinshaw, G., Jarosik, N., Kogut, A., Limon, M., Meyer, S. S., Page, L., Tucker, G. S., Weiland, J. L., Wollack, E., and Wright, E. L. (2003). First-Year Wilkinson Microwave Anisotropy Probe (WMAP) Observations: Determination of Cosmological Parameters. Astrophys. J., Suppl. Ser., 148:175–194.

Stecher, T. P. and Williams, D. A. (1967). Photodestruction of Hydrogen Molecules in HI Regions. , 149:L29.

Sunyaev, R. A. and Zeldovich, I. B. (1975). On the Possibility of Radioastronomical Investigation of the Birth of Galaxies. Mon. Not. R. Astron. Soc., 171:375–379.

Sunyaev, R. A. and Zeldovich, Y. B. (1972). Formation of Clusters of Galaxies; Protocluster Fragmentation and Intergalactic Gas Heating. Astron. Astrophys., 20:189.

Swarup, G. and Subrahmanyan, R. (1987). Search for Proto-clusters at Meter Wavelengths. In Hewitt, A., Burbidge, G., and Fang, L. Z., editors, Observational Cosmology, volume 124 of IAU Symposium, pages 441–444.

Switzer, E. R. and Liu, A. (2014). Erasing the Variable: Empirical Foreground Discovery for Global 21 cm Spectrum Experiments. , 793:102.

Tauscher, K., Rapetti, D., Burns, J. O., and Switzer, E. R. (2018). Global 21-cm Signal Extraction from Foreground and Instrumental Effects I: Pattern Recognition Framework for Separation Using Training Sets. Astrophys. J., 853:187–196.

Tegmark, M. and Efstathiou, G. (1996). A Method for Subtracting Foregrounds from Multifrequency CMB Sky Maps. , 281:1297–1314.

Tegmark, M., Eisenstein, D. J., Hu, W., and de Oliveira-Costa, A. (2000). Foregrounds and Forecasts for the Cosmic Microwave Background. Astrophys. J., 530:133–165.

Tegmark, M., Silk, J., Rees, M. J., Blanchard, A., Abel, T., and Palla, F. (1997). How Small Were the First Cosmological Objects? Astrophys. J., 474:1.

Tingay, S. J., Goeke, R., Bowman, J. D., Emrich, D., Ord, S. M., Mitchell, D. A., Morales, M. F., Booler, T., Crosse, B., Wayth, R. B., Lonsdale, C. J., Tremblay, S., Pallot, D., Colegate, T., Wicenec, A., Kudryavtseva, N., Arcus, W., Barnes, D., Bernardi, G., Briggs, F., Burns, S., Bunton, J. D., Cappallo, R. J., Corey, B. E., Deshpande, A., Desouza, L., Gaensler, B. M., Greenhill, L. J., Hall, P. J., Hazelton, B. J., Herne, D., Hewitt, J. N., Johnston-Hollitt, M., Kaplan, D. L., Kasper, J. C., Kincaid, B. B., Koenig, R., Kratzenberg, E., Lynch, M. J., Mckinley, B., Mcwhirter, S. R., Morgan, E., Oberoi, D., Pathikulangara, J., Prabu, T., Remillard, R. A., Rogers, A. E. E., Roshi, A., Salah, J. E., Sault, R. J., Udaya-Shankar, N., Schlagenhaufer, F., Srivani, K. S., Stevens, J., Subrahmanyan, R., Waterson, M., Webster, R. L., Whitney, A. R., Williams, A., Williams, C. L., and Wyithe, J. S. B. (2013). The Murchison Widefield Array: The Square Kilometre Array Precursor at Low Radio Frequencies. Proc. Astron. Soc. Aust., 30:7.

Trippe, S. (2014). [Review] Polarization and Polarimetry. Journal of Korean Astronomical Society, 47:15–39.

van Bemmel, I. (2007). Ionosperic Limits for LOFAR and SKA. In From Planets to Dark Energy: the Modern Radio Universe, page 12.

Van de Hulst, H. C. (1945). Radio waves from space. Ned. Tijdschr. Natuurk, 11:210–221.

van Haarlem, M. P., Wise, M. W., Gunst, A. W., Heald, G., McKean, J. P., Hessels, J. W. T., de Bruyn, A. G., Nijboer, R., Swinbank, J., Fallows, R., Brentjens, M., Nelles, A., Beck, R., Falcke, H., Fender, R., Hörandel, J., Koopmans, L. V. E., Mann, G., Miley, G., Röttgering, H., Stappers, B. W., Wijers, R. A. M. J., Zaroubi, S., van den Akker, M., Alexov, A., Anderson, J., Anderson, K., van Ardenne, A., Arts, M., Asgekar, A., Avruch, I. M., Batejat, F., Bähren, L., Bell, M. E., Bell, M. R., van Bemmel, I., Bennema, P., Bentum, M. J., Bernardi, G., Best, P., Bîrzan, L., Bonafede, A., Boonstra, A.-J., Braun, R., Bregman, J., Breitling, F., van de Brink, R. H., Broderick, J., Broekema, P. C., Brouw, W. N., Brüggen, M., Butcher, H. R., van Cappellen, W., Ciardi, B., Coenen, T., Conway, J., Coolen, A., Corstanje, A., Damstra, S., Davies, O., Deller, A. T., Dettmar, R.-J., van Diepen, G., Dijkstra, K., Donker, P., Doorduin, A., Dromer, J., Drost, M., van Duin, A., Eislöffel, J., van Enst, J., Ferrari, C., Frieswijk, W., Gankema, H., Garrett, M. A., de Gasperin, F., Gerbers, M., de Geus, E., Grießmeier, J.-M., Grit, T., Gruppen, P.,

Hamaker, J. P., Hassall, T., Hoeft, M., Holties, H. A., Horneffer, A., van der Horst, A., van Houwelingen, A., Huijgen, A., Iacobelli, M., Intema, H., Jackson, N., Jelic, V., de Jong, A., Juette, E., Kant, D., Karastergiou, A., Koers, A., Kollen, H., Kondratiev, V. I., Kooistra, E., Koopman, Y., Koster, A., Kuniyoshi, M., Kramer, M., Kuper, G., Lambropoulos, P., Law, C., van Leeuwen, J., Lemaitre, J., Loose, M., Maat, P., Macario, G., Markoff, S., Masters, J., McFadden, R. A., McKay-Bukowski, D., Meijering, H., Meulman, H., Mevius, M., Middelberg, E., Millenaar, R., Miller-Jones, J. C. A., Mohan, R. N., Mol, J. D., Morawietz, J., Morganti, R., Mulcahy, D. D., Mulder, E., Munk, H., Nieuwenhuis, L., van Nieuwpoort, R., Noordam, J. E., Norden, M., Noutsos, A., Offringa, A. R., Olofsson, H., Omar, A., Orrú, E., Overeem, R., Paas, H., Pandey-Pommier, M., Pandey, V. N., Pizzo, R., Polatidis, A., Rafferty, D., Rawlings, S., Reich, W., de Reijer, J.-P., Reitsma, J., Renting, G. A., Riemers, P., Rol, E., Romein, J. W., Roosjen, J., Ruiter, M., Scaife, A., van der Schaaf, K., Scheers, B., Schellart, P., Schoenmakers, A., Schoonderbeek, G., Serylak, M., Shulevski, A., Sluman, J., Smirnov, O., Sobey, C., Spreeuw, H., Steinmetz, M., Sterks, C. G. M., Stiepel, H.-J., Stuurwold, K., Tagger, M., Tang, Y., Tasse, C., Thomas, I., Thoudam, S., Toribio, M. C., van der Tol, B., Usov, O., van Veelen, M., van der Veen, A.-J., ter Veen, S., Verbiest, J. P. W., Vermeulen, R., Vermaas, N., Vocks, C., Vogt, C., de Vos, M., van der Wal, E., van Weeren, R., Weggemans, H., Weltevrede, P., White, S., Wijnholds, S. J., Wilhelmsson, T., Wucknitz, O., Yatawatta, S., Zarka, P., Zensus, A., and van Zwieten, J. (2013). LOFAR: The LOw-Frequency ARray. Astron. Astrophys., 556:A2.

Vedantham, H. K., Koopmans, L. V. E., de Bruyn, A. G., Wijnholds, S. J., Brentjens, M., Abdalla, F. B., Asad, K. M. B., Bernardi, G., Bus, S., Chapman, E., Ciardi, B., Daiboo, S., Fernandez, E. R., Ghosh, A., Harker, G., Jelic, V., Jensen, H., Kazemi, S., Lambropoulos, P., Martinez-Rubi, O., Mellema, G., Mevius, M., Offringa, A. R., Pandey, V. N., Patil, A. H., Thomas, R. M., Veligatla, V., Yatawatta, S., Zaroubi, S., Anderson, J., Asgekar, A., Bell, M. E., Bentum, M. J., Best, P., Bonafede, A., Breitling, F., Broderick, J., Brüggen, M., Butcher, H. R., Corstanje, A., de Gasperin, F., de Geus, E., Deller, A., Duscha, S., Eislöffel, J., Engels, D., Falcke, H., Fallows, R. A., Fender, R., Ferrari, C., Frieswijk, W., Garrett, M. A., Grießmeier, J., Gunst, A. W., Hassall, T. E., Heald, G., Hoeft, M., Hörandel, J., Iacobelli, M., Juette, E., Kondratiev, V. I., Kuniyoshi, M., Kuper, G., Mann, G., Markoff, S., McFadden, R., McKay-Bukowski, D., McKean, J. P., Mulcahy, D. D., Munk, H., Nelles, A., Norden, M. J., Orru, E., Pandey-Pommier, M., Pizzo, R., Polatidis, A. G., Reich, W., Renting, A., Röttgering, H., Schwarz, D., Shulevski, A., Smirnov, O., Stappers, B. W., Steinmetz, M., Swinbank, J., Tagger, M., Tang, Y., Tasse, C., ter Veen, S., Thoudam, S., Toribio, C., Vocks, C., Wise, M. W., Wucknitz, O., and Zarka, P. (2015). Lunar Occultation of the Diffuse Radio Sky: LOFAR Measurements between 35 and 80 MHz. Mon. Not. R. Astron. Soc., 450:2291–2305.

Vedantham, H. K., Koopmans, L. V. E., de Bruyn, A. G., Wijnholds, S. J., Ciardi, B., and Brentjens, M. A. (2014). Chromatic Effects in the 21 cm Global Signal from the Cosmic Dawn. , 437:1056–1069.

Voytek, T. C., Natarajan, A., Jáuregui García, J. M., Peterson, J. B., and López-Cruz,

O. (2014). Probing the Dark Ages at $z \sim 20$: The SCI-HI 21 cm All-sky Spectrum Experiment. Astrophys. J., Lett., 782:L9.

Vrabie, V., Granjon, P., Servière, C., et al. (2003). Spectral kurtosis: from definition to application.

Westfold, K. C. (1959). The Polarization of Synchrotron Radiation. Astrophys. J., 130:241.

Wilson, T. L., Rohlfs, K., and Hüttemeister, S. (2009). Tools of Radio Astronomy. 5th ed; Berlin, Germany: Springer-Verlag.

Wolleben, M., Landecker, T. L., Reich, W., and Wielebinski, R. (2006). An Absolutely Calibrated Survey of Polarized Emission from the Northern Sky at 1.4 GHz. Observations and Data Reduction. , 448:411–424.

Wouthuysen, S. A. (1952). On the Excitation Mechanism of the 21-cm (Radio-frequency) Interstellar Hydrogen Emission Line. Astron. J., 57:31–32.

Zygelman, B. (2005). Hyperfine Level-changing Collisions of Hydrogen Atoms and Tomography of the Dark Age Universe. Astrophys. J., 622:1356–1362.

Appendix A

Acronyms

ADC	Analog to Digital Converter
AUT	Antenna Under Test
BE	Back-end or Back End
BH4	4-term Blackman-Harris
BPF	Band Pass Filter
CEM	Computational Electromagnetics
CMB	Cosmic Microwave Background
CSK	Complex Signal Kurtosis
CR	Cosmic Ray
DAC	Digital to Analog Converter
DAQ	Data Acquisition
DM	Dark Matter
DUT	Device Under Test
FE	Front-end or Front End
FFT	Fast Fourier Transform
FFTW	Fastest Fourier Transform in the West
FM	Frequency Modulated
FOM	Figure of Merit
FOV	Field of View

FPGA	Field Programmable Gate Array
GPIB	General Purpose Interface Bus
HDD	Hard Disk Drive
HP	Hewlett-Packard
IGM	Intergalactic Medium
IXR	Intrinsic Cross Polarization
LNA	Low Noise Amplifier
LST	Local Sidereal Time
MCMC	Monte Carlo Markov Chain
MMIC	Monolithic Microwave Integrated Circuit
NCP	North Celestial Pole
NFA	Noise Figure Analyzer
PCA	Principle Component Analysis
PID	Proportional Integral Derivative
PIPE	Projection-Induced Polarization Effect
RBW	Resolution bandwidth, $\Delta\nu$
RF	Radio Frequency
RFI	Radio Frequency Interference
SCP	South Celestial Pole
SFR	Star Formation Rate
SK	Spectral Kurtosis
SNR	Supernova Eemnants
SVD	Singular Value Decomposition
S/N	Signal-to-Noise Ratio
TEC	Total Electron Content
VNA	Vector Network Analyzer
WF	Wouthuysen-Field

Appendix B

Frequency Definition Chart

To adhere to common terminology used in 21-cm cosmology literature, I refer low frequency as any frequency below 200 MHz throughout this thesis. However, according to both the IEEE (Institute for Electrical and Electronic Engineers) and ITU (International Telecommunication Union) standards, it is within the designated VHF (very high frequency) band, as shown in the tables below.

Table B.1: Frequency bands designated by the IEEE Standard 521-2002

Freq. Range	**Wavelength**	**Designation**	**IEEE**
3-30 MHz	100-10 m	High freq.	HF
30-300 MHz	10-1 m	Very high freq.	VHF
300 MHz - 1 GHz	1 m - 30 cm	Ultra high freq.	UHF
1-2 GHz	30-15 cm	Long wave	L
2-4 GHz	15-5 cm	Short wave	S
4-8 GHz	5-3.75 cm	Compromise between S & X	C
8-12 GHz	3.75-2.5 cm	_	X
12-18 GHz	2.5-1.6 cm	Kurz-under	K_u
18-26 GHz	1.6-1.2 cm	Kurz (German for "short")	K
26-40 GHz	1.2 cm - 750 mm	Kurz-above	K_a
40-75 GHz	750-40 mm	_	V
75-11 GHz	40-28 mm	_	W
Above 111 GHz	below 28 mm	Millimeter	mm

Table B.2: Frequency bands designated by the ITU standards, note the overlapping bands between the ITU and IEEE definitions

Freq. Range	**Designation**	**Abbrev.**	**ITU**	**IEEE**
3-30 Hz	Extremely low freq.	ELF	1	_
30-300 Hz	Super low freq.	SLF	2	_
300 Hz - 3 kHz	Ultra low freq.	ULF	3	_
3-30 kHz	Very low freq.	VLF	4	_
30-300 kHz	Low freq.	LF	5	_
300 kHz - 3 MHz	Medium freq.	MF	6	MF
3-30 MHz	High freq.	HF	7	HF
30-300 MHz	Very high freq.	VHF	8	VHF
300 MHz - 3 GHz	Ultra high freq.	UHF	9	UHF, L, S
3-30 GHz	Super high freq.	SHF	10	S, C, X, K_u, K, K_a
30-300 GHz	Extremely high freq.	EHF	11	K_a, V, W, mm
300 GHz - 3 THz	Tremendously high freq.	THF	12	_

Appendix C

Kurtosis-based RFI Excision

C.1 Definition of Kurtosis

Kurtosis, in a similar way to the concept of **skewness**, is a statistical quantity that describes the shape of a probability distribution function (pdf). It is a measure of the "peakedness" of a pdf. However, the term kurtosis has been used interchangeably between kurtosis, which is based on the formalism of the Pearson moments, and a slightly different quantity called **excess kurtosis**.

The former is commonly defined as the fourth standardized moment[1] , also known as "Pearson's kurtosis",

$$\mathrm{K} = \beta_2 = \frac{m_4}{\sigma^4} = \frac{m_4}{m_2^2} \tag{C.1}$$

where the nth central moment $m_n = \langle (x - \langle x \rangle)^n \rangle$. For a normal distribution, $m_n = 1 \cdot 3 \cdot \ldots \cdot (n-1)\sigma^n$. This implies $\mathrm{K} = 3$ for a Gaussian pdf, independent of σ. A sample will have $|\mathrm{K} - 3| > \sqrt{\mathrm{Var(K)}}$ if it is drawn from a non-Gaussian pdf, where Var(K) is the variance of K. The excess kurtosis (γ_2), or "Fisher's kurtosis"[2] , is defined as

$$\gamma_2 = \beta_2 - 3 = \frac{m_4}{m_2^2} - 3 \tag{C.2}$$

[1] A nth standardized moment of a pdf, as $\frac{m_n}{\sigma^n}$, where m_n is the nth moment about the mean (or central moment) and σ is the standard deviation. Noted that some time the nth central moment is denoted as μ_n, but we reserve that notation for the nth moments about the origin in this report.

[2] Historically, the kurtosis as $\gamma_2 = \beta_2 - 3$ is actually first defined by Karl Pearson in 1905 (Fiori and Zenga, 2009).

where $\gamma_2 = 0$ for a normal distribution because its β_2 equals 3.0. Implementations of kurtosis as non-Gaussian discriminator and RFI excision in signal processing hence are also developed based on both of definitions.

C.2 FDK or SK

Although there is a distinction between the **kurtosis** (K) in the time domain data and SK which is reserved for frequency domain data, they are mathematically equivalent. In practice, to estimate the Pearson kurtosis, the second and fourth central moments can be written in terms of the moments about the origin as

$$\widehat{m}_2 = \widehat{\mu}_2 - \widehat{\mu}_1^2 \tag{C.3}$$

$$\widehat{m}_4 = \widehat{\mu}_4 - 4\widehat{\mu}_3\widehat{\mu}_1 + 6\widehat{\mu}_2\widehat{\mu}_1^2 - 3\widehat{\mu}_1^4 \tag{C.4}$$

where $\widehat{\mu}_n = S_n/M$ is the estimator for the nth moment about the origin, and $S_n = \sum_{i=1}^{M} x_i^n$ is the nth power of the accumulated digitized voltage x_i after M number of samples. However, as seen in (C.4), four different orders of the averaged voltage are needed to calculate the $\widehat{m}_4$ for K. This means extra data for the extra moment estimators are saved during the data acquisition, which poses challenges to the real-time observation (De Roo, 2009). In addition, this kurtosis is calculated based on the cumulants of the voltage in time domain, but not in frequency domain as for most common observables like the power in the power spectral distribution (PSD).

When the kurtosis is estimated in the frequency domain data, only the averaged values of the power and its squares over M number of sample will be needed. Dwyer (1983) is the first one to employ frequency domain analysis for detecting non-Gaussian signals. The author points out that the real and imaginary part of the short-time Fourier transform (STFT) are zero-mean random variables. He used the moments about the origin of the real and imaginary parts of the FFT to define

$$\widehat{\mathrm{SK}}(f_k) = \frac{\langle A_k^4 \rangle}{\langle A_k^2 \rangle^2} \tag{C.5}$$

Table C.1: Comparison of different kurtosis estimators for RFI excision

SK Estimator	Def.	Data Used	Gauss. SK	Ref.
4^{th} moment, Eq. (C.5)	kurtosis	$\Re$[FFT] or $\Im$[FFT]	3	Dwyer (1983)
4^{th} moment, Eq. (C.6)	excess kurtosis	Mag(FFT)	0	Vrabie et al. (2003)
V_k^2, Eq. (C.17)	excess kurtosis	Mag(FFT)	1	Nita et al. (2007)

where A_k can be the real part of the STFT. This SK is expected to be exactly "3" for a Gaussian process. The author also suggested using a similar definition on the imaginary part of the STFT.

To simplify the outputs from the instrument to estimate the SK, (Ottonello and Pagnan, 1994) propose a modified definition based on the normalized fourth-order moment of the magnitudes of the STFT. Vrabie et al. (2003) point out that these estimators can be biased and hence they propose an unbiased version of the estimator,

$$\widehat{\mathrm{SK}}(f_k) = \frac{\langle |X_k|^4 \rangle - 2 \langle |X_k|^2 \rangle^2}{\langle |X_k|^2 \rangle^2} \tag{C.6}$$

where X_k is the FFT of the real discrete time random voltage and $|X_k|^2 \sim \widehat{P_k}$. This SK is expected to be zero for a Gaussian signal. However, it has been shown that this SK estimator does not reflect the purely real nature of the the data at discrete Fourier transform (DFT) coefficients at the DC and Nyquist frequencies (Antoni, 2006; Nita et al., 2007). To reconcile this discrepancy, Nita et al. (2007) propose a new unbiased SK estimator in terms of the spectral variability, V_k^2 that completely characterizes the statistical nature of a time-domain signal at all of its spectral components. These different SK estimators with the corresponding kurtosis definition are summarized in the following table.

C.3 Spectral Variability as SK

There two separate descriptions for the spectral variability SK estimator (Note that the kurtosis in this context). Nita et al. (2007) derive the original SK based on mathematical framework of spectral variability and its variance. Nita and Gary (2010) later proposed a

modified version for the SK estimator to accommodate the realistic data format output by many radio astronomical instruments. Although this modified version for the SK is adopted for the GB system, most of its description is similar to the original one, hence both will be summarized in the following.

C.3.1 Original Description

Nita et al. (2007) define their SK estimator for each frequency bin as

$$\widehat{\mathrm{SK}}(f_k) = \widehat{V}_k^2 = \frac{\widehat{\sigma}_k^2}{\widehat{\mu}_k^2} \tag{C.7}$$

where $\widehat{\sigma}_k^2 = \langle \widehat{P}_k^2 \rangle - \langle \widehat{P}_k \rangle$ and $\widehat{\mu}_k = \langle \widehat{P}_k \rangle$ are unbiased estimators for the variance and mean of the non-averaged power spectral density (PSD) estimate . These two estimators for the PSD can be rewritten as the sums of a number of M instantaneous PSD of N time-domain samples. By defining the sums as,

$$S_{1,k} = \sum_{i=1}^{M} \widehat{P}_{ki}, \qquad S_{2,k} = \sum_{i=1}^{M} \widehat{P}_{ki}^2 \tag{C.8}$$

where $\widehat{P}_{ki}$ is the PSD estimate with $k \in [0, N/2]$ and $i \in [1, M]$, Nita et al. (2007) define the unbiased estimators for μ_k and σ_k^2 as

$$\widehat{\mu}_k = \frac{S_{1,k}}{M}, \qquad \widehat{\sigma}_k^2 = \frac{MS_{2,k} - S_{1,k}^2}{M(M-1)} \tag{C.9}$$

Using these definitions, (C.7) becomes

$$\widehat{V}_k^2 = \frac{M}{M-1}\left(\frac{MS_{2,k}}{S_{1,k}^2} - 1\right) \tag{C.10}$$

As shown in Nita et al. (2007), the SK for Gaussian processes equals to "1". By comparing the deviation of SK estimator from "1" to the variance of the SK estimator, $\mathrm{Var}(\widehat{V}_k^2)$, the RFI in a given spectral bin can then be flagged. The authors find that the variance of the SK estimator is dependent on the particular shape of the time-domain windowing function,

$$\mathrm{Var}(\widehat{V}_k^2) = \frac{4M}{(M-1)^2}\left(1 + 5|W_{2k}|^2 - |W_{2k}|^4 + |W_{2k}|^6\right) \tag{C.11}$$

The RFI detection threshold is normally defined to be $|\widehat{V}_k^2 - 1| \leq 3\sigma$, where $\sigma = \sqrt{\mathrm{Var}(\widehat{V}_k^2)}$. In general, Nita et al. (2007) show that the $|W_{2k}| = 1$ at the DC and Niquist components; and $|W_{2k}| \approx 0$ at other bins. Therefore, with large M, (C.11) reduces to

$$\mathrm{Var}(\widehat{V}_k^2) \approx \begin{cases} 24/M & \text{if } k = 0, N/2 \\ 4/M & \text{if } k = 1, \ldots, (N/2 - 1) \end{cases} \tag{C.12}$$

In the context of the GB data format, if we are doing FFT for N time-domain samples, the power spectrum of each FFT of the samples will be the amplitude spectrum squared,

$$\widehat{P}_{ki} = \frac{|\mathrm{FFT(sample)}|^2}{N^2} = \frac{\Re[\mathrm{FFT(sample)}]^2 + \Im[\mathrm{FFT(sample)}]^2}{N^2} \tag{C.13}$$

So the finally saved power spectra, after being averaged over a set of M instantaneous PSD estimates, is

$$\langle \widehat{P}_{\mathrm{save}}(f_k) \rangle = \frac{\sum_{i=1}^{M} \widehat{P}_{ki}}{M} = \frac{\sum_{i=1}^{M} |\mathrm{FFT(sample)}|^2}{MN^2} \tag{C.14}$$

and the squared of M number of FFT averaged power spectra will be

$$\langle \widehat{P}^2_{\mathrm{save}}(f_k) \rangle = \frac{\sum_{i=1}^{M} \widehat{P}^2_{ki}}{M} = \frac{\sum_{i=1}^{M} |\mathrm{FFT(sample)}|^4}{MN^4} \tag{C.15}$$

These saved power and power squared can be related to the $S_{1,k}$ and $S_{2,k}$ as following,

$$S_{1,k} = M \langle \widehat{P}_{\mathrm{save}}(f_k) \rangle, \qquad S_{2,k} = M \langle \widehat{P}^2_{\mathrm{save}}(f_k) \rangle \tag{C.16}$$

Therefore, the $\widehat{V}_k^2$ is

$$\mathrm{SK} = \widehat{\mathrm{V}}^2_{\mathrm{k}} = \frac{\mathrm{M}+1}{\mathrm{M}-1} \left(\frac{\langle \widehat{\mathrm{P}}^2_{\mathrm{save}}(\mathrm{f_k}) \rangle}{\langle \widehat{\mathrm{P}}_{\mathrm{save}}(\mathrm{f_k}) \rangle^2} - 1 \right) \tag{C.17}$$

Then we can compute the $\widehat{V}_k^2$ as in (C.10) and compare it to the 3σ threshold.

However, in order to achieve this, it requires the experiment to save the power spectra and its squared values in high cadence. This can be impractical for implementing due to hardware limitation, such as limited space to store such a large amount of raw data. For most cases, a number of instantaneous FFT power spectra are averaged before saving. Nita and Gary (2010) have made the modifications to their SK estimator to accommodate such requirement.

C.3.2 Modified SK Estimator for Practical Applications

Nita and Gary (2010) provide a generalized spectral variability $\widehat{V}_k^2$ based on (C.10),

$$\widehat{V}_k^2 = \frac{MM_1d+1}{M-1}\left(\frac{MS_{2,k}}{S_{1,k}^2}-1\right) \tag{C.18}$$

where now $S_{1,k}$ and $S_{2,k}$ are redefined as

$$S_{1,k} = \sum_{i=1}^{M}\left(\frac{\sum_{j=1}^{M_1}\widehat{P}_{kj}}{M_1}\right)_i, \qquad S_{2,k} = \sum_{i=1}^{M}\left(\frac{\sum_{j=1}^{M_1}\widehat{P}_{kj}}{M_1}\right)_i^2 \tag{C.19}$$

where d is a constant that are set to 1 (for an exponential distribution) to reduce to (C.10), and M_1 is the number of instantaneous FFT spectra, and M is the number of consecutive outputs. This formalism will reduce to the original SK estimator if $M_1 = 1$, which is equivalent to only outputting single FFT spectra and then average them over M of them. Since the M and M_1 are canceled out when entering (C.18), the Ss can be rewritten as

$$S_{1,k} = \sum_{i=1}^{M}\left(\sum_{j=1}^{M_1}\widehat{P}_{kj}\right)_i, \qquad S_{2,k} = \sum_{i=1}^{M}\left(\sum_{j=1}^{M_1}\widehat{P}_{kj}\right)_i^2 \tag{C.20}$$

In the GB pipeline, the power spectra $\widehat{P}_{\text{save}}(f_k)$ and squared power spectra $\widehat{P}^2_{\text{save}}(f_k)$ will be saved after averaging over M_1 blocks of FFT and M consecutive outputs (or time stamps), (C.20). Hence, (C.20) become

$$S_{1,k} = MM_1\langle\widehat{P}_{\text{save}}(f_k)\rangle, \qquad S_{2,k} = MM_1^2\langle\widehat{P}^2_{\text{save}}(f_k)\rangle \tag{C.21}$$

where now in the new formalism,

$$\langle\widehat{P}_{\text{save}}(f_k)\rangle = \frac{\sum_{i=1}^{M}}{M}\left(\frac{\sum_{j=1}^{M_1}\widehat{P}_{kj}}{M_1}\right)_i = \frac{\sum_{i=1}^{M}}{M}\left[\frac{\sum_{j=1}^{M_1}|\text{FFT(sample)}|^2_{kj}}{M_1N^2}\right]_i \tag{C.22}$$

and

$$\langle\widehat{P}^2_{\text{save}}(f_k)\rangle = \frac{\sum_{i=1}^{M}}{M}\left(\frac{\sum_{j=1}^{M_1}\widehat{P}_{kj}}{M_1}\right)_i^2 = \frac{\sum_{i=1}^{M}}{M}\left\{\frac{\left[\sum_{j=1}^{M_1}|\text{FFT(sample)}|^2_{kj}\right]^2}{M_1^2N^4}\right\}_i \tag{C.23}$$

Therefore, the modified $\widehat{V}_k^2$ is

$$\widehat{V}_k^2 = \frac{MM_1d+1}{M-1}\left(\frac{\langle \widehat{P}^2_{\text{save}}(f_k)\rangle}{\langle \widehat{P}_{\text{save}}(f_k)\rangle^2} - 1\right) \tag{C.24}$$

This modified $\widehat{V}_k^2$ can still be compared to the $\text{Var}(\widehat{V}_k^2)$ in (C.11). Furthermore, as discussed in Nita et al. (2007), the SK estimator here can be considered as a second ordered statistics. Note there is the similarity between the two $\widehat{V}_k^2$ in (C.17) and (C.24). If we treat the $\widehat{P}_{\text{save}}(f_k)$ as the second moment, and the $\widehat{P}^2_{\text{save}}(f_k)$ as the fourth moment, then these descriptions of $\widehat{V}_k^2$ are mathematically equivalent to the definition of kurtosis in (C.1).

Appendix D

Correlation Spectrum Calibration and Stokes Spectra

To derive the formulae to convert the correlation spectra into equivalent temperatures, we first note that the complex E-fields for each polarization in the coherence matrix $\mathbf{C}(\nu, t_i)$ are equivalent to the complex antenna voltages, $\widetilde{V}_X(\nu, t_i)$ and $\widetilde{V}_Y(\nu, t_i)$, which are acquired from Fourier transforming the sampled antenna voltages. Furthermore, the power transducer gain $G_T(\nu, t_i)$ is defined as the square of the voltage gain $g_T(\nu, t_i)$, i.e., $G_T = g_T^2$. Meanwhile, the noise power $P_n(\nu, t_t)$ from the front-end (FE)[1] signal path can be written as the absolute square of the complex noise voltage $\widetilde{V}_n(\nu, t_i)$, and $P_n(\nu, t_i) = \langle|\widetilde{V}_n\widetilde{V}_n^*|\rangle = k_B\Delta\nu T_n(\nu, t_i)$. Hence the monochromatic E-fields of both polarizations can be parametrized as,

$$E_X(\nu, t_i) = \widetilde{V}_X(\nu, t_i) = g_{T,X}(\nu, t_i)\left(\widetilde{V}_{\mathrm{ant},X}(\nu, t_i) + \widetilde{V}_{n,X}(\nu, t_i)\right), \tag{D.1}$$

$$E_Y(\nu, t_i) = \widetilde{V}_Y(\nu, t_i) = g_{T,Y}(\nu, t_i)\left(\widetilde{V}_{\mathrm{ant},Y}(\nu, t_i) + \widetilde{V}_{n,Y}(\nu, t_i)\right), \tag{D.2}$$

where $\widetilde{V}_{\mathrm{ant}}(\nu, t_i)$ is the antenna voltage signal of each polarization when observing the sky, where $P_{\mathrm{ant}}(\nu, t_i) = \langle|\widetilde{V}_{\mathrm{ant}}\widetilde{V}_{\mathrm{ant}}^*|\rangle = k_B\Delta\nu T_{\mathrm{ant}}(\nu, t_i)$. With these two equations, we can write

[1] For the CTP, by definition, the FE includes the electronics from the input port of the RF module all the way to the end of the coaxial cable, right before it enters the Signatec digitizer, which is considered as the back-end (BE) in this case.

the correlation terms in the coherence matrix as,

$$\langle \widetilde{V}_X \widetilde{V}_X^* \rangle = G_{T,X} \left(\langle \widetilde{V}_{\mathrm{ant},X} \widetilde{V}_{\mathrm{ant},X}^* \rangle + \langle \widetilde{V}_{n,X} \widetilde{V}_{n,X}^* \rangle + \langle \widetilde{V}_{\mathrm{ant},X} \widetilde{V}_{n,X}^* \rangle + \langle \widetilde{V}_{\mathrm{ant},X}^* \widetilde{V}_{n,X} \rangle \right), \tag{D.3}$$

$$\langle \widetilde{V}_Y \widetilde{V}_Y^* \rangle = G_{T,Y} \left(\langle \widetilde{V}_{\mathrm{ant},Y} \widetilde{V}_{\mathrm{ant},Y}^* \rangle + \langle \widetilde{V}_{n,Y} \widetilde{V}_{n,Y}^* \rangle + \langle \widetilde{V}_{\mathrm{ant},Y} \widetilde{V}_{n,Y}^* \rangle + \langle \widetilde{V}_{\mathrm{ant},Y}^* \widetilde{V}_{n,Y} \rangle \right), \tag{D.4}$$

$$\langle \widetilde{V}_X \widetilde{V}_Y^* \rangle = \sqrt{G_{T,X} G_{T,Y}} \left(\langle \widetilde{V}_{\mathrm{ant},X} \widetilde{V}_{\mathrm{ant},Y}^* \rangle + \langle \widetilde{V}_{n,X} \widetilde{V}_{n,Y}^* \rangle + \langle \widetilde{V}_{\mathrm{ant},X} \widetilde{V}_{n,Y}^* \rangle + \langle \widetilde{V}_{\mathrm{ant},Y}^* \widetilde{V}_{n,X} \rangle \right), \tag{D.5}$$

$$\langle \widetilde{V}_Y \widetilde{V}_X^* \rangle = \sqrt{G_{T,X} G_{T,Y}} \left(\langle \widetilde{V}_{\mathrm{ant},X} \widetilde{V}_{\mathrm{ant},Y}^* \rangle + \langle \widetilde{V}_{n,Y} \widetilde{V}_{n,X}^* \rangle + \langle \widetilde{V}_{\mathrm{ant},Y} \widetilde{V}_{n,X}^* \rangle + \langle \widetilde{V}_{\mathrm{ant},X}^* \widetilde{V}_{n,Y} \rangle \right), \tag{D.6}$$

where the (ν, t_i) notation has been suppressed for the ease of reading, and the brackets are ensemble averages.

The equivalent antenna temperatures resulting from the powers of the auto-spectra and cross-spectra can be written as

$$T_{\mathrm{ant},XX} = \frac{\langle \widetilde{V}_{\mathrm{ant},X} \widetilde{V}_{\mathrm{ant},X}^* \rangle}{k_B \Delta\nu} = \frac{1}{k_B \Delta\nu} \left[\frac{\langle \widetilde{V}_X \widetilde{V}_X^* \rangle}{G_{T,X}} - T_{n,X} - 2\mathrm{Re} \left(\langle \widetilde{V}_{\mathrm{ant},X} \widetilde{V}_{n,X}^* \rangle \right) \right], \tag{D.7}$$

$$T_{\mathrm{ant},YY} = \frac{\langle \widetilde{V}_{\mathrm{ant},Y} \widetilde{V}_{\mathrm{ant},Y}^* \rangle}{k_B \Delta\nu} = \frac{1}{k_B \Delta\nu} \left[\frac{\langle \widetilde{V}_Y \widetilde{V}_Y^* \rangle}{G_{T,Y}} - T_{n,Y} - 2\mathrm{Re} \left(\langle \widetilde{V}_{\mathrm{ant},Y} \widetilde{V}_{n,Y}^* \rangle \right) \right], \tag{D.8}$$

$$\begin{aligned} T_{\mathrm{ant},XY} &= \frac{\langle \widetilde{V}_{\mathrm{ant},X} \widetilde{V}_{\mathrm{ant},Y}^* \rangle}{k_B \Delta\nu} \\ &= \frac{1}{k_B \Delta\nu} \left[\frac{\langle \widetilde{V}_X \widetilde{V}_Y^* \rangle}{\sqrt{G_{T,X} G_{T,Y}}} - \langle \widetilde{V}_{n,X} \widetilde{V}_{n,Y}^* \rangle - \langle \widetilde{V}_{\mathrm{ant},X} \widetilde{V}_{n,Y}^* \rangle - \langle \widetilde{V}_{\mathrm{ant},Y}^* \widetilde{V}_{n,X} \rangle \right], \end{aligned} \tag{D.9}$$

$$\begin{aligned} T_{\mathrm{ant},YX} &= \frac{\langle \widetilde{V}_{\mathrm{ant},Y} \widetilde{V}_{\mathrm{ant},X}^* \rangle}{k_B \Delta\nu} \\ &= \frac{1}{k_B \Delta\nu} \left[\frac{\langle \widetilde{V}_Y \widetilde{V}_X^* \rangle}{\sqrt{G_{T,X} G_{T,Y}}} - \langle \widetilde{V}_{n,Y} \widetilde{V}_{n,X}^* \rangle - \langle \widetilde{V}_{\mathrm{ant},Y} \widetilde{V}_{n,X}^* \rangle - \langle \widetilde{V}_{\mathrm{ant},X}^* \widetilde{V}_{n,Y} \rangle \right], \end{aligned} \tag{D.10}$$

The Stokes $I_{\mathrm{obs}}(\nu, t_i)$ and $Q_{\mathrm{obs}}(\nu, t_i)$ parameters hence can be computed with the auto-spectra

as,

$$
\begin{aligned}
I_{\rm obs} &= T_{{\rm ant},XX} + T_{{\rm ant},YY} \\
&= \frac{1}{k_B \Delta\nu} \left[\left(\frac{\langle \widetilde{V}_X \widetilde{V}_X^* \rangle}{G_{T,X}} + \frac{\langle \widetilde{V}_Y \widetilde{V}_Y^* \rangle}{G_{T,Y}} \right) - (T_{n,X} + T_{n,Y}) \right. \\
&\quad \left. -2{\rm Re}\left(\langle \widetilde{V}_{{\rm ant},X} \widetilde{V}_{n,X}^* \rangle \right) - 2{\rm Re}\left(\langle \widetilde{V}_{{\rm ant},Y} \widetilde{V}_{n,Y}^* \rangle \right) \right], \qquad \text{(D.11)} \\
Q_{\rm obs} &= T_{{\rm ant},XX} - T_{{\rm ant},YY} \\
&= \frac{1}{k_B \Delta\nu} \left[\left(\frac{\langle \widetilde{V}_X \widetilde{V}_X^* \rangle}{G_{T,X}} - \frac{\langle \widetilde{V}_Y \widetilde{V}_Y^* \rangle}{G_{T,Y}} \right) - (T_{n,X} - T_{n,Y}) \right. \\
&\quad \left. -2{\rm Re}\left(\langle \widetilde{V}_{{\rm ant},X} \widetilde{V}_{n,X}^* \rangle \right) + 2{\rm Re}\left(\langle \widetilde{V}_{{\rm ant},Y} \widetilde{V}_{n,Y}^* \rangle \right) \right], \qquad \text{(D.12)}
\end{aligned}
$$

Similarly, the Stokes $U_{\rm obs}(\nu, t_i)$ and $V_{\rm obs}(\nu, t_i)$ are computed from the cross-spectra as,

$$
\begin{aligned}
U_{\rm obs} &= T_{{\rm ant},XY} + T_{{\rm ant},YX} \\
&= \frac{1}{k_B \Delta\nu} \left[\left(\frac{\langle \widetilde{V}_X \widetilde{V}_Y^* \rangle}{\sqrt{G_{T,X} G_{T,Y}}} + \frac{\langle \widetilde{V}_Y \widetilde{V}_X^* \rangle}{\sqrt{G_{T,X} G_{T,Y}}} \right) - \left(\langle \widetilde{V}_{n,Y} \widetilde{V}_{n,X}^* \rangle + \langle \widetilde{V}_{n,X} \widetilde{V}_{n,Y}^* \rangle \right) \right. \\
&\quad \left. - \left(\langle \widetilde{V}_{{\rm ant},X} \widetilde{V}_{n,Y}^* \rangle + \langle \widetilde{V}_{{\rm ant},X}^* \widetilde{V}_{n,Y} \rangle \right) - \left(\langle \widetilde{V}_{{\rm ant},Y}^* \widetilde{V}_{n,X} \rangle + \langle \widetilde{V}_{{\rm ant},Y} \widetilde{V}_{n,X}^* \rangle \right) \right] \qquad \text{(D.13)} \\
&= \frac{1}{k_B \Delta\nu} \left[\frac{2{\rm Re}\left(\langle \widetilde{V}_X \widetilde{V}_Y^* \rangle \right)}{\sqrt{G_{T,X} G_{T,Y}}} - 2{\rm Re}\left(\langle \widetilde{V}_{n,X} \widetilde{V}_{n,Y}^* \rangle \right) - 2{\rm Re}\left(\langle \widetilde{V}_{{\rm ant},X} \widetilde{V}_{n,Y}^* \rangle \right) \right. \\
&\quad \left. -2{\rm Re}\left(\langle \widetilde{V}_{{\rm ant},Y} \widetilde{V}_{n,X}^* \rangle \right) \right], \qquad \text{(D.14)} \\
V_{\rm obs} &= j(T_{{\rm ant},XY} - T_{{\rm ant},YX}) \\
&= \frac{j}{k_B \Delta\nu} \left[\left(\frac{\langle \widetilde{V}_X \widetilde{V}_Y^* \rangle}{\sqrt{G_{T,X} G_{T,Y}}} - \frac{\langle \widetilde{V}_Y \widetilde{V}_X^* \rangle}{\sqrt{G_{T,X} G_{T,Y}}} \right) - \left(\langle \widetilde{V}_{n,Y} \widetilde{V}_{n,X}^* \rangle - \langle \widetilde{V}_{n,X} \widetilde{V}_{n,Y}^* \rangle \right) \right. \\
&\quad \left. - \left(\langle \widetilde{V}_{{\rm ant},X} \widetilde{V}_{n,Y}^* \rangle - \langle \widetilde{V}_{{\rm ant},X}^* \widetilde{V}_{n,Y} \rangle \right) - \left(\langle \widetilde{V}_{{\rm ant},Y}^* \widetilde{V}_{n,X} \rangle - \langle \widetilde{V}_{{\rm ant},Y} \widetilde{V}_{n,X}^* \rangle \right) \right] \qquad \text{(D.15)} \\
&= \frac{j}{k_B \Delta\nu} \left[\frac{2j{\rm Im}\left(\langle \widetilde{V}_X \widetilde{V}_Y^* \rangle \right)}{\sqrt{G_{T,X} G_{T,Y}}} - 2j{\rm Im}\left(\langle \widetilde{V}_{n,X} \widetilde{V}_{n,Y}^* \rangle \right) - 2j{\rm Im}\left(\langle \widetilde{V}_{{\rm ant},X} \widetilde{V}_{n,Y}^* \rangle \right) \right. \\
&\quad \left. -2j{\rm Im}\left(\langle \widetilde{V}_{{\rm ant},Y} \widetilde{V}_{n,X}^* \rangle \right) \right] \qquad \text{(D.16)}
\end{aligned}
$$

where $j = \sqrt{-1}$.

When the cross correlation between the noise terms in two polarizations, $\langle \widetilde{V}_{n,X} \widetilde{V}^*_{n,Y} \rangle$, in Eq. (D.14) and (D.16) averaged to zeros since the noise from two isolated signal paths for both polarization are uncorrelated, the other cross terms ($\langle \widetilde{V}_{\mathrm{ant},X} \widetilde{V}^*_{n,X} \rangle$, $\langle \widetilde{V}_{\mathrm{ant},Y} \widetilde{V}^*_{n,Y} \rangle$, $\langle \widetilde{V}_{\mathrm{ant},X} \widetilde{V}^*_{n,Y} \rangle$, $\langle \widetilde{V}_{\mathrm{ant},Y} \widetilde{V}^*_{n,X} \rangle$) do not necessarily averaged to zero. It is plausible for the noise temperature of the system to couple to the receiving signal, such as when the noise power is reflected internally within the FE stages and emits from one polarization to couple into the other polarization. This can be quantified by the beam's polarization leakage.

By design, symmetry of the sleeved dipole antenna ensures minimal cross-polarization leakage between the X and Y dipoles. This is evidenced by estimating the intrinsic cross-polarization ratio (IXR) (Carozzi and Woan, 2011) for the ground-parallel CST beam. The IXR is a figure of merit to determine the amount cross polarization leakage between the two dipoles

$$\mathrm{IXR} = \left(\frac{\sigma_{\max} + \sigma_{\min}}{\sigma_{\max} - \sigma_{\min}} \right)^2 = \left[\frac{\kappa(J) + 1}{\kappa(J) - 1} \right]^2 \tag{D.17}$$

where $\sigma_{\max}$ and $\sigma_{\min}$ are the maximum and minimum singular values of the Jones matrix J for the antenna beam as defined in Chapter 3.4.1, and the condition number $\kappa(J) = \sigma_{\max}/\sigma_{\min}$. The IXR measures the leakage between one polarization to another. The smaller the IXR is, the stronger the beam leakage is, where when IXR = 1 presented the total intrinsic leakage. As shown in Figure D.1, the IXR value for main beam of the sleeved dipole are large (> 20). This indicates that the beam for this antenna design is close to orthogonal and well balanced in terms of gains, with minimal leakage.

Hence it is adequate to assume the cross terms are relatively small for the purpose of constraining the foreground. However, extra care is needed when calibrating the system to achieve the sensitivity for the global 21-cm signal. Nonetheless, if the cross terms can be

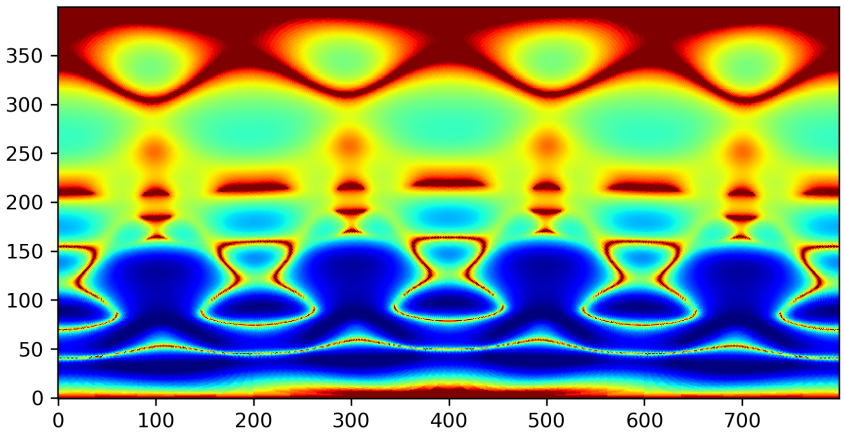

Figure D.1: The IXR values for the simulated CTP's sleeved dipole beam, when the ground plane is parallel to the soil slab, are shown here for 80 MHz. The vertical axis is θ and horizontal axis is ϕ. The red indicates regions of the beam that have IXR much larger than unity, hence no intrinsic cross-polarization leakage.

averaged away, the observed Stokes parameters reduce to the simpler form as,

$$I_{\rm obs} = \frac{1}{k_B \Delta\nu}\left[\left(\frac{\langle \widetilde{V}_X \widetilde{V}_X^* \rangle}{G_{T,X}} + \frac{\langle \widetilde{V}_Y \widetilde{V}_Y^* \rangle}{G_{T,Y}}\right) - (T_{n,X} + T_{n,Y})\right], \tag{D.18}$$

$$Q_{\rm obs} = \frac{1}{k_B \Delta\nu}\left[\left(\frac{\langle \widetilde{V}_X \widetilde{V}_X^* \rangle}{G_{T,X}} - \frac{\langle \widetilde{V}_Y \widetilde{V}_Y^* \rangle}{G_{T,Y}}\right) - (T_{n,X} - T_{n,Y})\right], \tag{D.19}$$

$$U_{\rm obs} = \frac{2}{k_B \Delta\nu}\frac{{\rm Re}\left(\langle \widetilde{V}_X \widetilde{V}_Y^* \rangle\right)}{\sqrt{G_{T,X} G_{T,Y}}}, \tag{D.20}$$

$$V_{\rm obs} = \frac{-2}{k_B \Delta\nu}\frac{{\rm Im}\left(\langle \widetilde{V}_X \widetilde{V}_Y^* \rangle\right)}{\sqrt{G_{T,X} G_{T,Y}}} \tag{D.21}$$